ABSTRACT

Title of dissertation: CONTRIBUTIONS TO THE
CHARACTERIZATION AND MITIGATION
OF ROTORCRAFT BROWNOUT

John Tritschler, Doctor of Philosophy, 2012

Dissertation directed by: Professor Roberto Celi
Department of Aerospace Engineering

Rotorcraft brownout, the condition in which the flow field of a rotorcraft mobilizes sediment from the ground to generate a cloud that obscures the pilot's field of view, continues to be a significant hazard to civil and military rotorcraft operations. This dissertation presents methodologies for: (i) the systematic mitigation of rotorcraft brownout through operational and design strategies and (ii) the quantitative characterization of the visual degradation caused by a brownout cloud.

In Part I of the dissertation, brownout mitigation strategies are developed through simulation-based brownout studies that are mathematically formulated within a numerical optimization framework. Two optimization studies are presented. The first study involves the determination of approach-to-landing maneuvers that result in reduced brownout severity. The second study presents a potential methodology for the design of helicopter rotors with improved brownout characteristics. The results of both studies indicate that the fundamental mechanisms underlying brownout mitigation are aerodynamic in nature, and the evolution of a ground vortex ahead of the rotor disk is seen to be a key element in the

development of a brownout cloud.

In Part II of the dissertation, brownout cloud characterizations are based upon the Modulation Transfer Function (MTF), a metric commonly used in the optics community for the characterization of imaging systems. The use of the MTF in experimentation is examined first, and the application of MTF calculation and interpretation methods to actual flight test data is described. The potential for predicting the MTF from numerical simulations is examined second, and an initial methodology is presented for the prediction of the MTF of a brownout cloud. Results from the experimental and analytical studies rigorously quantify the intuitively-known facts that the visual degradation caused by brownout is a space and time-dependent phenomenon, and that high spatial frequency features, i.e., fine-grained detail, are obscured before low spatial frequency features, i.e., large objects. As such, the MTF is a metric that is amenable to Handling Qualities (HQ) analyses.

Contributions to the Characterization
and Mitigation of Rotorcraft Brownout

by

John Kirwin Tritschler

Dissertation submitted to the Faculty of the Graduate School of the
University of Maryland, College Park in partial fulfillment
of the requirements for the degree of
Doctor of Philosophy
2012

Advisory Committee:
Professor Roberto Celi, Chair/Advisor
Alfred Gessow Professor Inderjit Chopra
Professor David Jacobs, Dean's Representative
Professor Sung Lee
Minta Martin Professor J. Gordon Leishman

Dedicated to my wife, Becky.

I can't wait to see what adventures come next.

Acknowledgments

I have been very fortunate to learn from some outstanding teachers over the course of my time at the University of Maryland. I am indebted to my advisor, Professor Roberto Celi, for being my coach in this marathon. I am also grateful to Professor Gordon Leishman, who was a "second advisor" in much of my research. It has been my pleasure to learn from, and collaborate with, both of them. I must also thank the other three members of my advisory committee, Professor Inderjit Chopra, Professor Sung Lee, and Professor David Jacobs. I had the privilege of taking courses taught by each and, to a greater or lesser extent, getting to know each of them on a personal level. I am thankful for both of these opportunities. Additionally, I must acknowledge the Air Force Office of Scientific Research, which supported this work under a Multidisciplinary University Research Initiative, Grant W911NF0410176. The contract monitor was Dr. Douglas Smith.

My colleagues made this experience most enjoyable. My research was closely linked to Monica Syal's, and she patiently explained various aspects of aerodynamics to me on multiple occasions. My research would not have been possible without her expertise, and I am grateful to her for her constant support. Ondrej Juhasz provided many opportunities to break from my research and engage in technical (or non-technical) discussions. With the completion of this dissertation, he officially owes me $20. Cal Sargent was likewise a source of much-needed diversions—it's a shame St. Patrick's day comes but once a year. I will also fondly remember discussions with Bharath Govindarajan, who was the only other morning person in the office, and with Kumar Ravichandran, with whom I enjoyed many post-lunch walks around campus. Jürgen Rauleder also provided

iii

Table of Contents

List of Tables

List of Figures

x

Nomenclature

Symbols

a	Particle radius (μm)
a_n, b_n	Scattering coefficients
A	Rotor disk area (ft^2), $A = \pi R^2$
A_a	Absorption coefficient (m^{-1})
$B(\mathbf{X})$	Brownout objective function
$\mathbf{B}$	Magnetic induction (T)
$b(\mathbf{X},t)$	Particle count in the "best" region of the pilot's field of view, $B(\mathbf{X}) = \int b(\mathbf{X},t)\,dt$
$\bar{b}(\mathbf{X},t)$	Normalized and smoothed $b(\mathbf{X},t)$
C_{abs}	Absorption cross section (m^2)
C_{ext}	Extinction cross section (m^2)
C_{sca}	Scattering cross section (m^2)
c	Blade chord (ft)
C_T	Rotor thrust coefficient, $C_T = T/\rho A(\Omega R)^2$
C_T/σ	Blade loading coefficient
D	Main rotor diameter (ft)
DL	Rotor disk loading (lb ft^{-2}), $DL = T/A$
$\mathbf{D}$	Electric displacement (C m^{-2})
$E(x,y)$	Helicopter edge mask
$\mathbf{E}$	Electric field (V m^{-1})
$\hat{e}_s$	Unit vector in the s-direction
$\mathbf{F}_d$	Drag force (lb)
$\mathbf{F}_g$	Gravitational force (lb)
$\mathbf{F}_i$	Interparticle force (lb)
$\mathbf{F}_l$	Lift force (lb)
$\mathbf{F}_{\Delta p}$	Pressure force (lb)
$\mathcal{F}[\ ]$	Fourier transform
$F(\mathbf{X})$	Additional design objective
G	Particle cross-sectional area (m^2)
$g(\mathbf{X})$	Constraint equation
g	Gravitational acceleration (ft s^{-2}), $g = 32.2$ ft s^{-2}
H	Irradiance (W m^{-2})
$\mathbf{H}$	Hessian matrix
$\mathbf{H}$	Magnetic Field (A m^{-1})
h	Rotor hub height above ground (ft)
I	Specific intensity (W m^{-2} ster^{-1} Hz^{-1})
i	Grayscale pixel value, $0 \le i \le 255$
$i_\perp, i_\parallel$	Dimensionless intensity parameters
$\mathbf{J}_F$	Current density (A m^{-2})
$[\mathbf{J}]$	Jacobian matrix
k	Wave number, $k = 2\pi/\lambda$

k	Grayscale threshold pixel value for image segmentation, $0 \leq k \leq 255$
k_r	Roughness height of the ground surface (m)
k_s	Reduced frequency of the convecting vortical wake
L	Optical path length (m)
$M(x,y)$	Correlation mask
$\boldsymbol{M}$	Magnetization (A m^{-1})
m	Complex refractive index, $m = n + i\kappa$
MTF_0	Initial MTF magnitude, $\mathrm{MTF}_0 = \mathrm{MTF}(0)$
$\overline{\mathrm{MTF}}_{\mathrm{macro}}$	Mean macrotexture MTF
$\overline{\mathrm{MTF}}_{\mathrm{micro}}$	Mean microtexture MTF
$\mathrm{MTF}_{\mathrm{prac}}$	Practical, instrumentation-based MTF
N	Number of particles per unit volume (μm^{-3})
N	Number of pixels in an image
N_b	Number of blades
N_x, N_y	Correlation mask size limits
n	Phase speed, i.e., the real part of refractive index m
n_{ent}	Number of entrained particles
n_i	Number of pixels in an image with a grayscale value of i
n_P	Number of particles
$n(x)$	Particle size distribution
$P(\theta)$	Normalized phase function
$P_n^m(\cos\theta)$	Legendre function
$\boldsymbol{P}$	Electric polarization (C m^{-2})
p_i	Probability that a pixel in an image will have a grayscale value of i
$\mathbf{p}_{\mathrm{app}}(\mathbf{X})$	Series of discrete points describing approach $\mathbf{X}$
$\mathbf{p}_{\mathrm{HV}}$	Series of discrete points describing the "avoid" region boundaries on a H-V diagram
$\mathbf{p}_{\mathrm{VRS}}$	Series of discrete points describing flight regime boundaries where VRS may occur
Q_{abs}	Absorption efficiency
Q_{ext}	Extinction efficiency
Q_{sca}	Scattering efficiency
R	Rotor radius (ft)
r	Longitudinal range from landing point (ft)
$\boldsymbol{r}$	Position vector (ft)
r_c	Vortex core radius (ft)
r_{pd}	Range from landing point at which peak deceleration occurs (ft)
$S(\omega_x, \omega_y)$	Fourier transform of the Point Spread Function
$\boldsymbol{S}$	Poynting vector (W m^{-2})
S_1, S_2	Complex amplitudes of the scattered electric fields
S_a	Scattering coefficient (m^{-1})
$s(x,y)$	Point Spread Function
T	Rotor thrust (lb)
$[T]$	Transformation matrix

T_{eff}	Effective optical depth, $T_{\text{eff}} = -\ln\left(\text{MTF}\left(\infty\right)\right)$
T_x, T_y	Correlation mask translation limits (pixels)
t	Time (s)
$u(z)$	Boundary layer profile (m s^{-1})
$u_\star$	Friction velocity (ft s^{-1})
$u_{\star t}$	Threshold friction velocity (ft s^{-1})
$\mathbf{V}$	Velocity induced at a point by a vortex element (ft s^{-1})
V_θ	Swirl velocity (ft s^{-1})
v_0	Initial (asymptotic) velocity (ft s^{-1} or kts)
v_d	Descent velocity (ft s^{-1})
W	Power, i.e., rate of change of energy transfer (W)
w	Average downwash velocity (ft s^{-1}), $w = 2\sqrt{T/2\rho A}$
$\mathbf{X}$	Vector of design variables for trajectory optimization, $\mathbf{X} = [\alpha_{\text{app}} \; v_0 \; r_{\text{pd}}]^T$
X_u	Aircraft stability derivative $\partial X/\partial u$
x	Particle size parameter, $x = 2\pi a/\lambda$
z	Path length (m)
$z_n(\rho)$	Bessel function
α_{app}	Approach angle (deg)
β	Blade flapping angle (deg)
β_{1c}	Lateral blade flap angle (deg)
β_{1s}	Longitudinal blade flap angle (deg)
Γ	Vortex circulation strength (ft^2 s^{-1})
Γ_w	Total wake strength (ft^2 s^{-1}), $\Gamma_w = N_b\Gamma_v = N_b k (C_T/\sigma)(\Omega R)c$
δ	Eddy viscosity coefficient
ε	Tolerance value for defining behavior constraints
ε	Complex permittivity (F m^{-1}
$\varepsilon_{\text{conv}}$	Optimization convergence tolerance
ε_0	Permittivity of free space (F m^{-1}
ζ	Wake age of a vortex filament (deg)
θ	Aircraft pitch angle (deg)
θ	Scattering angle (deg)
θ_0	Collective pitch angle (deg)
θ_{1c}	Lateral cyclic angle (deg)
θ_{1s}	Longitudinal cyclic angle (deg)
θ_P, ϕ_P, ρ	Particle location (azimuth, elevation, distance) in a spherical coordinate system (deg)
κ	Extinction coefficient or absorption loss, i.e., the imaginary part of refractive index m
λ	Wavelength (nm)
λ	Weighting coefficients for a RBF-based approximation
λ_c	Climb inflow ratio, $\lambda_c = V_c/(\Omega R)$
λ_h	Hover inflow ratio, $\lambda_h = v_h/(\Omega R)$

μ	Advance ratio, $\mu = V/(\Omega R)$
μ	Permeability (H m^{-1})
$\mu^\star$	Thrust-normalized advance ratio, $\mu^\star = \mu/\sqrt{C_T/2}$
μ_0	Permeability of free space (H m^{-1})
$\mu(k)$	Mean level of pixels in an image with grayscale value between 0 and k
μ_T	Mean level of an entire image, $0 \leq \mu_T \leq 255$
ν	Kinematic viscosity of air (m^2 s^{-1})
π_n, τ_n	Angle-dependent functions for Mie calculation
ρ	Non-dimensionalized particle radius, $\rho = kr$
ρ	Air density (slugs ft^{-3})
ρ_F	Charge density (C m^{-3})
ρ_s	Mass density (kg m^{-3})
σ	Rotor solidity, $\sigma = N_b c/\pi R$
σ	Conductivity (S m^{-1})
σ	Extinction coefficient (m^{-1})
σ_a	Absorption coefficient (per particle)
σ_s	Scattering coefficient (per particle)
$\sigma_B^2(k)$	Segmentation threshold selection factor
τ	Optical Transfer Function
ϕ	Azimuthal angle (deg)
χ	Wake skew angle (deg)
χ	Electric susceptibility
ψ	Blade azimuth angle (deg)
ψ_{emn}, ψ_{omn}	Spherical generating function
ψ_n, ξ_n	Ricatti-Bessel functions
Ω	Rotational frequency (rad s^{-1})
ω	Spatial frequency (cycles deg^{-1})
ω	Angular frequency (rad s^{-1})
ω	Solid angle (ster)
$\vec{\omega}$	Vorticity (rad s^{-1})
$\omega(k)$	Cumulative probability of a pixel value being between 0 and k
ω_c	Cutoff spatial frequency (cyc deg^{-1})
ω_{cutoff}	Cutoff spatial frequency (cyc deg^{-1})

Subscripts and Superscripts

$(\ )_{abs}$	Contribution from absorption
$(\ )_{app}$	Approximation
$(\ )_{ext}$	Contribution from extinction
$(\ )_i$	Incident
$(\ )_{max}$	Maximum allowable value (upper bound)
$(\ )_{min}$	Minimum allowable value (lower bound)
$(\ )_s$	Scattered
$(\ )_{sca}$	Contribution from scattering
$(\ )_{\parallel}$	Parallel components of a field

$( )_\perp$	Perpendicular components of a field
$( )^*$	Value for optimum configuration
$\overset{\star}{( )}$	Azimuthal derivative, $\overset{\star}{( )} = \partial( )/\partial\psi = \Omega\partial( )/\partial t$
$\dot{( )}$	Time derivative, $\dot{( )} = \partial( )/\partial t$
$( )^{3b}$	Three-bladed rotor design
$( )^{4b}$	Four-bladed rotor design
$( )^{5b}$	Five-bladed rotor design
$( )^{6b}$	Six-bladed rotor design

Abbreviations

ALU	Arithmetic Logic Unit
B&B	Branch and Bound algorithm
CPU	Central Processing Unit
CSF	Contrast Sensitivity Function
DVE	Degraded Visual Environments
ERF	Edge Response Function
ESF	Edge Spread Function
FOV	Field Of View
FVM	Free Vortex Method
GA	Genetic Algorithms
GPU	Graphics Processing Unit
HQ	Handling Qualities
IGE	In-Ground-Effect
LP	Linear Programming Problem
LSF	Line Spread Function
MILP	Mixed Integer Linear Programming Problem
MINLP	Mixed Integer Non-Linear Programming Problem
MTF	Modulation Transfer Function
NLP	Non-Linear Programming
OGE	Out-of-Ground-Effect
OTF	Optical Transfer Function
PSF	Point Spread Function
PTF	Phase Transfer Function
RBF	Radial Basis Function
RSM	Response Surface Method
RTT	Radiative Transfer Theory
TPP	Tip Path Plane
UCE	Usable Cue Environment
VCR	Visual Cue Ratings
VRS	Vortex Ring State
3DV	Three-Design-Variable
4DV	Four-Design-Variable

Chapter 1

Introduction

1.1 Rotorcraft Brownout

Rotorcraft brownout is the condition in which the flow field of a rotorcraft, while operating in proximity to the ground in a desert or an otherwise dry, dusty environment, mobilizes loose dust from the ground, uplifting it to generate a cloud that obscures the pilot's field of view (Fig. 1.1). In many instances, the resulting obscurations result in severe degradation of visual cues for the pilot, and it can potentially lead to the perception of spurious visual cues. Furthermore, abrasion from the dust impacting the main rotor

Figure 1.1: A helicopter encountering brownout conditions during a landing maneuver (courtesy of Optical Air Data Systems LLC).

blades and engine components may lead to increased maintenance costs after only a few encounters with brownout conditions.

While the brownout phenomenon is not a new one, recent military operations in austere environments have brought forth renewed efforts to promote a better fundamental understanding of brownout and to seek methods for its mitigation. Beyond the present military emphasis on brownout (Ref. 1), it is a phenomenon that has been historically problematic for civilian operators. Brownout, and the closely related to the "whiteout" phenomenon that occurs for rotorcraft operating in snowy conditions, have remained particularly troublesome for Helicopter Emergency Medical Services (HEMS) providers (Ref. 2), who frequently need to land on unimproved surfaces. In a broader scope, brownout is an example of a Degraded Visual Environment (DVE), a topic that continues to be of high priority in the civil and military Handling Qualities (HQ) communities (Refs. 3–5).

Brownout is a complex physical phenomenon, and a better fundamental understanding necessitates a multidisciplinary approach. A sampling of the myriad of technical disciplines contributing to the brownout phenomenon includes:

1. **Fluid dynamics:** The interaction between the flow field produced by the rotorcraft and the ground is responsible for the initial mobilization of the dust and its entrainment into the brownout cloud. Furthermore, the flow field can affect the resulting geometry of the brownout cloud.

2. **Flight dynamics:** The chosen profiles for approach to landing and take off can affect the severity of the brownout conditions. In certain operational conditions,

pilots have been noted to adopt specific landing techniques to mitigate the severity of the brownout cloud.

3. **Sedimentology:** The characteristics of the sediment bed covering the ground can likewise influence the overall development of the brownout cloud. For example, the inter-particle forces can have an effect on the volume of particles that are entrained in the flow field, and the particle sizes and weights can impact the paths that they follow and the durations for which they remain suspended.

4. **Human perception:** With an understanding that brownout is fundamentally a piloting problem, it is important to note that the way that human pilots perceive the necessary information through their sensory inputs (particularly visual) is vital to fully understanding the brownout phenomenon.

5. **The physics of light scattering and absorption:** The primary mechanism by which the brownout cloud obscures the pilot's field of view is through the scattering and absorption of light by the dust particles.

These topics illustrate the technical breadth of the brownout problem, and the role of each of these disciplines in brownout could be studied in depth on its own. In actual brownout conditions, these diverse disciplines are interrelated in many ways and so contribute to the overall technical complexity of understanding the brownout phenomenon.
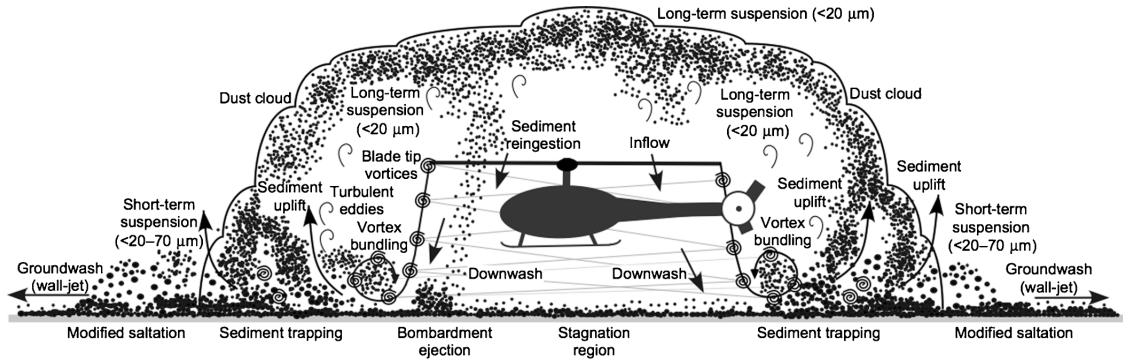
Figure 1.2: A schematic of in-ground-effect aerodynamics and the brownout problem.

1.1.1 Brownout Cloud Development

Brownout is a complex phenomenon that involves dust clouds that consist of evolving space- and time-dependent two-phase flows. The schematic in Fig. 1.2 shows the relationship between the In-Ground-Effect (IGE) aerodynamics of a hovering helicopter and the development of a brownout cloud, with at least some of the known primary physical mechanisms for brownout cloud development being identified. The characteristics of the rotor wake and the downwash flow during IGE operations are of primary importance in understanding the development of the brownout cloud because they are responsible for the various fluid dynamic forces that mobilize and uplift the dust particles. Such forces involve shear, pressure, turbulence, interparticle cohesion, and gravity.

The flow field that results from a rotor operating in ground-effect, even in the absence of dust, is clearly complicated. A flow visualization image and schematic diagram of an IGE rotor flow is shown in Fig. 1.3. The rotor wake is turns from a predominantly downward direction below the rotor, i.e., axial with respect to the rotor shaft, to a predominantly radially outward direction, i.e., radial with respect to the rotor shaft, as it

4

approaches the ground plane. The resulting flow field contains high streamline curvature and steep velocity gradients. The tip vortices that are trailed from the tip of each blade are stretched along their lengths, intensifying their vorticity and increasing their swirl velocities. This intensification may reduce, balance, or even counter the typical diffusive behavior of the tip vortices at older wake ages, causing them to persist in the flow for much longer than for the out-of-ground-effect (OGE) case. The persistence of the vortices is now known to significantly impact the development of a brownout cloud (Refs. 6, 7). The rotor wake also consists of a vortex sheet trailed behind the span of the blade, as seen in Fig. 1.3. These sheets have lower levels of vorticity but higher levels of turbulence, and they eventually become entrained in the near-wall flow at the ground. The end result is a downstream flow, i.e., flow outward from the rotor, which develops into an unsteady, turbulent wall jet containing embedded regions of concentrated vorticity.

When this flow then interacts with a sediment bed, a number of sediment transport mechanisms can contribute to the development of a brownout dust cloud. Some of these mechanisms are shown in Fig. 1.4. Once entrained, particles are rapidly convected away by the three-dimensional, turbulent, unsteady flow. Larger particles tend to be suspended for shorter durations while smaller particles can remain in long-term suspension. In some instances, suspended dust particles may be reingested through the rotor disk, leading to a particularly significant situation in which the particles impact the ground and eject many more dust particles through "splash" or bombardment ejection mechanisms. Analysis of photography and video footage of rotorcraft encountering brownout conditions indicates that this form of entrainment may lead to rapid increases in the severity of the dust cloud
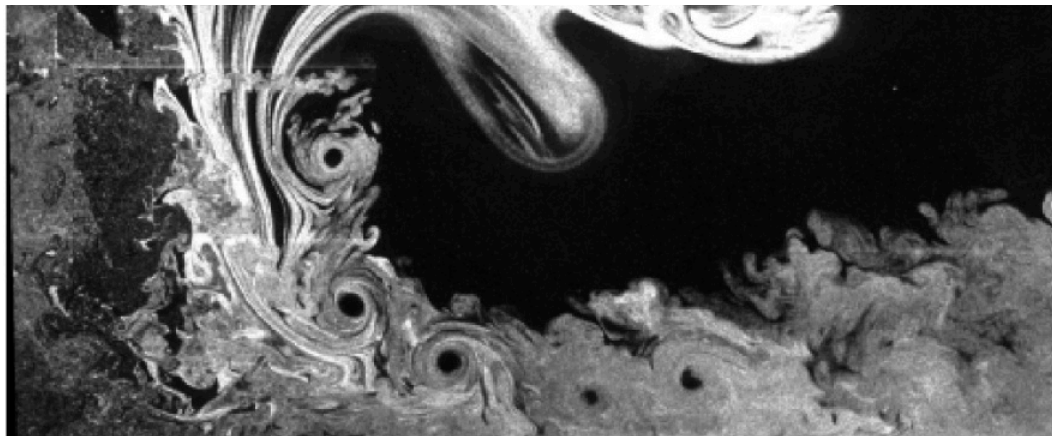
(a)
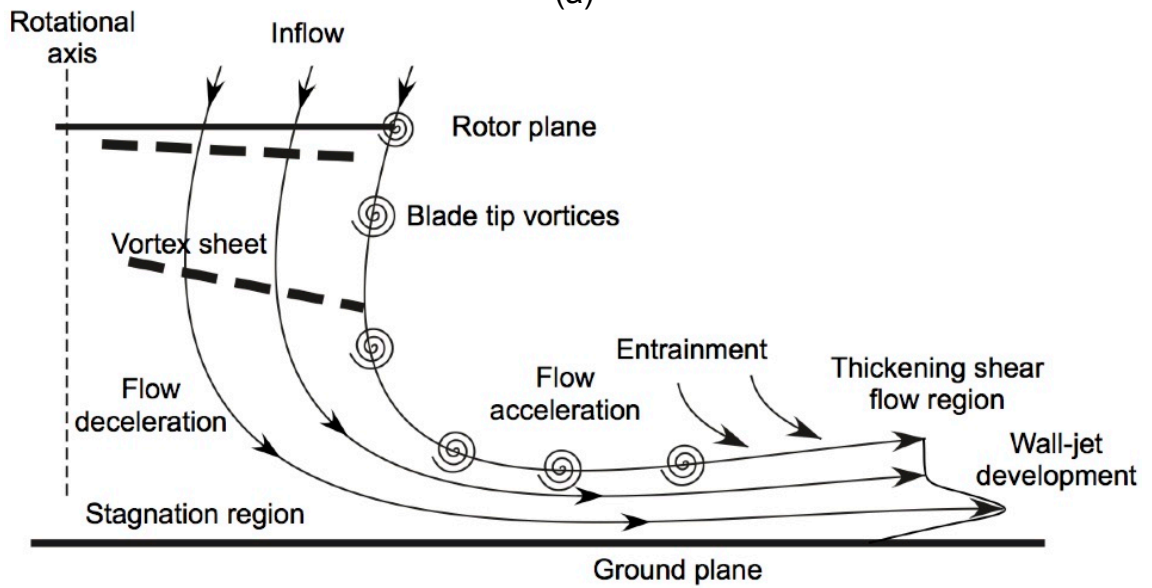
(b)

Figure 1.3: A rotor in ground-effect: (a) flow visualization and (b) schematic diagram (from Ref. 8).
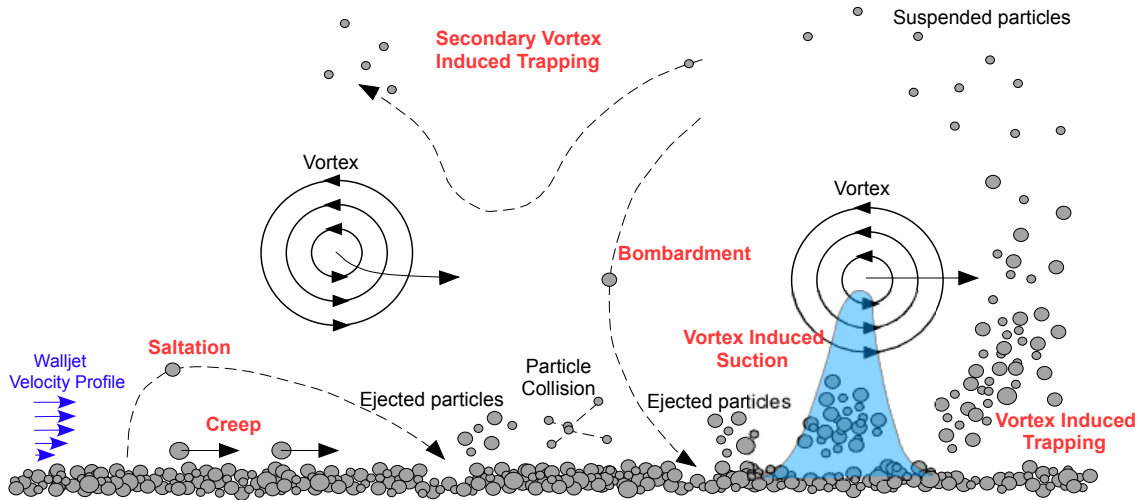
Figure 1.4: Schematic showing the different modes of dust particle motion and the fundamental uplift mechanisms seen in the near-wall region (from Ref. 7).

(Ref. 9).

Through extensive examinations of photographs and video footage (Ref. 9), it has been noted that certain rotorcraft tend to have more severe brownout characteristics where a large dust cloud completely envelops the rotorcraft, often exacerbated by the occurrence of particle reingestion into the rotor disk. Conversely, other rotorcraft have been noted to have particularly benign brownout characteristics where the cloud develops in a radially-expanding, toroidal geometry which leaves regions with minimal visual obscuration within the cloud. Additionally, certain takeoff and landing techniques have been employed to minimize the severity of the developing brownout cloud such as using techniques to "outrun" the developing brownout cloud.

1.1.2 Flight in Brownout Conditions

Within the coupled pilot-vehicle system, the pilot performs a variety of control tasks over different temporal and spatial scales. These tasks can be classified in three primary groups (as identified by Padfield, Ref. 5): (i) navigation and general situational awareness, (ii) guidance, and (iii) stabilization. It can be helpful to consider the pilot as an element in a feedback system, as shown in Fig. 1.5. The outermost loop is that of navigation, with typical time/space scales measured in minutes to hours and miles, respectively. This function does not require constant monitoring by the pilot, rather, he/she will simply perform periodic checks to ensure that he/she is progressing along the proper course. Pilot control inputs in response to the navigation task are minimal, aside from selecting and maintaining suitable altitudes and airspeeds. In some modern rotorcraft, the navigation function can be performed by a Flight Management System (FMS) coupled to an autopilot, and the human pilot is only required to provide a list of "waypoints." The middle loop is that of guidance, the task that focuses on maintaining suitable clearance from obstacles or other flight hazards. Typical time/space scales for the guidance function are measured in a few seconds and tens to hundreds of feet. The closer the pilot must fly to obstacles and other hazards, the more difficult the guidance task becomes. The inner loop is that of stabilization, with typical time/space scales measured in fractions of a second and feet. This function focuses on the control of the aircraft attitudes and can be augmented through the use of advanced flight control systems. In brownout conditions, the stability and guidance functions can be intermittently or continuously degraded, potentially leading to catastrophic outcomes.
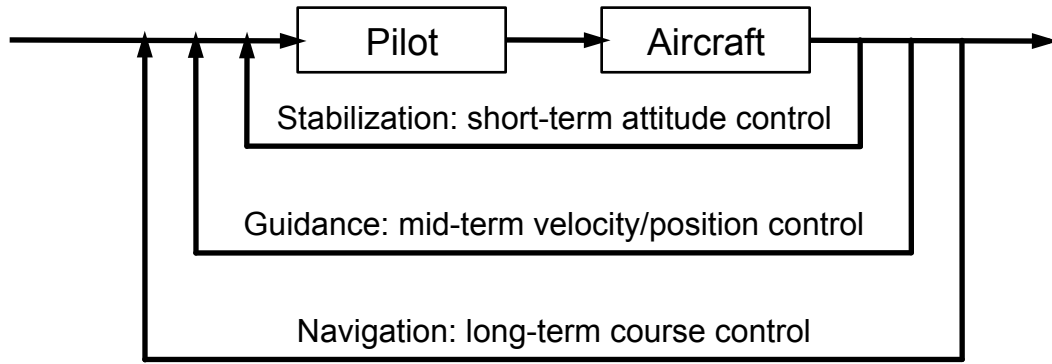
Figure 1.5: The three piloting functions (adapted from Ref. 5).

To accomplish the functions described previously, pilots must integrate multiple sensory inputs. Over the course of a typical flight, the pilot processes information from his/her auditory, tactile, vestibular, proprioceptive, and visual systems. The auditory system provides important information to the pilot, including aircraft warnings, crew-member instructions, or audible cues of an impending failure (e.g., a change in the engine noise). The tactile system can also provide important cues to the pilot, for example, the bump of a skid touching the ground during landing or the difference in control touch from a slung load. When it comes to basic aircraft stabilization and control, however, the most important cues are perceived through the vestibular, proprioceptive and visual systems (Ref. 10). These are the systems of the human body which, taken in concert, are primarily responsible for the maintenance of balance and equilibrium. The vestibular system is located within the inner ear and contains the sense organs, i.e., the semicircular canals and the otolith organ, which detect motion and gravity. The proprioceptive system reacts to sensations resulting from pressure on sensors in the joints, muscles, and skin and from slight changes in the position of internal organs. Lastly, the visual system is the most important of all the sensory systems for the pilot. While the pilot typically as-

similates information from all three of these systems, the vestibular and proprioceptive systems tend to be unreliable for safe flight without the visual system. This condition is particularly problematic in brownout because the dust cloud degrades the pilot's visual cues, and it can even lead to spurious visual cues, e.g., false sensations of motion. These sensory illusions, i.e., the perception of conflicting information from multiple sensory inputs, oftentimes leads to spatial disorientation, a condition in which the pilot is unable to determine his/her position, attitude, and motion relative to the ground and other obstacles.

With the knowledge that visual cues are essential for piloting, it is important to understand the primary cues that are used to perform the essential piloting functions. To estimate depth or distance, speed, closure rate, or other primary control information, a pilot may make use of a variety of visual cues (Refs. 5, 10):

1. **Geometric perspective:** The apparent shape of an object can provide the pilot with cues on its relative distance and angular orientation (e.g., a circular lake, when viewed from a distance, appears elliptical to the pilot).

2. **Retinal image size:** The size and orientation of an object provide the pilot with cues on its relative location and his/her speed (e.g., an object increases in size as it becomes closer; overlapping contours, or occlusions, indicate one object may be closer or further than another).

3. **Aerial perspective:** The clarity and shadow of an object provides a pilot with cues on its distance (e.g., a cornfield appears to be a solid color from a distance, but more fine-grained details emerge at closer viewing distances).
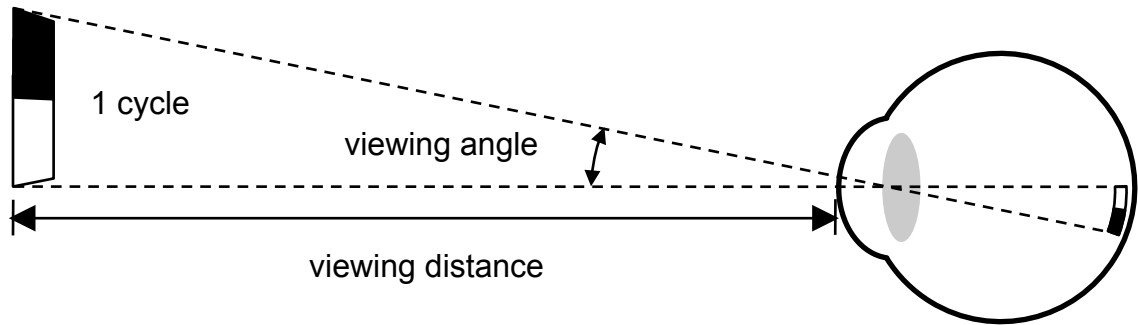
Figure 1.6: Schematic diagram depicting the calculation of spatial frequency (from Ref. 11).

4. **Differential motion parallax:** The apparent relative motion of stationary objects provides a moving pilot with cues on way-finding (i.e., establishing the direction of flight), speed, and the relative distance of the objects.

5. **Optical flow:** The *pattern* of the apparent motion of stationary objects, surfaces, and edges in the pilot's field of view that is cause by his/her motion relative to the scene provides the pilot with cues on speed and direction of motion.

6. **Edge rate:** Related to optical flow, the rate at which optically specified edges within the surface texture pass some reference in the pilots field of vision, e.g., the cockpit frame, provides the pilot with speed cues.

Within the visual scene, it is helpful to differentiate between the visual "texture" scales of different cues to have an understanding of what information they can provide to the pilot. A typical measure of texture scale is that of spatial frequency, given in cycles per visual angle. An idealized example is given in Fig. 1.6, in which a black/white pattern is viewed at a distance such that it subtends an angle within the field of view of the observer. The pattern can be characterized by a spatial frequency given by the ratio of the number

11

Figure 1.7: A typical desert scene, consisting of visual cues with a range of texture scales.

of black/white cycles to the subtended viewing angle, in units of cycles per degree.

While the world is clearly not made up of regularly-spaced black and white cycles, virtually any visual scene contains a broad range of texture scales. "Macro-textures" consist of larger objects (e.g., trees, buildings, etc.) and are classified as low spatial frequencies. Conversely, fine-grained details of the visual scene (e.g., blades of grass, the textures of the paved road) are considered "micro-textures" and are characterized by high spatial frequencies. A typical desert scene is shown in Fig. 1.7, and it contains a number of visual cues with a range of texture scales. For example, the texture of the sand in the foreground is a micro-texture cue, containing high spatial frequencies. The mountains in the background or the barricades in the mid-ground. however, are macro-texture cues, consisting of low spatial frequencies.
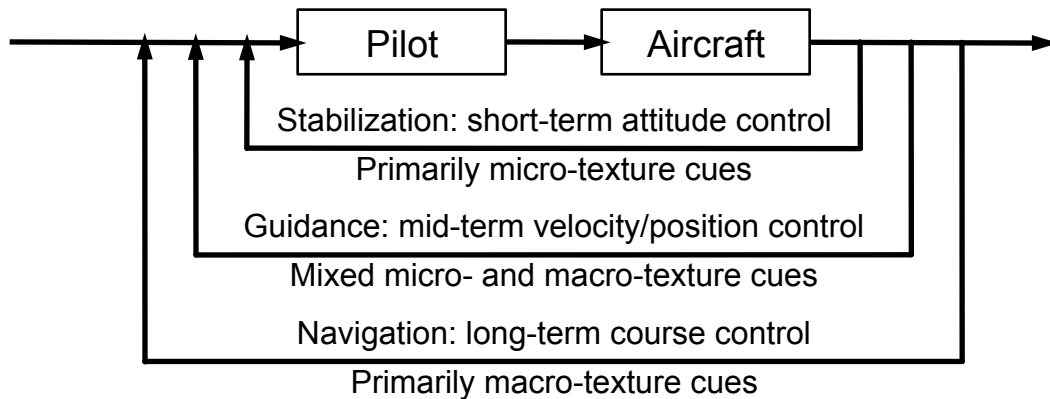
Figure 1.8: The three piloting functions (adapted from Ref. 5) and associated texture scales needed for visual feedback.

The different piloting functions require visual cues over a range of spatial frequencies; see Fig. 1.8. For example, large objects, i.e., macro-texture cues, are often used as landmarks in the navigation function. The guidance function requires the identification of obstacles or hazards, which are typically macro-texture, but the pilot utilizes micro-texture cues (through optical flow, differential motion parallax, edge rate, etc.) to ensure that his/her obstacle avoidance strategies are providing adequate course corrections and speeds. The stabilization function requires the perception of small amounts of drift and small excursions in attitude, and micro-texture cues are the most essential (Ref. 12).

The development of a brownout cloud can impair a pilot's ability to close the necessary control loops, particularly those associated with the stabilization and guidance functions. This impairment occurs because of a degradation of visual cues and the associated spatial disorientation that results for the pilot. What is not well-known, however, is exactly *how* the brownout cloud degrades the visual cues. For example, are certain texture scales more or less susceptible to degradation? How does this impact the piloting functions? These questions, and others, will be addressed in this dissertation.

13

1.2 A Survey of Research on Brownout and Related Topics

Because of the multidisciplinary nature of the brownout problem, the breadth of brownout research is far-reaching. Furthermore, there is a large amount of research from other fields that is relevant to the topic. An overview of brownout research is presented within this section, as well as a survey of research on related topics from other fields, particularly (i) Handling Qualities (HQ), (ii) light scattering and absorption, and (iii) numerical optimization.

1.2.1 Brownout Research

Research into rotorcraft brownout has seen a sharp increase in recent years. A myriad of approaches have been pursued to better understand the physics of brownout and, in some cases, to formulate mitigation measures. In a broad sense, the bulk of the existing body of research can be divided into four topics: (i) measurement and characterization, (ii) modeling, (iii) experimentation, and (iv) sensors and cueing aids. While some works contain elements of more than one of these categories, the use of these focus areas can be helpful in understanding the breadth of the ongoing research. A small amount of research may be grouped into a fifth category, maintenance considerations, and this is briefly mentioned within this section section.

Measurement and Characterization

The complexity of the brownout phenomenon makes the dust clouds difficult to characterize through quantitative metrics, though a few researchers have proposed mea-

surement and characterization methods to differentiate a "bad" brownout cloud from a "good" one. Milluzzo and Leishman (Ref. 9) proposed key rotor design parameters that may impact the intensity and rapidity of brownout cloud developments, and they performed an extensive review of photographs and video footage of rotorcraft in brownout to assess their hypotheses.

Rodgers (Ref. 13) reported data on the particulate composition of a brownout cloud generated by a H-21 helicopter. In more recent years, two technical reports from the DOD Sandblaster program (Refs. 14, 15) as well as work from Gillies et al. (Ref. 16) provided detailed test data on the particulate composition of brownout clouds generated by various rotorcraft in flight testing. These data included particle size distributions. Wong and Tanner (Ref. 17) and Tanner (Ref. 18) also provided data on brownout clouds generated in flight test, though they did not include an analysis of the particulate composition. Rather, they focused on measuring the geometry of the cloud using photogrammetry, particularly the dimensions of its external structure.

Modeling

A wide range of brownout simulation models have been presented in the literature in recent years, and they have significantly contributed to achieving a better fundamental understanding of the development of the brownout cloud. Furthermore, these models have proven to be useful in the investigation of potential brownout mitigation strategies. Each of these simulation methods has involved the coupling of an aerodynamic solution for the rotorcraft flow field with a model for the dust particle dynamics within the flow.

Syal, Leishman, and colleagues (Refs. 19, 20) of the University of Maryland have developed a Lagrangian dust-cloud simulation methodology that models multiple mechanisms of particle entrainment, to include entrainment by: (i) shear forces, (ii) pressure forces, and (iii) bombardment ejection. When coupled with a Free Vortex Method (FVM) to model the flow field induced by the main rotor, predicted brownout clouds were shown to be in good agreement with the photogrammetric measurements from Wong and Tanner (Ref. 17). Syal et al. (Ref. 21) extended this model to examine the possibility of brownout mitigation using a slotted-tip rotor blade by implementing a semi-empirical modification to the tip vortex characteristics. Govindarajan et al. (Ref. 22) examined the utility of particle clustering algorithms in this prediction model and Hu et al. (Ref. 23) drastically improved the computational efficiency of the brownout calculations through parallelization on Graphics Processing Units (GPUs) and other algorithmic modifications. Kalra et al. (Ref. 24) and Thomas et al. (Ref. 25) developed a CFD-based methodology for modeling a hovering rotor in ground effect and coupled it to Syal's Lagrangian dust-cloud simulation methodology.

D'Andrea (Refs. 26–29) also developed a brownout modeling capability. The flow field surrounding the rotorcraft was simulated by coupling a Constant Vorticity Contour (CVC) model of the rotorcraft's vortex wake with a panel method for modeling the fuselage. This aerodynamic modeling capability was integrated with a Lagrangian particle transport model that allowed for entrainment by shear forces. In recent work (Refs. 28, 29), D'Andrea utilized these models to illustrate the effect of rotorcraft configuration on the potential brownout signature.

Keller, Wachspress, Whitehouse, and colleagues (Refs. 30–34) of Continuum Dynamics, Inc. (CDI) have also developed a methodology for brownout simulation. The flow field surrounding the rotorcraft was modeled using a version of the NASA/Army GenHel, which was coupled with CDI's Comprehensive Hierarchical Aeromechanics Rotorcraft Model (CHARM) for modeling the rotor wake. A Lagrangian approach was used to model the brownout cloud development, allowing for particle entrainment by shear forces. This simulation capability has been used for modeling brownout in pilot-in-the-loop flight simulation (Refs. 30–32), as well as for studies on brownout mitigation (Refs. 33, 34).

Phillips, Brown, and colleagues (Refs. 35–38) developed similar brownout modeling capabilities, although they adopted an Eulerian approach. The aerodynamic flow field was simulated using a Vorticity Transport Model (VTM). The aerodynamic model was coupled to a particle transport model that allows for entrainment by shear forces. Compared to Lagrangian simulations of the dust cloud development, which entrain and track individual particles, their Eulerian approach relied on a semi-empirical particle flux that was calculated from the flow velocities near the ground plane. Using this simulation methodology, Phillips et al. (Ref. 38) examined the sensitivity of a developing brownout cloud to rotor configuration and rotor blade design.

Ryerson, Haehnel, and colleagues (Refs. 39, 40) also sought to model brownout using Eulerian approaches. The aerodynamic flow field was modeled using both ROT3DC (a RANS solver) and SAGE (a time-dependent Euler solver using vorticity confinement methods), which were coupled to a particle entrainment and dispersion model. Particle entrainment through shear forces was modeled. Ryerson et al. (Ref 39) used this brownout

simulation methodology to model anticipated sensor performance in brownout conditions.

Experimentation

In addition to the ongoing computational work, a range of experimental work has provided much insight into the brownout problem. This work has used rotors of various scales and has included both single-phase and dual-phase investigations.

A number of laboratory experiments have provided insight into the fluid dynamics of the in-ground-effect flow field. Lee et al. (Ref. 41) utilized flow visualization and phase-resolved Particle Image Velocimetry (PIV) to investigate the interactions of blade tip vortices with a ground plane. Milluzzo et al. (Ref. 8) examined the effect of blade tip design on the in-ground-effect flow field through flow visualization, as well as both time-resolved and phase-resolved PIV measurements. These experimental results were incorporated into a semi-empirical prediction model by Syal et al. (Ref. 21), as described in the previous section. For forward flight, Curtiss et al. (Ref. 42) performed an investigation of the aerodynamic characteristics of an isolated rotor operating at low advance ratios through flow visualization as well as through the measurement of forces and moments acting on the rotor.

A number of dual-phase laboratory experiments have identified key elements of the fluid-sediment interactions of rotorcraft brownout. Johnson et al. (Ref. 6) examined a dual-phase flow environment created by a laboratory-scale rotor hovering above a sediment bed using high-speed flow visualization and particle image velocimetry (PIV). This study presented a first-principles assessment of the temporal evolution of the rotor wake

18

in ground-effect, as well as an examination of the processes of dust particle entrainment and transport by the rotor flow. Sydney et al. (Ref. 7) extended this research by examining the two-phase flow environment produced by 1- and 2-bladed laboratory-scale rotors operating in-ground-effect over a mobile sediment bed. This study employed the use of time-resolved flow visualization, particle image velocimetry, and particle tracking velocimetry. At least six fundamental uplift and sediment transport mechanisms were identified.

Rauleder and Leishman (Ref. 43) analyzed single-phase and dual-phase PIV measurements in comparison with simpler, canonical flows to better understand the in-ground-effect flow in the boundary layer region and the effect of this flow on sediment mobility. Nathan and Green (Ref. 44) examined the development of a brownout cloud for a laboratory-scale rotor in ground-effect at low advance ratios through PIV and dual-phase flow visualization. Haehnel and Dade (Ref. 45) performed experiments on the physics of particle entrainment using an axisymmetric jet as an idealized surrogate for a rotorwash flow field.

At the full-scale, Wadcock et al. (Ref. 46) presented data obtained from a flight test in which tufts were fixed to both the fuselage of a UH-60 helicopter as well as the ground. The tufts were recorded for various hover heights to visualize the flow around and beneath the helicopter.

Sensors and Cueing Aids

Perhaps the most prevalent approach to solving the problem of rotorcraft brownout in recent years has been through the use of advanced sensors and pilot cueing aids. The fundamental philosophy of this approach has been to supplement the pilot with artificial cues in an effort to compensate for the visual cues that are eliminated or degraded by the formation of a brownout cloud.

One of the most widely-used cueing aids has been the Brownout Symbology System (BOSS), a standardized avionics display to present pilots with necessary information (altitude, airspeed, etc.) during a brownout landing. BOSS was developed at the US Army Aeroflighdynamics Directorate (AFDD). Szoboszlay, Neiswander, and colleagues (Refs. 47–49) documented the development of the symbology set. Turpin et al. (Ref 50) reported on the use of BOSS and another symbology set in assessing the effectiveness of a sensor system, the details of the sensor system were documented by Sykora (Ref. 51).

One prominent sensor-based product is known as the 3D-LZ landing system. This system combines: (i) a dust tolerant imaging Laser Detection and Ranging (LADAR) system, (ii) a dynamic navigation database and graphics generation subsystem, and (iii) the BOSS to provide the pilot with increased landing zone situational awareness, as well as aircraft guidance and obstacle avoidance information in brownout conditions. Harrington, Szoboszlay, and colleagues (Ref. 52, 53) provided a technical overview of the system and details of its performance during brownout flight testing.

A number of other systems have been developed outside the United States. The Assisted Low Level Flight and Landing on Unprepared Landing Sites (ALLFlight) Sys-

tem utilizes a suite of sensors and imaging devices to provide the pilot with necessary cueing information. Its development has been documented by Lueken, Doehler, and colleagues (Refs. 54,55). Link et al. (Ref. 56) reported on the development of an Augmented Visionics System (AVS) and its integration with a LIDAR sensor. Jansen et al. (Ref. 57) described the development of a tactile display that provides supplemental cues to the pilot.

While the majority of the research on sensors and cueing aids has occurred for the sake of specific product development programs in government labs and in industry, some related research has also been conducted in academia. Cummings and Smith (Ref. 58) performed research on the use of displays for improved pilot cueing in brownout.

Maintenance Considerations

Limited research has focused on the maintenance implications of frequent flight in brownout conditions. Pfledderer and Pepi (Ref. 59) presented a methodology for testing polymer-based protective rotor blade coatings to failure by sand erosion in a laboratory environment. Thomas et al. (Ref. 60) investigated the effects of one such blade coating on the blade dynamics, ice protection, and lightning strike protection in a rotorcraft operating environment. The relative lack of material in the literature on the maintenance considerations of brownout may not be indicative of a lack of emphasis on this topic because there may be work that has been as yet unpublished.

1.2.2 Relevant Research from Other Fields

Beyond the brownout-specific research that has been discussed in previously, a variety of other research topics can provide important insight into the brownout problem. For the purposes of this dissertation, the most relevant research topics to be considered are: (i) Handling Qualities (HQ), Degraded Visual Environments (DVE), and human perception (ii) the physics of light scattering and absorption, and (iii) numerical optimization.

Handling Qualities, Degraded Visual Environments, and Human Perception

In their seminal work on Handling Qualities (HQ), *The Use of Pilot Ratings in the Evaluation of Aircraft Handling Qualities*, Cooper and Harper (Ref. 61) define HQ as "Those qualities or characteristics of an aircraft that govern the ease and precision with which a pilot is able to perform the tasks required in support of an aircraft role." It is clear from this definition that the study of HQ is broadly defined and has an intrinsically subjective, human element to it. Indeed, in his account of the development of the earliest HQ specifications, Vincenti (Ref. 62) points out that, "[Handling] qualities are a property of the aircraft, though their identification depends on the perceptions of the pilot." It is clear that there is an inherent link between HQ and pilot *perception*, and modern assessments of HQ are, therefore, predicated on complementary assessments of the available cueing environments (Refs. 5, 63). Because visual cues are known to be the most important sensory input for pilots (as discussed in section 1.1.2), it is reasonable that a great deal of research has focused on flight operations in Degraded Visual Environments (DVE). The body of research is large, and only a small sample of the research that is most important

and relevant to the present dissertation, will be covered herein.

In recent years, Padfield and colleagues (Refs. 5,64,65) presented HQ-related work that utilizes the optical "tau," a parameter from psychophysics that gives a measure of time to closure on a point. This work initially showed the way in which tau can be used to develop a model of the "prospective control" that a pilot attempts to employ, i.e., a control that is based on a pilot's mental model of the future flight path (Ref. 64). In later work, Padfield et al. (Ref. 65) utilized tau to explain the way in which DVE impact the pilot's ability to control a rotorcraft. In particular, it was asserted that the impact of the DVE is to reduce the ability of the pilot to build his/her prospective mental model for a suitable duration into the future. A consolidated summary of Padfield's tau-related research is given in Ref. 5.

While the tau research has provided insight on how a pilot utilizes visual information to inform his/her control strategies, other work has focused on precisely what visual information the pilot needs to do so. Hoh (Ref. 12) performed flight testing that gave significant insight into the role of outside visual cues required for low speed and hover. In particular, the pilot's Field of View (FOV) was varied along with the presence of macro-texture and microtexture in the pilot's visual scene. This research provided unique insights into the piloting task at low speeds and in hover, particularly for DVE considerations:

1. First, it was determined that microtexture is essential for stabilization. In a later report, Hoh (Ref. 66) succinctly summarized this conclusion: "the primary cue for stabilization in the low speed and hover flight regime is *microtexture*" (the emphasis is Hoh's). Furthermore, Hoh and Mitchell (Ref. 67) later stated that "tests have
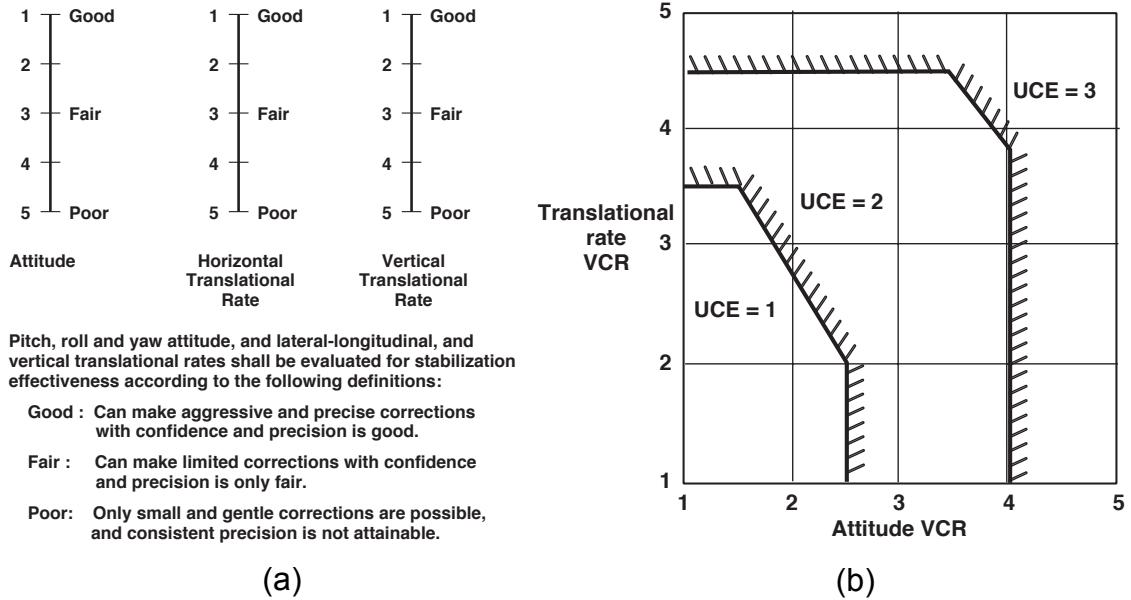
Figure 1.9: The (a) Visual Cue Rating (VCR) and (b) Usable Cue Environment (UCE) scales (from Ref. 63).

shown that the effect of insufficient fine-grained texture in the pilot's field of view is identical to degrading the aircraft handling qualities."

2. These flight tests also formed the basis for a later analysis by Hoh (Ref. 66) that examined flight in DVE as a form of divided attention operation for the pilot, a topic that had been previously researched extensively by McRuer et al. (Ref. 68).

3. Another important outcome of the testing was the development of the Visual Cue Rating (VCR) scale, as shown in Fig. 1.9(a), a scale that formed the basis for subjective pilot ratings of the Usable Cue Environment (UCE); see Fig. 1.9(b). The UCE is used to quantify the suitability of a visual cue environment for performing stabilization and control during low-speed and hover operations near the ground. In the U.S. Army rotorcraft HQ specification, ADS-33 (Ref. 63), adequate perfor-
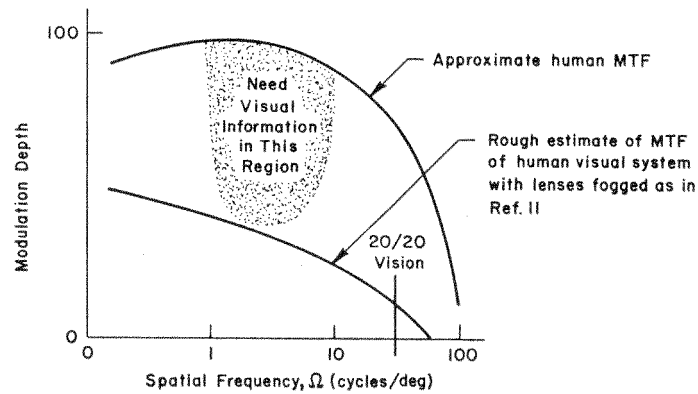
Figure 1.10: Plot of the approximate human MTF and degraded MTF due to fogged lenses (from Ref. 12).

mance at low levels of UCE requires flight control systems with greater amounts of stability augmentation.

A final important contribution of Hoh's flight test work was the introduction of the concept of the Modulation Transfer Function (MTF) as a potential metric for assessing visual cue degradation. He wrote that (Ref. 12):

The concept of the modulation transfer function (MTF) from the theory of visual perception shows considerable promise as a way to define the level of texture or detail visible to the pilot as a useable cue in terms of the spatial frequency and the modulation of the image.

Hoh suggested that fogged lenses worn by the test pilots degraded the contrast (or "modulation") of the visual cues at high spatial frequencies, resulting in a lack of useable visual cues from the spatial frequency ranges that a pilot typically needs for stabilization. This effect is intuitively depicted in Fig. 1.10, where the approximate human MTF contains sufficient contrast in the range of spatial frequencies where pilots "need visual informa-

25

tion," and the rough estimate of the MTF with the fogged goggles yields contrast levels that are below human visual thresholds.

The shaded region in Fig. 1.10 depicts a very important point: the human visual system is tuned to certain combinations of spatial frequency and contrast. While the intricacies of the human visual system are beyond the scope of this dissertation, an intuitive explanation for this phenomenon can be attributed to the relative position of photoreceptors (e.g., cone cells for photopic vision) in the fovea, as shown in Fig. 1.11. The position of the photoreceptors are shown relative to low- and high-frequency gratings in the top row and the resulting perception in the bottom row. At lower frequencies, Fig. 1.11(a), the grating can be reconstructed, while at higher frequencies, Fig. 1.11(b), the grating results in a perception of constant gray.

This effect is captured in the Contrast Sensitivity Function (CSF) of the human visual system, as demonstrated by Campbell and Robson (Ref. 69). A Campbell-Robson CSF chart, see Fig. 1.12, displays a continuous sinusoidal grating that logarithmically varies spatial frequency along horizontal lines and contrast along vertical lines. This image gives the observer a perception of an inverted "U" or "J" shape, outside of which (i.e., towards the upper-left and upper-right regions of the image) the grating blends to constant shades of gray. The *perception* of a peak, despite the fact that the luminance (contrast) of the sine-wave pattern is constant along any horizontal path through the image, indicates that the human eye's ability to discriminate contrast is strongly affected by spatial frequency.

Although the MTF showed great promise as a metric for visual cue degradation, the
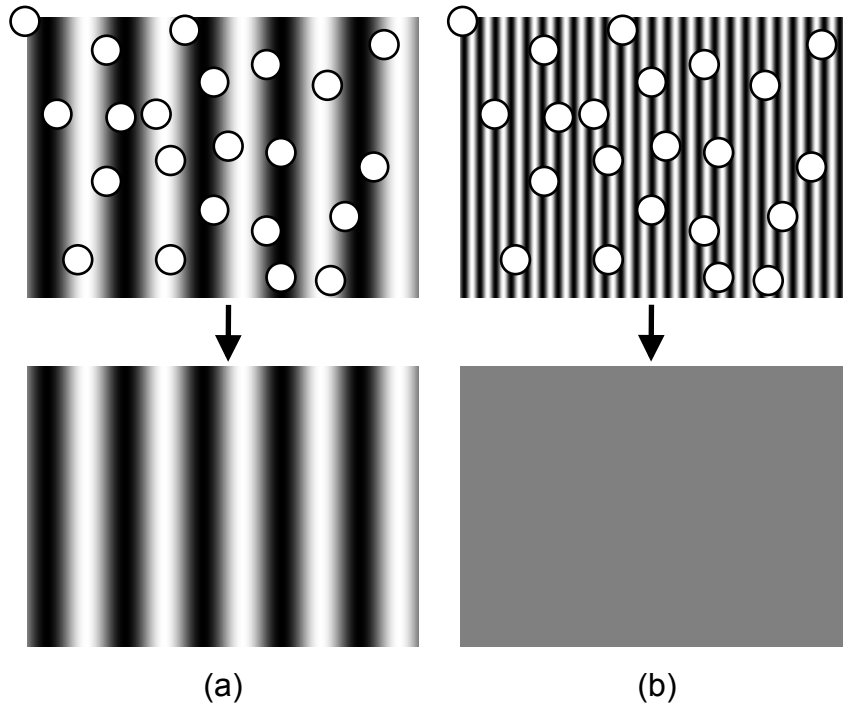
Figure 1.11: Schematic diagram of the relative position of photoreceptors (depicted as circles) on the fovea relative to (a) low-frequency and (b) high-frequency gratings, and the resulting perceptions (adapted from Ref. 11).
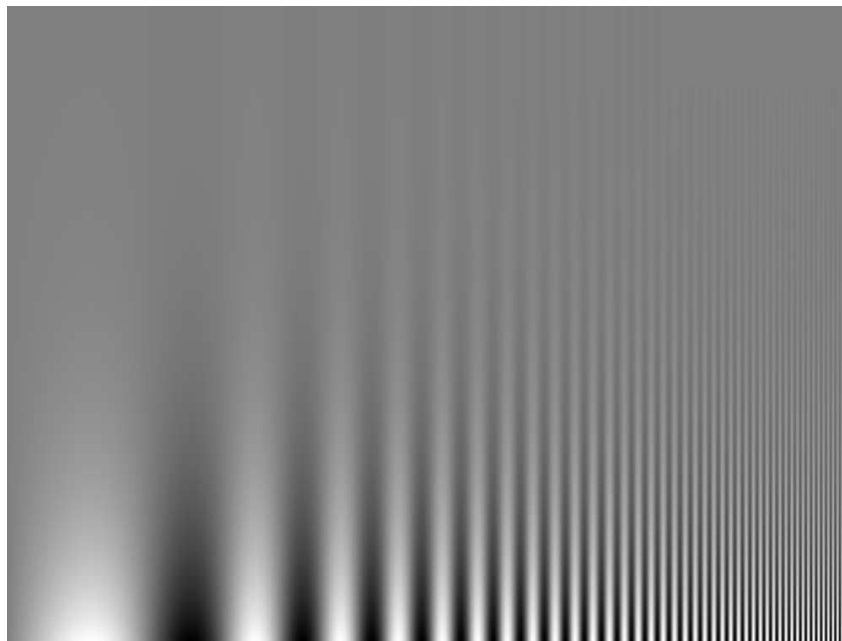
Figure 1.12: Campbell-Robson Contrast Sensitivity Function (CSF) chart.

concept was not pursued further with the rotorcraft HQ community. Hoh (Ref. 67) stated:

> Unfortunately, the technology is not sufficiently mature to allow the specification of the MTF limits required for the pilot to accomplish low-speed and hover tasks with an acceptable level of workload.

This dissertation will seek to advance the state of the art of MTF characterization of DVE, as demonstrated for rotorcraft brownout.

The Physics of Light Scattering and Absorption

To better understand the mechanisms by which brownout degrades (or eliminates) the pilot's visual cues, one must turn to the fundamental physics of light scattering and absorption. This field holds unique potential to act as a bridge between the existing bodies of research on brownout and HQ/DVE. For the purposes of this dissertation, only the most pertinent research will be reviewed, particularly work on the MTF. A comprehensive treatment of the formulations used in this dissertation is given in Section 5.1.

The MTF has seen wide use in the optics community as a metric for characterizing a variety of imaging systems in a range of environments. Yura (Ref. 70) reported theoretical MTF calculations for the scattering of light through ocean water. Fante (Ref. 71) presented MTF (in this case, referred to as the Mutual Coherence Function) calculations for a laser beam propagating through atmospheric turbulence. Kuga and Ishimaru (Ref. 72) reported results for controlled experiments in which the MTF was calculated through a random distribution of polystyrene microspheres suspended in water. Rovamo et al. (Ref. 73) presented calculations of the foveal MTF of the human eye for varied pupil

size. Kohm (Ref. 74) presented a methodology for calculating the MTF as well as results from a high-resolution imaging satellite. Bravo-Zanoguera et al. (Ref. 75) presented a methodology for utilizing the MTF to measure the quality of digital cameras.

The closest existing application of MTF-related research to the brownout problem is that of atmospheric imaging in desert environments, as reported extensively by Kopeika, Sadot, Dror, and colleagues (Refs. 76–84). This body of work has included both experimental and theoretical studies. The experimental work from Kopeika et al. (Ref. 76) and Dror and Kopeika (Refs. 77, 78) presented multiple methods for extracting the MTF from test patterns imaged at a distance. A "practical, instrumentation-based" MTF prediction methodology was detailed by Sadot and Kopeika (Refs. 79, 80) that utilized MTF formulations from radiative transfer theory (RTT), as derived by Lutomirski (Ref. 85) and Ishimaru (Ref. 86) with a correction proposed by Sadot and Kopeika (Ref. 81). The prediction methodology has been verified against experimental measurements by Sadot, Kopeika, and colleagues (Refs. 82, 83). A consolidated summary of the research can be found in Ref. 84.

Numerical Optimization

Numerical optimization is a fertile area for continuing research in engineering and scientific computing. Consequently, a broad review of the optimization literature is beyond the scope of this dissertation. The discussion herein will therefore focus on optimization research in which: (i) objective function evaluations are very costly, (ii) nonlinearity (and perhaps nonconvexity) is a likely to be a property of the problem, and (iii) the

vector of variables may contain a mix of continuous-valued and integer/discrete-valued variables. Particular attention will be given to aerospace applications. A thorough review of the specific methods used in this dissertation is given in Section 2.2.

In instances where the computational cost of a single objective function evaluation is particularly high, it can be helpful to perform an approximate optimization. In an approximate optimization, the objective function (and, in some cases, constraint functions as well) is fit by an approximation at each step, and it is the approximate function—not the true objective function—that is linked to the optimizer. There are a myriad of variations of such a methodology, including those that utilize response surface (RS) approximations. Jones (Ref. 87) provided a concise summary and taxonomy of response surface methods (RSM), as well as assessments of the potential weaknesses of certain variations of the methodology. Vanderplaats (Ref. 88) formulated an airfoil optimization as an approximate problem using quadratic approximations to the objective function, and the methodology is further summarized in his textbook (Ref. 89). Ganguli (Ref. 90) also used quadratic approximations to optimize main rotor designs for reduced vibrations using RSM. Hosder et al. (Ref. 91) proposed a method for the design optimization of a high-speed civil transport using quadratic approximations to the objective function.

Functions other than quadratic polynomials may also be used to approximate the objective function. For example, Venter et al. (Ref. 92) utilized cubic and quartic RS approximations that were constructed from numerical experiments conducted with a finite element analysis procedure to find the minimum-weight optimum design of a structural plate. Gutman (Ref. 93) examined the use of Radial Basis Functions (RBF) for approx-

imating the objective function in formulating approximate optimizations. Simpson et al. (Ref. 94) utilized Kriging models in approximating the objective function in the design optimization of a rocket nozzle. Batill et al. (Ref.95) presented a framework for the multidisciplinary design otimization (MDO) of aerospace systems using discipline-specific sets of RS approximations.

Optimization problems that take on mixed integer/discrete and continuous design variables tend to be considerably more challenging than problems that consist solely of continuous design variables. One method for solving such problems is through the Branch-and-Bound (B&B) algorithm. This algorithm involves the separation of an optimization into several "sub-problems" in which integer-only variables are held fixed; this is called "branching." If it can be determined that solutions for one value of an integer-only variable are always better than solutions for another value, B&B dictates that the branch corresponding to the worse of the two can be "fathomed" or "pruned;" this is the "bounding" step. Haftka and Gürdal (Ref. 96) presented a methodology for implementing B&B in Mixed Integer Linear Programming (MILP) problems. However, B&B becomes more difficult to implement for Mixed Integer Non-Linear Programming problems (MINLP), particularly when they are nonconvex. Grossman (Ref. 97) reviewed nonlinear mixed-integer and disjunctive programming techniques, including B&B, and pointed out that, "the B&B method is generally only attractive if the NLP subproblems are relatively inexpensive to solve, or when only few of them need to be solved."

Genetic Algorithms (GA) and other evolutionary algorithms have also seen use in solving optimization problems with a mix of integer/discrete and continuous design vari-

ables. Thanedar and Vanderplaats (Ref. 98) reported on the use of both GA and B&B within an approximate problem formulation for structural optimization. Buonanno and Mavris (Refs. 99–101) presented a method for aerospace vehicle concept selection utilizing GA in which a variety of discrete design choices may be evaluated in the preliminary design phase.

In recent years, advances to both B&B and GA have focused on reducing the number of function evaluations needed for convergence. Eele and Richards (Ref. 102) utilized nonlinear B&B optimization for path-planning and obstacle avoidance for aerospace vehicles. Gantovnik et al. (Refs. 103, 104) demonstrated the use of a modified GA for reducing the number of function evaluations needed for convergence in MINLP structural optimization problems. The reduction of function evaluations to convergence is particularly important for studies in which each function evaluation is costly, though the choice of which algorithm is best suited for a particular problem remains difficult to determine a priori.

1.3 The State of the Art of Brownout Characterization and Mitigation

The prior section has provided a glimpse of the breadth of the body of research on brownout and related topics. This section will seek to describe the depth of the current body of research in two specialized areas: (i) brownout mitigation and (ii) brownout characterization.

1.3.1 Mitigation

A variety of methods have been pursued to mitigate the effects of brownout. To begin, it is helpful to consider three primary categories into which prior mitigation research may be loosely classified: (i) cue supplementation, (ii) operational mitigation, and (iii) aerodynamic mitigation.

Cue Supplementation

Mitigation through cue supplementation is an approach by which sensors and cueing aids are used to compensate for the degraded (or spurious) cues that result from the brownout cloud. Many of these approaches have been discussed in Section 1.2.1, and they will not be discussed further here. It is important to realize, however that there is an implicit assumption in this approach that it is more effective in attempting to "see through" the cloud using combined sensor-avionics suites than to pursue methods that affect the characteristics of the cloud itself (e.g., geometry, rate of development, etc.). Furthermore, it is important to understand that this mitigation method attempts to only solve the issue of piloting in brownout and not the problem of increased wear on mechanical components (e.g., engines and rotor blades) or the difficulties for ground personnel under brownout conditions.

Operational Mitigation

Operational mitigation is an approach by which the pilot adopts specific strategies to minimize the effect of brownout during a maneuver. In practice, such techniques of-

ten involve an attempt to "outrun" the developing brownout cloud to maintain sufficient visual cues for as long as possible. While such methods are generally accepted among operational pilots, they are the result of anecdotal experiences and are not documented in the technical literature. Furthermore, the fundamental mechanisms for mitigation behind these strategies are not well understood.

Within the operational community, Gant (Ref. 105) described brownout training measures for pilots preparing to deploy to theaters in which brownout may be encountered. Pickford (Ref. 106) presented unit-specific standard operating procedures for dust landings. Within the research community, it should be noted that Neiswander (Ref. 49) examined a variety of approach profiles for brownout landings, though with the specific goal of improving deceleration guidance for a pre-programmed approach using instruments. Because these aproach profiles are designed for instrument flight, it is not expected that they would bear any significant similarity to the visual approaches that are typically associated with operational mitigation.

Aerodynamic Mitigation

The final mitigation category is that of aerodynamic mitigation. In this approach, experimental and simulation studies are employed to determine rotorcraft design strategies or modifications that may result in a more benign brownout signature. This method for mitigation has been the focus of significant recent effort from within the research community, and it appears likely that some degree of mitigation may be achievable through vehicle design. It should be emphasized however, in contrast to the approaches to miti-

gation through cue supplementation, aerodynamic mitigation holds the potential to solve the issue of piloting in brownout as well as the problem of increased wear on mechanical components and the difficulties for ground personnel.

Predicated on an understanding that the vortex wake of the rotor is responsible for much of the sediment mobilization and uplift in brownout (Refs. 6, 7), Milluzzo et al. (Ref. 8) have examined the effect of blade tip shape on the interaction between the vortex wake and the ground. Flow visualization and particle image velocimetry were utilized to examine the differences in the flow fields resulting from four tip geometries: (i) rectangular, (ii) swept, (iii) BERP-like, and (iv) slotted. The experimental results indicated that the slotted tip, which was originally designed for reduced blade-vortex interaction noise (Ref. 107), was particularly effective in diffusing the tip vortices and reducing the overall intensity of the flow at the ground. A schematic of the slotted tip is depicted in Fig. 1.13. Syal et al. (Ref. 21) utilized the measured data to develop a semi-empirical modification for the tip vortex characteristics as modeled by a FVM, and coupled the model with a Lagrangian dust-cloud simulation methodology to investigate the potential for brownout mitigation.

Whitehouse et al. (Refs. 33,34) have also utilized simulation and experimentation in examining the potential for aerodynamic mitigation of brownout. In initial work (Ref. 33), the simulation and experimental methodologies were outlined, and a brownout parameter, $\kappa_b = \sqrt{C_T}/N_b$, was suggested as a potential indicator for brownout severity. In subsequent work (Ref. 34), a strategy was presented for mitigating brownout by inhibiting the tip vortex bundling process near to the ground, along with several retrofittable active concepts to
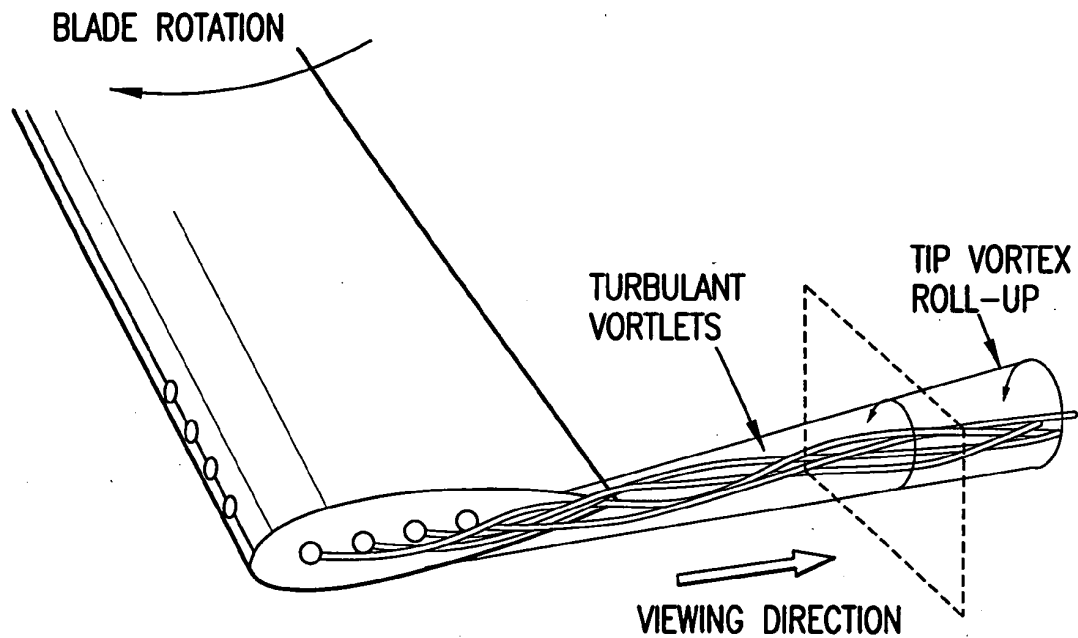
Figure 1.13: Schematic of a rotor blade with a slotted tip (from Ref. 107).

achieve this desired effect. Such concepts include the use of deployable vortex generators

and flaps or tabs; see Fig. 1.14.

Phillips et al. (Refs. 35–38, 108) have also examined the potential for aerodynamic

mitigation through simulation, examining configurational effects as well as the sensitivity

of brownout to rotor design parameters such as blade twist, tip shape, and number of

blades. In initial work, Phillips and Brown (Ref. 36) presented a model for predicting the

brownout cloud generated by tandem and single main rotor configurations. They noted,

"...relatively coarse features of the geometry and strength of the rotor wakes (in particular,

the location of the ground vortex and the size of any regions of recirculatory flow, should

they exist) play a primary role in governing the extent of the dust cloud that is created

by the helicopter." In subsequent studies, they examined sensitivities to blade twist for

36
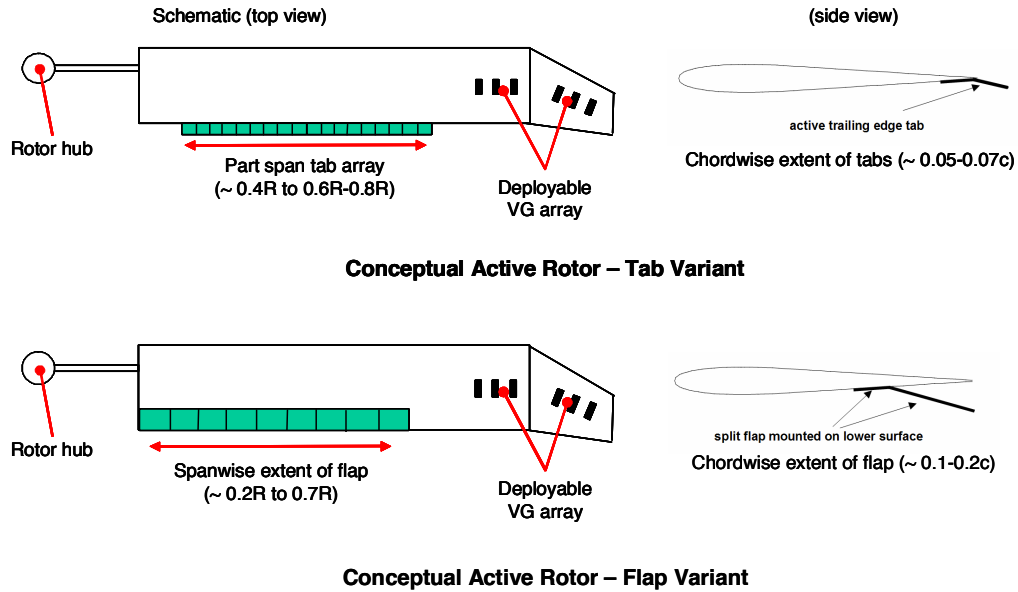
Figure 1.14: Conceptual active rotor designs for brownout mitigation (from Ref. 34).

tandem rotor configurations (Ref. 35) and blade twist and number of blades for single main rotor configurations (Ref. 108). In both of these studies, greater amounts of blade twist were found to result in less dense clouds, and designs with more rotor blades resulted in less dense clouds for single main rotor configurations.

In another study, Phillips et al. (Ref. 38) examined the sensitivity to blade twist and tip shape for a five-bladed single main rotor helicopter. The results indicated that less twist leads to less dense brownout clouds. Furthermore, the tip shape appeared to have little impact on the resulting brownout cloud, with the exception of the BERP rotor, which "seems to produce a greater preponderance of dust in the ground vortex and significantly less immediately below the rotor than the blades with other tip geometries." They further hypothesized that the inherent instability of the flow field produced by the helicopter, as depicted in Fig. 1.15, will tend to complicate attempts to mitigate brownout through
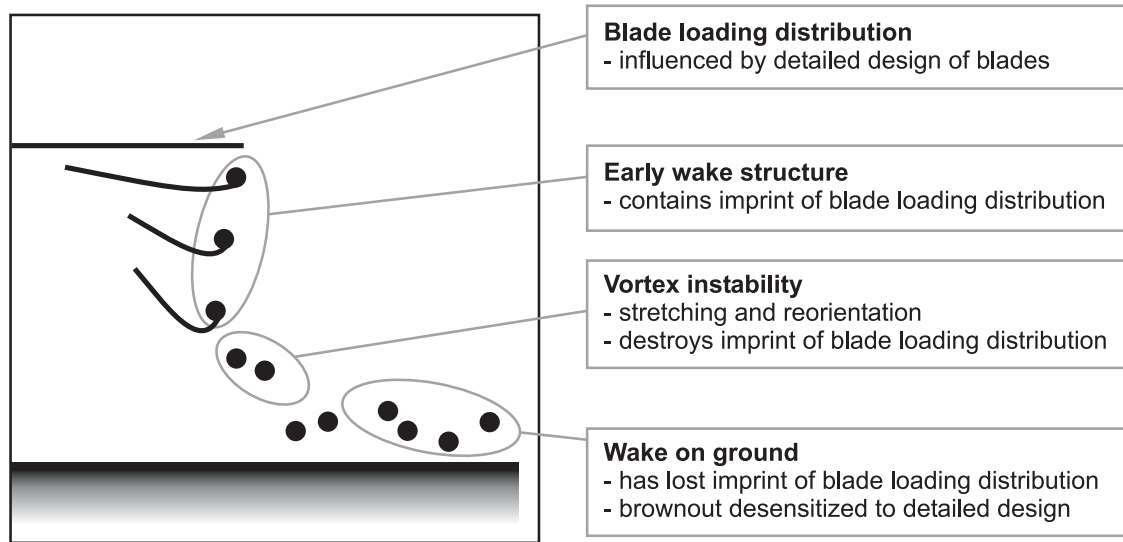
Figure 1.15: Schematic of the proposed link between blade loading and the formation of the brownout cloud, as moderated by the natural instability within the rotor wake (from Ref. 38).

modifications to the rotor design. In light of this hypothesis, they concluded that the sensitivity (or insensitivity) of the dust cloud to the details of the rotor design is perhaps best understood by focusing on "...the manner in which the tip vortices interact with the ground in order to entrain particulate matter into the flow...."

Mitigation: Next Steps

A variety of approaches have been pursued towards the goal of mitigating brownout. The technical literature contains very little material dealing with methods for operational mitigation, and the potential for such strategies will be examined further in this dissertation. Some research has explored the potential for aerodynamic mitigation, and these approaches have provided significant insight into the brownout problem through parametric studies and proposed "point-design" solutions. The state of the art of brownout

mitigation, however, still lacks a methodology or framework in which brownout may be systematically mitigated by operational or design strategies. A fundamental aim of this dissertation is to propose such a methodology.

1.3.2 Characterization

An overview of the existing research on brownout characterization was provided in the context of the broader brownout research in Section 1.2.1. The present section will provide a detailed examination of the state of the art.

Subjective Assessment

Milluzzo and Leishman (Ref. 9) suggested a number of rotor design parameters that may significantly impact brownout severity. The proposed parameters included:

1. Average downwash velocity, $w = 2\sqrt{T/2\rho A}$

2. Normalized average downwash velocity, $w/(\Omega R)$

3. Total wake strength (circulation), $\Gamma_w = N_b \Gamma_v = N_b k (C_T/\sigma)(\Omega R)c$

4. Normalized total wake strength, $\Gamma_w/(\Omega R^2)$

5. Wake-reduced frequency, $k_s = (N_r N_b \Omega c)/(2V_{tip})$

To assess the correlation, they examined extensive amounts of photographs and video footage and made subjective assessments of severity. The results of the correlation were presented in a series of figures. An example of one of these plots is given in Fig. 1.16,
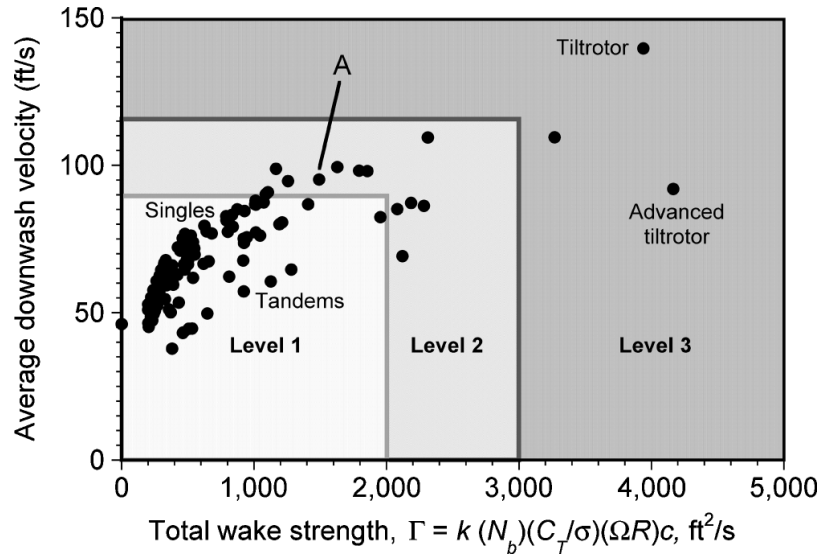
Figure 1.16: Variation of average downwash velocity versus total wake strength (from Ref. 9).

in which the average downwash velocities and total wake strengths of a variety of helicopters are presented on axes overlaid with assessments of brownout severity (Level 1 corresponds to low severity, Level 3 corresponds to high severity). This work represents the first instance of a systematic assessment of brownout severity based on rotor design parameters to appear in the archival literature, and it provided an initial framework for understanding the key aerodynamic contributors to the brownout problem.

Measurements: Cloud Geometry

Wong and Tanner (Refs. 17, 18) utilized an image processing technique known as photogrammetry to provide quantitative measurements of the external geometry of a developing brownout cloud. In this method, accurate measurements of the external dimensions of a developing brownout cloud may be extracted from synchronized video record-
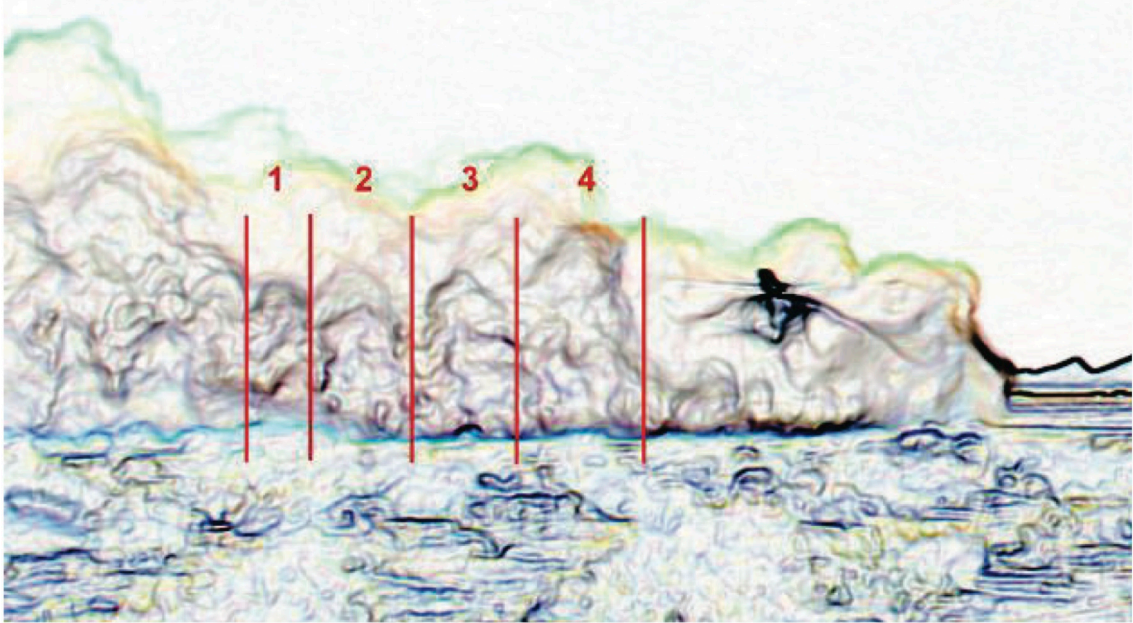
Figure 1.17: Columnar features of a brownout cloud (from Ref. 18).

ings from different vantage points. Such measurements have proven to be useful as a validation set for predictive brownout simulations (Ref. 20). Additionally, Tanner (Ref. 18) used advanced image processing techniques to isolate key external geometric features of the brownout cloud, particularly the presence of columnar features; see Fig. 1.17.

Measurements: Cloud Composition

A number of recent works have provided detailed information on the particulate composition of brownout clouds. In particular, two technical reports from the DOD Sandblaster program have provided unique data sets. One of the reports, from Muleski (Ref. 14), presented details on the dust concentration and particle size distribution of a brownout cloud generated by a taxiing UH-1 helicopter. These results were obtained using a variety of time-integrating and continuous air monitors placed in multiple locations
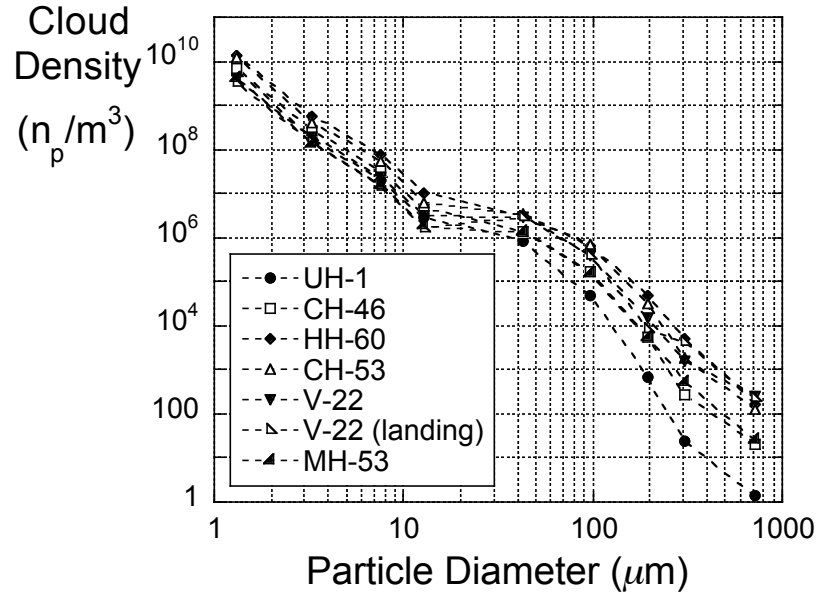
Figure 1.18: Particle size distributions for brownout clouds generated by various rotor-craft (from Ref. 15).

in the vicinity of the helicopter. The other report, from Cowherd (Ref. 15), reported detailed data on the brownout clouds generated by six different rotorcraft. Representative particle size distributions from this work are shown in Fig. 1.18.

Gillies et al. (Ref. 16) also presented experimental data from flight testing. In this work, dust emissions of two diameter ranges, specifically $d \leq 10\mu$m and $d \leq 2.5\mu$m, were measured for hover taxi maneuvers of varying advance ratio. For the $d \leq 10\mu$m range, emission rates were seen to scale as a function of forward speed, decreasing roughly exponentially as speed increased. The primary focus of the data presented in this work is for an assessment of the environmental impact resulting from military testing and training activities, and the results are therefore focused on the total dust emissions rather than the specifics of the brownout cloud itself (i.e., geometry, rate of development, etc.).

42

Characterization: Next Steps

Each of these works provides a unique method for characterizing the brownout phenomenon. However, the state of the art in brownout characterization still lacks a brownout metric that is simultaneously: (i) rigorously quantitative, (ii) measurable from experimentation, (iii) predictable from fundamental physical theories, and (iv) directly relevant to HQ considerations. A fundamental aim of this dissertation is to present such a characterization metric.

1.4 Research Objectives

In light of the foregoing discussion, the overall objective of this dissertation is to advance the state of the art of brownout mitigation and characterization. The specific objectives of the present dissertation are:

1. To propose a numerical optimization framework within which simulation-based brownout mitigation studies may be formulated. Such formulations require the rigorous mathematical definition of an objective function that is representative of the severity of a given dust cloud.

2. To use the proposed framework to examine the potential for "operational" brownout mitigation through flight path optimization. In particular, an approach-to-landing maneuver is optimized, subject to operational constraints on the maneuver, to determine piloting strategies that could potentially mitigate brownout.

3. To use the proposed framework to assess the possibility of "aerodynamic" brownout

mitigation through main rotor design. In particular, the basic design of a main rotor in a conventional helicopter is optimized to identify design features that may be effective for mitigating brownout.

4. To propose a method for characterizing the severity of a brownout cloud by its optical degradation, specifically through the use of the Modulation Transfer Function (MTF).

5. To demonstrate techniques for, and results from, MTF extraction from brownout clouds generated in flight testing. Additionally, methods must be developed for interpreting these results, given the significant variations in space and time that are characteristic of brownout clouds.

6. To present a methodology for predicting the MTF of a simulated brownout cloud from the fundamental physics of light scattering and absorption, and to identify the key issues in the modeling procedure that affect the accuracy of the results and the efficiency of the computations.

1.5   Contributions of the Present Research

The most significant contributions of this dissertation to the state of the art of rotorcraft brownout research are:

1. The development of a numerical optimization-based framework in which brownout may be systematically mitigated by operational or design strategies.

2. The advancement of a method for rotorcraft brownout characterization via the MTF

that is: (i) rigorously quantitative, (ii) measurable from experimentation, (iii) predictable from fundamental physical theories, and (iv) directly relevant to HQ considerations.

The following are also original contributions in this study:

3. The definition of a a handling qualities-oriented, quantitative metric for brownout severity that is suitable for rotorcraft trajectory and design optimization studies.

4. An analysis of the fundamental physical mechanisms underlying operational and aerodynamic brownout mitigation strategies.

5. The formulation of initial steps toward the formal development of operational criteria and preliminary design guidelines for brownout mitigation.

6. The adaptation of existing optics test techniques for the purposes of measuring the MTF of a brownout cloud from flight test and the determination of practical guidelines for MTF extraction from brownout flight testing (i.e., camera selection criteria and recommendations for optical target design).

7. The development of new techniques for interpreting the temporal and spatial variations of the MTF of a brownout cloud.

8. The proposal of an initial methodology for the prediction of the MTF of a brownout cloud from fundamental light scattering and absorption theory.

1.6 Organization of the Dissertation

Chapters 2 through 4 comprise Part I of the dissertation and focus on brownout mitigation. Chapter 2 provides essential background into the numerical optimization and brownout simulation methods that will be employed, and Chapters 3 and 4 contain studies of the potential for brownout mitigation through trajectory optimization and rotor design optimization, respectively.

Chapters 5 and 6 comprise Part II of the dissertation and focus on brownout characterization. Chapter 5 presents an experimental examination of the applicability of the MTF to the problem of rotorcraft brownout, and Chapter 6 contains an investigation into the potential for predicting the MTF of a simulated brownout cloud.

Chapters 7 and 8 comprise Part III of the dissertation. Chapter 7 contains the conclusions from the present work, and Chapter 8 provides recommendations for future work.

Part I

Brownout Mitigation

Chapter 2

Theoretical Approach to Brownout Mitigation

In the introductory chapter, the problem of rotorcraft brownout is presented as a Degraded Visual Environment (DVE) with the potential for causing catastrophic mishaps. A variety of methods have been pursued to mitigate the effects of brownout, which may be loosely classified into three categories: (i) cue supplementation, (ii) operational mitigation, and (iii) aerodynamic mitigation. The present work will focus on the latter two forms of mitigation.

The subsequent chapters of this dissertation will present formal methodologies by which brownout may be systematically mitigated through operational and design strategies. Within these methodologies, brownout mitigation is formulated as a numerical optimization problem. A simulation based approach has been adopted in the present work, within which the effects of varied operational and design strategies on the severity of brownout are examined. To this end, a novel objective function is taken to be a surrogate for the visual degradation experienced by the pilot. The present chapter presents the theoretical foundations of: (i) the models that were employed to simulate the brownout clouds, (ii) the numerical optimization techniques that were utilized in the present study, and (iii) the objective function that was adopted to characterize the severity of the simulated brownout clouds.

2.1 Simulating Brownout

A simulation-based approach to brownout mitigation has been adopted in the present dissertation, and each function evaluation within the numerical optimization framework requires a simulation of the brownout cloud that results from a set of specified parameters (these may be operational or design parameters, depending on the study). The brownout simulations begin with the modeling of the rotor flow generated by a maneuvering rotorcraft in ground-effect. Once the flow field has been predicted, the resulting brownout cloud is modeled under the assumption of a one-way coupling (i.e., assuming that the particle motion is driven by the air, but not vice-versa). The present section provides an overview of the numerical models utilized for simulating the rotor flow and resulting brownout cloud.

2.1.1 Rotor Flow Field Modeling

To model the development of a brownout cloud with a satisfactory level of fidelity, the flow field generated by the rotor flow generated by a rotorcraft maneuvering near the ground must be modeled accurately. This is a challenging proposition in itself. In the present work, the rotor flow in ground-effect was modeled using a free-vortex method (FVM) which was configured to predict the flow for a rotorcraft under arbitrary maneuvering flight conditions (Ref. 109). Ground effect was modeled using an image rotor system (Ref. 110). An inviscid-viscous method was utilized to predict the flow field arising from a combination of the rotor flow (modeled as an inviscid potential flow by the FVM) and the resulting viscous flow in the boundary layer region at the ground (Ref. 19).

Modeling the Rotor Flow in Ground-Effect

The FVM utilized in the present work is a Lagrangian representation of the rotor flow field in which the evolution of the rotor wake is computed numerically. What separates a "free" vortex method from other "rigid" or "prescribed" wake models is that the geometry of the rotor wake, as modeled using discrete vortex filaments, is allowed to distort freely under the influence of the local induced velocity field (rather than follow a pre-determined trajectory in space and time). The initial vorticity of each discrete filament is determined, in part, by the blade aerodynamic loading, and the flow elsewhere is assumed to be inviscid, incompressible, and irrotational.

Computing Induced Velocities using the Biot-Savart Law In a FVM, the velocity induced by the wake at any location may be computed by the repeated application of the Biot-Savart Law, and by numerically integrating the induced velocity contribution from each vortex element over the entire flow field. Figure 2.1(a) shows a schematic of how the application of the Biot-Savart law may be used to compute the velocity induced $\mathbf{V}$ at a point, 'P', from a curved vortex filament of strength Γ. This velocity is given in analytical form by

$$\mathbf{V} = \int \frac{\Gamma}{4\pi} \frac{d\mathbf{l} \times \mathbf{r}}{|\mathbf{r}|^3} \qquad (2.1)$$

where $\mathbf{r}$ is the position vector of the point 'P' with respect to the vortex element $d\mathbf{l}$.

In the present work, the curved vortex filaments were approximated by straight line segments, resulting in a reconstruction of the induced velocity field that is second-order accurate (Ref. 112). For a line vortex with constant circulation, Γ, (see Fig. 2.1(b)) an
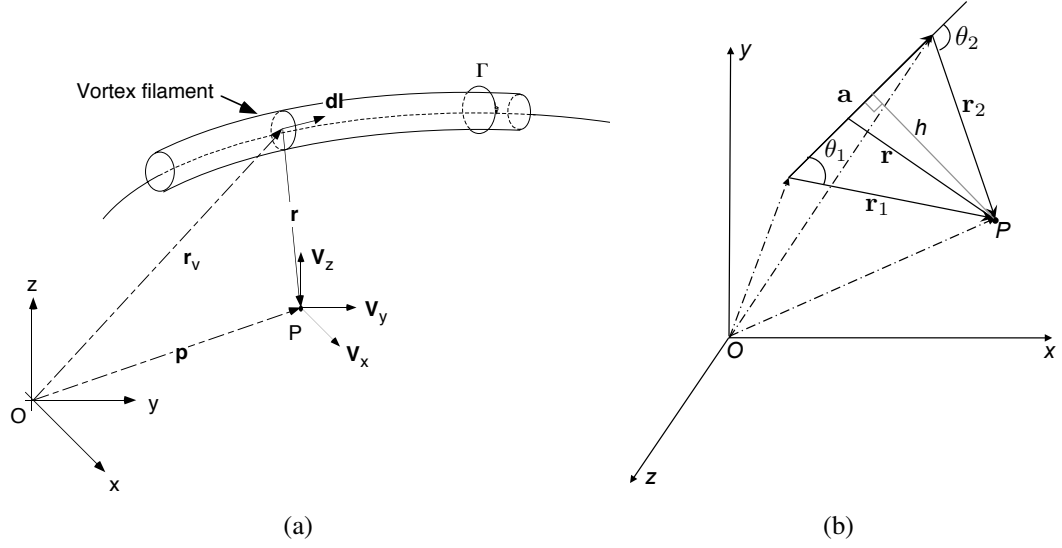
Figure 2.1: Velocity induced at point 'P' from (a) a curved vortex filament and (b) a straight vortex segment of constant strength (from Ref. 111).

exact solution of Eq. (2.1) can be expressed as

$$\mathbf{V} = \frac{\Gamma}{4\pi h} \left(\cos\theta_1 - \cos\theta_2\right) \frac{\mathbf{a} \times \mathbf{r}}{|\mathbf{a} \times \mathbf{r}|} \qquad (2.2)$$

An alternate representation is

$$\mathbf{V} = \frac{\Gamma}{4\pi} \left\{ \mathbf{a} \cdot \left(\frac{\mathbf{r}_1}{|\mathbf{r}_1|} - \frac{\mathbf{r}_2}{|\mathbf{r}_2|} \right) \frac{d\mathbf{l} \times \mathbf{r}_1}{|d\mathbf{l} \times \mathbf{r}_1|^2} \right\} \qquad (2.3)$$

Notice that the formulation of Eq. (2.3) has eliminated the trigonometric functions of Eq. (2.2). It may, therefore, be solved at lower computational costs when implemented numerically.

Blade Aerodynamic Model   The main rotor was modeled as N_b rigid, articulated blades, which may execute fully independent, time-accurate, flapping motion. In the present
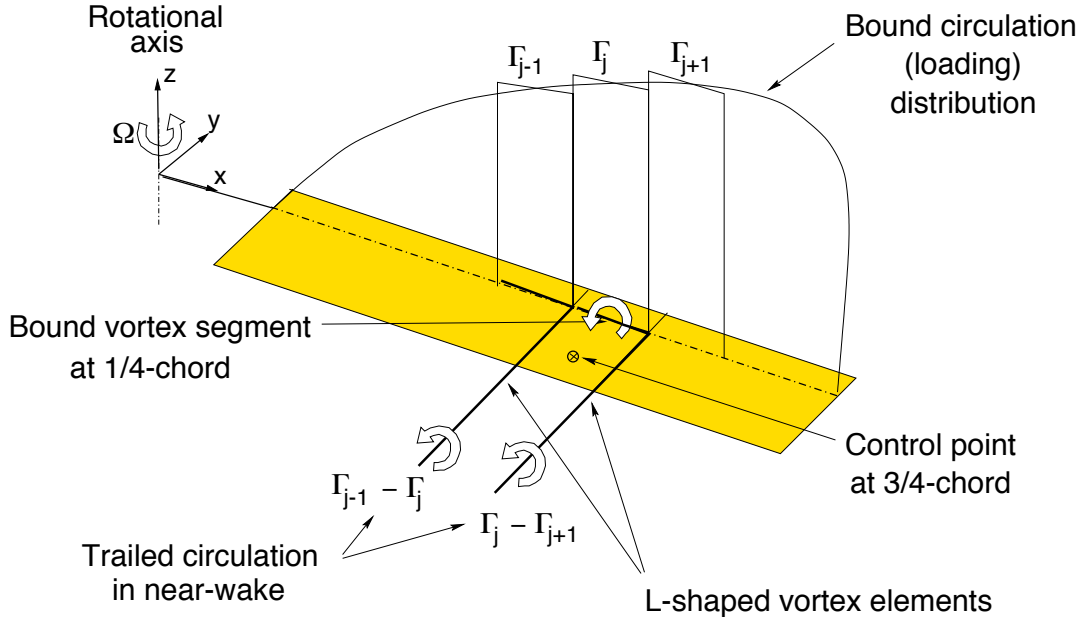
Figure 2.2: Schematic of the Weissinger-L model used to represent the blade (from Ref. 114).

work, each blade was modeled as a distribution of vortex singularities (bound vortices) in the flow field using the Weissinger-L lifting surface model (Ref. 113); see Fig. 2.2. Each blade was discretized into N_s spanwise segments and one chordwise segment.

In a general sense, the wake from each rotor blade consists of a vortex sheet and a concentrated tip vortex. The vortex sheet includes vorticity with components normal and parallel to the trailing edge of the blade, which are known as trailed and shed vortices, respectively. In the present work, the trailed vortices (i.e., the near wake), was assumed to be rigid and fixed to the blade. The near wake was truncated at $\Delta\psi = 30°$, and was coupled by means of a circulation-preserving boundary condition to a far wake consisting of a rolled-up tip vortex farther downstream.

Free-Vortex Wake Modeling   Unlike the bound vortices, whose location was determined by the blade position, the vortices of the far wake, which consist of Lagrangian

markers that define straight line segment approximations to the curved vortex filaments (see Fig 2.3), were free to convect to force-free locations under the influence of the local velocity field. The motion of the Lagrangian markers was governed by the three-dimensional, incompressible Navier-Stokes equations, which can be written in the form of the vorticity transport equation, i.e.,

$$\frac{D}{Dt}(\vec{\omega}) = \left(\vec{\omega} \cdot \vec{\nabla}\right) \vec{V} + \nu \Delta \cdot \vec{\omega} \tag{2.4}$$

This equation determines the rate of change of vorticity of a fluid element in terms of the instantaneous values of vorticity $\vec{\omega}$ and velocity $\vec{V}$. The left-hand side of Eq. (2.4) is the substantive derivative of vorticity, which includes both the time rate of change of vorticity and its convection rate. The first term on the right-hand side of Eq. (2.4) accounts for the changes in the length of a vortex filament (i.e., the "straining" of the vortex filament) as it is convected in the flow field. The second term on the right-hand side of Eq. (2.4) accounts for the diffusion of vorticity under the action of the viscosity of the fluid.

The straight line segment approximations of the curved vortex filaments mean that all the vorticity is concentrated along the axis of each vortex filament, forming a vortex line singularity. Under inviscid, incompressible, irrotational flow conditions, the vortex lines move as material lines at the local flow velocities. Thus, Eq. (2.4) may be reduced to an advection (wave) equation of the form

$$\frac{d}{dt}(\mathbf{r}) = \mathbf{V}(\mathbf{r}) \tag{2.5}$$

53
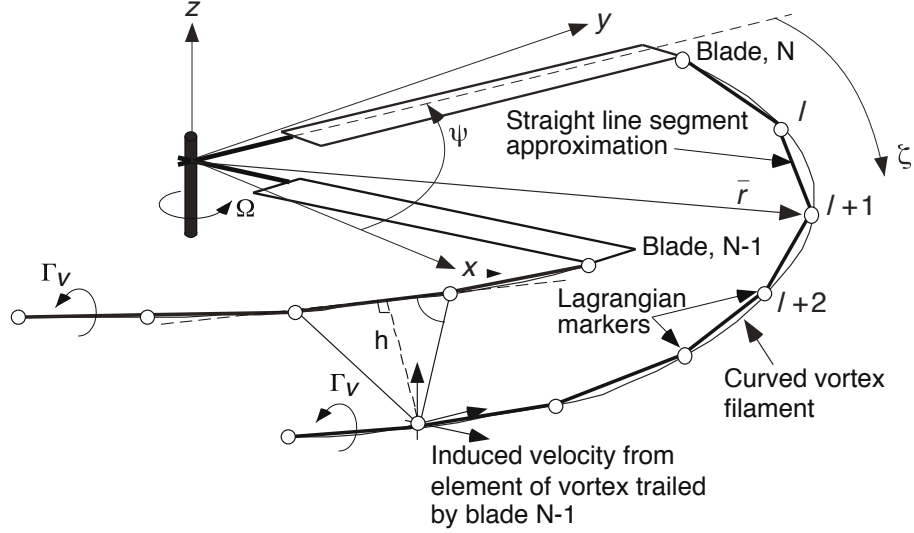
Figure 2.3: Schematic showing the Lagrangian markers used to represent the rotor wake (from Ref. 115).

where **r** is the position vector of the Lagrangian markers in the vortical wake.

For a rotor blade that rotates with constant angular velocity, **r** may be expressed as a function of the azimuthal position of the blade, ψ, and the age of the filament, ζ, relative to the blade when it was deposited into the wake. In the non-rotating, hub-fixed coordinate system, Eq. (2.5) may be expressed as

$$\frac{\partial \mathbf{r}}{\partial \psi} + \frac{\partial \mathbf{r}}{\partial \zeta} = \frac{\mathbf{V}}{\Omega} \tag{2.6}$$

where the velocity, **V**, includes contributions from free-stream effects, induced effects, and additional velocities imposed during the maneuver. This equation is solved using finite difference approximations. The time-accurate, two-step backward, predictor-corrector scheme (PC2B) developed by Bhagwat and Leishman (Ref. 116) was used in the present work.

Viscous Diffusion and Filament Straining Effects The second term in the right-hand side of Eq. (2.4), which included viscous diffusion and filament strain effects, was neglected in the formulation of Eq. (2.6) because of the smaller scales over which these effects act (i.e., within the dimensions of the vortex cores). However, under certain conditions (e.g., maneuvering flight or flight in ground-effect) these effects cannot be ignored. In the present work, these effects were modeled by sequential sub-processes in the solution of the various components of Eq. (2.6).

The effects of viscous diffusion were modeled by Vatistas's generalized viscous vortex core model (Ref. 117), i.e.,

$$V_\theta(r) = \frac{\Gamma_v}{2\pi} \left(\frac{r}{(r^{2n} + r_c^{2n})^{1/n}} \right) \tag{2.7}$$

where V_θ is the swirl velocity, r_c is the vortex core radius and $n = 2$ in the present work. The growth of the viscous core radius as a function of time was modeled by Bhagwat and Leishman's semi-empirical model (Ref. 115, 118), i.e.,

$$r_c(\zeta) = \sqrt{4\alpha\delta\nu \left(\frac{\zeta + \zeta_0}{\Omega} \right)} \tag{2.8}$$

where ζ_0 and δ are coefficients to be defined empirically from a generalization of various tip vortex core growth measurements (Ref. 119). The eddy viscosity coefficient, δ, is a function of the vortex Reynolds number, Γ_v/ν, i.e.,

$$\delta = 1 + a_1 \left(\frac{\Gamma_v}{\nu} \right) = 1 + a_1 Re_v \tag{2.9}$$
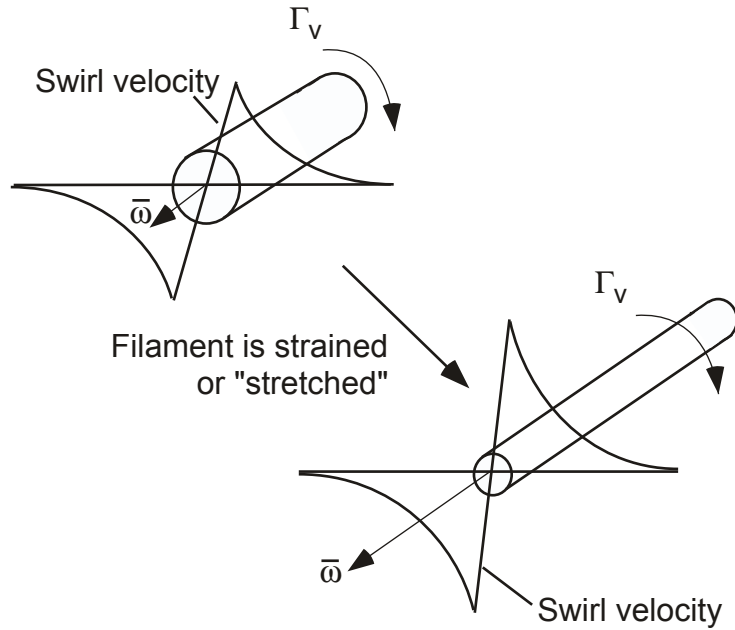
Figure 2.4: Schematic showing stretching of a vortex filament, and intensification of vorticity within the vortex core (from Ref. 114).

where $a_1 = 2 \times 10^{-4}$ in the present work (Ref. 114).

The effects of vortex filament strain (i.e., filament straining) were modeled using the method developed by Ananthan and Leishman (Ref. 120). Under the assumptions of the FVM used in the present work, the net circulation of a vortex filament should remain constant. As a result, any change in the length of the vortex filament is accompanied by a change in the vorticity confined within the vortex core radius; see Fig. 2.4. This effect may be modeled by changing the vortex core size as a function of the filament strain

$\varepsilon = \Delta l / l$, i.e.,

$$\pi r_c^2 l = \pi (r_c - \Delta r_c)^2 (l + \Delta l)$$

$$\left(\frac{r_c - \Delta r_c}{r_c} \right)^2 = \frac{l}{l + \Delta l}$$

$$\Delta r_c = r_c \left(1 - \frac{1}{\sqrt{1 + \varepsilon}} \right) \tag{2.10}$$

By combining Eqs. (2.10) and (2.8), the expression for the effective core at a given time is

$$r_c(\zeta, \varepsilon) = \sqrt{r_{c0}^2 + \frac{4\alpha\delta(Re_v)\nu}{\Omega} \int_0^\zeta (1 + \varepsilon)^{-1} d\zeta} \tag{2.11}$$

Blade Flapping Dynamics Within the FVM, the blade flapping will be dependent upon the blade aerodynamic response, and therefore on the wake solution. For the present work, each blade is assumed to be rigid and flaps about a flapping hinge such that the equation of motion is

$$\overset{\star\star}{\beta} + \nu_\beta^2 \beta = \frac{M_\beta}{I_\beta \Omega^2} + \frac{\omega_0^2}{\Omega^2} \beta_p \tag{2.12}$$

This latter equation may be expressed as a linear system of first-order ODEs with two variables, β and $\overset{\star}{\beta}$, i.e.,

$$\frac{d}{d\psi} \left\{ \begin{array}{c} \overset{\star}{\beta} \\ \beta \end{array} \right\} + \left[\begin{array}{cc} 0 & \nu_\beta^2 \\ -1 & 0 \end{array} \right] \left\{ \begin{array}{c} \overset{\star}{\beta} \\ \beta \end{array} \right\} = \left\{ \begin{array}{c} \dfrac{M_\beta}{I_\beta \Omega^2} + \dfrac{\omega_0^2}{\Omega^2} \beta_p \\ 0 \end{array} \right\} \tag{2.13}$$

which is also be solved using the PC2B scheme.

Modeling Ground-Effect using the Method of Images   The FVM can model ground effect problems by either an image rotor system (Ref. 110) or a surface singularity method. An image approach has been used exclusively in the present work because of its better computational efficiency, although this approach is less suited to modeling non-planar or otherwise irregular ground surfaces.

The method of images involves the concurrent simulation of two rotors: a "real" rotor system and an "image" rotor system; see Fig. 2.5. The image rotor system is located at the same lateral and longitudinal positions as the real rotor system, though beneath the ground plane at a negative height of equal magnitude to the height of the real system. The strength of the vortex filaments of the two rotor systems are equal and opposite to each other such that the total normal component of velocity at the ground plane becomes zero when the Lagrangian markers of the real rotor are convected under the influence of of both rotor systems. This method, therefore, implicitly satisfies the no-penetration condition at all points over the ground plane.

Notice, however, that doubling the number of Lagrangian markers (by adding a second rotor) will increase the Biot-Savart calculations by a factor of four (because the cost is $\sim O(N_v^2)$ where N_v is the total number of vortices from the real rotor system). To save on computational cost, the Lagrangian markers of the image rotor system may be obtained by inverting the normal component of the real rotor marker positions at each time step.

Rotor Trim Methodology   In an actual maneuver, the pilot must continuously adjust the flight controls to command the desired motion of the aircraft. In the present work,
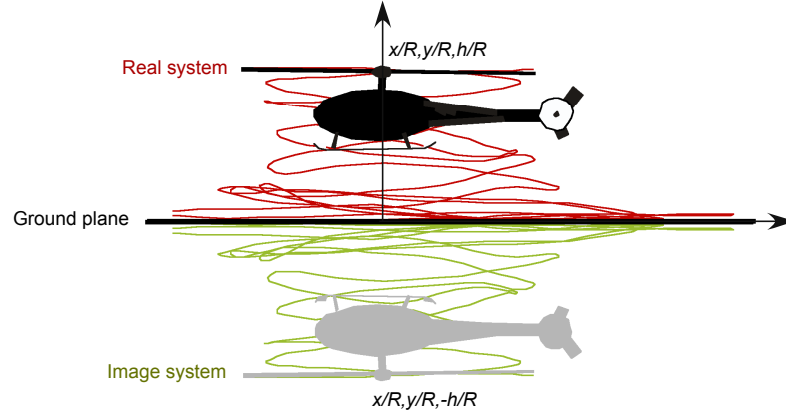
Figure 2.5: A representative free-vortex wake solution obtained using the "method of images" for a rotor in ground-effect (from Ref. 110).

however, a simplified trim methodology was used to calculate the flight control input angles required to obtain the prescribed flight condition, i.e., a prescribed time history of thrust and tip-path-plane (TPP) orientation (Ref. 114). Additionally, the flight control input angles were solved to result in a TPP that was always perpendicular to the rotor axis of rotation, effectively eliminating cyclic flapping. Only the effects of an isolated main rotor system were considered (i.e., no fuselage and no tail rotor).

In the trim methodology, the rotor control inputs are assembled into a vector, i.e.,

$$\mathbf{x} = \{\theta_0, \theta_{1c}, \theta_{1s}\}^T \tag{2.14}$$

where θ_0 is the collective pitch angle, θ_{1c} is the lateral cyclic angle and θ_{1s} is the longitudinal cyclic angle. The control input vector, $\mathbf{x}$ is updated during the trim procedure by solving a linearized system of coupled equation that relate the control inputs, $\mathbf{x}$, to an output vector, $\mathbf{y}$, i.e.,

$$\mathbf{y} = \{C_T, \beta_{1c}, \beta_{1s}\}^T \tag{2.15}$$

59

where C_T is the rotor coefficient of thrust, β_{1c} is the lateral flap angle and β_{1s} is the longitudinal flap angle.

The change of the response vector, $\mathbf{y}$, caused by a perturbation of the input vector, $\mathbf{x}$, can be expressed as a Taylor series expansion, i.e.,

$$\mathbf{y}(\mathbf{x} + \Delta\mathbf{x}) = \mathbf{y} + [\mathbf{J}]\Delta\mathbf{x} + \dots \tag{2.16}$$

where the Jacobian matrix, $[\mathbf{J}]$ is given by:

$$[\mathbf{J}] = \frac{\partial \mathbf{y}}{\partial \mathbf{x}} = \begin{bmatrix} \dfrac{\partial C_T}{\partial \theta_0} & \dfrac{\partial C_T}{\partial \theta_{1c}} & \dfrac{\partial C_T}{\partial \theta_{1s}} \\[2mm] \dfrac{\partial \beta_{1c}}{\partial \theta_0} & \dfrac{\partial \beta_{1c}}{\partial \theta_{1c}} & \dfrac{\partial \beta_{1c}}{\partial \theta_{1s}} \\[2mm] \dfrac{\partial \beta_{1s}}{\partial \theta_0} & \dfrac{\partial \beta_{1s}}{\partial \theta_{1c}} & \dfrac{\partial C_T \beta_{1s}}{\partial \theta_{1s}} \end{bmatrix} \tag{2.17}$$

By ignoring higher-order terms in the Taylor series expansion, the perturbation of the control input vector, $\Delta\mathbf{x}$, may be expressed:

$$\Delta\mathbf{x} = [\mathbf{J}]^{-1}\left(\mathbf{y}\left(\mathbf{x} + \Delta\mathbf{x}\right) - \mathbf{y}\right) = [\mathbf{J}]^{-1}\left\{ \begin{array}{c} C_T - C_{T_{req}} \\[2mm] \beta_{1c} \\[2mm] \beta_{1s} \end{array} \right\} \longrightarrow 0 \tag{2.18}$$

where $C_{T_{req}}$ is the target total thrust coefficient of the rotor system. An initial guess for the control variables is typically obtained as the converged values from the previous iteration, and Eq. (2.18) is solved iteratively until the perturbation vector, $\Delta\mathbf{x}$, is below a specified threshold.
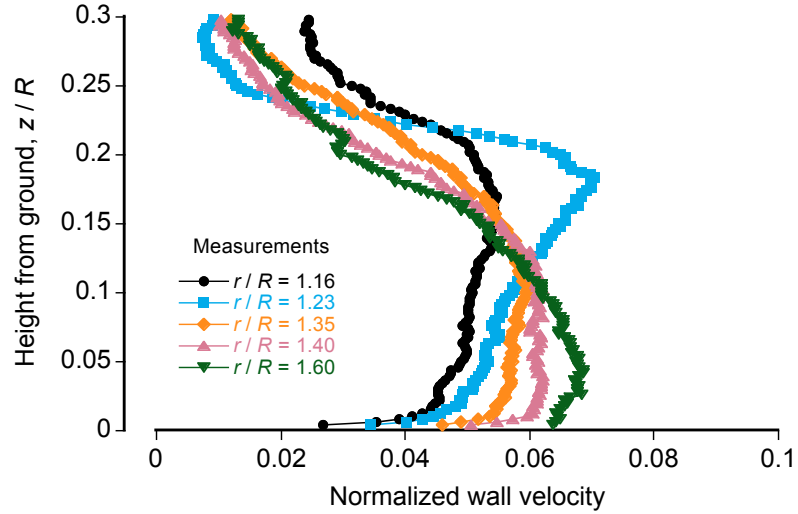
Figure 2.6: Representative measurements of the flow on the ground below a hovering rotor at several downstream distances from a point below the rotational axis of the rotor (from Ref. 111).

Modeling the Viscous Flow Near the Ground

The FVM is a fundamentally inviscid method, so it does not satisfy the no-slip condition at the ground plane. For the purposes of modeling the entrainment of dust particles in a brownout simulation, such a model would therefore be inadequate because the near-wall region has a fundamental impact on the entrainment of sediment from the ground.

Figure 2.6 shows a series of representative flow velocity measurements at several downstream locations in an experimental rotor flow (Ref. 8), and Fig. 2.7 shows similar results from a FVM simulation. Although the simulation results show good qualitative agreement with experimental measurements away from the wall, the developing wall-jet and boundary layer region that are evident in the experimental data are not predicted in the inviscid simulation.

In the present work, a semi-empirical inviscid-viscous method was utilized for pre-
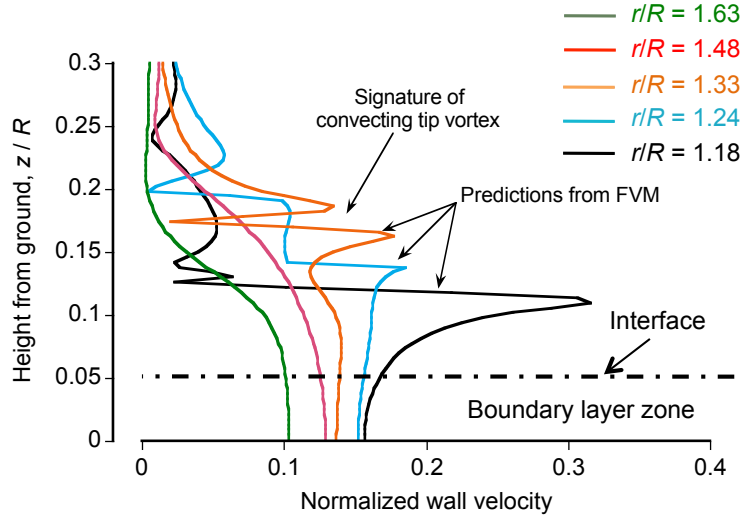
Figure 2.7: Representative velocity profiles computed from the FVM below the rotor at the ground. (from Ref. 111)

dicting the flow field arising from a combination of the rotor flow (modeled as an inviscid potential flow) and the resulting (viscous) flow in the boundary layer region at the ground (Ref. 19); see Fig. 2.8. In this model, the inviscid results from the FVM provide the induced velocity and unsteady pressure fields at a computational interface that is located a small distance above the ground. The velocities and unsteady pressures in the near-wall viscous region are then matched to the appropriate values at the interface using a semi-empirical boundary layer profile, i.e.,

$$u(z) = \frac{u_\star}{k} \log \left(\frac{z}{k_r} \right) \tag{2.19}$$

where k_r is the assumed equivalent roughness height of the ground surface, $k = 0.4$ is the Von Kármán constant, z is height above the ground within the boundary layer region, and $u_\star$ is the friction velocity. In the present work, k_r is assumed to be $0.0333d_p$ when the particles are at rest (Ref. 121), where d_p is the particle diameter. The friction velocity,
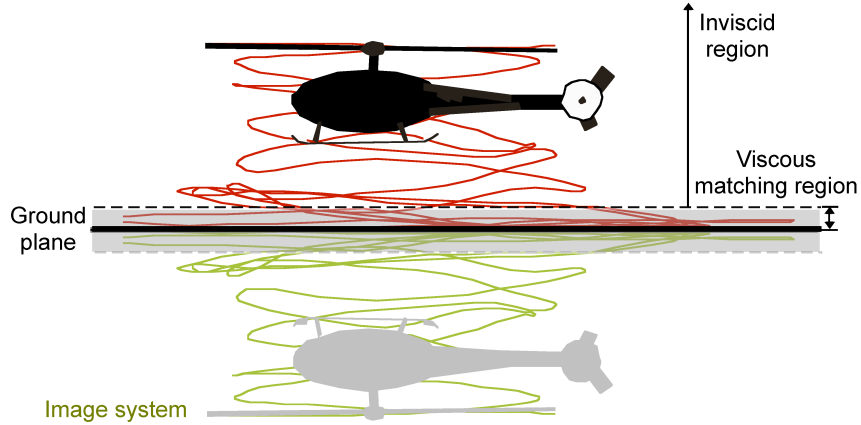
Figure 2.8: Free-vortex wake solution and matching viscous interface for the particle mobility calculations (from Ref. 111).

$u_\star$, is a representation of the shear stresses on the ground, and it was approximated by matching the flow parameters in the viscous region to the inviscid calculations at the interface, i.e.,

$$u_\star = \frac{u(\delta)}{k \, \log(\delta/k_r)} \tag{2.20}$$

where δ is the representative boundary layer thickness, which has been shown in recent rotor flow experiments (Refs. 6, 8, 41) to be of the order of five percent of the rotor radius. An approximate fit of the assumed logarithmic profile given by Eq. (2.19) to experimental results is shown in Fig. 2.9.

Key Assumptions in Modeling the Flow Field

A number of assumptions have been identified in the preceding description of the flow field modeling methodology. A consolidated review of the primary assumptions includes:

1. The FVM is an inviscid method and the flow outside of the wake model is assumed
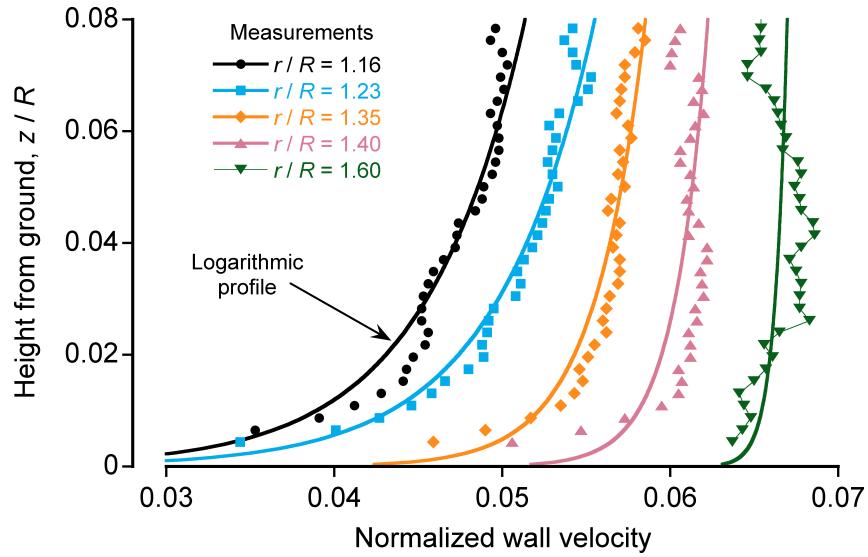
Figure 2.9: Near-wall boundary layer measurements in the flow below the rotor (from Ref. 111).

to be incompressible and irrotational.

2. The bound circulation and lift are assumed constant over each blade segment within the Weissinger-L model, and thin airfoil theory is assumed in finding the relation between lift and circulation in the formulation of the model.

3. The viscous region near the ground is matched to the inviscid flow away from the ground using a inviscid-viscous method that applies a semi-empirical boundary layer profile.

4. The rotor controls are trimmed at each time step to achieve a prescribed time-history of thrust and TPP orientation (i.e., there is no pilot model and no inverse simulation to determine the control positions for the maneuver).

2.1.2 Brownout Cloud Modeling

Once the rotor flow has been predicted, the resulting brownout cloud may be modeled. Notice that a one-way coupling is assumed in the present work, meaning that the particle motion is driven by the air but not vice-versa. The brownout cloud modeling problem is particularly complicated, in that the model must be capable of modeling multiple modes of particle uplift and entrainment. Furthermore, the model must contain a sufficient number of dust particles to represent the essential features and characteristics of the brownout cloud, but not so many particles as to prohibitively increase the computational expense of the calculations.

Entrainment of Sediment from the Bed

Accurately modeling the conditions by which individual dust particles become mobilized under the action of the an unsteady, turbulent, vorticity-laden rotor flow field is essential for modeling the development of a brownout cloud. Although most prior entrainment models have been based upon the the exceeding of a threshold friction velocity, Syal and Leishman (Refs. 19, 20) proposed a brownout cloud development model that includes: (i) direct entrainment by exceeding a threshold velocity and/or the action of unsteady pressure effects as well as (ii) entrainment by bombardment ejection. This new entrainment model was used in the present work.

Forces Acting on Stationary Particles on the Bed   Stationary particles in a sediment bed below a rotor are subjected to several types of forces, such as shear (which may be
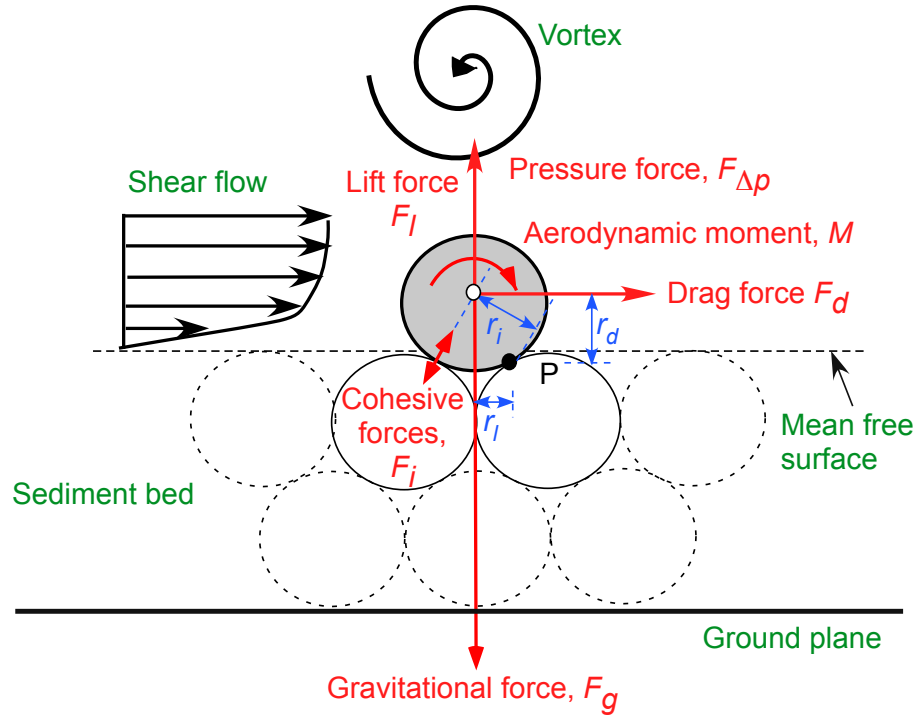
Figure 2.10: Forces acting on sediment particles at the surface (from Ref. 111).

resolved into components of lift, $\mathbf{F}_l$, and drag, $\mathbf{F}_l$), pressure ($\mathbf{F}_{\Delta p}$), inter-particle ($\mathbf{F}_i$), and gravitational ($\mathbf{F}_g$); see Fig. 2.10. Under the action of these forces, a particle may become mobilized about a point (labeled 'P' in Fig. 2.10) if the moments created by the aerodynamic forces about the point exceed those from the gravitational and inter-particle forces. This process is known as direct aerodynamic entrainment. While the effects of shear forces on sediment entrainment have been studied previously (Refs. 121–123) in steady, unidirectional flow fields, the effects of unsteady pressure forces are less known.

Direct Aerodynamic Entrainment Direct aerodynamic entrainment occurs when the shear and pressure forces on a particle exceed the gravitational and inter-particle forces. The accurate modeling of this process, however, is fraught with challenges (Ref. 111). In the first instance, solving for the moment equilibrium condition at each sediment particle

requires a knowledge of its immediate neighbors, which significantly increases the computational expense of the problem. Furthermore, the entrainment of very small particles (which play an important part in the development of a brownout cloud) is primarily determined by inter-particle forces that are difficult to model because there are no general mathematical expressions to describe the physical effects.

Because of the questionable applicability of existing threshold models to the brownout problem, Syal (Ref. 111) developed a new model for simulating the entrainment of particles in a rotor flow field. This model, which has been used to model the brownout clouds in the present work, builds upon an existing model from Shao and Lu (Ref. 124). The new model, however, includes the contributions of unsteady pressure effects. The model may be expressed

$$u_{\star t} = A\sqrt{\frac{3}{2}\frac{\Delta P}{\rho} + \frac{\rho_p - \rho}{\rho}gd_p + \frac{\gamma}{\rho d_p}} \tag{2.21}$$

where $u_{\star t}$ is the equivalent threshold velocity, $A = 0.1109$, $\gamma = 3 \times 10^{-4}$ N m^{-1}, ΔP is the unsteady pressure difference on the bed (calculated from Kelvin's equation), ρ is the fluid density, ρ_p is the particle density, d_p is the particle diameter, and g is gravitational acceleration. From a practical standpoint, when the local friction velocity, $u_\star$, exceeds the threshold friction velocity, $u_{\star t}$, the particle will become mobilized.

Notice from Eq. (2.21) that $u_\star$ will decrease with ΔP until $u_{\star t} = 0$. From a practical standpoint, this means that particles may be mobilized even if $u_\star = 0$. For these conditions, a particle may be mobilized in the absence of shear stress when ΔP exceeds the threshold given by

$$\Delta P_t = -\frac{2}{3}\left[(\rho_p - \rho)gd_p + \frac{\gamma}{d_p}\right] \tag{2.22}$$

In this sense, the present model is unique in its ability to model direct aerodynamic mobilization by both shear and pressure forces.

Bombardment Ejection   Another form of particle mobilization occurs when a suspended particle impacts the sediment bed and, in the process, ejects many more particles from the bed. This form of entrainment is known as bombardment ejection. Shao, Raupach, and Findlater (Ref. 125) showed that bombardment ejection was primarily responsible for the uplift of very small dust particles, for which the the inter-particle forces are strong enough to prevent them from being dislodged by direct mobilization. These smaller-sized particles are known to comprise a large portion of the particulate composition of a typical brownout cloud (Refs. 14, 15) and can be particularly problematic in brownout scenarios because of their propensity for staying entrained in the flow field for longer durations than larger particles. Recent dual-phased experiments by Johnson, Leishman, and Sydney (Ref. 6) and Sydney, Baharani, and Leishman (Ref. 7) have demonstrated that bombardment ejection is indeed an important contributor to sediment uplift in rotor flows, and that bombardment ejection may occur in a variety of forms; see Fig. 2.11.

Because of the inability of existing threshold models to account for particle entrainment, Syal and Leishman (Ref. 19) developed a probabilistic approach to modeling the bombardment ejection process in brownout. The brownout ejection model sought to calculate the volume of the crater in the sediment bed formed by the impacting particles and approximate the initial velocities of the ejected particles.

Figure 2.12 shows a schematic of a particle impacting the sediment bed, forming
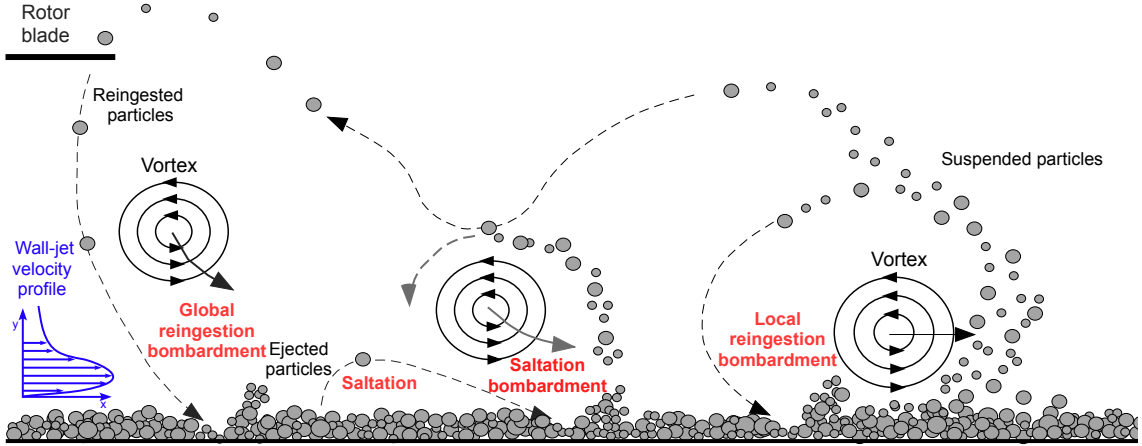
Figure 2.11: Schematic showing the different modes of dust particle motion and the fundamental uplift mechanisms seen in the near-wall region (from Ref. 7).

a crater, and ejecting new particles. The volume of the crater, ϑ, may be expressed as a function of the impact velocity, $\mathbf{V}_0$, and the trajectory of the impacting particle, α_0, i.e.,

$$\vartheta = \frac{\pi \rho_p d_p^3 |\mathbf{V}_0|^2}{12 p_s} \left(\sin 2\alpha_0 - 4 \sin^2 \alpha_0 + \frac{7.5\pi |\mathbf{V}_0| \sin^3 \alpha_0}{\beta_v d_p} \right) \qquad (2.23)$$

where $\beta_v = \sqrt{\left(\frac{2\, p_s\, d_p}{m_0} \right)}$, d_p is the particle diameter, and p_s is the horizontal component of plastic pressure of the bed exerted on the particle (Ref. 126). For the present analysis, p_s was considered to be 1,000 N m^{-2}, which is representative of smooth and fine-grained, unaggregated beds (Ref. 126). The number of particles removed from the bed was computed under the assumption that the dust particles in the sediment bed are tightly packed. Key assumptions in this model include: (i) that the impacting particle forms a void-shaped crater, (ii) that the volume of particles ejected from the bed is equal to the volume of the crater that is formed, (iii) that a constant plastic pressure acts upon the particle impacting the bed as it ploughs through the bed, (iv) that the impacting particle does not shatter
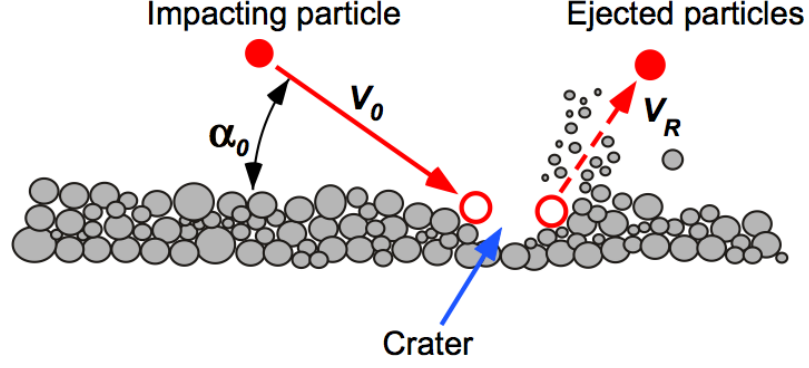
Figure 2.12: Schematic of a sediment particle impacting the ground, forming a crater, and ejecting new particles (from Ref. 111).

upon impact, and (v) that the ratio of the vertical force to the horizontal force acting on the impacting particle is constant as the particle passes through the sediment bed.

In the present work, the rebound velocity, $\mathbf{V}_R$, was calculated using a hard-sphere model after integrating the equations of motion. The coefficient of restitution was assumed to be 0.6 (Ref. 19). The velocities of the emitted particles was assumed to be normally distributed, i.e.,

$$\Phi = \frac{1}{2\pi^{k/2}|\Sigma_B|^{k/2}} \exp \frac{-1}{2}(\mathbf{V}_n - \mu_B)^T \Sigma_B^{-1}(\mathbf{V}_n - \mu_B) \qquad (2.24)$$

where $\Phi(\mu_B, \Sigma_B)$ is a multivariate normal distribution with mean, μ_B, and covariance matrix, Σ_B, and $\mathbf{V}_n$ is velocity of the nth ejected particle. The mean of the velocity distribution is given by

$$\mu_B = \frac{1}{N_b + 1} \sum_{n=1}^{N_b+1} \mathbf{V}_n \qquad (2.25)$$

70

and the covariance matrix is given by

$$\Sigma_B = \begin{bmatrix} \sigma_{xx}^2 & \sigma_{xy}^2 & \sigma_{xz}^2 \\ \sigma_{yx}^2 & \sigma_{yy}^2 & \sigma_{yz}^2 \\ \sigma_{zx}^2 & \sigma_{zy}^2 & \sigma_{zz}^2 \end{bmatrix} \tag{2.26}$$

where

$$\sigma_{ij}^2 = \frac{1}{N_b + 1} \sum_{i=1}^{N_b+1} \left(\mathbf{V}_{n_i} - \mu_{B_i} \right) \left(\mathbf{V}_{n_j} - \mu_{B_j} \right) \tag{2.27}$$

is the variance of ith dimension with j.

The mean and covariance matrix are estimated by applying the principles of momentum and energy conservation. For example, the principle of conservation of momentum states that the momentum of the particle rebounding with velocity $\mathbf{V}_R$ will be equal to the momentum gained by N_b bombarded particles, i.e.,

$$m_R \mathbf{V}_R = \sum_{n=1}^{N_b+1} m_n \mathbf{V}_n \tag{2.28}$$

where $\mathbf{V}_n$ is the velocity of the nth bombarded particle, and m_R and m_n are masses of the rebounding and bombarded particles, respectively. In the present work, all particles in the simulation are assumed to have the same mass, i.e., $m_R = m_n$. The mean of the velocity distribution may therefore be expressed

$$\mu_B = \frac{1}{N_b + 1} \sum_{n=1}^{N_b+1} \mathbf{V}_n = \frac{\mathbf{V}_R}{N_b + 1} \tag{2.29}$$

71

Furthermore, conservation of the total kinetic energy of the rebounding particle gives

$$E_R = \frac{1}{2} m_R |\mathbf{V}_R|^2 = \frac{1}{2} \sum_{n=1}^{N_b+1} m_n |\mathbf{V}_n|^2 \tag{2.30}$$

where E_R is the total kinetic energy of the rebounding particle. Assuming the covariance matrix to be diagonal (i..e, neglecting any coupling between the different dimensions in Eq. (2.26), it may be expressed as

$$\Sigma_B = \begin{bmatrix} \sigma_{xx}^2 & 0 & 0 \\ 0 & \sigma_{yy}^2 & 0 \\ 0 & 0 & \sigma_{zz}^2 \end{bmatrix} \tag{2.31}$$

where σ_{xx}^2, σ_{yy}^2 and σ_{zz}^2 are variances along the x, y and z directions, respectively. Using Eq. (2.27), the variance along the x-direction becomes

$$\begin{aligned} \sigma_{xx}^2 &= \frac{1}{N_b+1} \sum_{n=1}^{N_b+1} (V_{n_x} - \mu_{B_x})^2 \\ &= \frac{1}{N_b+1} \left(\sum_{n=1}^{N_b+1} V_{n_x}^2 - 2\mu_{B_x} \sum_{n=1}^{N_b+1} V_{n_x} + \mu_{B_x}^2 \right) \end{aligned} \tag{2.32}$$

The first term in Eq. (2.32) can be estimated from Eq. (2.30) under the assumption that the fraction of the total rebound kinetic energy, which is proportional to the x-component of velocity, goes along the x-direction, i.e.,

$$\sum_{n=1}^{N_b+1} V_{n_x}^2 = E_R \frac{V_{R_x}^2}{V_{R_x}^2 + V_{R_y}^2 + V_{R_z}^2} \tag{2.33}$$

Similar expressions may be derived for the y and z dimensions. Using Eqs. (2.29) and (2.33) in Eq. (2.32) gives

$$\sigma_{xx}^2 = \left(\frac{E_R}{N_b+1}\right)\frac{V_{R_x}^2}{V_{R_x}^2+V_{R_y}^2+V_{R_z}^2} - \frac{V_{R_x}^2}{(N_b+1)^2} \tag{2.34}$$

$$\sigma_{yy}^2 = \left(\frac{E_R}{N_b+1}\right)\frac{V_{R_y}^2}{V_{R_x}^2+V_{R_y}^2+V_{R_z}^2} - \frac{V_{R_y}^2}{(N_b+1)^2} \tag{2.35}$$

$$\sigma_{zz}^2 = \left(\frac{E_R}{N_b+1}\right)\frac{V_{R_z}^2}{V_{R_x}^2+V_{R_y}^2+V_{R_z}^2} - \frac{V_{R_z}^2}{(N_b+1)^2} \tag{2.36}$$

Therefore, using the mean, μ_B, given by Eq. (2.29) and the covariance, Σ_B, given by Eq. (2.36), the initial velocities of the bombarded particles can calculated by Eq. (2.24).

Syal (Ref. 111) conducted a computational study of the effects of the velocity and size of the impacting particle on the process of bombardment ejection and, in particular, on its significance in the development of a brownout cloud. The results of this study indicated that, for constant impact velocity, the impact of a larger particle on the bed will eject a larger number of particles, in general, and that the ejected particles will include a maximum of smaller-sized particles, in particular (as seen experimentally in Ref. 125). Another result of this study is that, for constant initial conditions (i.e., particle location and flow field velocity), the size of the impact crater does not necessarily vary directly with the particle size. This counterintuitive result is largely a consequence of the effects of the particle in the flow prior to impact, and it demonstrates the complexity of the problem.

Particle Convection

Once a particle has been entrained into the flow field, a variety of forces will govern its motion. A one-way coupling has been assumed in the present work, meaning that the particle motion is driven by the air (but not vice-versa). Although this assumption is not valid in all regions of the flow (particularly in the regions that are closest to the ground), it is an assumption that makes an overall solution of the problem much more computationally tractable.

Particle Equations of Motion   The forces acting on an individual particle in the flow field are shown in Fig. 2.13, and include: a drag force $\mathbf{F}_d$, a lift force $\mathbf{F}_L$, gravity force $\mathbf{F}_g$, buoyancy force $\mathbf{F}_b$, apparent mass forces $\mathbf{F}_m$, and Basset forces $\mathbf{F}_{\text{Basset}}$. The Basset-Boussinesq-Oseen (BBO) equation governs the resulting dynamic behavior of the particles, and it can be simplified significantly under a variety of assumptions, i.e.,

$$m\frac{d\mathbf{V}_p}{dt} \; = \; \sum \mathbf{F} \tag{2.37}$$

$$= \; \mathbf{F}_d + \mathbf{F}_g + \mathbf{F}_L + \mathbf{F}_m + \mathbf{F}_b + \mathbf{F}_{\text{Basset}} \tag{2.38}$$

$$\simeq \; \mathbf{F}_d + \mathbf{F}_g \tag{2.39}$$

$$= \; -\frac{1}{2}\rho \, C_d A \left| \mathbf{V}_p - \mathbf{V} \right| (\mathbf{V}_p - \mathbf{V}) + m\mathbf{g} \tag{2.40}$$

where $\mathbf{V}_p$ and $\mathbf{V}$ are the particle and flow velocities, respectively, at any instant in time. Notice that the Basset force, which depends on the time-history of the particle motion, manifests as an apparent drag force, although it was neglected in the present work because it is important only in flows with light particles and steep velocity gradients. Notice
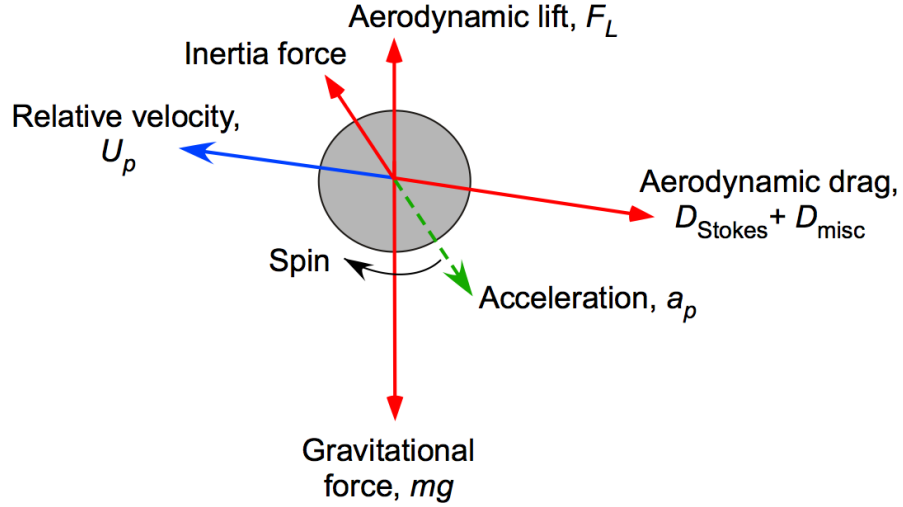
Figure 2.13: Forces acting on an airborne particle (from Ref. 111).

that the lift, apparent mass, and buoyancy forces are assumed to be negligible under the assumption of a dilute flow.

In the present work, monodisperse spherical particles with a diameter of d_p were assumed, such that $A = \pi d_p^2/4$. The drag coefficient, C_d is a function of the particle Reynolds number Re_p, i.e.,

$$C_d(Re_p) = \frac{24}{Re_p}\left(1 + 0.15 Re_p^{0.687}\right) \qquad (2.41)$$

where

$$Re_p = \frac{|\mathbf{V}_p - \mathbf{V}|d_p}{\nu} \qquad (2.42)$$

Under Stokes flow assumptions, i.e., for $Re_p \ll 1$, C_d may be expressed

$$C_d = \frac{24}{Re_p} \qquad (2.43)$$

75

The equations of motion for the particles then become

$$\frac{d\mathbf{V}_p}{dt} = -\frac{(\mathbf{V}_p - \mathbf{V})}{\tau_p} + g\hat{k} \qquad (2.44)$$

$$\frac{d\mathbf{X}_p}{dt} = \mathbf{V}_p \qquad (2.45)$$

where $\mathbf{V}_p$ and $\mathbf{V}$ are particle and flow velocities at $\mathbf{X}_p$ at a time t, g is the acceleration under gravity, $\hat{k}$ is the unit vector in the vertical z-direction, and τ_p is the particle response time, i.e.,

$$\tau_p = \frac{m}{\frac{1}{2}\rho C_d \left(Re_p\right) A \left|\mathbf{V}_p - \mathbf{V}\right|} \qquad (2.46)$$

Notice that the particle response time is a function of particle and flow properties. Using Eqs. (2.41) and (2.42) for spherical particles, τ_p can be written as

$$\tau_p = \frac{\tau_{p_s}}{1 + 0.15 Re_p^{0.687}} \qquad (2.47)$$

where τ_{p_s} is the particle response time under Stokes flow conditions, i.e.,

$$\tau_{p_s} = \frac{\rho_p d_p^2}{18\mu} \qquad (2.48)$$

Substituting Eq. (2.47) into Eq. (2.44), the equations of motion of the particle become

$$\frac{d\mathbf{V}_p}{dt} = -\frac{\left(1 + 0.15 Re_p^{0.687}\right)}{\tau_{p_s}}(\mathbf{V}_p - \mathbf{V}) + g\hat{k} \qquad (2.49)$$

$$\frac{d\mathbf{X}_p}{dt} = \mathbf{V}_p \qquad (2.50)$$

where Eq. (2.49) is a nonlinear ordinary differential equation, and therefore, must be solved using iterative methods.

In the present work, Stokes flow assumptions were used to linearize Eq. (2.49) and, therefore, reduce the computational cost (Ref. 111). Under this assumption, the particle equations of motion may be expressed

$$\frac{d\mathbf{V}_p}{dt} = -\frac{(\mathbf{V}_p - \mathbf{V})}{\tau_{p_s}} + g\hat{k} \tag{2.51}$$

$$\frac{d\mathbf{X}_p}{dt} = \mathbf{V}_p \tag{2.52}$$

Furthermore, under the assumptions of dilute gas-particle suspensions, the particle equations of motion may be decoupled in the three spatial dimensions, i.e.,

$$\frac{dV_{p_x}}{dt} = -\frac{(V_{p_x} - V_x)}{\tau_{p_s}} \tag{2.53}$$

$$\frac{dV_{p_y}}{dt} = -\frac{(V_{p_y} - V_y)}{\tau_{p_s}}$$

$$\frac{dV_{p_z}}{dt} = -\frac{(V_{p_z} - V_z)}{\tau_{p_s}} - g$$

and

$$\frac{dX_{p_x}}{dt} = V_{p_x} \tag{2.54}$$

$$\frac{dX_{p_y}}{dt} = V_{p_y}$$

$$\frac{dX_{p_z}}{dt} = V_{p_z}$$

Solution to the Particle Equations of Motion   The decoupled particle equations can be written in a simplified form, i.e.,

$$\frac{dV_{p_i}(X_{p_i},t)}{dt} = -\frac{V_{p_i}(X_{p_i},t) - f_i(X_{p_i},t)}{\tau_{p_s}} \tag{2.55}$$

$$\frac{dX_{p_i}(t)}{dt} = V_{p_i}(X_{p_i},t) \tag{2.56}$$

where $i = x, y, z$, $f_x = V_x$, $f_y = V_y$, and $f_z = V_z - g\tau_{p_s}$. Equations (2.55) and (2.56) are three sets of ODEs, where each set can be expressed as

$$\frac{d}{dt}\left\{ \begin{array}{c} V_{p_i} \\ X_{p_i} \end{array} \right\} - \left[\begin{array}{cc} -1/\tau_{p_s} & 0 \\ 1 & 0 \end{array} \right] \left\{ \begin{array}{c} V_{p_i} \\ X_{p_i} \end{array} \right\} = \left\{ \begin{array}{c} f_i \\ 0 \end{array} \right\} \tag{2.57}$$

Each set of ODEs is solved to compute the positions of the particles, $\mathbf{X}_p$, at different times. In the first instance, the particle velocities, $\mathbf{V}_p$, are determined from Eq. (2.55) under the influence of the rotor flow velocities, $\mathbf{V}$, which appear as the source term, $\mathbf{f}$, on the right-hand side. These velocities include induced velocities from all the vortex elements in the flow field, as well as any maneuver velocities and free-stream velocities. The computed particle velocities, $\mathbf{V}_p$, are then used to convect the particles to new positions in time, $\mathbf{X}_p$, as given by Eq. (2.56).

These ODEs are numerically solved by a time-marching scheme in which the left-hand side is discretized and the source term, $\mathbf{f}$, is computed by the Biot-Savart law (see Section 2.1.1). In the present work, a modified form of a two-point backward difference formula EI-BDF2(E), which is second-order accurate in time, was utilized (Ref. 111).

Numerical Implementation and Computational Considerations

A variety of simplifications must be adopted for the numerical modeling of large-scale brownout clouds. In the present work, the sediment bed was assumed to consist of monodisperse spherical particles that were arranged in layers; see Fig. 2.14(a). Initially, only the particles in the top-most layer of the sediment bed were considered to be "active," i.e., eligible to be entrained under the action of the aerodynamic forces. As these particles become entrained in the flow by the mechanisms described in Section 2.1.2, the particles directly beneath become active; see Fig. 2.14(b). Because only a finite number of layers can be computationally modeled, however, a particle only becomes active after a specified time delay, δt, after the particle in the layer just above it had became active. This delay can be qualitatively justified from videographic analysis of the actual brownout clouds, which shows that the process of mobilization and entrainment of successive layers of particles from a sediment bed is not a continuous one (rather, it depends upon the moisture content, cohesion, etc. of the bed).

Once the particles are entrained, they convect in the flow, as described in Section 2.1.2. When the entrained particles bombard the sediment bed with enough kinetic energy to eject particles through bombardment ejection (see Section 2.1.2), the bombarded particles are treated as new (additional) particles that are introduced into the simulation; see Fig. 2.14(c). For example, if N_I is the total number of particles initially lying on the sediment bed and N_b is the total number of particles ejected from the bed from bombardment, then the total number particles at the end of the simulation will be $N_I + N_b$

One of the primary challenges in numerically modeling brownout clouds is the
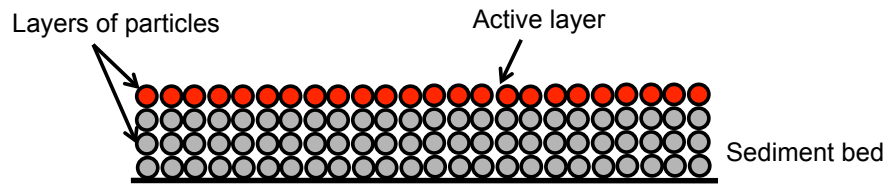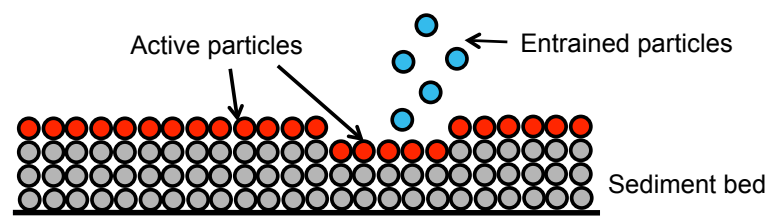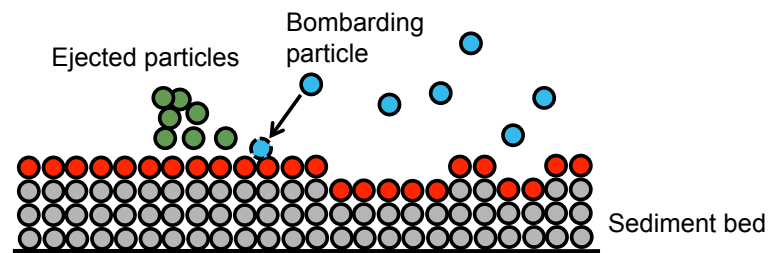
Figure 2.14: Schematic of (a) the stationary sediment bed structured in the form of layers, (b) active and entrained particles, and (c) new particles ejected through bombardment (from Ref. 111).

tracking of a very large number of particles over long durations of time. A rotorcraft landing or takeoff maneuver may involve time scales that are measured in tens of seconds and hundreds of rotor revolutions, and the associated computational costs climb rapidly.

To contain this cost, techniques for the judicious sizing of the sediment bed were examined on a case-by-case basis, and these techniques will be detailed in subsequent chapters. Although particle clustering algorithms have been shown to be effective in increasing the particle counts in a simulated brownout cloud without adding substantially to the computational cost (Ref. 22), they were not utilized in the present work because they result in significantly increased file sizes. While this increase in file sizes may not be a major factor when performing small numbers of cloud simulations, the associated file management overhead precluded their use in the present work, which consists of scores of brownout simulations performed simultaneously on (and transferred in between) a number of machines. In a more general sense, however, other approaches were employed to limit the computational costs associated with the brownout modeling.

A variety of methods exist to take advantage of hardware parallelism for computational accelerations. In the present work, Message Passing Interface (MPI) was utilized for parallelization of processes on multicore central processing units (CPUs), Ref. 127, and Compute Unified Device Architecture (CUDA) was utilized for parallelization on graphical processing units (GPUs), Ref. 128.

In the present work, MPI enabled a brownout cloud post-processing procedure to be performed more efficiently by dividing the computations among multiple processors. Each "thread" of the analysis could be completed independently from the others, which is
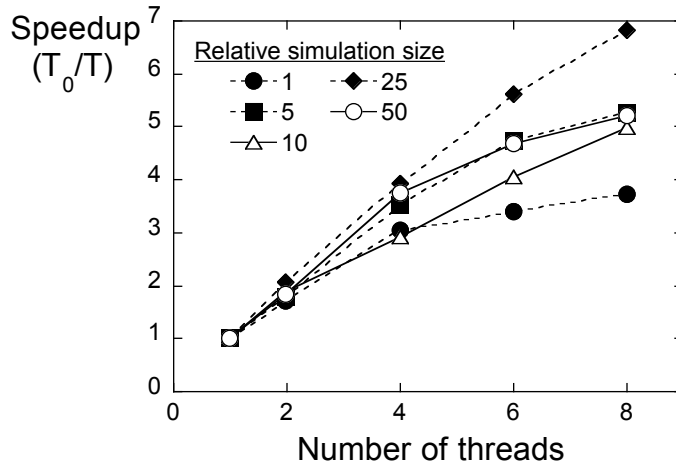
Figure 2.15: Speedup achieved as a function of the number of MPI processes.

known as a single instruction multiple data (SIMD) problem. An analysis of the speedup, i.e., the ratio of the computational cost of the serial code, T_0, to that of the parallelized code, T, for a variety of test cases is shown in Fig. 2.15.

The brownout cloud simulations were made drastically more efficient through the use of GPUs (Ref. 23). GPUs are designed for efficient SIMD computations, with more transistors being devoted to data processing rather than data caching and flow control; see Fig. 2.16. In the present work, GPUs were utilized to compute the induced velocity computations within the dust cloud model. At each time step, the particle positions were transferred from the CPU to the GPU, and the induced velocities at these locations were transferred back. The parameters of the rotor wake solution, i.e., the wake geometry, the vortex strength and the core radius, were transferred from the CPU to the GPU only once per simulation time step, and they were subsequently stored in the constant memory of GPU for use by all GPU threads.

Figure 2.17 shows the results of a comparison study in which the computational cost
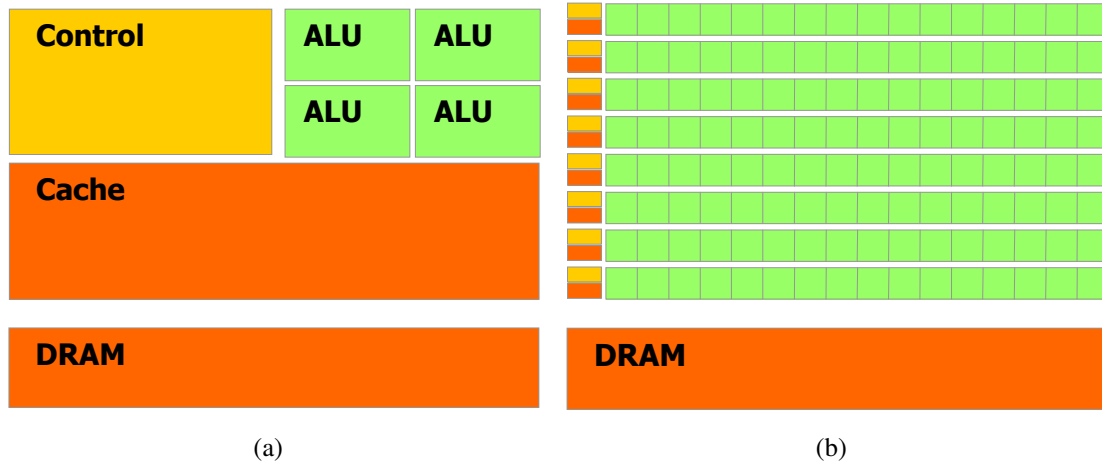
Figure 2.16: Memory architecture on a (a) CPU and (b) GPU (from Ref. 128).

benefit of single-precision and double-precision GPU computations, relative to a double-precision CPU simulation, was examined (Ref. 111). The results obtained were clearly very good: up to a $250\times$ speed-up for single-precision and up to a $25\times$ speed-up for double-precision.

Key Assumptions in Modeling the Dust Cloud

A number of assumptions have been identified in the preceding description of the dust cloud modeling methodology. A consolidated review of the primary assumptions includes:

1. One-way coupling has been assumed in the present work, meaning that the particle motion is driven by the air but not vice-versa.

2. All simulations in the present work consist of monodisperse, spherical particles of uniform density arranged in a sediment bed that consists of a finite number of layers.
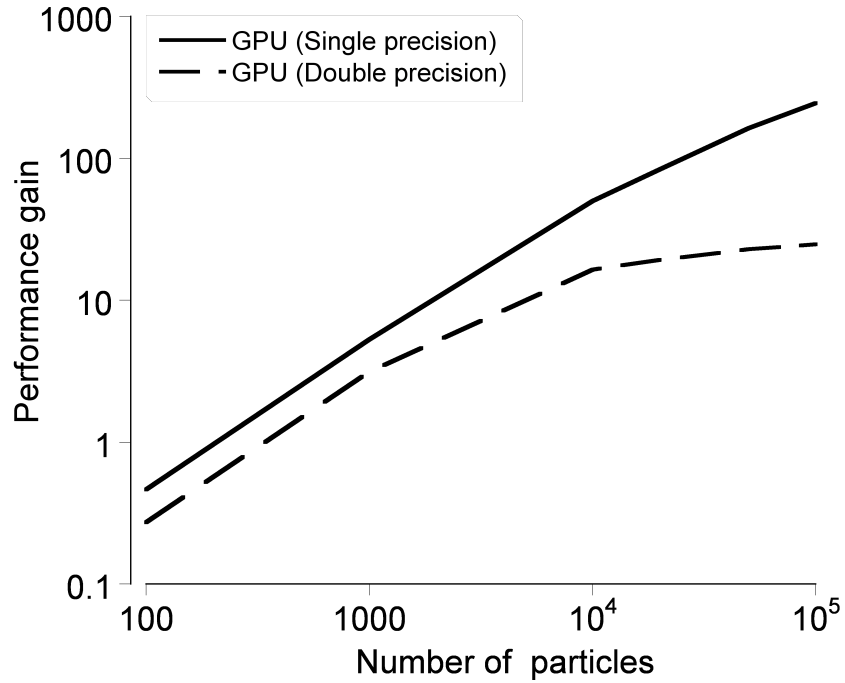
Figure 2.17: Performance gain with GPU implementation of the dust cloud simulation (from Ref. 111).

3. The numerical implementation of the dust cloud model allows only the top layer of particles to be active at any time, i.e., the particles directly adjacent to the flow field, and there is a small time delay between the activation of each layer.

4. The volume of particles ejected from the bed in a bombardment event equals the volume of the crater that is formed, and the particles that are ejected in the bombardment simulation are in addition to those that are included in the initial sediment bed.

2.2 Numerical Optimization

Griva, Nash, and Sofer (Ref. 129) introduce the concept of numerical optimization by asserting that, "Optimization models attempt to express, in mathematical terms, the goal of solving a problem in the 'best' way." In recent years, numerical optimization has become an essential tool in the fields of finance, economics, operations, science, and engineering. In the present work, numerical optimization provides a foundation for the formulation of brownout mitigation strategies.

The key elements of an optimization problem are succinctly summarized by Nocedal (Ref. 130). The first step is to identify an objective, i.e., "a quantitative measure of the performance of the system under study." The objective is dependent on certain characteristics of the system known as variables, and the goal of the optimization is to identify the combination of variables that will minimize or maximize the objective. Typically some, if not all, of the variables will be subjected to constraints.

The construction of a suitable optimization model involves the proper identification of the objective, variables, and constraints (if applicable) for the given problem. Once the model has been formulated, an optimization algorithm may be selected to find the solution to the problem. There are many optimization algorithms, and selecting the proper algorithm for the specific problem will determine whether the solution can be obtained and, if it can be obtained, how rapidly the problem can be solved.

From a purely mathematical standpoint, optimization is the minimization (or maximization) of an objective function subject to constraints on its variables. In its canonical

form, an optimization problem may be stated as follows:

$$B(\mathbf{X}) \rightarrow \min \tag{2.58}$$

$$\text{subject to:} \quad g_j(\mathbf{X}) = 0 \qquad j = 1,\ldots,m \tag{2.59}$$

$$g_j(\mathbf{X}) \leq 0 \qquad j = m+1,\ldots,n \tag{2.60}$$

where $\mathbf{X}$ is the vector of variables, $B(\mathbf{X})$ is the objective function that is to be minimized, and $g_j(\mathbf{X})$ are constraint functions that define certain equations and inequalities that $\mathbf{X}$ must satisfy.

A broad review of optimization theory is beyond the scope of this dissertation. This section will, therefore, focus on optimization methods for solving problems in which (i) objective function evaluations are very costly, (ii) nonlinearity is a likely property of the problem (and perhaps it exhibits nonconvexity), and (iii) the vector of variables may contain a mix of continuous-valued and integer/discrete-valued variables.

2.2.1 Approximate Optimization

In instances where the computational cost of a single objective function evaluation is high, it can be helpful to perform an approximate optimization. The fundamental approach of an approximate optimization is to create some approximating functions to the objective as well as the constraint(s), and to perform the optimization using the approximations. The optimum that is solved from the approximate functions is then analyzed precisely, and the approximate objective and constraint functions are updated. A subse-

quent optimization step may be performed using the new approximations, and the process

is continued until convergence to a precise optimum is achieved.

A single iteration of a representative approximate optimization procedure is shown

in Fig. 2.18. At the beginning of the iteration, a set of precise evaluations of a one-

dimensional objective function, $B(x)$, have been performed; see Fig. 2.18(a). An approx-

imating function, $B_{\text{app}}(x)$, is fit to the precise evaluations; see Fig. 2.18(b). Next, the

variable value, x^*, corresponding to the minimum of the approximate objective function,

$B_{\text{app}}(x^*)$, is computed; see Fig. 2.18(c). The true objective function value correspond-

ing to the approximate optimum, $B(x^*)$, is then computed precisely, and this new precise

evaluation will be included in the subsequent iterations; see Fig. 2.18(d). The imposition

of constraint functions is performed in an identical manner.

There are a number of variations of the basic approximate optimization methodol-

ogy that are commonly employed. In the first instance, the user must select an appropriate

type of approximating function. Jones (Ref. 87) provides a comprehensive review of many

of the potential approximation methods. In the analyses included in subsequent chapters,

two approximating functions will be utilized: a second-order Taylor series expansion and

a Radial Basis Function (RBF) approximation.

Vanderplaats (Ref. 89) details the use of a Taylor series expansion as an approxi-

mating function, i.e.,

$$F(\mathbf{X}) \approx F_{\text{app}}(\mathbf{X}) = F(\mathbf{X}^0) + \nabla F(\mathbf{X}^0) \cdot \delta\mathbf{X} + \frac{1}{2}\delta\mathbf{X}^T \mathbf{H}(\mathbf{X}^0)\delta\mathbf{X} + \dots \qquad (2.61)$$

where $F(\mathbf{X})$ is taken to be any objective or constraint function, $\nabla F(\mathbf{X}^0)$ is the gradient,
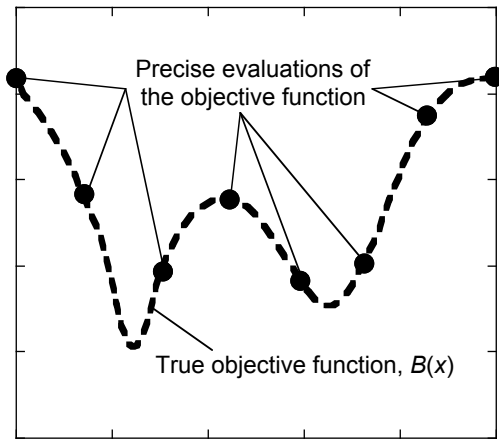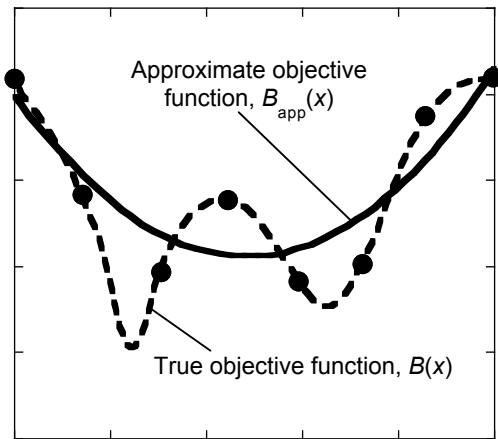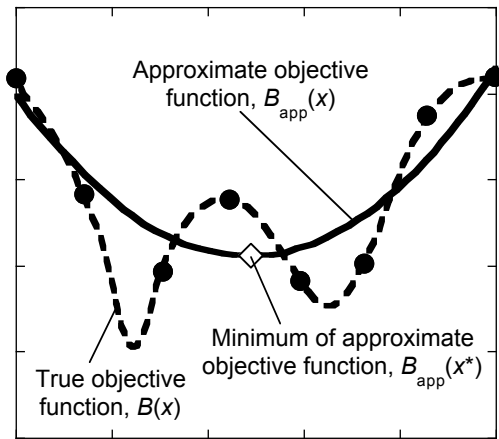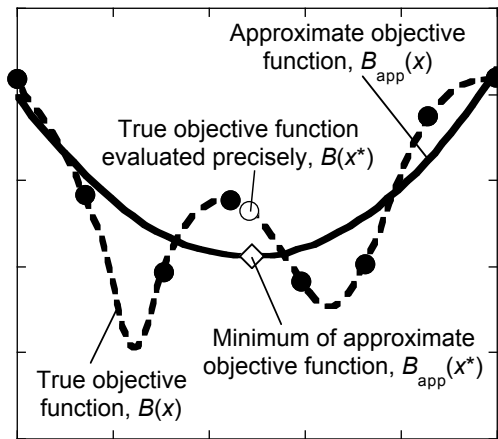
Figure 2.18: One iteration of a representative approximate optimization procedure (adapted from Ref. 87).

and $\mathbf{H}(\mathbf{X}^0)$ is the Hessian matrix. The perturbation vector, $\delta\mathbf{X}$, is

$$\delta\mathbf{X} = \mathbf{X} - \mathbf{X}^0 \qquad (2.62)$$

Typically a second-order Taylor series expansion is used. When the precise evaluations of the objective and constraint functions are not "finite difference close," the Taylor series approximations are interpreted as general quadratic polynomial interpolations that are valid for broad regions of the design space, rather than being rigorous, but only locally valid, Taylor series expansions. To compute the full expansion for a n-dimensional vector of variables, $1 + n + n(n+1)/2$ precise evaluations are needed. Therefore, it can be helpful to begin the optimization procedure with only a small number of precise evaluations, and then continue to add terms in the expansion as successive approximate optimization problems are solved.

Radial Basis Functions (RBFs) are functions whose values depend only on distances from a "center," and they provide a flexible framework for constructing approximations to highly non-linear, and even nonconvex, functions. In practice, function approximations are easily computed as weighted sums of RBFs, where each RBF is associated with a different "center." A general equation for a RBF-based approximation is given by Ref. 131, i.e.,

$$F(\mathbf{X}) \approx F_{\text{app}}(\mathbf{X}) = \sum_{i=1}^{n} \lambda_i \phi\left(||\mathbf{X} - \mathbf{X}_i||\right) + p(\mathbf{X}) \qquad (2.63)$$

where $||\cdot||$ is the Euclidean norm, λ is a vector of weighting coefficients, $p(\mathbf{X})$ is a low degree polynomial (typically linear or quadratic), ϕ is a real-valued function called the

basic function, and $\mathbf{X}_i$ for $i = 1, ..., n$ is the collection of points that have been evaluated precisely. The basic function in this formulation may take on any number of formats, as shown in Table 2.1

Table 2.1: Radial Basis Function (RBF) types

Type	Expression
Gaussian	$\phi(\lVert\mathbf{X}-\mathbf{X}_i\rVert) = e^{-(\varepsilon\lVert\mathbf{X}-\mathbf{X}_i\rVert)^2}$
Multiquadric	$\phi(\lVert\mathbf{X}-\mathbf{X}_i\rVert) = \sqrt{1+(\varepsilon\lVert\mathbf{X}-\mathbf{X}_i\rVert)^2}$
Inverse Quadratic	$\phi(\lVert\mathbf{X}-\mathbf{X}_i\rVert) = \frac{1}{1+(\varepsilon\lVert\mathbf{X}-\mathbf{X}_i\rVert)^2}$
Inverse Multiquadric	$\phi(\lVert\mathbf{X}-\mathbf{X}_i\rVert) = \frac{1}{\sqrt{1+(\varepsilon\lVert\mathbf{X}-\mathbf{X}_i\rVert)^2}}$

The Taylor series expansion and RBF-based approximation are two common types of approximating functions, but functions of any form may be used in an approximate optimization. The overall success (or failure) of the method is affected by this choice, and it is, therefore, imperative to select a function that can reasonably approximate the "true" objective and constraint functions.

This latter point may be made more clear with an example. Figures 2.19 and 2.20 show differing approximations to the Branin test function. The Branin test function is a common function for testing global optimization algorithms, expressed mathematically as

$$f(x_1, x_2) = \left(x_2 - \frac{5.1x_1^2}{4\pi^2} + \frac{5x_1}{\pi} - 6\right)^2 + 10\left(1 - \frac{1}{8\pi}\right)\cos(x_1) + 10 \qquad (2.64)$$

The test function has three global optima

$$(x_1^*, x_2^*) = (-\pi, 12.275), (\pi, 2.275), (9.42478, 2.475)$$

90

such that $f(x_1^*, x_2^*) = 0.397887$.

The Branin function is shown in Fig. 2.19(a), and it was sampled at 25 points. Using those 25 points as precise function evaluations, the test function was approximated using three different methods. The first method, shown in Fig. 2.19(b), involved using the "best" of the sampled points (i.e., the point corresponding to the lowest function value) and its five nearest neighbors to construct a second-order Taylor series expansion about the "best" point. The "best" of the sampled points in Fig. 2.19(a) is the point closest to $(x_1^*, x_2^*) = (9.42478, 2.475)$. The fit in Fig. 2.19(b) is not an effective approximation of the test function on a global scale. The second method, shown in Fig. 2.19(c), consisted of a least-squares fit to all 25 sampled points using a quadratic polynomial. Again, this method does not appear to give an adequate approximation of the test function on a global scale. The third method, shown in Fig. 2.19(d), involved a multiquadric RBF fit to all 25 sampled points. Although there are differences between the approximation and the "true" test function, it is clear that this method better models the complicated test function on a global scale; the approximation captures three local minimum regions in relatively close agreement to the actual minima of the test function.

The Branin function is shown again in Fig. 2.20(a), this time with 100 sampled points. Using those 100 points as precise function evaluations, the test function was again approximated using three different methods. This time, the "best" of the sampled points was in the vicinity of $(x_1^*, x_2^*) = (\pi, 2.275)$. Notice that the second-order Taylor series expansion about this point, while not an effective approximation of the test function on global scales, well approximates the test function on a local scale; see Fig. 2.20(b).
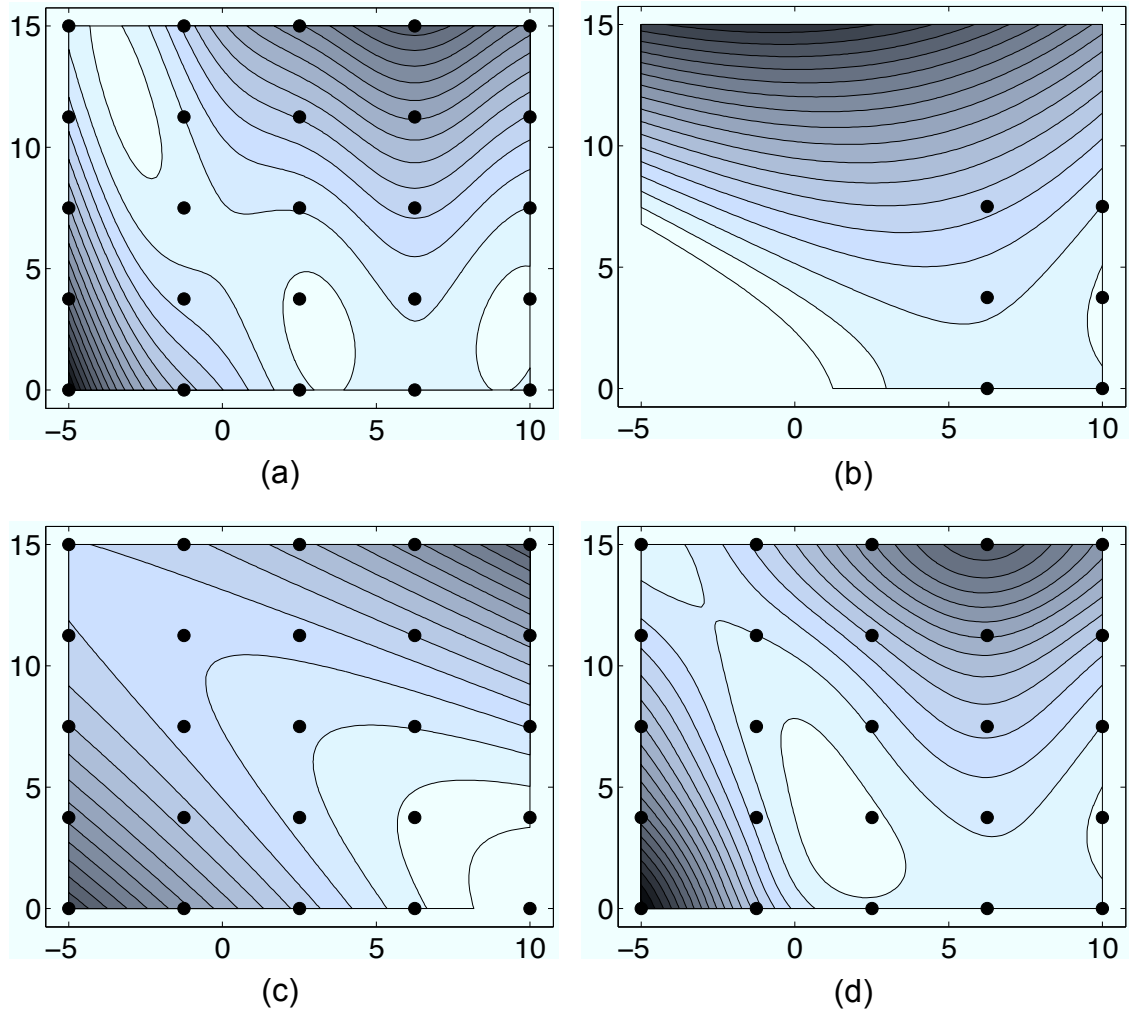
Figure 2.19: Illustration of differing approximations to the Branin test function using 25 sampled points: (a) the Branin test function, (b) a second order Taylor series fit using the "best" sampled point and its five closest neighbors, (c) a least squares fit to all 25 sampled points using a quadratic polynomial, and (d) a multiquadric RBF fit to all 25 sampled points.

92

This observation emphasizes an important point: as an approximate optimization procedure continues towards an optimum, the precise evaluations will tend to converge and the second-order Taylor series expansion will become much a more accurate approximation at local scales. Notice that the least squares fit to all 100 points using a quadratic polynomial still appears to do a poor job of approximating the test function on a global scale; see Fig. 2.20(c). If the "true" function contains multiple minima, a global least-squares fit using a quadratic is simply incapable of approximating it. The multiquadric RBF fit to all 100 sampled points, see Fig. 2.20(d), approximates the test function very well on both local and global scales. This example clearly illustrates the ability of an RBF-based approximation to represent complicated functions.

Another potential variation in the basic methodology is the optimization algorithm that is used to find the minimum of the approximate objective function. For simple approximating functions, such as the second-order Taylor series expansion or a general least-squares polynomial fit, the choice of optimization algorithm is trivial. Indeed, in certain instances the optimum of the approximation may even be solved analytically with negligible computational cost. For more complicated approximating functions, such as the multiquadric RBF, the selection of an appropriate optimization algorithm requires further consideration. For example, the optimum determined by a gradient-based optimization algorithm will likely be sensitive to the initial guess when operating on an approximation that contains multiple minima (e.g., Figs. 2.19(d) and 2.20(d)). Because each function evaluation of the approximate objective function is computationally inexpensive, however, global optimization algorithms (such as Genetic Algorithms, GA, discussed in
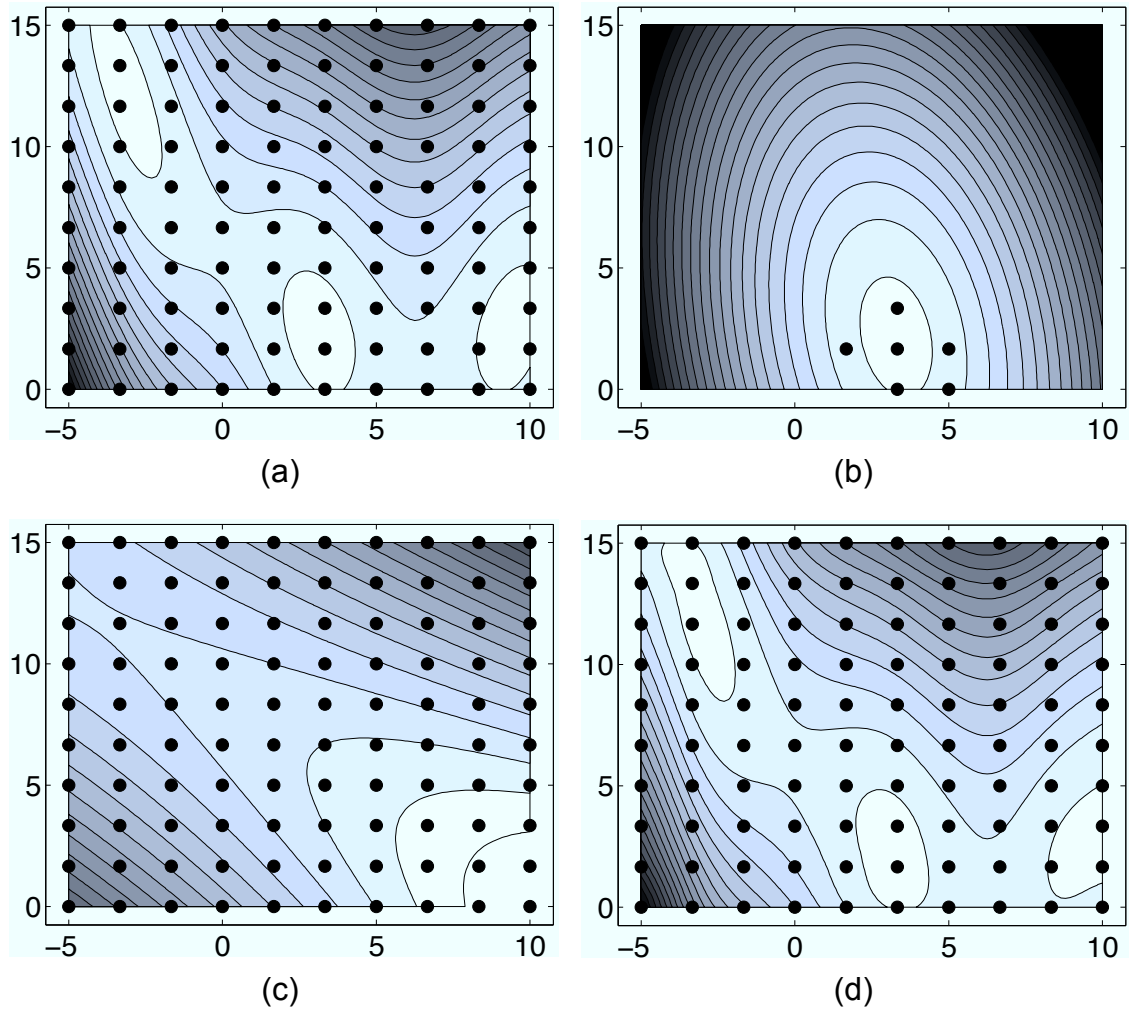
Figure 2.20: Illustration of differing approximations to the Branin test function using 100 sampled points: (a) the Branin test function, (b) a second order Taylor series fit using the "best" sampled point and its five closest neighbors, (c) a least squares fit to all 100 sampled points using a quadratic polynomial, and (d) a multiquadric RBF fit to all 100 sampled points.

Section 2.2.2) may be reasonably utilized for more complicated approximating functions.

Approximate optimizations provide a number of benefits, but they are also subject to some important limitations. In the first instance, approximate optimization techniques can be a powerful design tool if individual function evaluations are very expensive, because they can obtain optimum or near-optimum designs using a relatively small number of function evaluations. Additionally, multiple optimizations may be performed using a common inventory of precise function evaluations. Vanderplaats (Ref. 89) states that, "experience suggests that the method is competitive only for problems of a few variables, say less than 10, where the computational cost of analysis is very high or where the same data can be used in several separate optimizations."

Another important limitation of the methodology is that it is not ideally suited to handle multiple local minima, if they exist. Even if the approximating function is capable of capturing multiple optima (as shown in Figs. 2.19 and 2.20), multiple minima will only be discovered when those regions are sampled sufficiently by precise function evaluations. As such, an approximate objective function may not reflect the global minimum of the "true" objective function if the methodology has resulted in a sequence of precise function evaluations that are converging to a local minimum.

To alleviate these problems, "additional designs" may be generated and evaluated precisely over the course of an optimization procedure that are determined based on criteria other than their approximate objective function value. For example, such additional designs may be selected to sample regions of the design space that have not been sampled previously during the optimization procedure. Although these additional designs may not
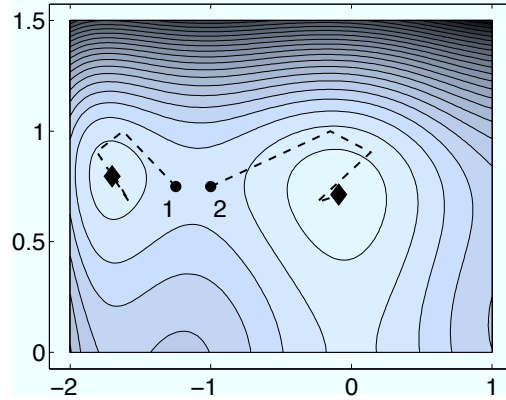
Figure 2.21: Two potential optimization paths using a gradient-based algorithm. Optimization 1 results in the local minimum, whereas optimization 2 results in the global minimum. The only difference in these optimizations is the initial guess.

actually be "better" than the designs that have been precisely evaluated previously, their inclusion improves the global convergence characteristics of the optimization method as a whole.

2.2.2   Genetic Algorithms

Genetic Algorithms (GA) are a type of heuristic optimization algorithms that attempt to mimic evolutionary processes to arrive at the the optimum solution. They have been shown to be particularly effective at solving optimization problems that contain multiple optima, whereas gradient-based algorithms may be prone to finding local minima, depending on the initial guess. This point is illustrated in Fig. 2.21, which shows two potential optimization paths using a gradient-based algorithm. Both optimizations were identical, with the exception of a small difference in the starting guess. Optimization 1 results in the local minimum, whereas optimization 2 results in the global optimum. GA are also capable of accommodating problems in which the variables take on a mix of

96

continuous and discrete values.

The basic structures upon which GA operate are known as chromosomes, which are simply a string of 0's and 1's, as shown in Fig. 2.22. In practice, chromosomes are constructed by transforming each variable in the optimization into a sequence of binary digits. Notice that there is no requirement for these variables to be numerical. For example, a given variable may allow for one of four discrete options. In this instance, two binary digits are required to capture all of the potential variable values, i.e., 00 being option one, 01 being option two, 10 being option three, and 11 being option four. If a given variable is numerical, it can be transformed to a string of binary digits by using the standard binary representation common in computer science. An alternate method for transforming a numerical variable to a string of binary digits is to map the feasible range of that variable, say $a < x_1 < b$, to a binary string of length, ℓ, such that the precision achieved is

$$\frac{b-a}{2^\ell - 1} \tag{2.65}$$

If a known precision is required, this expression may be used to find a suitable length for ℓ. Notice that ℓ may differ between the individual variables, depending on the necessary precision and the ranges of permissible values.

The first step in a GA is to generate an initial population. The two major considerations in generating an initial population are the size of the population and the method

$$\underbrace{10101011}_{x_1}, \underbrace{01101010}_{x_2}, \underbrace{10101000}_{x_3}$$
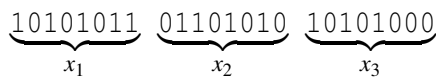
Figure 2.22: A chromosome representing three variables, x_1–x_3.

97

by which the individuals are chosen. The question of population size has been addressed by many researchers, but the underlying motives have always been to strike the right balance between efficiency and effectiveness. Too large a population will add unnecessary computational expense to the method, while too small a population will compromise performance. It is generally accepted that the size of the population should scale with the chromosome length, but more simple methods have also been proposed (e.g., scaling the population size based on the number of variables). The individuals of the initial population are almost always chosen randomly, however, a population chosen in this way will not necessarily cover the search space. Other methods for generating the initial population that more uniformly covers the search space have been proposed. Another potential variation on the method for generating an initial population is to seed the population with known "good" designs, although this method may induce premature convergence to a poor solution (Ref. 132).

Once an initial population has been generated, the next step in GA is known as selection. This step mimics the "survival of the fittest" philosophy of natural selection, and it step begins with the evaluation of the "fitness" (i.e., the objective function value) of each of the individuals in the population. Individuals with higher fitness levels (i.e., more desirable objective function values) will be more likely to serve as parents for the next generation. The most common way to select the individuals who will serve as parents is known as "Roulette Wheel Selection," which uses a probability distribution in which the selection probability of a given individual is directly proportional to its fitness. The selection process typically continues until there are as many parents as there are members

in the population. Some individuals (i.e., the most "fit") may be selected more than once, and others (i.e., the least "fit") may not be selected at all.

Once the parents of a generation have been selected, the next step is to mate those parents, two at a time, to form a new generation. Each pair of parents will typically create two children, and thus each generation retains the same population size. Mating consists of two steps: crossover and mutation. In practice, some forms of GA use "crossover-and-mutation" while others utilize "crossover-or-mutation." The crossover method of mating involves the random selection of a "crossover point" in the parent chromosomes. Each of the children consists of a portion of each of the parent chromosomes, where the crossover point determines which portion of each parent chromosome goes to which child.

This process is shown in Fig. 2.23 for the case where the two parent chromosome consist of all 0s and all 1s. Again, a number of variations exist in the crossover process, to include multi-point crossovers. The other form of mating is called mutation, and it is meant to mimic the random genetic mutations that occur in nature. Mutation involves the random selection of an individual bit in a chromosome, and the bit is potentially changed based on the outcome of a random number generator. Note that the mutation process is typically governed by a user-selected "mutation rate." Small changes in chromosomes from mutation may translate into large changes to the variables, depending on which bits are changed. In this sense, the effect of the mutations is to ensure that all regions of the search space have been examined and all potential minima have been considered.

Beyond the many variations that can be made to the crossover and mutation methods, another variation in the mating process involves the passing of the best (i.e., most

```
Parent A   0 0 0 0 | 0 0 0 0 0 0
Parent B   1 1 1 1 | 1 1 1 1 1 1

        ↓ crossover point is 4 ↓

Child a    0 0 0 0 | 1 1 1 1 1 1
Child b    1 1 1 1 | 0 0 0 0 0 0
```

Figure 2.23: The one-point crossover process.

"fit") individuals from one generation directly to the next generation, creating what are known as "elite children." The processes of selection and mating are continued for multiple generations, continuing until a termination condition is met.

The basic algorithm for GA is shown in Fig. 2.24 and a graphical representation of the progression of a GA on an example function is shown in Fig. 2.25. Notice that the global minimum of the test function is located at $(x_1^*, x_2^*) = (-0.0898, 0.7126)$ and that there is also a local minimum. Figure 2.25(a) shows the initial population, and Fig. 2.25(b)–(e) show the progression of a few selected generations. Notice that the populations tend to converge towards the optimum as the generations progress, ultimately converging after 50 generations for this example; see Fig. 2.25(f). Notice that each generation consisted of 20 individuals, therefore, the method required 1×10^3 function evaluations to converge. This observation illustrates an important limitation: although GA have demonstrated ability to handle problems with multiple optima, they typically require orders of magnitude more function evaluations than other methods. While this is not necessarily problematic when function evaluations are inexpensive, GA may prove to be cost prohibitive when function evaluations are costly.

```
Choose an initial population of chromosomes;
while termination condition not satisfied do
  repeat
    if crossover condition satisfied then
      {select parent chromosomes;
      choose crossover parameters;
      perform crossover};
    if mutation condition satisfied then
      {select chromosome(s) for mutation;
      choose mutation points;
      perform mutation};
    evaluate fitness of offspring;
  until sufficient offspring created
  select new population;
end while
```

Figure 2.24: A genetic algorithm template (from Ref. 132).

2.2.3   Branch & Bound Algorithm

In optimization, problems that take on mixed continuous and discrete/integer variables tend to be more complicated than problems with only continuous variables. Although Genetic Algorithms (GA) are capable of solving such problems, they are accompanied by significant computational cost and are not viable when function evaluations are costly. An alternative method for solving these problems is a transformation method known as the Branch & Bound algorithm (B&B). Transformation methods are commonly applied in an attempt to transform complicated optimization problems into more manageable ones; however, they are only effective when the original problem is known to exhibit some specific properties.

In particular, B&B divides the original optimization problem into multiple "subproblems," this is called "branching." If it can be determined based on some a priori knowledge of the original problem that solutions to one of the sub-problems are always
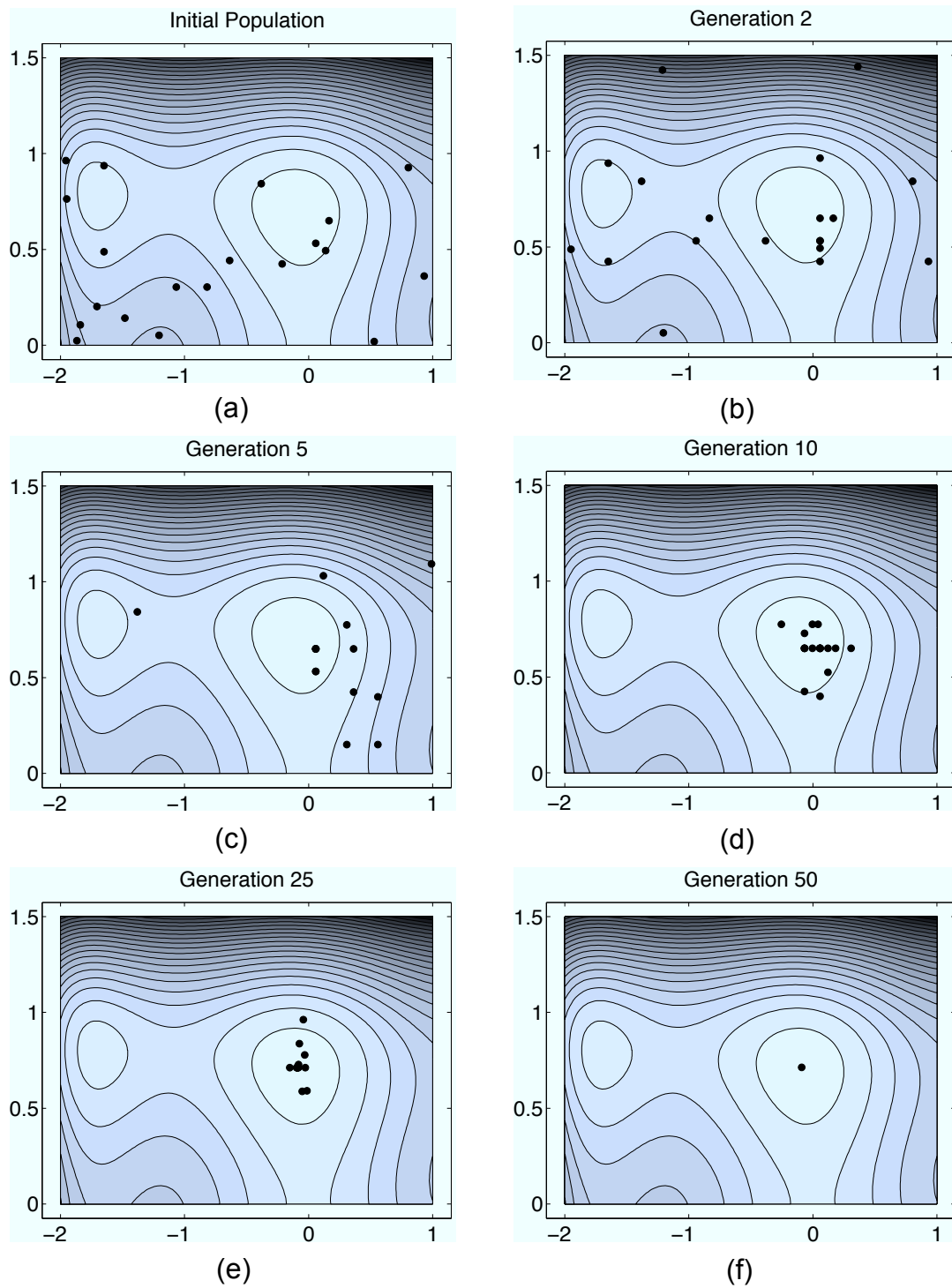
Figure 2.25: Progression of a genetic algorithm for finding the global optimum of an example problem.

better than solutions to one of the other sub-problems, B&B dictates that the branch cor-responding to the worse of the two can be "fathomed" or "pruned," this is the "bound-ing" step. If sub-problems may be fathomed, significant computational savings can be achieved.

The fundamental methodology of B&B may be illustrated with a brief example for a mixed integer linear programming (MILP) problem (from Ref. 96), i.e.,

$$\text{minimize:} \quad f = (2x_1 + x_2)$$

$$\text{subject to:} \quad x_1 \geq 2.5$$

$$x_2 \geq 1.25$$

$$x_1 + 2x_2 \geq 7.5$$

$$x_1 \geq 0 \text{ integer}, \quad i = 1, 2$$

To begin, the original linear programming problem is solved treating x_1 and x_2 as contin-uous variables. The result of this optimization (called LP-1) is

$$x_1^1 = 2.5 \qquad x_2^1 = 2.5 \qquad f_1 = 7.5$$

This step is represented by the first node in the enumeration tree shown in Fig. 2.26 and the results are shown graphically in Fig. 2.27. The optimum of problem LP-1 is a lower bound on the objective function that may be achieved overall, i.e., $f_1 = f_L$, because the overall problem includes only a portion of the feasible space of LP-1.

The next step is to branch LP-1 into sub-problems. Only one integer variable may
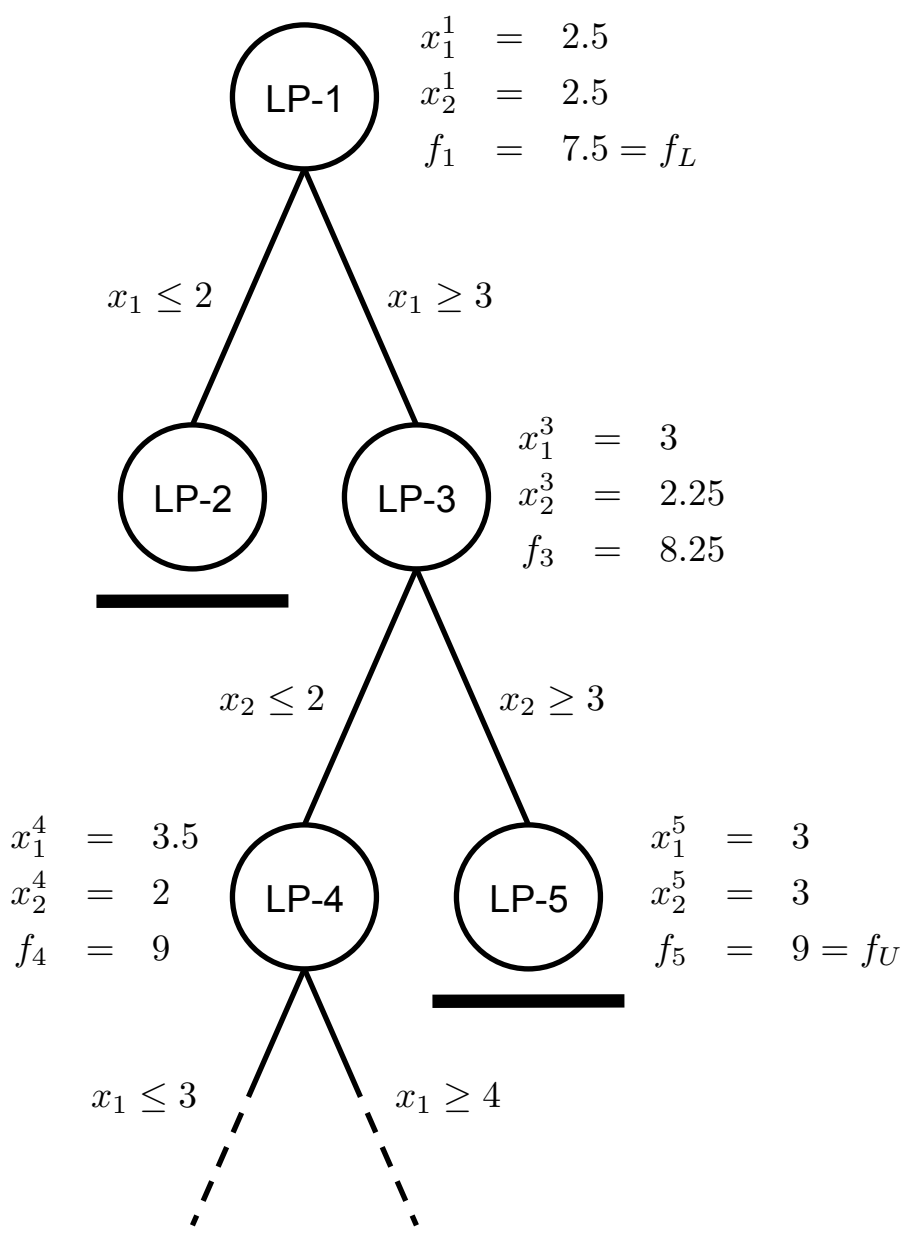
Figure 2.26: Enumeration tree (adapted from Ref. 96).
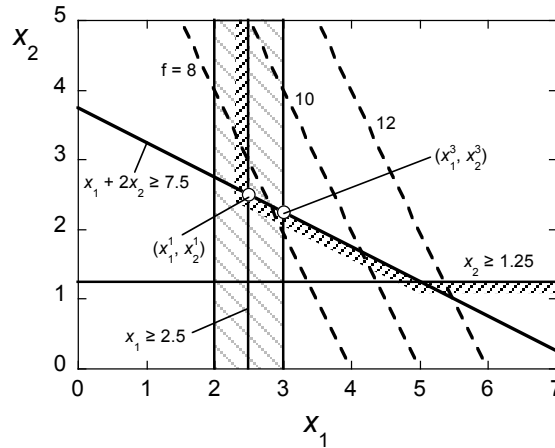
Figure 2.27: Graphical solution of LP-3 (from Ref. 96).

be branched in a given step. Because there is more than one integer variable in the present

problem, one of them must be selected. Variable x_1 is chosen, and LP-1 is divided into

sub-problems LP-2, in which $x_1 \leq 2$, and LP-3, in which $x_1 \geq 3$; see Fig. 2.26. The first

sub-problem, LP-2, results in no feasible solutions (because of the existing constraint that

$x_1 \geq 2.5$), so that branch may be fathomed; see Fig. 2.26. The second sub-problem, LP-3,

results in

$$x_1^3 = 3 \qquad x_2^3 = 2.25 \qquad f_3 = 8.25$$

as shown graphically in Fig. 2.27.

At this point, LP-3 may be branched into sub-problems LP-4 (subject to $x_2 \leq 2$) and

LP-5 (subject to $x_2 \geq 3$); see Fig. 2.26. Sub-problem LP-4 results in

$$x_1^4 = 3.5 \qquad x_2^4 = 2 \qquad f_4 = 9$$
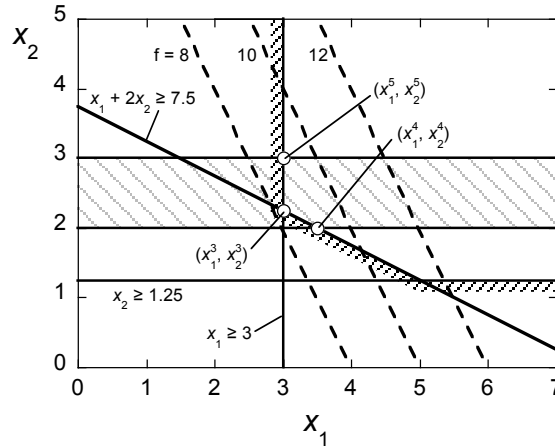
Figure 2.28: Graphical solutions of LP-4 and LP-5 (from Ref. 96).

and sub-problem LP-5 results in

$$x_1^5 = 3 \qquad x_2^5 = 3 \qquad f_5 = 9$$

Both of these results are shown graphically in Fig. 2.28. Sub-problem LP-4 may again be branched on its non-integer variable, x_1. The solution to LP-5, however, satisfies the integer-only constraints of the original problem and it is therefore fathomed; see Fig. 2.26. Additionally, because LP-5 results in a solution that satisfies the integer-only constraints, it may be considered to be the upper bound on the original problem. Furthermore, notice that $f_4 = f_5$. Because the solutions to any sub-problem of LP-4 will be no better than the solution to LP-4, i.e., $f_4 \leq f_6, f_7, \ldots$, it is clear that continuing the procedure will not result in any feasible solutions that are improvements upon f_5. As such, the procedure is terminated and the solution to LP-5 is determined to be the solution to the overall problem.

The performance of B&B relies heavily on the selection of which variable should be used for branching. If the selected variable leads to an upper bound that is close to the

objective function value of the solution to LP-1, i.e., f_1, early in the procedure, then significant computation savings may be obtained because of the elimination of branches that would not be capable of generating solutions lower than the upper bound (Ref. 96). As such, B&B has been shown to particularly effective in MILP problems although its utility in mixed integer nonlinear programming (MINLP) problems is less straightforward.

Notice from the example that, at each step of B&B, the solution to any sub-problem may not be better than the solution to the preceding problem (i.e., that $f_{k+1} \geq f_k$ where $k+1$ is a sub-problem of k). This property is guaranteed in the example because each sub-problem is simply a re-formulation of the preceding problem with the imposition of an additional constraint. Furthermore, this property is only guaranteed in the example because each problem is solved exactly before further dividing the problem into sub-problems. This aspect of the implementation of B&B makes its extension to approximate problem formulations particularly challenging.

2.3 Defining an Objective Function

In the present work, brownout mitigation is formulated as a numerical optimization problem, within which the effects of varied operational and design strategies on brownout severity are evaluated through simulation. To evaluate these effects, however, a quantitative measure of brownout severity is required. A simple objective function is adopted in the present work, in which the distribution of particle density is taken to be a surrogate for the visual degradation experienced by the pilot in brownout conditions. This objective function is described in the present section, and it can be seen as the first step toward a
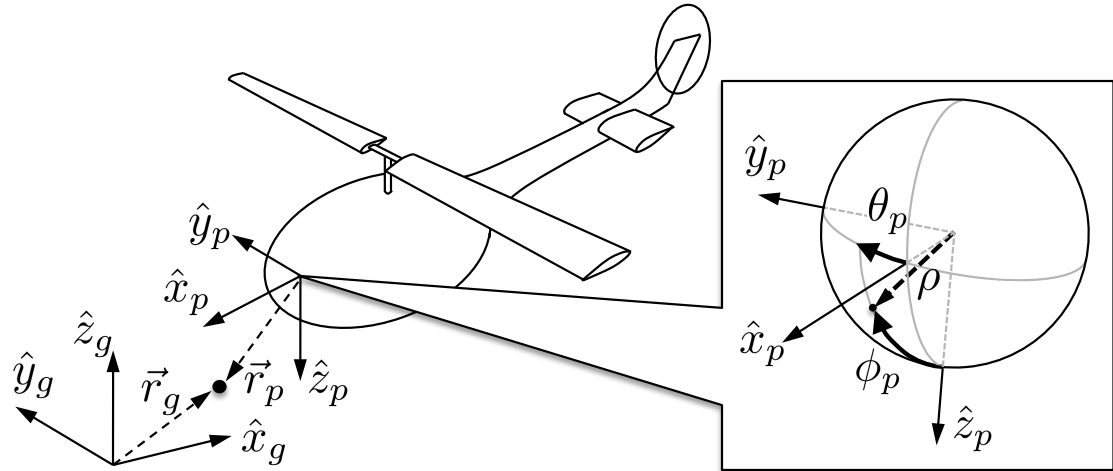
Figure 2.29: Schematic of the pertinent coordinate systems for projecting the cloud in the pilot's FOV.

metric that would more directly reflect a degradation in HQs.

2.3.1 Projecting the Brownout Cloud in the Pilot's FOV

From a practical standpoint, the objective function, $B(\mathbf{X})$, represents the cloud density in the best region of the FOV that the pilot could potentially use to perceive visual cues. The calculation of the objective function begins by projecting the position of each particle of the cloud, at each instant in time, onto a sphere, centered at the pilot's head. A schematic diagram showing the coordinate systems of interest is shown in Fig. 2.29, and the particles of the simulated brownout cloud are projected in the pilot's FOV via a series of coordinate transformations.

Each particle of the cloud is first transformed from the inertial Cartesian coordinate

system to a pilot-fixed Cartesian coordinate system using

$$
\left\{ \begin{array}{c} x_2 \\ y_2 \\ z_2 \end{array} \right\} = [T] \left\{ \begin{array}{c} x_1 \\ y_1 \\ z_1 \end{array} \right\} + \left\{ \begin{array}{c} \Delta x \\ \Delta y \\ \Delta z \end{array} \right\}
\tag{2.66}
$$

where

$$
T_{11} = \cos\theta \cos\psi
\tag{2.67}
$$

$$
T_{12} = \cos\theta \sin\psi
\tag{2.68}
$$

$$
T_{13} = -\sin\theta
\tag{2.69}
$$

$$
T_{21} = \sin\phi \sin\theta \cos\psi - \cos\phi \sin\psi
\tag{2.70}
$$

$$
T_{22} = \sin\phi \sin\theta \sin\psi + \cos\phi \cos\psi
\tag{2.71}
$$

$$
T_{23} = \sin\phi \cos\theta
\tag{2.72}
$$

$$
T_{31} = \cos\phi \sin\theta \cos\psi + \sin\phi \sin\psi
\tag{2.73}
$$

$$
T_{32} = \cos\phi \sin\theta \sin\psi - \sin\phi \cos\psi
\tag{2.74}
$$

$$
T_{33} = \cos\phi \cos\theta
\tag{2.75}
$$

and $[x_1 \, y_1 \, z_1]^T$ is the position vector of a generic particle in the inertial coordinate system, $[x_2 \, y_2 \, z_2]^T$ is the position vector of the same particle in the pilot-centered coordinate system, $[\Delta x \, \Delta y \, \Delta z]^T$ is the position vector of the origin of the inertial coordinate system, with respect to the pilot-centered coordinate system, and θ, ψ, and ϕ are the aircraft pitch, yaw, and roll angles, respectively. Each particle is next transformed from the pilot-centered
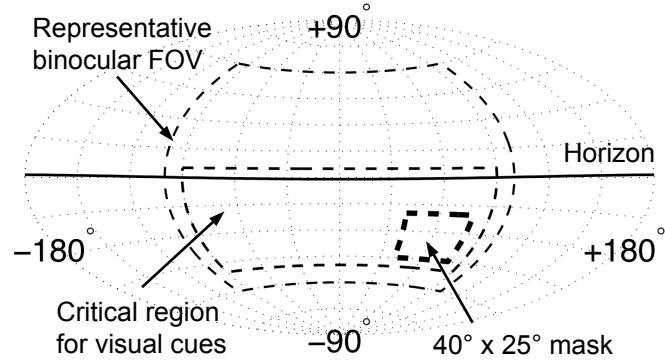
Figure 2.30: Representation of the pertinent regions of a pilot's field of view for calculation of the objective function.

Cartesian coordinate system to a spherical coordinate system with a co-located origin using

$$\rho = \sqrt{x_2^2 + y_2^2 + z_2^2} \tag{2.76}$$

$$\theta_P = \tan^{-1}\left(\frac{y_2}{x_2}\right) \tag{2.77}$$

$$\phi_P = \cos^{-1}\left(\frac{z_2}{\rho}\right) \tag{2.78}$$

where ρ is the distance of the particle from the pilot, θ_P is the azimuthal location of the particle in the pilot's FOV, and ϕ_P is the elevation of the particle in the pilot's FOV. These coordinate transformations are performed at each time step in the cloud simulation, and the procedure results in a distribution of particle density as seen by the pilot.

2.3.2 Objective Function Formulation

The pilot does not require clear visual paths in all directions during a landing maneuver. Rather, the pilot can safely land a helicopter with a relatively small FOV, provided

it is oriented towards a region that provides sufficient cueing. The regions of a pilot's FOV that are most critical during a landing maneuver are depicted in Fig. 2.30. A 200° by 120° region to the front of the aircraft is typical of a pilot's binocular FOV (Ref. 133). Within that FOV, a 180° by 55° subregion was identified as being representative of the portion of the pilot's FOV where essential visual cues are found, specifically the regions in the pilot's near-field (labeled the "critical region for visual cues" in Fig. 2.30). Research has shown that, in the presence of sufficient microtexture cues, i.e., fine-grained detail in the visual scene, a pilot can maintain satisfactory control over the aircraft with a FOV as small as approximately 40° laterally by 25° vertically (Ref. 12); such a region is also depicted in Fig. 2.30. Assuming a pilot will scan intuitively to find the regions of his or her FOV that are the least obscured during brownout, the 40° by 25° sector with the lowest particle count may be considered to be the "best" region in which the pilot should focus attention.

At a given instant in time, the number of particles, n_p, in this "best" 40° by 25° sector of the pilot's FOV is given by

$$b(\mathbf{X},t) = \min \left[\sum_{\phi_P=i}^{i+25°} \sum_{\theta_P=j}^{j+40°} n_P\left(\phi_P, \theta_P, t\right) \right] \qquad (2.79)$$

$$\text{for} \quad \begin{array}{c} -50° \leq i \leq -20° \\ -90° \leq j \leq 50° \end{array}$$

where $n_P(\phi_P, \theta_P, t)$ is the number of dust particles in the one-degree solid angle centered at ϕ_P and θ_P at time t, and the values selected for i and j restrict the scan area to the "critical region for visual cues" identified in Fig. 2.30. The brownout objective function,

$B(\mathbf{X})$, is then defined as

$$B(\mathbf{X}) = \int_{t_1}^{t_2} b(\mathbf{X},t)dt \qquad (2.80)$$

where t_1 is the starting time and t_2 is the ending time of the maneuver.

It is emphasized that this objective function formulation is highly idealized. For example, it does not consider the constraints on FOV that are imposed by cockpit obstructions or any additional equipment (such as night vision goggles). Figure 2.31 depicts the constrained FOV that results from the instrument panel and structural design of a UH-1H helicopter, and it is clear that these considerations are not insignificant. Additionally, some fundamental human factors are not considered in the present analysis. For example, the movements of the "best" $40°$ by $25°$ sector between time steps in the brownout simulation may be faster than typical eye saccades. Nevertheless, the present objective function is the first formal brownout objective function to be used for the purposes of brownout mitigation, and, as such, it represents an important building block for future analyses.
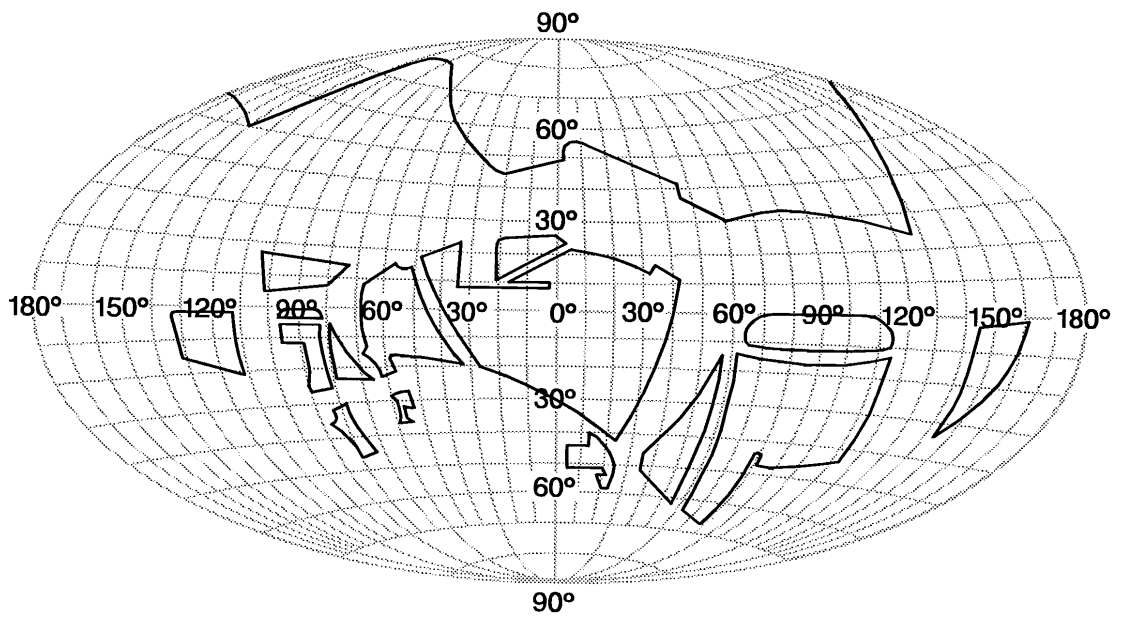
Figure 2.31: Field of view from a UH-1H Iroquois helicopter (from Ref. 134).

Chapter 3

Brownout Mitigation Through Flight Path Management

A variety of methods for brownout mitigation were cited in the introductory chapter, including operational mitigation. Operational mitigation is a method in which the pilot adopts specific piloting strategies to minimize the effect of brownout during a maneuver. Although techniques for operational mitigation are generally accepted among pilots, they are the results of anecdotal experiences rather than systematic analyses. Furthermore, operational mitigation techniques are not documented in the technical literature, and the fundamental mechanisms for mitigation behind these strategies are not well understood.

The goal of the present chapter is to propose and demonstrate, through simulation, a systematic procedure to optimize a visual approach-to-landing profile for brownout mitigation. The specific objectives are:

1. To present a systematic brownout mitigation procedure based on flight path optimization that incorporates operational constraints to ensure the safety of flight over the duration of the maneuver.

2. To present the results of a brownout mitigation study that highlight the key physical mechanisms involved in the mitigation process.

3. To compare the results with prior experimental results and examine potential operational interpretations of the outcomes.

3.1 Optimization Methodology

In the present work, brownout mitigation is formulated mathematically as a numerical optimization problem and cast into nonlinear mathematical programming form. Therefore, the procedure consists of finding the value of a vector of design variables, $\mathbf{X}$, such that a scalar objective function, $B(\mathbf{X})$, is minimized, i.e.,

$$B(\mathbf{X}) \rightarrow \min \tag{3.1}$$

subject to:

behavior constraints $\quad g_j(\mathbf{X}) \leq 0 \quad j = 1,\ldots,m \tag{3.2}$

side constraints $\quad \mathbf{X}_{\min} \leq \mathbf{X} \leq \mathbf{X}_{\max} \tag{3.3}$

3.1.1 Design Vector, $\mathbf{X}$

The design vector, $\mathbf{X}$, consists of three variables that describe a nominal approach profile: (i) the approach angle, α_{app}, (ii) the initial (asymptotic) velocity, v_0, and (iii) the range at which peak deceleration occurs, r_{pd} (i.e., how late into the maneuver the pilot waits to decelerate), such that

$$\mathbf{X} = \left\{ \begin{array}{c} x_1 \\ x_2 \\ x_3 \end{array} \right\} = \left\{ \begin{array}{c} \alpha_{\mathrm{app}} \\ v_0 \\ r_{\mathrm{pd}} \end{array} \right\} \tag{3.4}$$

Two of these parameters, v_0 and r_{pd}, can be used to generate longitudinal deceleration and velocity profiles for a general approach maneuver after the formulation in Ref. 135, i.e.,

$$\ddot{r} = \frac{\left(v_0/2r_{pd}\right)^2 r}{\left(1 + r/2r_{pd}\right)^3} \tag{3.5}$$

$$\dot{r} = \frac{\left(v_0/2r_{pd}\right) r}{\left(1 + r/2r_{pd}\right)} \tag{3.6}$$

where r is the longitudinal range from landing point. Representative longitudinal deceleration and velocity profiles are depicted in Fig. 3.1(a) and (b), respectively. The vertical velocity, v_d, can be approximated for the assumption of a constant approach angle, α_{app}, i.e.,

$$v_d = \dot{r} \tan\left(\alpha_{app}\right). \tag{3.7}$$

For the present study, the baseline approach profile was calculated as a best fit to the flight test data from Ref. 136 for an approach with nominal starting conditions of 80 kts at 500 ft above the ground, as shown in Fig. 3.1(a). The parameters of the best fit were calculated to be $\mathbf{X}_1 = \left[\alpha_{app}\ v_0\ r_{pd}\right]^T = \left[6°\ 90\ \text{kts}\ 300\ \text{ft}\right]^T$.

It must be emphasized that the approach formulation utilized in the present study is just one of many potential formulations that could be used (see Ref. 49 for others). Alternate parameterizations with more design variables will require more objective function evaluations over the course of the optimization procedure.

Each design variable is subjected to side constraints, Eq. (3.3). For the present study
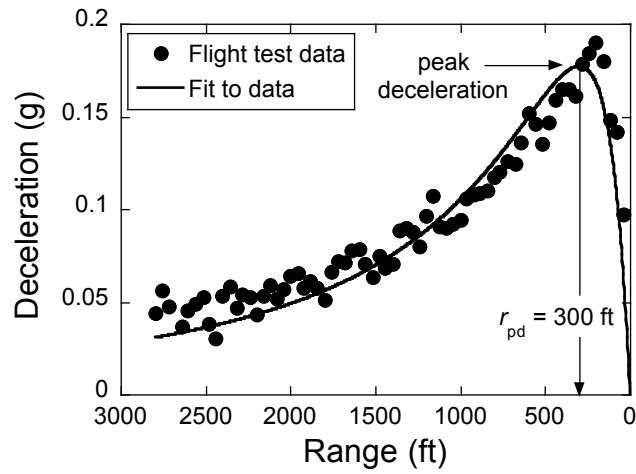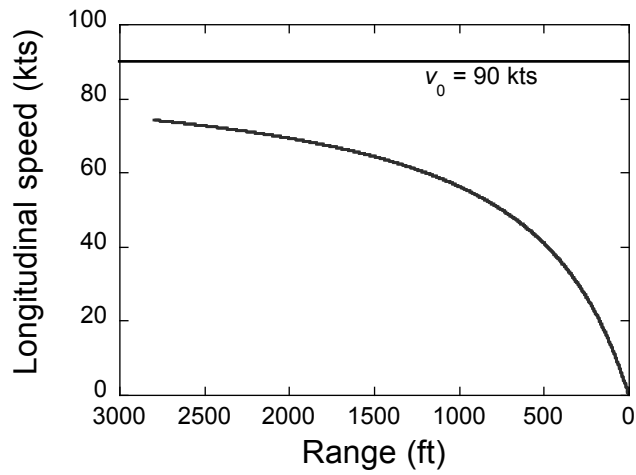
Figure 3.1: Longitudinal (a) deceleration and (b) velocity profiles for the baseline approach (the data fit formulation is adapted from Ref. 135, the flight test data are from Ref. 136).

they were

$$1° \leq \quad \alpha_{\text{app}} \quad \leq 12° \tag{3.8}$$

$$60 \text{ kts} \leq \quad v_0 \quad \leq 130 \text{ kts} \tag{3.9}$$

$$100 \text{ ft} \leq \quad r_{\text{pd}} \quad \leq 500 \text{ ft} \tag{3.10}$$

3.1.2 Objective Function, $B(\mathbf{X})$

The brownout objective function, $B(\mathbf{X})$, has been described in detail in Section 2.3 and is mathematically defined as

$$B(\mathbf{X}) = \int_{t_1}^{t_2} b(\mathbf{X},t)dt \tag{2.80}$$

where t_1 is the starting time and t_2 is the ending time of the maneuver, and

$$b(\mathbf{X},t) = \min \left[\sum_{\phi_P=i}^{i+25°} \sum_{\theta_P=j}^{j+40°} n_P(\phi_P,\theta_P,t) \right] \tag{2.79}$$

$$\text{for} \quad \begin{array}{c} -50° \leq i \leq -20° \\ -90° \leq j \leq 50° \end{array}$$

where $n_P(\phi_P,\theta_P,t)$ is the number of dust particles in the one-degree solid angle centered at ϕ_P and θ_P at time t, and the values selected for i and j restrict the scan area to the "critical region for visual cues" identified in Fig. 2.30

3.1.3 Behavior Constraints, $g_j(\mathbf{X})$

Behavior constraints were applied to the optimization procedure to ensure that the resulting approach profiles were realistic and safe. The first behavior constraint was imposed to limit the maximum approach angle over the duration of the maneuver. A nominal pitch attitude profile is given in Ref. 136 as

$$\theta = \frac{57.3}{g}(\ddot{r} - X_u \dot{r}) \tag{3.11}$$

where g is gravitational acceleration and X_u is the stability derivative $\partial X/\partial u$. Note that X_u will vary based on the specific aircraft, and a value of $X_u = 0.019$ is assumed for the present study after the medium transport helicopter used in the flight testing of Ref. 136. In the present study, the maximum pitch angle over the duration of the maneuver was constrained to be no more than $30°$, i.e.,

$$g_1(\mathbf{X}) = \theta_{\max}(\mathbf{X}) - 30° \leq 0 \tag{3.12}$$

Notice that a $30°$ pitch attitude would correspond to an aggressive deceleration, much more aggressive than would be typical of a standard visual approach. However, given the anecdotal reports that a common operational tactic for brownout landings is to "outrun" the cloud and rapidly decelerate just prior to landing, this constraint was purposefully constructed to allow the optimizer to select very aggressive approaches.

A second behavior constraint was imposed to prevent flight in conditions that are conducive to the onset of vortex ring state (VRS). Figure 3.2 shows boundaries within
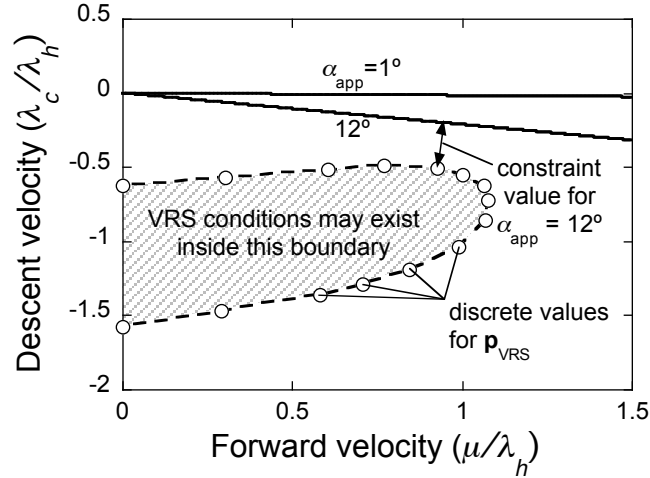
Figure 3.2: Graphical depiction of the behavior constraint for vortex ring state avoidance.

which VRS may be expected to occur, as identified in Ref. 137. Although such boundaries

are only approximate, their explicit definition is essential for the mathematical description

of a constraint function. Approach profiles for $\alpha_{app} = 1°$ and $12°$ are plotted on the same

axes. Notice that the approach profiles are shown to be straight lines when plotted on these

axes. This attribute is an outcome of the specific mathematical formulation chosen for the

approach profiles in the present study, i.e., Eqs. (3.5)–(3.7), and may not be the case for

other formulations. The constraint value is simply the distance between the closest points

on the approach profile and the VRS boundary, as illustrated for the $\alpha_{app} = 12°$ case in

Fig. 3.2.

While it is possible to express this constraint by utilizing analytical expressions

for the approach profile and VRS boundaries, an alternate approach is to express each

boundary as a series of discrete points, i.e., $\mathbf{p}_{app}(\mathbf{X})$ and $\mathbf{p}_{VRS}$. The discrete points that

comprise $\mathbf{p}_{VRS}$ are depicted in Fig. 3.2 for illustrative purposes; however, there are too

many points in $\mathbf{p}_{app}(\mathbf{X})$ to be depicted clearly. The constraint can then be expressed

120

mathematically, i.e.,

$$g_2(\mathbf{X}) = \varepsilon - \min ||\mathbf{p}^i_{\text{app}}(\mathbf{X}) - \mathbf{p}^j_{\text{VRS}}|| \leq 0 \text{ for all } i, j \qquad (3.13)$$

where ε is a small number (the exact value will depend on how finely $\mathbf{p}_{\text{app}}(\mathbf{X})$ and $\mathbf{p}_{\text{VRS}}$ are discretized), $||\cdot||$ is the Euclidean norm, $\mathbf{p}^i_{\text{app}}(\mathbf{X})$ is the i-th point of the entire series of points, i_{all}, defining the approach profile, $\mathbf{X}$, and $\mathbf{p}^j_{\text{VRS}}$ is the j-th point of the entire series of points, j_{all}, defining the VRS boundaries.

A third behavior constraint was imposed to prevent flight in the "avoid" region of a representative multi-engine height-velocity diagram. Figure 3.3 shows the boundaries of a representative height-velocity diagram for a multi-engine helicopter (after Ref. 138). A representative approach profile is plotted on the same axes. Similar to the VRS-based constraint, the constraint value is the distance between the closest points on the approach profile and the boundary of the "avoid" region. The constraint is expressed

$$g_3(\mathbf{X}) = \varepsilon - \min ||\mathbf{p}^i_{\text{app}}(\mathbf{X}) - \mathbf{p}^j_{\text{HV}}|| \leq 0 \text{ for all } i, j \qquad (3.14)$$

where ε is a small number (the exact value depends on the discretization of $\mathbf{p}_{\text{app}}(\mathbf{X})$ and $\mathbf{p}_{\text{HV}}$) and $\mathbf{p}^j_{\text{HV}}$ is the j-th point of the entire series of points, j_{all}, defining the H-V "avoid" region boundaries.
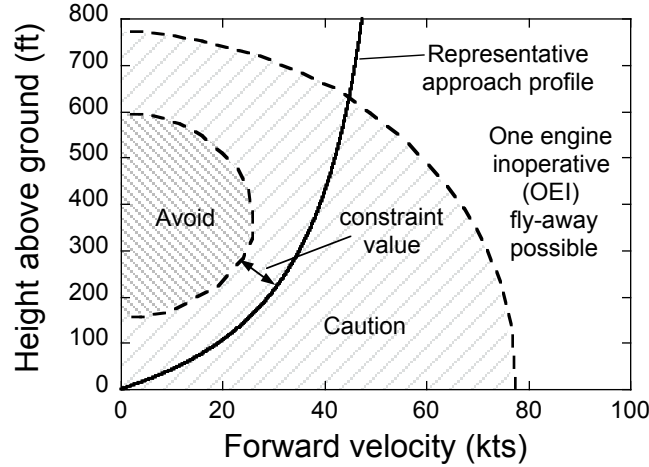
Figure 3.3: Graphical depiction of the behavior constraint for flight outside the "avoid" region on a typical H-V diagram (representative H-V boundaries are from Ref. 138).

3.1.4 Approximate Problem Formulation

Because of the high computational cost of a brownout simulation, the optimization problem cannot be solved by directly connecting the simulation and the optimizer. Instead, the baseline optimization problem is converted into a sequence of computationally inexpensive approximate optimization problems in which objective function and behavior constraint are replaced by Taylor series expansions that are updated at each step of the sequence. The general approach is to replace the objective function, $B(\mathbf{X})$, by a second-order Taylor series expansion about the current design, $\mathbf{X}_k$, i.e.,

$$B(\mathbf{X}) \approx B_{\text{app}}(\mathbf{X}) = B(\mathbf{X}_k) + \nabla B^T(\mathbf{X}_k) \cdot \delta \mathbf{X}_k + \frac{1}{2} \delta \mathbf{X}_k^T \mathbf{H}(\mathbf{X}_k) \delta \mathbf{X}_k \qquad (3.15)$$

where $\mathbf{X}_k$ is the current design, $\delta \mathbf{X}_k = \mathbf{X} - \mathbf{X}_k$, and $\nabla B(\mathbf{X}_k)$ and $\mathbf{H}(\mathbf{X}_k)$ are the gradient and Hessian matrix at the current design, respectively.

This approach was implemented in the form originally proposed by Vanderplaats

122

(Refs. 88,89), in which the optimization begins from the *linear* expansion and the quadratic terms are built one at the time as successive approximate optimization problems are solved; the resulting approximate optima are analyzed precisely. A full quadratic expansion may never be actually built, especially for larger problems where the number of objective function evaluations needed to complete the Hessian of the expansion may never become available. Given the way in which the approximation is constructed, the gradient and Hessian of the expansion are built from designs that may not be "finite difference close," i.e., with small increments of the design variables. As a consequence, the expansion is to be interpreted more as a general quadratic polynomial interpolation that is valid for broad regions of the design space, rather than a rigorous, but only locally valid, Taylor series expansion.

For a 2-design variable case, the components of the gradient and the Hessian are obtained from the solution of a linear system arising directly from Eq. (3.15), i.e.,

$$
\begin{bmatrix}
\delta x_{11} & \delta x_{21} & \frac{1}{2}(\delta x_{11})^2 & \frac{1}{2}(\delta x_{21})^2 & \delta x_{11}\delta x_{21} \\
\delta x_{12} & \delta x_{22} & \frac{1}{2}(\delta x_{12})^2 & \frac{1}{2}(\delta x_{22})^2 & \delta x_{12}\delta x_{22} \\
\delta x_{13} & \delta x_{23} & \frac{1}{2}(\delta x_{13})^2 & \frac{1}{2}(\delta x_{23})^2 & \delta x_{13}\delta x_{23} \\
\delta x_{14} & \delta x_{24} & \frac{1}{2}(\delta x_{14})^2 & \frac{1}{2}(\delta x_{24})^2 & \delta x_{14}\delta x_{24} \\
\delta x_{15} & \delta x_{25} & \frac{1}{2}(\delta x_{15})^2 & \frac{1}{2}(\delta x_{25})^2 & \delta x_{15}\delta x_{25}
\end{bmatrix}
\begin{Bmatrix}
\frac{\partial B}{\partial x_{1k}} \\
\frac{\partial B}{\partial x_{2k}} \\
\frac{\partial^2 B}{\partial x_{1k}^2} \\
\frac{\partial^2 B}{\partial x_{2k}^2} \\
\frac{\partial^2 B}{\partial x_{1k}\partial x_{2k}}
\end{Bmatrix}
=
\begin{Bmatrix}
\Delta B_{1k} \\
\Delta B_{2k} \\
\Delta B_{3k} \\
\Delta B_{4k} \\
\Delta B_{5k}
\end{Bmatrix}
$$

(3.16)

where δx_{ik} is the *i*-th component of the vector $\delta \mathbf{X}_k$, and $\Delta B_{ik} = B(\mathbf{X}_i) - B(\mathbf{X}_k)$. If fewer than 6 designs are available (for $N = 2$ design variables, or $1 + N + N(N+1)/2$ for general N), then an incomplete Hessian can be calculated, e.g., starting from the diagonal terms.

The same procedure may be used for the expansion of each of the three behavior constraints, i.e.,

$$g_j(\mathbf{X}) \approx g_{j,\text{app}}(\mathbf{X}) = g_j(\mathbf{X}_k) + \nabla g_j^T(\mathbf{X}_k) \cdot \delta\mathbf{X}_k + \frac{1}{2}\delta\mathbf{X}_k^T \mathbf{H}_g(\mathbf{X}_k)\delta\mathbf{X}_k \qquad (3.17)$$

where $\nabla g_j(\mathbf{X}_k)$ and $\mathbf{H}_g(\mathbf{X}_k)$ are the gradient and Hessian matrix at the current design, respectively.

It is prudent to impose move limits on the design when formulating the optimization as an approximate problem. In the present study, two sets of move limits are utilized. Initially, move limits were imposed such that each design variable could not vary by more than 10% between optimization steps, i.e.,

$$-0.1\mathbf{X}_{k-1} \leq \mathbf{X}_k - \mathbf{X}_{k-1} \leq 0.1\mathbf{X}_{k-1} \qquad (3.18)$$

As the optimization commenced, however, it was apparent that these move limits were too restrictive for the given design space. As a result, alternate move limits were formulated that allowed each new design to traverse up to 25% of the design space in a single optimization step, i.e.,

$$-0.25(\mathbf{X}_{\text{max}} - \mathbf{X}_{\text{min}}) \leq \mathbf{X}_k - \mathbf{X}_{k-1} \leq 0.25(\mathbf{X}_{\text{max}} - \mathbf{X}_{\text{min}}) \qquad (3.19)$$

3.1.5 Additional Designs

The polynomial approximation-based procedure previously described may occasionally generate a sequence of nearly linearly dependent designs, which slows convergence and reduces accuracy. Furthermore, the procedure is not ideally suited to deal with multiple local minima, if they exist. To help alleviate these problems, additional designs are generated during the course of the optimization based on the minimization of the following objective function

$$F(\mathbf{X}) = \frac{\sum_{i=1}^{k-1} |\mathbf{S}^T \mathbf{S}_i|}{\sum_{k=1}^{N} (\mathbf{X} - \mathbf{X}_k)^T (\mathbf{X} - \mathbf{X}_k)} \rightarrow \min \qquad (3.20)$$

The vector $\mathbf{S} = (\mathbf{X} - \mathbf{X}_k)/|\mathbf{X} - \mathbf{X}_k|$ is the unit vector in the direction from the candidate new design $\mathbf{X}$ to the current design $\mathbf{X}_k$, $\mathbf{S}_i = (\mathbf{X}_i - \mathbf{X}_k)/|\mathbf{X}_i - \mathbf{X}_k|, i = 1, 2, \ldots, k-1$ are the unit vectors in the direction from each of the previous designs $\mathbf{X}_i$ to the current design, and $|\mathbf{S}^T \cdot \mathbf{S}_i|$ is the absolute value of the projection of $\mathbf{S}^T$ onto $\mathbf{S}_i$, which will be equal to zero if the two vectors are perpendicular. Therefore, Eq. (3.20) is meant to minimize the numerator and generate a new design, $\mathbf{X}$, that is as perpendicular as possible to the previous designs.

The denominator of $F(\mathbf{X})$ is the sum of the squares of the distances of the candidate design from the existing designs. Minimizing $F(\mathbf{X})$ is also meant to maximize this distance and, therefore, to explore regions of the design space far away from the current designs and inject information about these regions in the polynomial approximations. The additional designs are used in an attempt to reproduce, in a deterministic context, the

global convergence benefits provided by mutation in Genetic Algorithms (GA).

The objective $F(\mathbf{X})$ is minimized subject to the same constraints as the baseline optimization. The resulting optimization can have multiple minima, therefore, it is solved using a GA. Because $F(\mathbf{X})$ is computationally simple, the GA solution is still rapid. The designs computed in this way are not necessarily better designs. However, they can improve the mathematical properties of the overall optimization, by improving the accuracy of the Taylor series expansions used for the approximate problems and also give it a measure of global convergence.

3.1.6 Summary of the Optimization Procedure

In summary, the computational procedure for brownout mitigation consists of the following steps:

1. Compute the objective function $B(\mathbf{X})$ and constraint $g(\mathbf{X})$ for a baseline and N additional designs (in the present study, $N = 3$). The first $k = N + 1$ designs need not be close and may be infeasible.

2. Compute the polynomial approximations to objective $B_{\text{app}}(\mathbf{X})$ and constraint $g_{\text{app}}(\mathbf{X})$. If more than $M = 1 + N + N(N + 1)/2$ designs are available, use the M designs closest to the current best design. Otherwise, build only a portion of the Hessian, starting from the diagonal terms.

3. Solve the approximate optimization problem:

Find $\mathbf{X}^*$ such that $B_{\text{app}}(\mathbf{X}^*) \to \min$ Subject to:

<u>Behavior Constraints</u>

$$g_{j,\text{app}}(\mathbf{X}) \leq 0 \quad \text{for } j = 1,2,3$$

<u>Side Constraints</u>

$$1° \leq \alpha_{\text{app}} \leq 12°$$

$$60 \text{ kts} \leq v_0 \leq 130 \text{ kts}$$

$$100 \text{ ft} \leq r_{\text{pd}} \leq 500 \text{ ft}$$

<u>Move Limits</u>

$$-0.1\mathbf{X}_{k-1} \leq \mathbf{X}_k - \mathbf{X}_{k-1} \leq 0.1\mathbf{X}_{k-1}$$

or

$$-0.25(\mathbf{X}_{\max} - \mathbf{X}_{\min}) \leq \mathbf{X}_k - \mathbf{X}_{k-1} \leq 0.25(\mathbf{X}_{\max} - \mathbf{X}_{\min})$$

and let $\mathbf{X}_{k+1}$ be the optimum for the approximate problem.

4. Compute $B(\mathbf{X}_{k+1})$ and $g(\mathbf{X}_{k+1})$. If (i) the design is feasible, (ii) the new design $\mathbf{X}_{k+1}$ is close to the previous design $\mathbf{X}_k$ within a specified tolerance, and (iii) the objective function $B(\mathbf{X}_{k+1})$ is also close to $B(\mathbf{X}_k)$ within a specified tolerance, assume that the sequence of solutions of the approximate problems has converged to the solution of the original optimization problem, and terminate the procedure. Otherwise, add the solution $\mathbf{X}_{k+1}$ of the approximate optimization problem to the current solution set, update the polynomial approximations, and repeat Step 2. The optimization procedure may also be terminated early if a sufficient reduction of the

objective function $B(\mathbf{X})$ has been achieved.

5. For every N executions of Step 2, compute one additional design based on Eq. (3.20).

There is some flexibility in the procedure summarized above. For example, if multiple computers are available to perform brownout calculations for different designs, and they complete the calculations at different times, the polynomial approximations can be constructed with whatever designs are available at that time. Such procedural modifications do not affect the overall optimization in any significant way. Similarly, if designs are available from previous optimizations, or are formulated outside the optimization procedure, they can all be used in the optimization. In fact, while not all designs may directly represent improvements, they all contribute to improving the accuracy of the polynomial approximations to the objective function and behavior constraints and, therefore, the accuracy of the sequence of approximate optimization problems. In this sense, the procedure is very robust.

3.1.7 Sizing the Brownout Cloud Model

In the present study, it was essential to define what constituted an adequate simulation size for the brownout cloud model. In the first instance, the physical dimensions of the sediment bed must be carefully selected. It is clear that the rotor wake will interact with the ground differently for the range of potential approach profiles, and the sediment bed must be sized appropriately to provide accurate assessments of the various potential approaches. After a preliminary examination of the extent to which the rotor wake expanded after impinging upon the ground for a variety of approach profiles, it was deter-

mined that a square sediment bed of $20R \times 20R$ would be suitably large to accommodate the resulting brownout cloud for a wide range of potential approaches. The landing point over the bed was held constant for all of the approaches, and it is the origin of a Cartesian coordinate system relative to which the approach profile is formulated. The bed dimensions in this coordinate system are $15R \leq x \leq -5R$ and $-10R \leq y \leq 10R$. The approach profiles are defined in the positive x direction.

Another important aspect in sizing the simulation is the selection of the number of particles to be included in the sediment bed. While maximizing the number of particles in the simulation certainly maximizes the fidelity of the simulation and may be necessary for a detailed analysis of the brownout cloud, it greatly increases the computational and file storage cost of each objective function evaluation. As such, it is desirable to select a sediment bed size that provides only enough particles to achieve consistent relative comparisons between competing approach trajectories. To examine these effects, a sensitivity study was conducted in which the number of particles per sediment layer in the bed was successively increased (the particles were distributed evenly throughout the $20R \times 20R$ bed) and the resulting clouds were compared. This study was performed for a single approach profile that was expected to provide a severe brownout cloud (i.e., an approach profile that was relatively low and slow over the sediment bed).

Figure 3.4(a) shows time histories of the total number of particles entrained, n_{ent}, for simulations with varied number of particles per layer, n_p. Notice that the $n_p = 200 \times 200$ simulation terminated at approximately 38 s into the approach. At this point, the memory requirements for tracking so many particles became prohibitive. Figure 3.4(b) provides
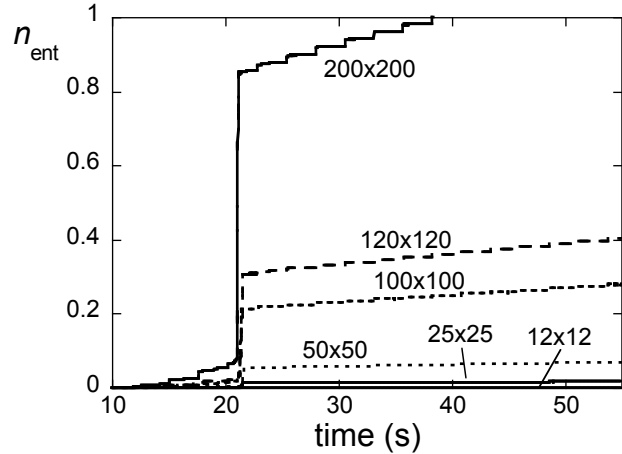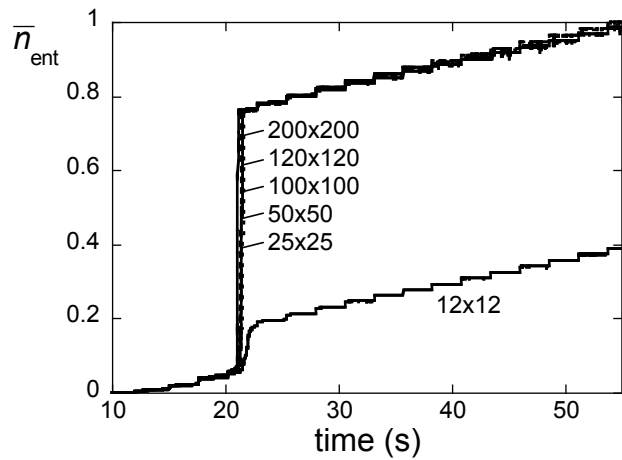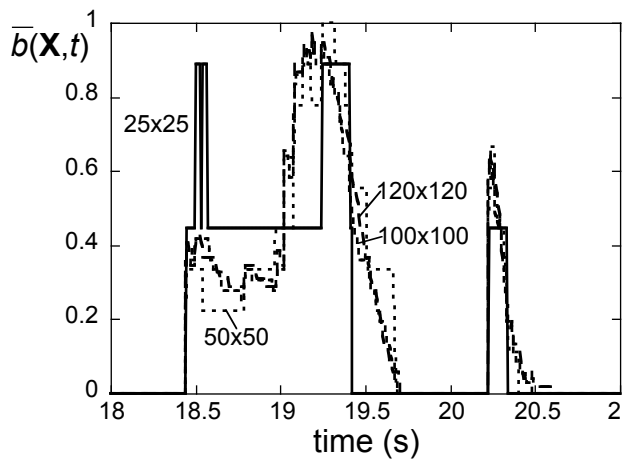
Figure 3.4: Results of the particle count sensitivity study to determine a suitable simulation size: the (a) total number of entrained dust particles, (b) total number of entrained particles divided by the number of particles per layer, and (c) $b(\mathbf{X},t)$ divided by the number of particles per layer. For clarity the y-axis in each plot has been normalized to a maximum value of unity.

the same time histories, although the number of particles entrained have been normalized by the total number of particles per layer, i.e., $\bar{n}_{\text{ent}} = n_{\text{ent}}/n_p$. Notice that the trends for simulations ranging from 25×25 to 200×200 particles per layer are in close agreement. This outcome indicates that, so long as the simulation contains at least $n_p = 25 \times 25$ (a relatively coarse distribution), the overall trend of total particle entrainment is consistent and scales with n_p. While this is an interesting observation, the objective function, i.e., Eq. (2.80), is sensitive to details of the cloud geometry over the duration of the maneuver rather than the total number of particles entrained; see Eq. (2.79).

Figure 3.4(c) shows a brief portion of the time history of $\bar{b}(\mathbf{X},t) = b(\mathbf{X},t)/n_p$. Notice that the trends for 120×120, 100×100, and 50×50 are in relatively close agreement. This result indicates that, over this range of n_p, the objective function values will scale with n_p. Therefore, the relative comparisons, upon which the optimization procedure is based, would remain consistent regardless of n_p. For lower values of n_p, (e.g., $n_p = 25 \times 25$), the trends for $b(\mathbf{X},t)$ do not agree. This result indicates that lower values of n_p do not afford sufficient spatial resolution for calculating an objective function that is directly affected by the brownout cloud geometry. From this study, it was determined that a brownout cloud model consisting of $n_p = 100 \times 100$ was suitable for the optimization.

3.1.8 Assumptions and Limitations

A number of key assumptions are included in the present work:

1. Only the main rotor is modeled (i.e., the effects of the fuselage and tail rotor are ignored), and the flow is modeled using an inviscid method (i.e., a FVM).

2. From a flight dynamics perspective, the formulation of the approach profile involves only a simple prescription of the linear motion of the rotor. The angular motion, i.e., Eq. (3.11), is only an approximation of the motion that would result from the prescribed linear motion.

3. The rotor controls at each time step are determined for a prescribed thrust (i.e., there is no pilot model and no inverse simulation procedure to determine the control positions for the given maneuver).

4. From the standpoint of the dust cloud simulation, the brownout model assumes a one-way coupling of the air and dust particles (i.e., the air affects the dust particles but the particles do not have an impact on the fluid flow).

5. The dust cloud simulation model includes only monodisperse dust particles, and the total number of particles in the initial sediment bed is, in comparison with an actual brownout cloud, realtively small (although the sensitivity study indicated this was sufficient for the present analysis).

3.2   Results

This section presents the results of a brownout mitigation study for a medium-lift, single main rotor helicopter executing a visual approach to landing. In the present case, mitigation strategies are developed only through the variation of the approach profile (i.e., the design of the rotor is unchanged). Notice that the optimization is for a specific formulation of the approach profile, and certain operational techniques may not be replicable.

For example, this approach model would not be able to simulate the technique to perform the approach to a high hover, hold a stationary hover while loose layers of sediment are blown clear of the landing zone, then descend vertically to the ground. The main rotor design includes four rectangular planform blades with a 26.8 ft radius, 1.9 ft chord, and 18° of linear nose-down twist.

Much of the simulation work was performed on an Apple MacPro work station, and the cloud projection and assessment routines were parallelized via MPI (Message Passing Interface). The dust cloud model was executed on a custom machine with a NVIDIA Tesla C2050 GPU, and it was parallelized for GPU execution using the CUDA parallel computing architecture. Each objective function evaluation required approximately 30 hours (the exact time depended on the particulars of the simulation and the computing load at the time) from the initial setup to the point that the objective function could be calculated for the brownout cloud. Each case required approximately 100 GB of disk storage space.

3.2.1 Optimization Results

A summary of the progression of the optimization procedure is given in Fig. 3.5, and two-dimensional contour maps through the three-dimensional approximate objective function, $B_{\mathrm{app}}(\mathbf{X})$, are shown in Figs. 3.6 through 3.17. The approach profiles evaluated over the course of the procedures are depicted in the contour maps as circles and the optimum approach profiles are denoted by diamonds. Only three values are shown for r_{pd}, and the approach profiles are plotted for the closest r_{pd} value. In some instances,
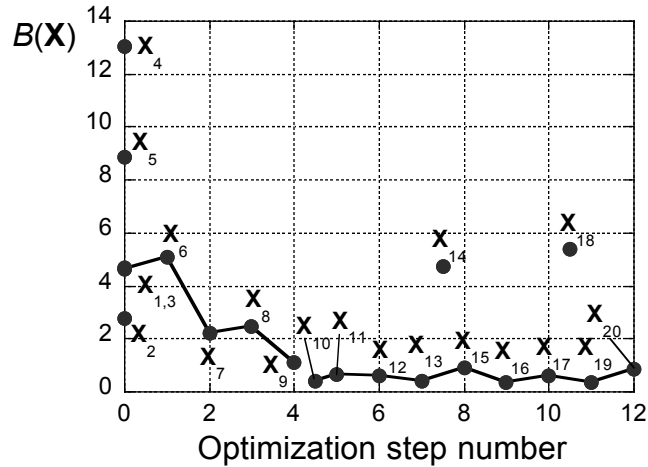
Figure 3.5: Optimization history, i.e., objective function value versus optimization step number.

multiple approach profiles may be overlaid in this representation if they have the same values for α_{app} and v_0, and similar values for r_{pd}. Notice also that the contour plots are empty in regions where $B_{\mathrm{app}}(\mathbf{X}) < 0$. A listing of all of the function evaluations is provided in Table 3.1.

The approach profiles described by $\mathbf{X}_1$–$\mathbf{X}_5$ were the initial runs needed to explore the design space before beginning any formal optimization steps. As mentioned in the methodology section, only four approach profiles were necessary to build the gradients of the approximate objective and constraint functions. The fifth approach profile was utilized for the brownout cloud model sizing study, and its inclusion in the initial runs allowed for one element of the Hessian of the approximate objective and constraint functions to be included in the initial optimization step, as shown in Fig. 3.6.

The approach profiles described by $\mathbf{X}_6$–$\mathbf{X}_9$ (i.e., optimization steps 1–4) show the initial progress of the optimization procedure, and they clearly resulted in a reduction of the objective function. It was apparent through designs $\mathbf{X}_6$–$\mathbf{X}_9$ that the optimization

134

methodology was seeking to reduce approach angle, α_{app}, and range of peak deceleration, r_{pd}; see Figs. 3.6–3.9. Design $\mathbf{X}_{10}$, however, was the result of an "additional design" optimization step that showed significant improvement over $\mathbf{X}_9$. This outcome indicates that the methodology had possibly been converging towards a local minimum. The procedure, therefore, directed its progress towards a different region of the design space with a second optimization path.

It was apparent in the second optimization path, given by $\mathbf{X}_{10}$–$\mathbf{X}_{13}$ and $\mathbf{X}_{15}$ (i.e., optimization steps 5–8), that the methodology was searching a new region of significantly higher approach angles; see Figs. 3.10–3.13. Notice that, as more function evaluations became available, not all of them were needed for the Taylor series expansion. Designs that were omitted from the Taylor series expansion are indicated by a gray-filled marker (e.g., $\mathbf{X}_4$ in Fig. 3.11). Notice also that $\mathbf{X}_{14}$ was an "additional design" optimization step, although it did not spawn any new search directions because it did not appear to indicate any improvement over the existing search regions.

To assess if the optimizer would continue to attempt to maximize approach angle, the side constraint on α_{app} was relaxed for design $\mathbf{X}_{16}$ (i.e., optimization step 9). The move limits and behavior constraints, however, remained. Interestingly, $\mathbf{X}_{16}$ did not continue the trend to increase α_{app}; see Fig. 3.14. This approach did, however, result in the overall optimum design of the procedure. The procedure was continued for designs $\mathbf{X}_{17}$– $\mathbf{X}_{20}$ (i.e., optimization steps 10–12), without the upper constraint on α_{app}; see Figs. 3.15– 3.17. Design $\mathbf{X}_{18}$ was an "additional design" optimization step, although it did not spawn any new search directions because it did not appear to indicate any improvement over the
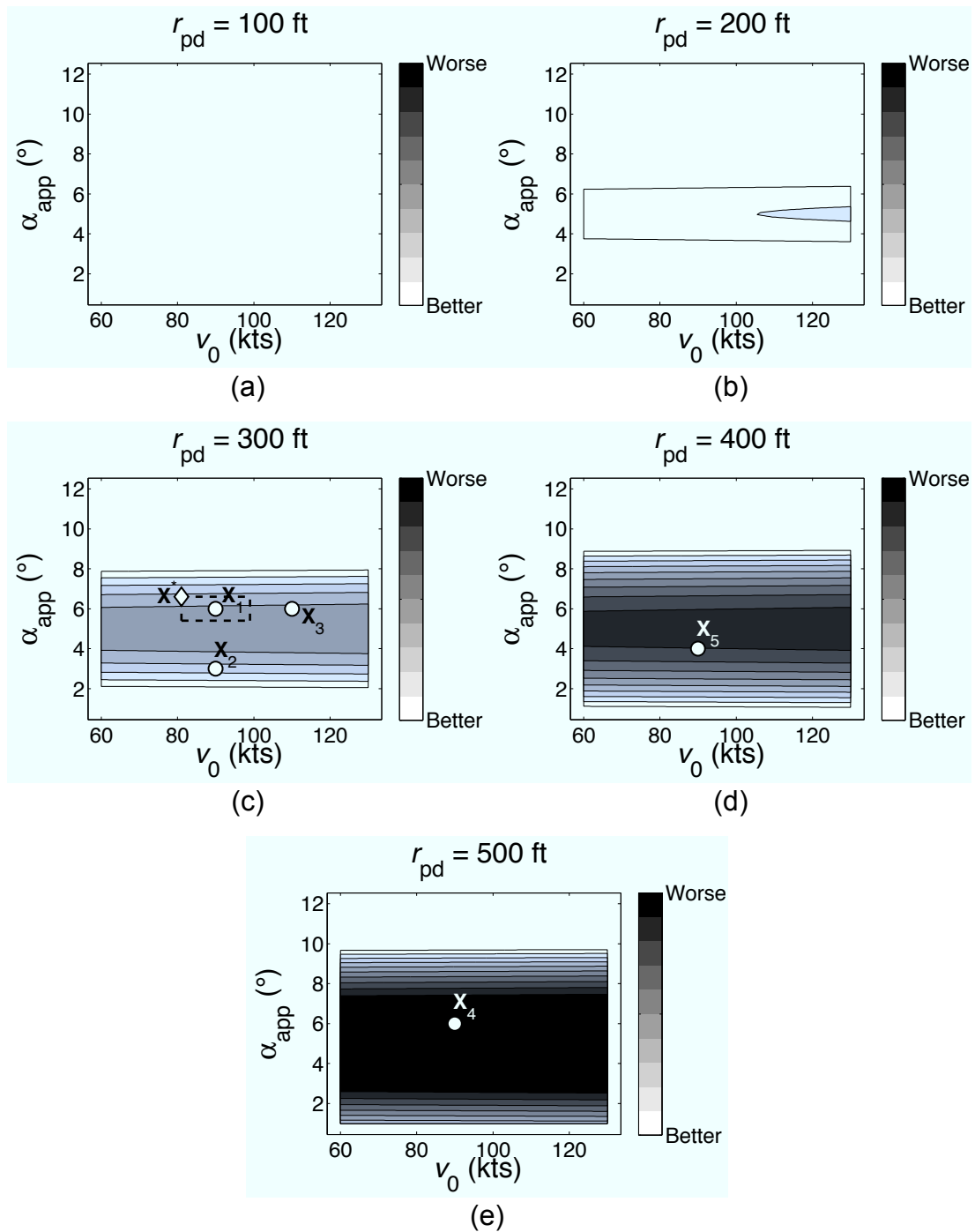
Figure 3.6: Two-dimensional contour maps through the three-dimensional approximate objective function, $B_{\text{app}}(\mathbf{X})$, for the first optimization step. Move limits are shown as dashed lines.
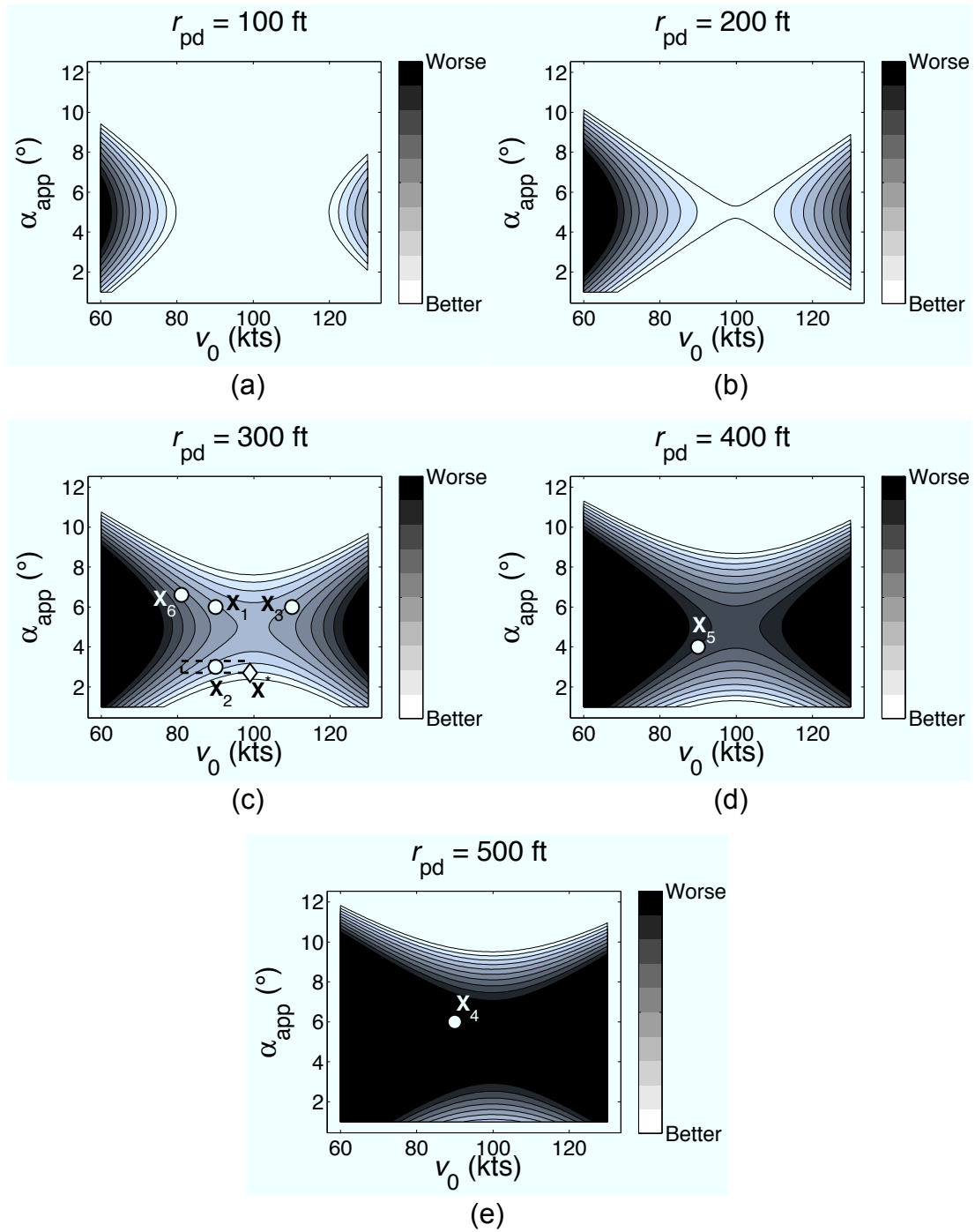
Figure 3.7: Two-dimensional contour maps through the three-dimensional approximate objective function, $B_{\text{app}}(\mathbf{X})$, for the second optimization step. Move limits are shown as dashed lines.
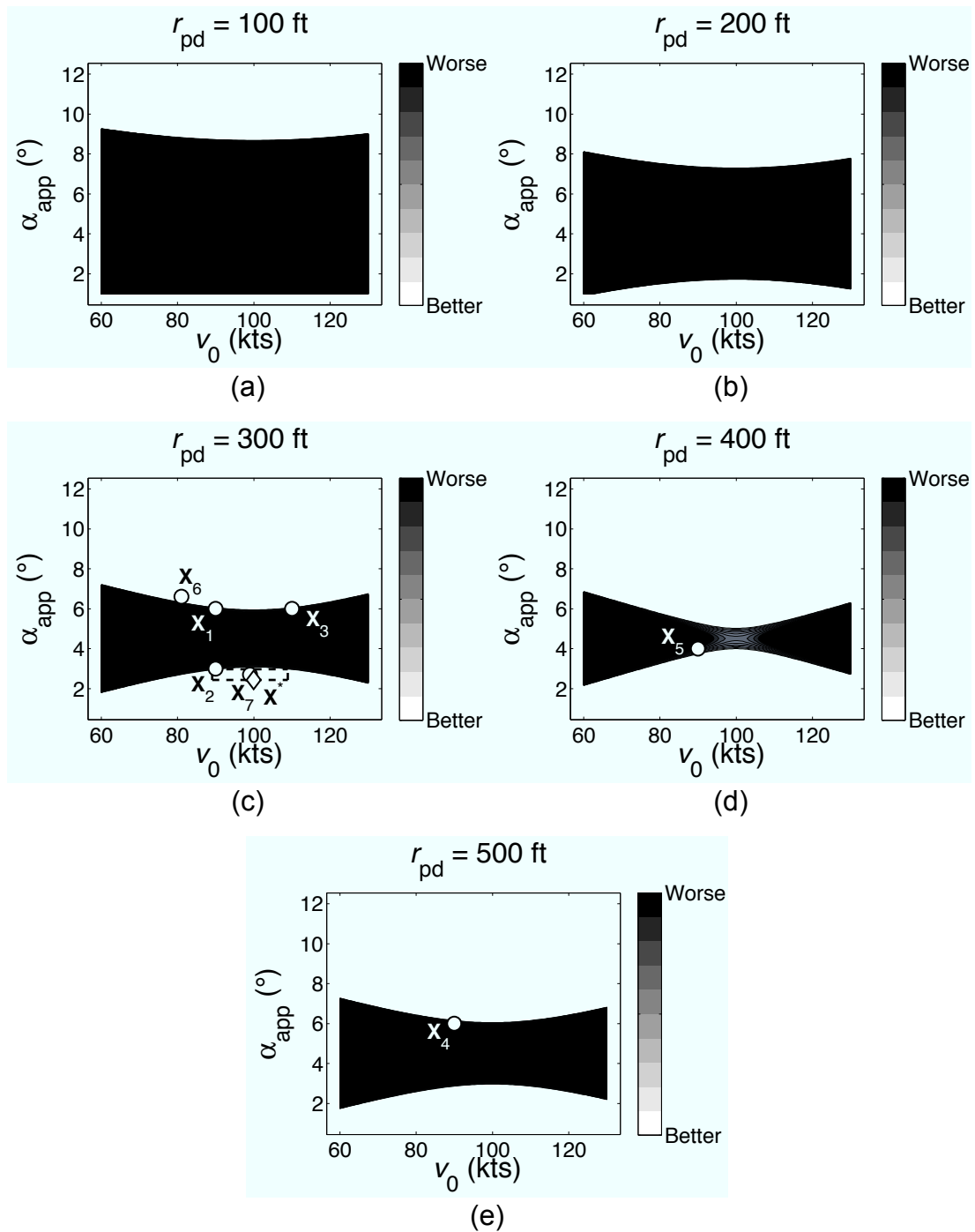
Figure 3.8: Two-dimensional contour maps through the three-dimensional approximate objective function, $B_{\mathrm{app}}(\mathbf{X})$, for the third optimization step. Move limits are shown as dashed lines.
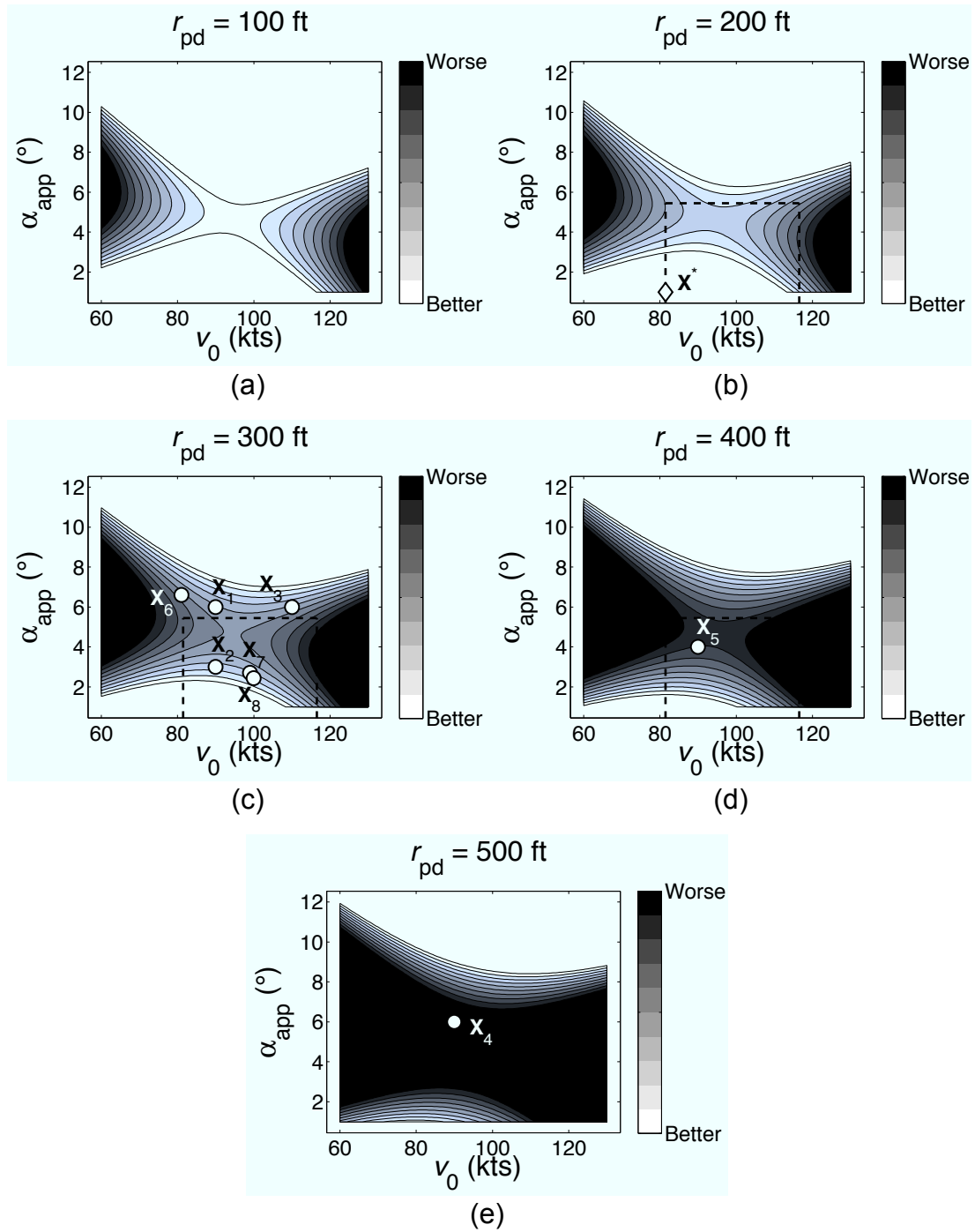
Figure 3.9: Two-dimensional contour maps through the three-dimensional approximate objective function, $B_{\mathrm{app}}(\mathbf{X})$, for the fourth optimization step. Move limits are shown as dashed lines.
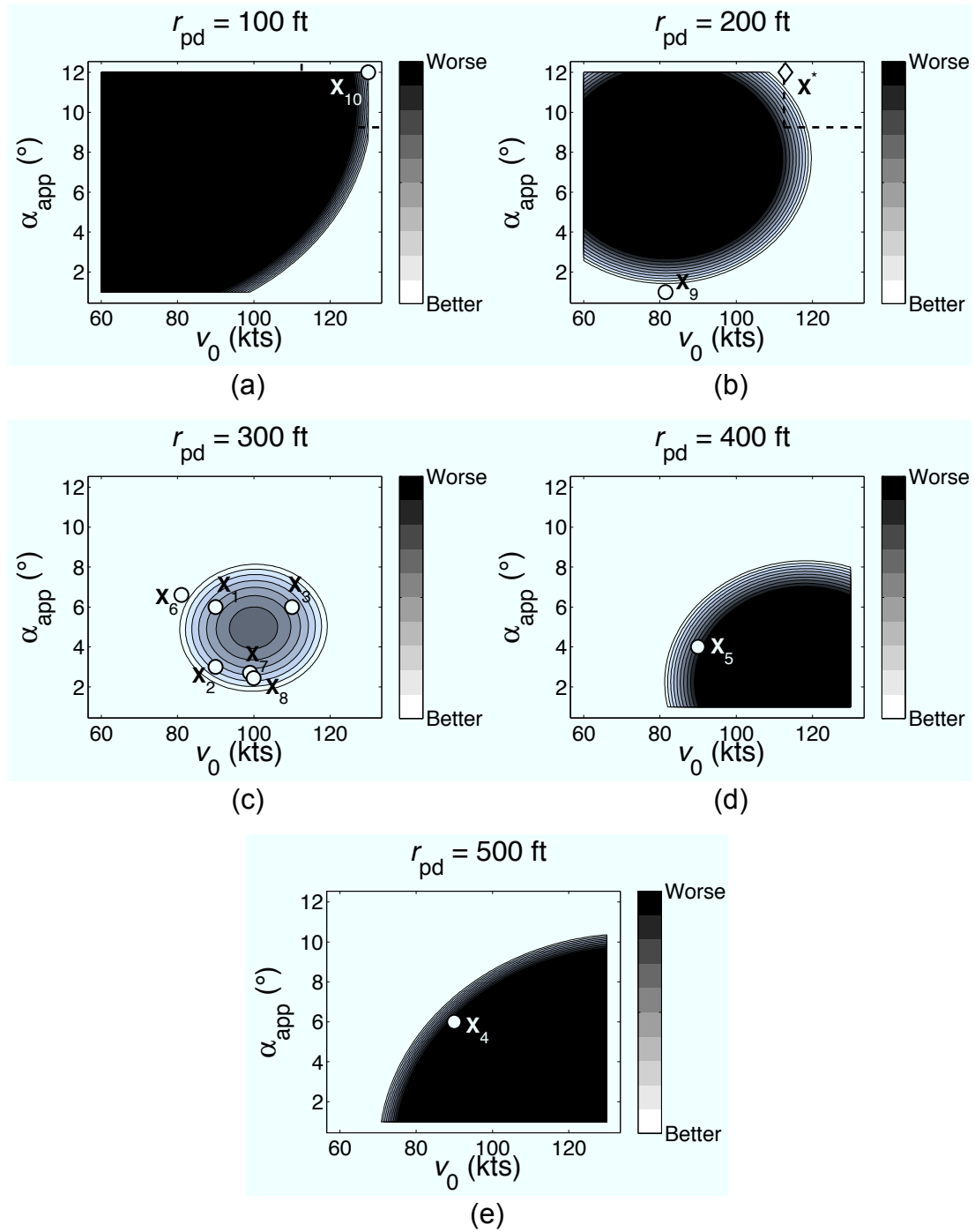
Figure 3.10: Two-dimensional contour maps through the three-dimensional approximate objective function, $B_{\mathrm{app}}(\mathbf{X})$, for the fifth optimization step. Move limits are shown as dashed lines.
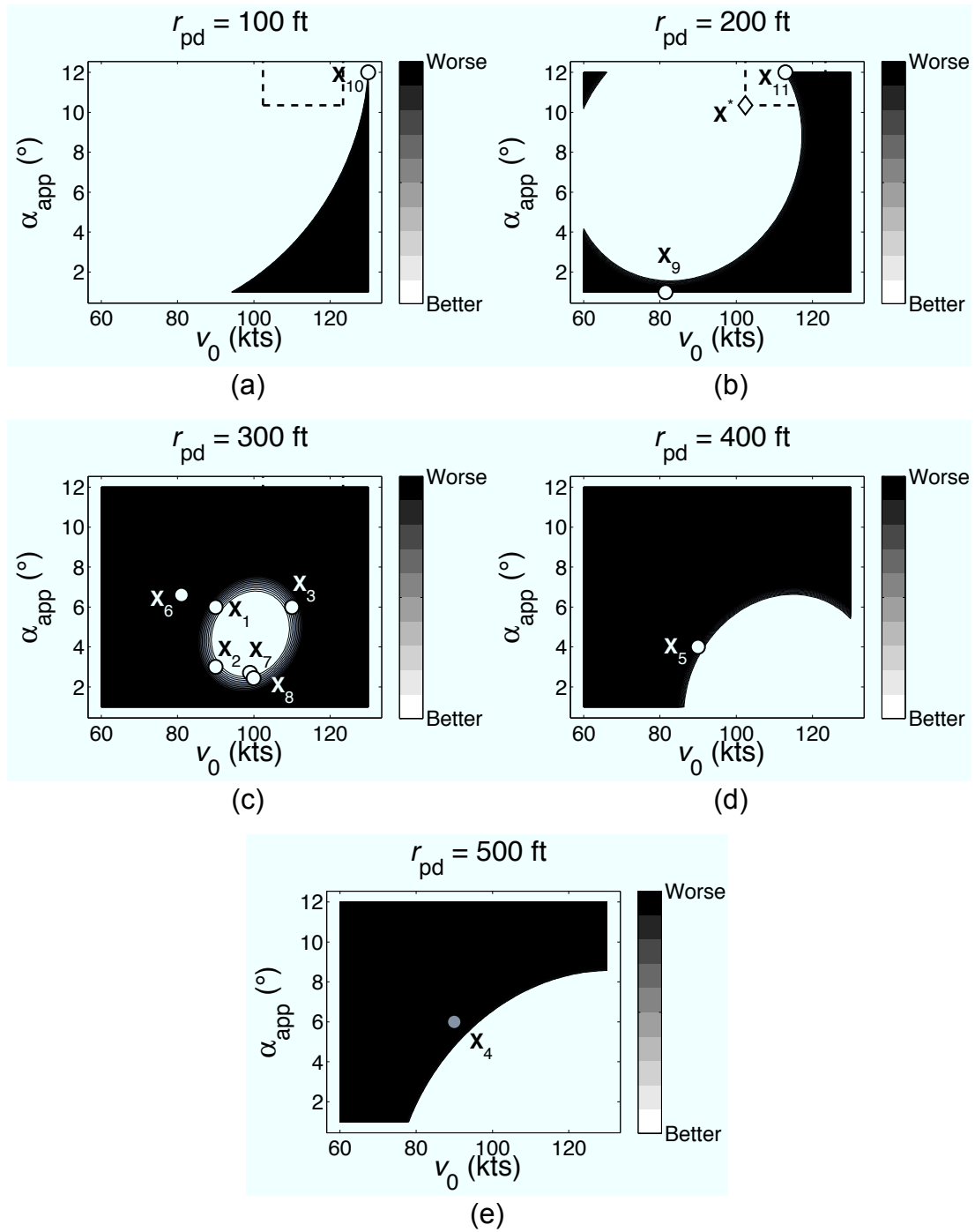
Figure 3.11: Two-dimensional contour maps through the three-dimensional approximate objective function, $B_{\mathrm{app}}(\mathbf{X})$, for the sixth optimization step. Move limits are shown as dashed lines.
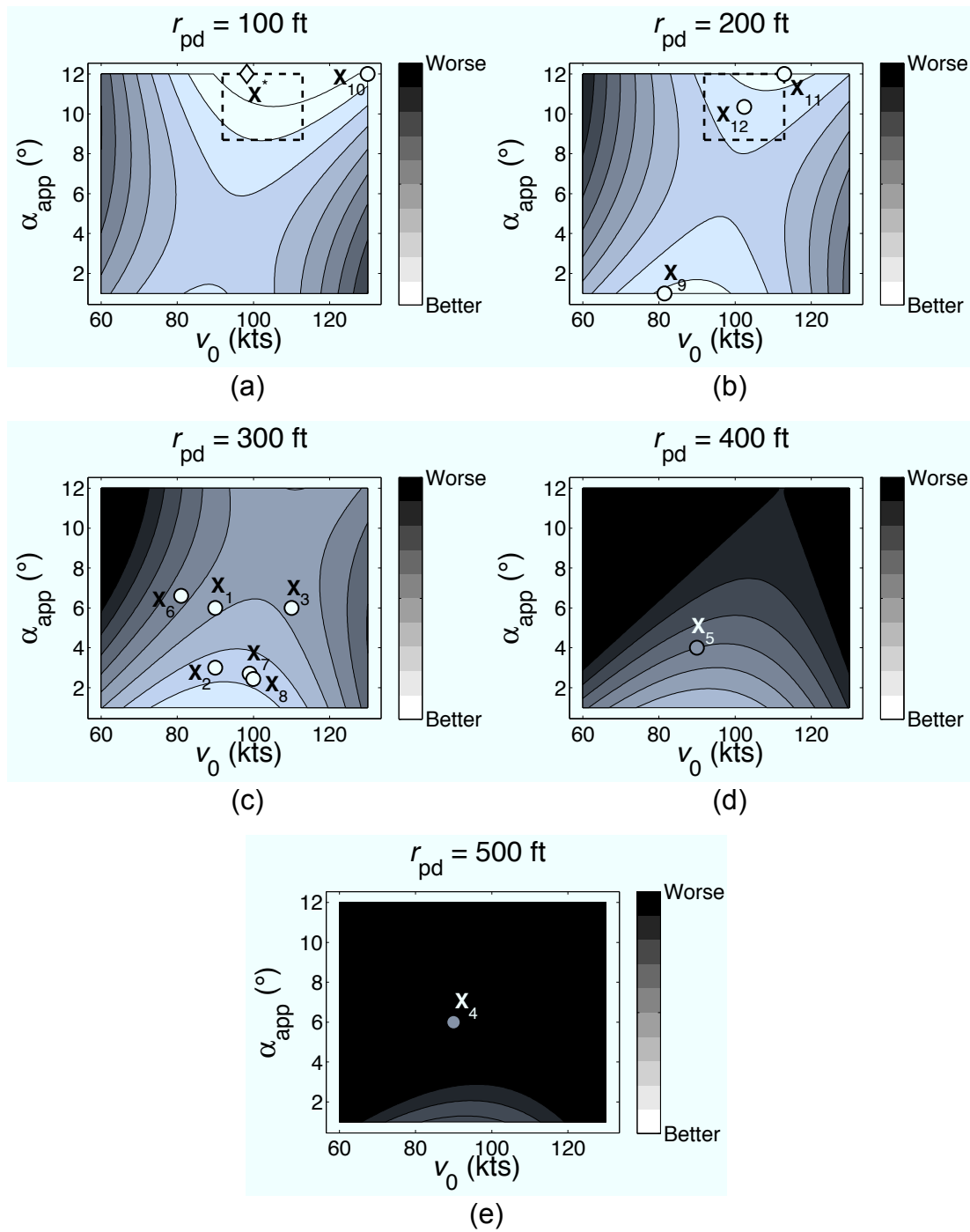
Figure 3.12: Two-dimensional contour maps through the three-dimensional approximate objective function, $B_{app}(\mathbf{X})$, for the seventh optimization step. Move limits are shown as dashed lines.
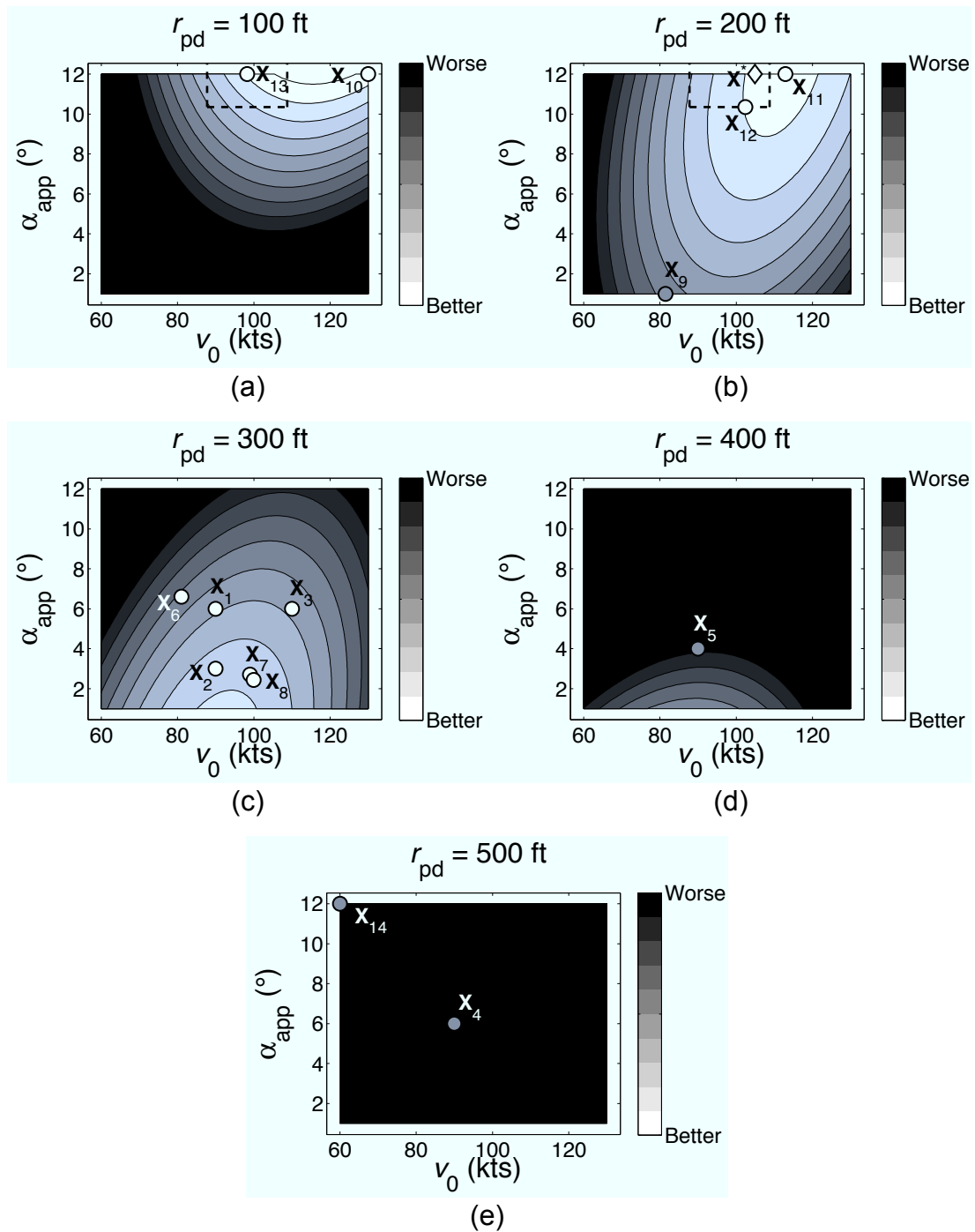
Figure 3.13: Two-dimensional contour maps through the three-dimensional approximate objective function, $B_{\text{app}}(\mathbf{X})$, for the eighth optimization step. Move limits are shown as dashed lines.
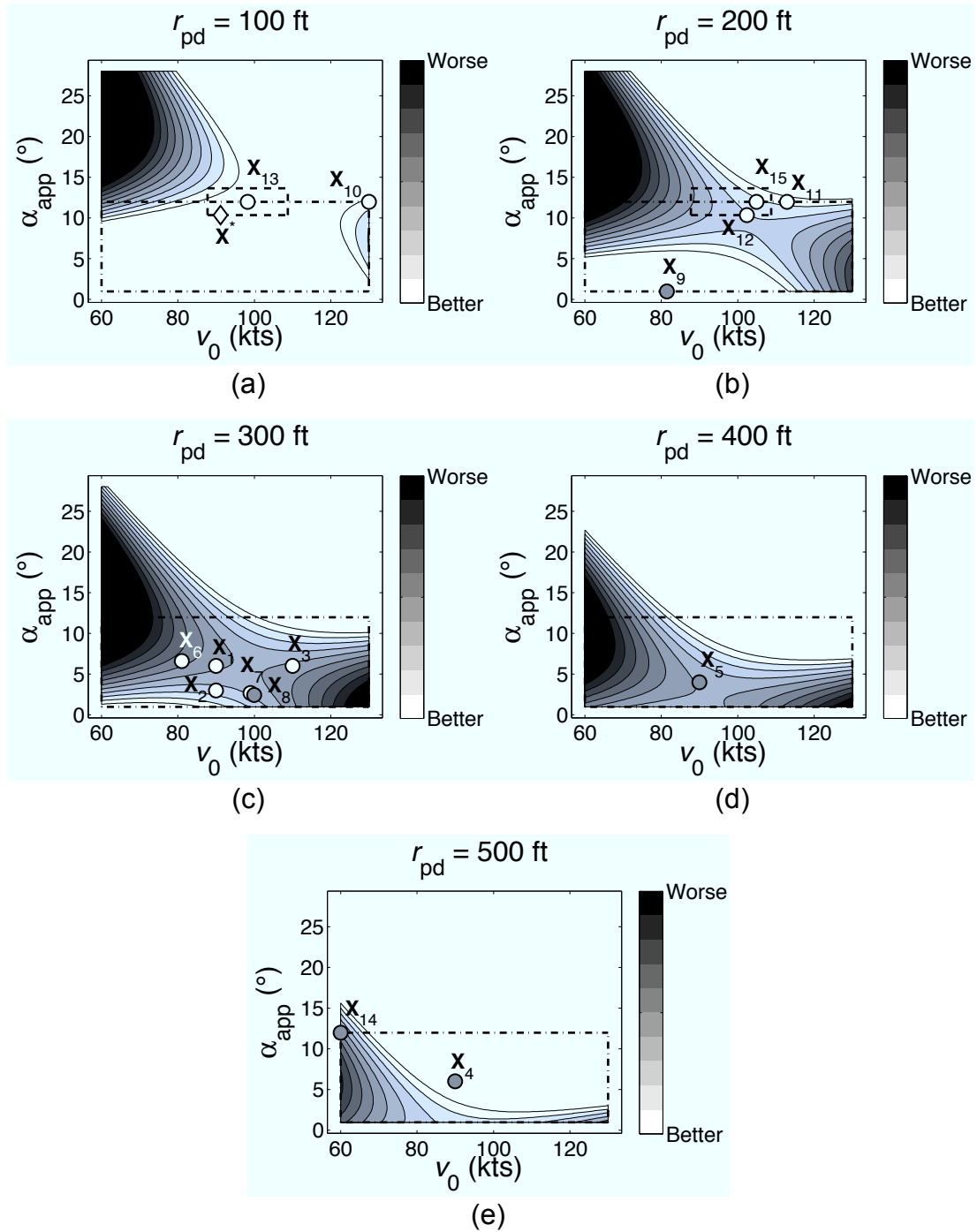
Figure 3.14: Two-dimensional contour maps through the three-dimensional approximate objective function, $B_{app}(\mathbf{X})$, for the ninth optimization step. Move limits are shown as dashed lines and the original side constraints are shown as dot-dashed lines.
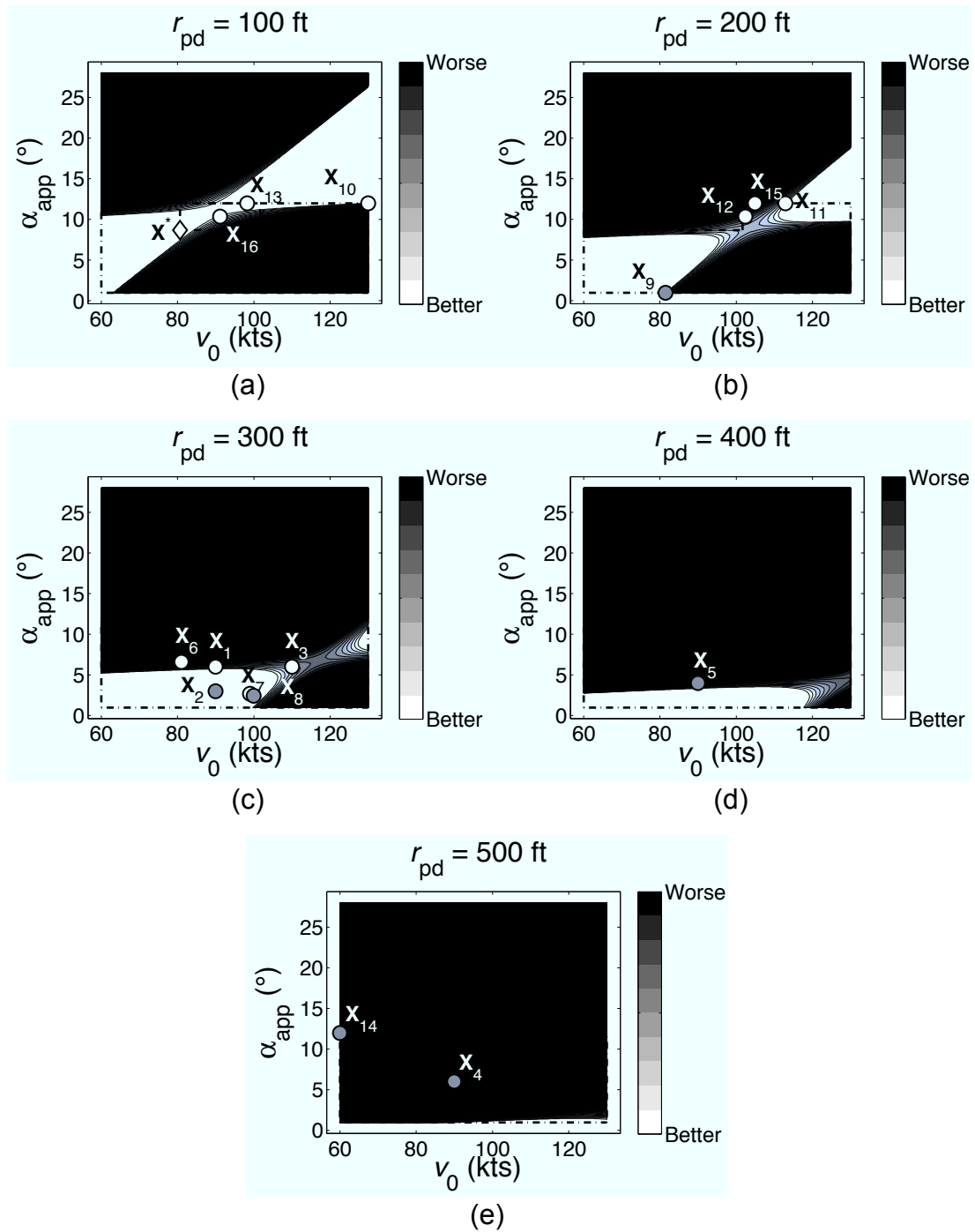
Figure 3.15: Two-dimensional contour maps through the three-dimensional approximate objective function, $B_{app}(\mathbf{X})$, for the tenth optimization step. Move limits are shown as dashed lines and the original side constraints are shown as dot-dashed lines.
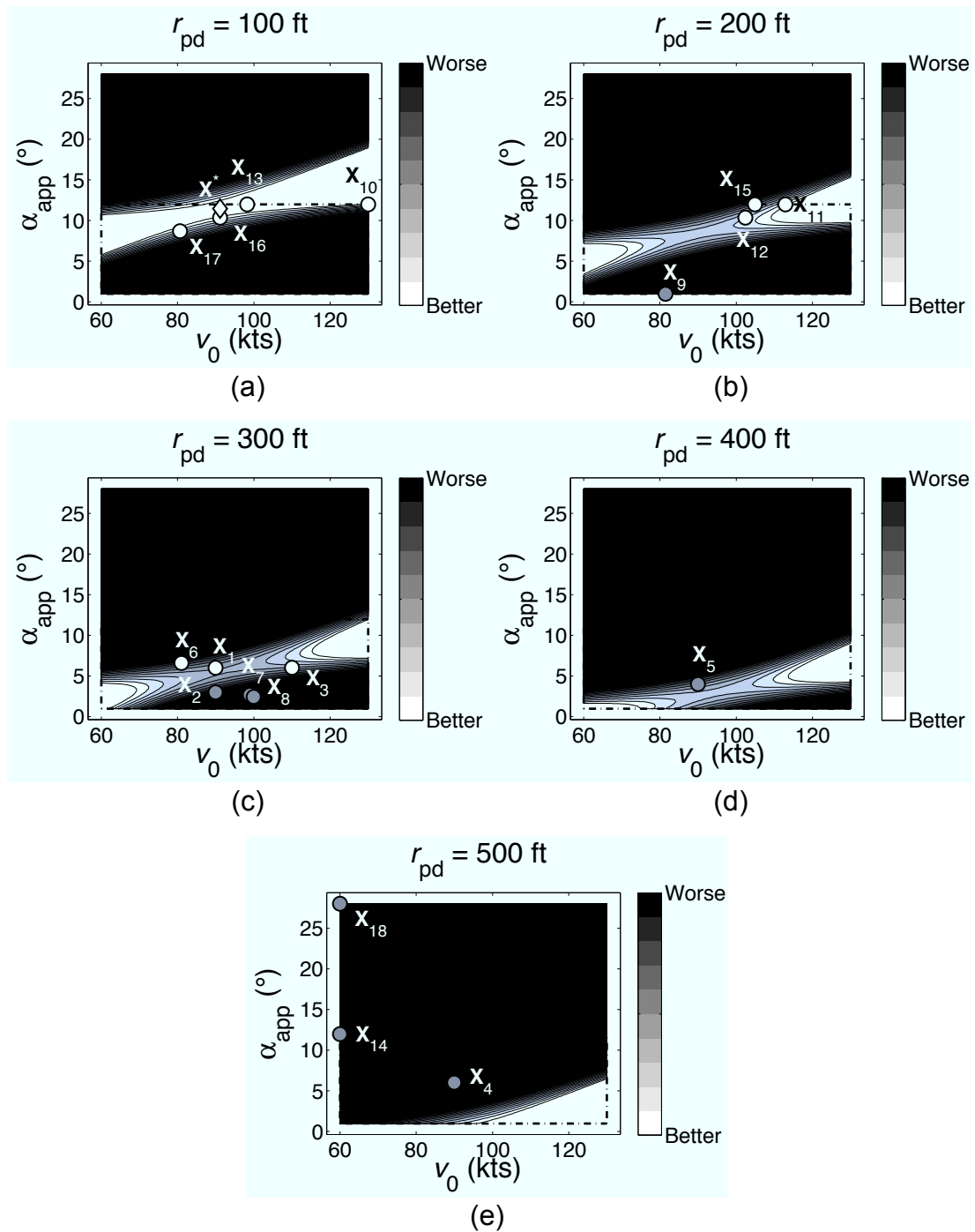
Figure 3.16: Two-dimensional contour maps through the three-dimensional approximate objective function, $B_{app}(\mathbf{X})$, for the eleventh optimization step. The original side constraints are shown as dot-dashed lines.
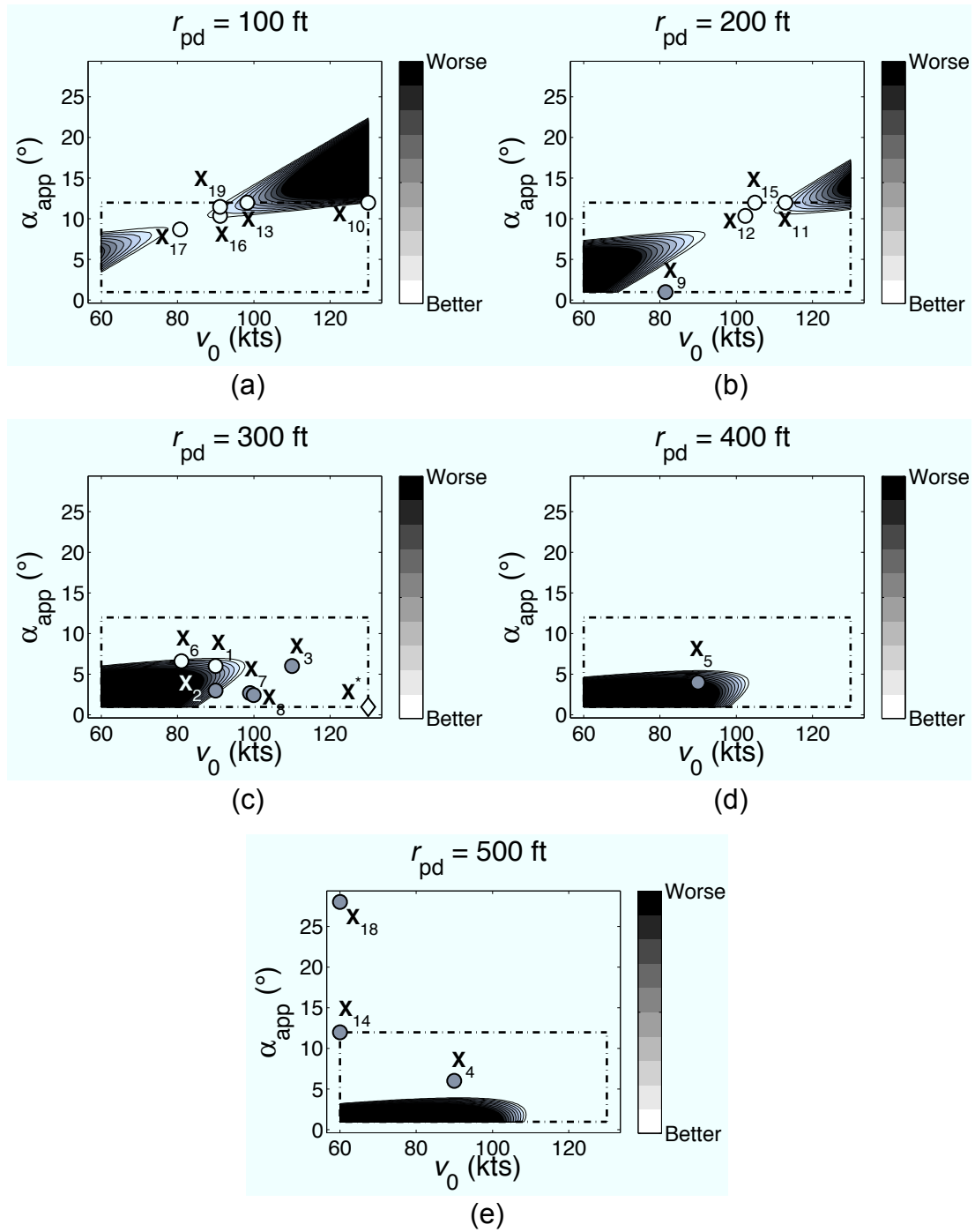
Figure 3.17: Two-dimensional contour maps through the three-dimensional approximate objective function, $B_{\text{app}}(\mathbf{X})$, for the twelfth optimization step. The original side constraints are shown as dot-dashed lines.

Table 3.1: Function evaluations for the approach-to-landing trajectory optimization.

Optimization Step	Approach, $\mathbf{X} = [\alpha_{\mathrm{app}} \; v_0 \; r_{\mathrm{pd}}]^T$	Function Value, $B(\mathbf{X})$
0	$\mathbf{X}_1 = [6.0°\ 90.0\text{ kts } 300.0\text{ ft}]^T$	4639
0	$\mathbf{X}_2 = [3.0°\ 90.0\text{ kts } 300.0\text{ ft}]^T$	2787
0	$\mathbf{X}_3 = [6.0°\ 110.0\text{ kts } 300.0\text{ ft}]^T$	4708
0	$\mathbf{X}_4 = [6.0°\ 90.0\text{ kts } 500.0\text{ ft}]^T$	13055
0	$\mathbf{X}_5 = [4.0°\ 90.0\text{ kts } 400.0\text{ ft}]^T$	8857
1	$\mathbf{X}_6 = [6.6°\ 81.0\text{ kts } 270.0\text{ ft}]^T$	5069
2	$\mathbf{X}_7 = [2.7°\ 99.0\text{ kts } 270.0\text{ ft}]^T$	2196
3	$\mathbf{X}_8 = [2.4°\ 100.0\text{ kts } 297.0\text{ ft}]^T$	2473
4	$\mathbf{X}_9 = [1.0°\ 81.5\text{ kts } 170.0\text{ ft}]^T$	1123
additional design	$\mathbf{X}_{10} = [12.0°\ 130.0\text{ kts } 100.0\text{ ft}]^T$	383
5	$\mathbf{X}_{11} = [12.0°\ 112.9\text{ kts } 200.0\text{ ft}]^T$	673
6	$\mathbf{X}_{12} = [10.4°\ 102.4\text{ kts } 150.9\text{ ft}]^T$	600
7	$\mathbf{X}_{13} = [12.0°\ 98.2\text{ kts } 131.8\text{ ft}]^T$	380
additional design	$\mathbf{X}_{14} = [12.0°\ 60.0\text{ kts } 500.0\text{ ft}]^T$	4758
8	$\mathbf{X}_{15} = [12.0°\ 104.9\text{ kts } 162.6\text{ ft}]^T$	906
9	$\mathbf{X}_{16} = [10.4°\ 91.2\text{ kts } 100.0\text{ ft}]^T$	350
10	$\mathbf{X}_{17} = [8.7°\ 80.7\text{ kts } 128.6\text{ ft}]^T$	597
additional design	$\mathbf{X}_{18} = [28.0°\ 60.0\text{ kts } 500.0\text{ ft}]^T$	5371
11	$\mathbf{X}_{19} = [11.5°\ 91.2\text{ kts } 100.0\text{ ft}]^T$	365
12	$\mathbf{X}_{20} = [1.0°\ 130.0\text{ kts } 283.5\text{ ft}]^T$	876

existing search regions. The move limits were also removed for designs $\mathbf{X}_{19}$ and $\mathbf{X}_{20}$, although no improved designs were achieved. The optimization was terminated at this point because sufficient improvement had been demonstrated over the course of the procedure, and it appeared that further improvements were not likely.

Notice that the objective function approximations were prone to drastic changes between optimization steps; see Figs. 3.6–3.17. These variations clearly illustrate the challenge of approximating a complicated objective function by a relatively simple approximation, as discussed in Section 2.2.1. Nevertheless, it is interesting to note that the optimization procedure was still capable of identifying multiple optima within the design space.

The initial progress towards a local optimum, $\mathbf{X}_9 = [1°\ 81.5\ \text{kts}\ 170\ \text{ft}]^T$ resulted in a significantly more aggressive approach than the baseline case, $\mathbf{X}_1 = [6°\ 90\ \text{kts}\ 300\ \text{ft}]^T$, consistent with anecdotal reports that a common "operational mitigation" strategy involves an attempt by pilots to "outrun" the developing brownout cloud. The global optimum of the procedure, $\mathbf{X}_{16} = [10.4°\ 91\ \text{kts}\ 100\ \text{ft}]^T$, however, was found in a region of the design space corresponding to considerably steeper approach angles.

The baseline, $\mathbf{X}_1$, local (shallow) optimum, $\mathbf{X}_9$, and global (steep) optimum, $\mathbf{X}_{16}$, are compared in Fig. 3.18. Notice in Fig. 3.18(a) that the local and global optimal approaches, $\mathbf{X}_9$ and $\mathbf{X}_{16}$, exhibit greater velocities over the duration of the maneuver, indicating that they are more aggressive than the baseline maneuver. This latter point is emphasized in Fig. 3.18(b), which shows the pitch angle (i.e., the main rotor shaft tilt) profiles for the three approaches. Notice that the local and global optimal approach pro-

149

files exhibit greater pitch angles than the baseline. In fact, the approximate constraint on pitch angle is active for approach $\mathbf{X}_{16}$, though, because of the formulation as an approximate constraint, the true maximum pitch angle for $\mathbf{X}_{16}$ was slightly less than the maximum allowable of $30°$. The positions of the rotor hub (i.e., longitudinal range and altitude) with respect to the landing point are depicted in Fig. 3.18(c) for the three approaches, and it is clear that the local and global optimal approaches spend less time than the baseline case in close proximity to the final landing point.

3.2.2 Physical Interpretation of the Results

To gain a better understanding of the physical mechanisms at play within the present study, the baseline, local (shallow) optimum, and global (steep) optimum approach profiles were examined in detail. Figure 3.19 shows instantaneous realizations of the flow velocities and cloud development in a longitudinal plane through the flow field for the baseline and local (shallow) optimum approach profiles, and Fig. 3.20 shows a similar comparison for the baseline and global (steep) optimum approach profiles. Because the time-histories of the approach profiles varied drastically, comparisons are made for common stages in the flow developments, regardless of the time at which those flow developments actually occur.

It is instructive to first consider only the flow field. Examining the baseline case (i.e., Fig. 3.19(a)–(e)), it is apparent that the blade tip vortices, seen as concentrated regions of high velocity in the plane, impinge upon the ground and interact with each other to form a "super-vortex" or ground vortex, as noted in prior research (Refs. 9, 42, 44).

150
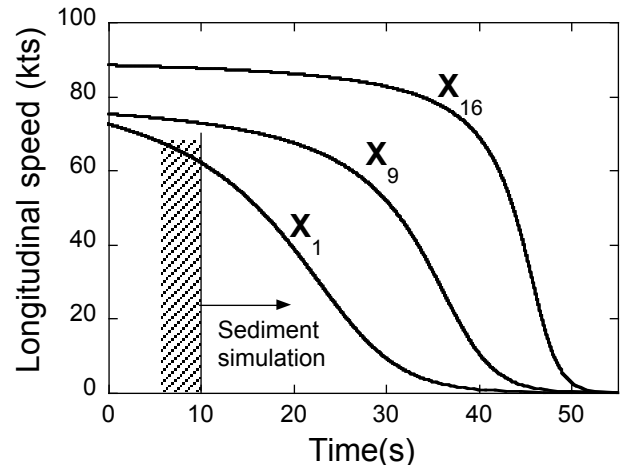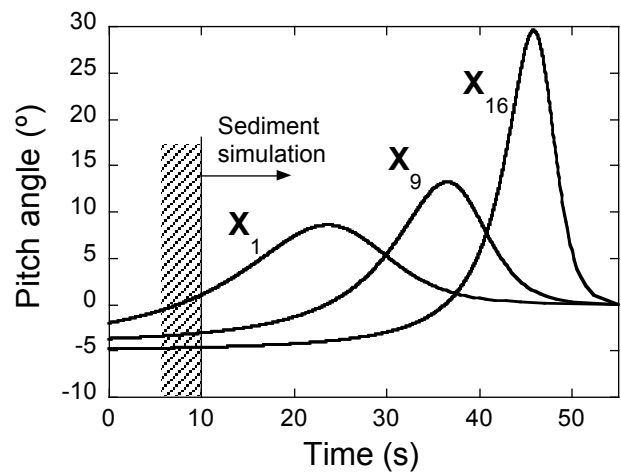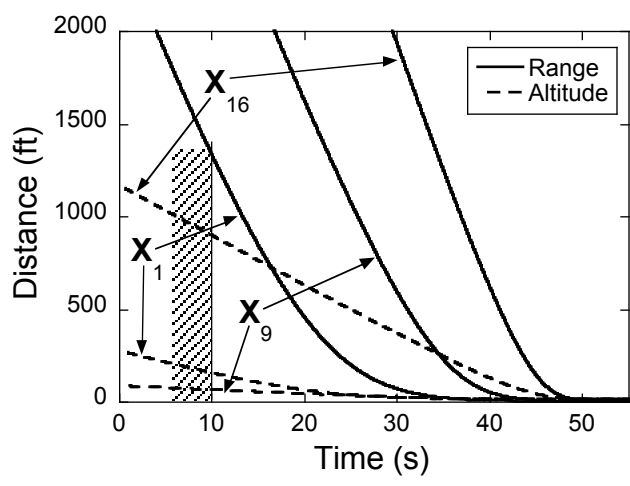
Figure 3.18: Comparison of the (a) velocity profiles, (b) main rotor shaft tilt profiles, and (c) range and altitude profiles for the baseline, $\mathbf{X}_1$, local (shallow) optimum, $\mathbf{X}_9$, and global (steep) optimum, $\mathbf{X}_{16}$, approaches.

The ground vortex begins to form beneath the forward part of the rotor disk (Fig. 3.19(a)) and convects forward (Fig. 3.19(b)–(c)) as the rotor continues into hovering flight. Once the ground vortex has convected forward and restructured (Fig. 3.19(d)) the flow field becomes more representative of that of an in-ground-effect (IGE) hover (Fig. 3.19(e)), in which the blade tip vortices convect along the slipstream boundary and impinge upon the ground.

In examining the results in Figs. 3.19 and 3.20, it is apparent that the initial uplift of particles can primarily be attributed to the ground vortex. This observation is reasonable because the ground vortex contains multiple individual tip vortices that interact to form concentrated regions of circulation that are directly responsible for mobilizing and uplifting large amounts of dust. It is interesting to notice, however, that the rate and geometry of the brownout cloud as it develops can vary significantly depending on the characteristics of the flow field. A comparison of the flow fields and brownout clouds for the baseline design, local (shallow) optimum design, and global (steep) optimum design reveals some interesting differences.

Figure 3.19(a) and (f) depicts the instant at which the vortex wake is beginning to form a ground vortex for the baseline and local (shallow) optimum cases. Notice that the optimum case lags the baseline (i.e., the ground vortex forms later in the approach) by about 10 s. This lag will remain throughout the development of the brownout cloud. Notice also that the ground vortex tends to trap dust and uplift it into the flow field for both cases. The ground vortex continues to convect forward to distances about 45–60 ft forward from the hub location in Fig. 3.19(b)–(c) and (g)–(h). Notice that the ground
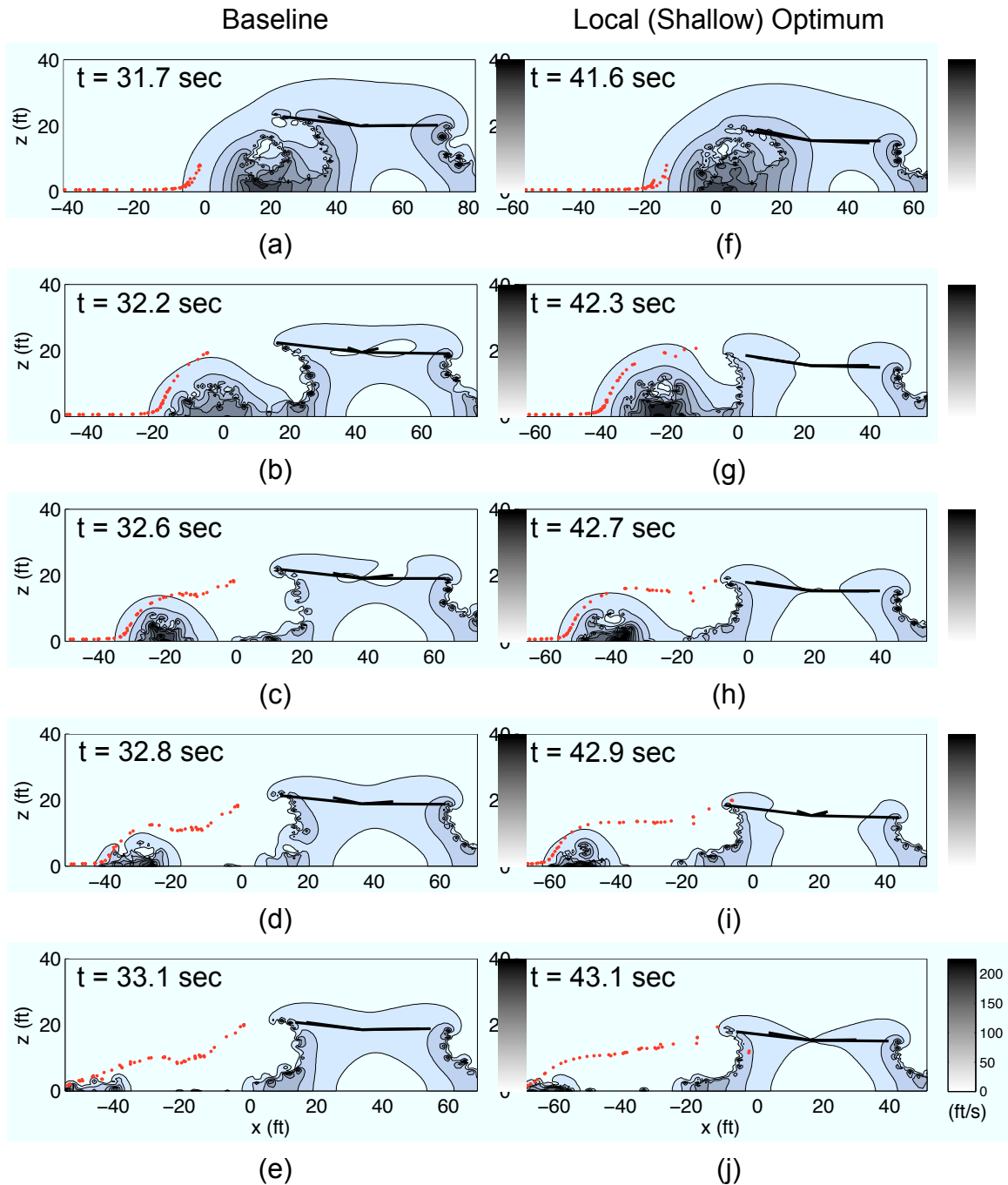
Figure 3.19: Instantaneous realizations of the velocity magnitudes and developing cloud in a longitudinal plane through the flow field for (a)–(e) the baseline, $\mathbf{X}_1$, and (f)–(j) the local (shallow) optimum, $\mathbf{X}_9$, approach profiles. The motion of the rotor over the ground is from right to left. Particles are enlarged for illustrative purposes.

153

vortex continues to entrain the dust particles into more quiescent regions of the flow field for both the baseline and local (shallow) optimum approach profiles.

The ground vortex restructures as it reaches distances about 75–90 ft forward from the hub location in Fig. 3.19(d)–(e) and (i)–(j). For both approach profiles, the restructuring of the ground vortex serves to diminish the regions of concentrated circulation that resulted from the interacting tip vortices. Notice that the particles that had been uplifted previously are now being entrained in the flow towards the rotor disk. The dust particles may, after some time, be reingested through the rotor disk, leading to a phenomenon known as reingestion bombardment (Ref. 7). This phenomenon is known to precipitate a sharp increase in the volume and severity of the developing brownout cloud; it is seen to be beginning in Fig. 3.19(j). Notice, once again, that the optimum case still lags the baseline case by about 10 s. From a practical standpoint, this latter result indicates that a pilot may minimize the duration spent in brownout conditions by adopting specific landing strategies.

Similarly, Fig. 3.20(a) and (f) depicts the instant at which the vortex wake is impinging on the ground directly beneath the leading edge of the main rotor. Notice that the optimum case once again lags the baseline, this time by about 18 s. As identified previosuly, a ground vortex is beginning to form for the baseline case. It is interesting to notice, however, that a ground vortex has not yet begun to form for the optimum case, the lack of which results in the uplift of significantly less sediment. The differences in the flow fields continue to be pronounced as the maneuver progresses. For the baseline case, the ground vortex continues to convect forward to distances about 45–60 ft forward from

Baseline   Global (Steep) Optimum
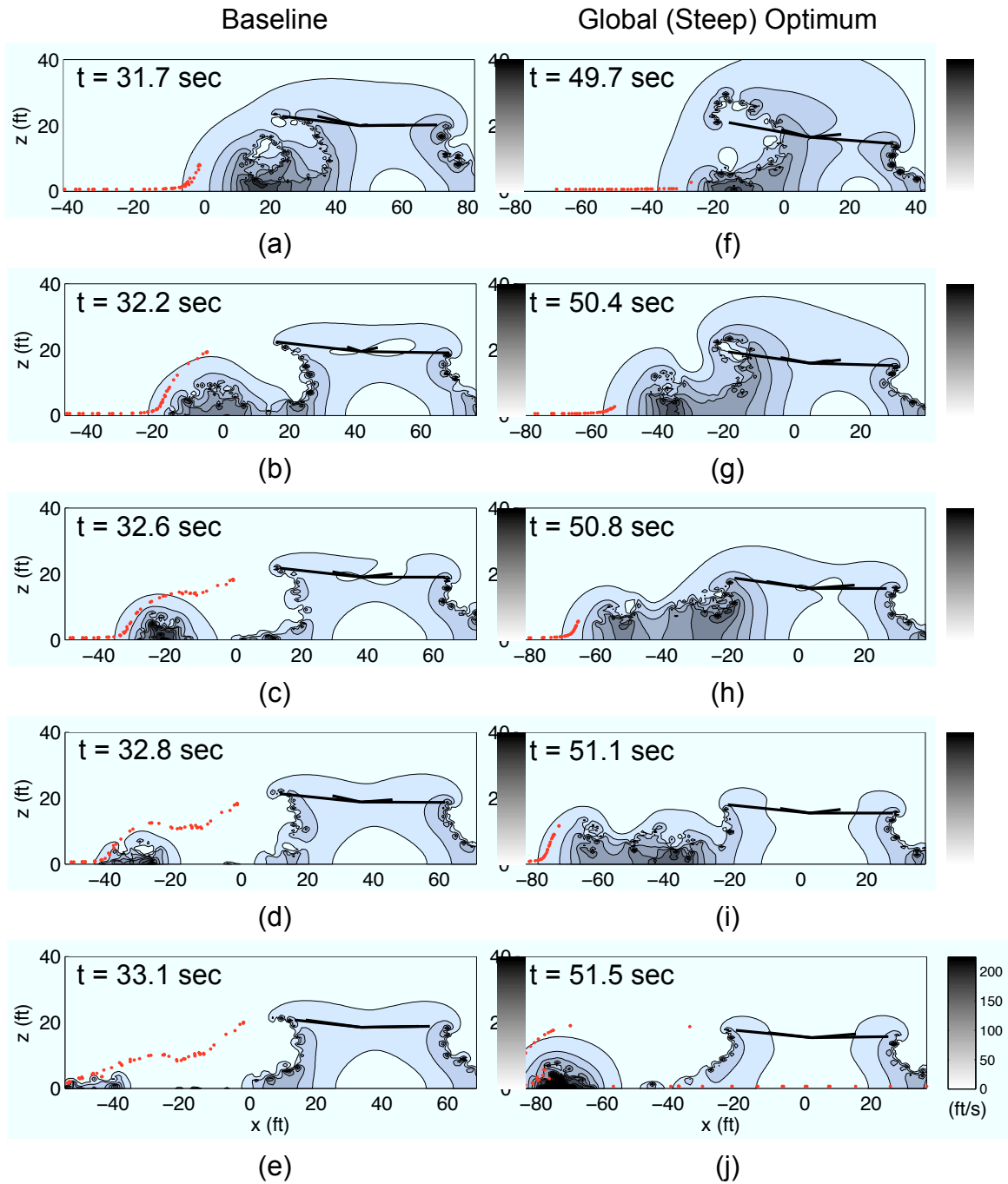
Figure 3.20: Instantaneous realizations of the velocity magnitudes and developing cloud in a longitudinal plane through the flow field for (a)–(e) the baseline, $\mathbf{X}_1$, and (f)–(j) the global (steep) optimum, $\mathbf{X}_{16}$, approach profiles. The motion of the rotor over the ground is from right to left. Particles are enlarged for illustrative purposes.

155

the hub location in Fig. 3.19(b)–(c), and the ground vortex continues to entrain the dust particles into more quiescent regions of the flow field. For the optimum case, however, the formation of a ground vortex in Fig. 3.20(g) is followed by the formation of a second ground vortex; see Fig. 3.20(h). In this case, the primary ground vortex may be seen approximately 60 ft forward of the hub position, the secondary ground vortex may be seen approximately 25 ft forward of the hub position.

The ground vortex for the baseline case restructures as it reaches distances about 75–90 ft forward from the hub location in Fig. 3.19(d)–(e), although a very different effect is seen for the optimum. For the optimum case, the secondary ground vortex convects forward at a faster rate than the primary vortex, Fig. 3.20(i), and the two ground vortices interact to form a larger, single super-vortex, Fig. 3.20(j). Notice that this feature of the flow causes the initial uplift of particles to occur at distances much farther from the rotor than for the baseline case. This difference in the developing cloud geometry is an important one because it leaves the global (steep) optimum with a clear region in close proximity to the landing helicopter.

These results illustrate the drastic effect that the approach profile can have on the resulting brownout cloud, specifically on the timing of its development and on its overall geometry. While the flow developments resulting from the baseline and local (shallow) optimum approach profiles appear similar in nature, the local (shallow) optimum approach profile encounters these developments much later in the approach (about 10 s later) than the baseline approach profile. This means that a pilot who adopts the local (shallow) optimum approach profile will spend significantly less time in brownout condi-

156

tions. The flow developments occur even later for the global (steep) optimum approach profile. Additionally for the global (steep) optimum approach profile, the formation of a secondary ground vortex leads to a brownout cloud that forms at greater distances from the pilot, leaving the near regions significantly less obscured.

3.2.3 Comparison of Observed Flow Features with Experimental Results

The foregoing results clearly indicate the potential for significant brownout mitigation through modifications to the baseline approach profile. The mechanism for mitigation is through the effect that the approach profile has on the flow field, particularly on the way in which the vortex wake interacts with the ground. In this regard, it should be recognized that the FVM is fundamentally an inviscid approach (and, therefore, it is vorticity-preserving) and so the present results must be interpreted within this context.

To further explore these effects, a comparison study was performed between the FVM and prior experimental results. In Ref. 42, an experimental study into the aerodynamics of an isolated rotor in ground effect at low advance ratios is presented. The study included flow visualization as well as performance measurements. An outcome of the study was the identification of approximate boundaries of the recirculation and ground vortex flow regimes, as depicted in Fig. 3.21. Flow visualization images from Ref. 42 are shown side-by-side with FVM simulation results in Fig. 3.22, and it is apparent that the FVM, at least qualitatively, is capable of modeling these flow regimes. Notice that the nondimensionalized height and velocities for these cases were similar, although the experiments were performed at subscale and the FVM simulations were performed for
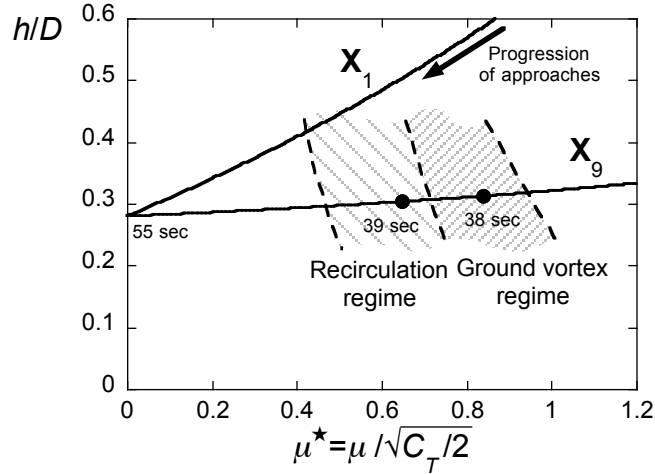
Figure 3.21: Approximate boundaries of the recirculation and ground vortex flow regimes (from Ref. 42). Overlaid on the axes are the baseline, $\mathbf{X}_1$, and local (shallow) optimum, $\mathbf{X}_9$, approach profiles.

the full-scale rotor design used in the optimization study.

The flow regimes identified in Fig. 3.21 are shown relative to the nondimensionalized rotor hub height, h/D, and normalized advance ratio, $\mu^\star$. Notice that the normalized advance ratio is the given by

$$\mu^\star = \frac{\mu}{\lambda_h} = \frac{\mu}{\sqrt{C_T/2}} \tag{3.21}$$

where μ is the advance ratio, λ_h is the hover inflow ratio, and C_T is the rotor coefficient of thrust. As such, $\mu^\star$ may be directly related to the wake skew angle, i.e.,

$$\chi = \tan^{-1}\left(\frac{\mu}{\lambda_h}\right) = \tan^{-1}\left(\mu^\star\right) \tag{3.22}$$

as shown in Fig. 3.23. The wake skew angle increases as $\mu^\star$ increases, and the wake will trail farther behind the rotor system, preventing the development of the ground vortex and flow recirculation regimes ahead of the rotor.

(a) Recirculation regime

(b) Ground vortex regime
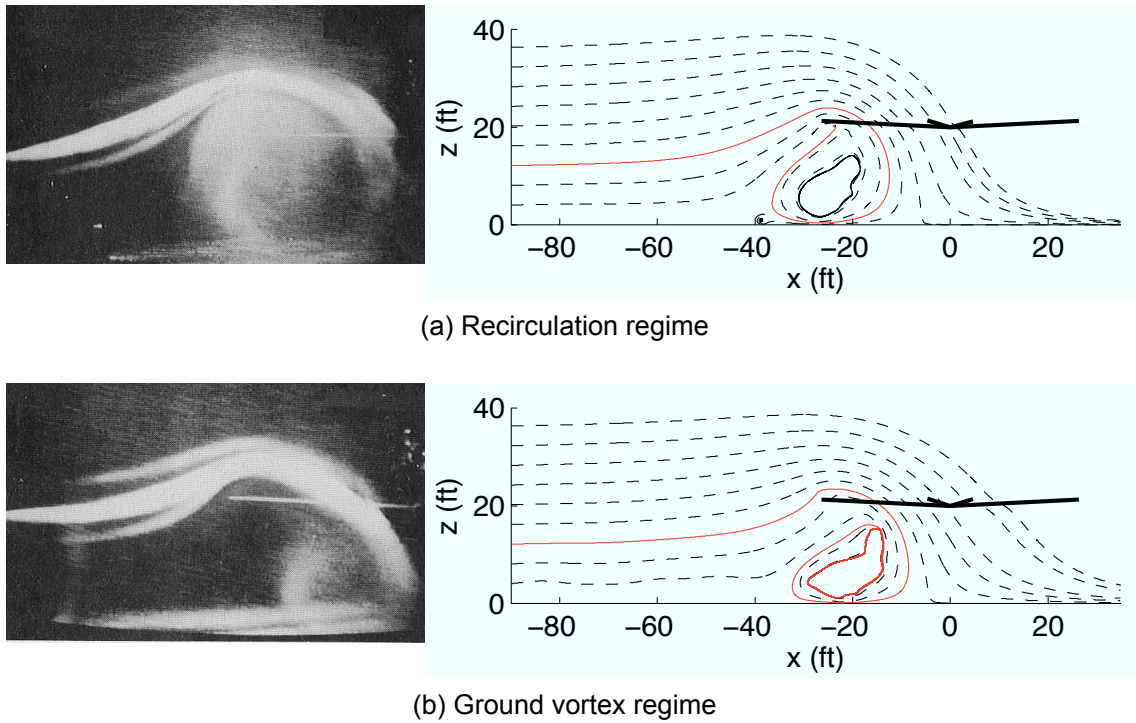
Figure 3.22: Comparison of flow patterns for the (a) recirculation regime and (b) ground vortex regime as illustrated by experimentation (from Ref. 42) and simulation using the FVM.
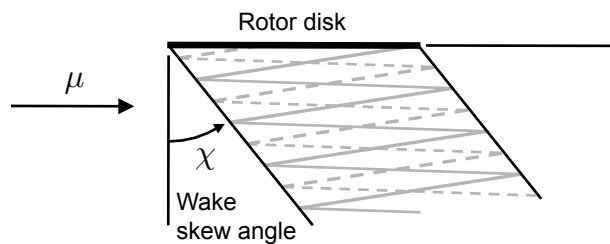
Figure 3.23: Schematic diagram of the rotor wake skew angle (adapted from Ref. 139).

159

It is important to note that the flow regimes given in Fig. 3.21 and the results presented in Fig. 3.22 are for steady flight at a constant rotor height above the ground. For the case of a maneuver, however, it can not be assumed that these flow regimes are applicable. The baseline, $\mathbf{X}_1$, and local (shallow) optimum, $\mathbf{X}_9$, approach profiles are overlaid on the axes in Fig. 3.21, and it is apparent that the local (shallow) optimum approach, $\mathbf{X}_9$, passes directly through the steady-flight ground vortex and recirculation flow regimes. Notice that the normalized height and normalized advance ratio at 38 and 39 s into the approach are within the steady-flight ground vortex and recirculation flow regimes, respectively. Instantaneous realizations of the velocity magnitudes in a longitudinal plane through the flow field are shown in Fig. 3.24 for these two instants of the approach. The results show that the flow field resulting from the maneuver is significantly different from what would be expected in steady flight at the same normalized height and normalized advance ratio. This difference can be attributed to the prior time history or "hereditary effects" of the rotor wake over the course of the maneuver.

3.2.4 Operational Interpretation of the Results

Because of the critical role that the formation of a ground vortex plays in the development of a brownout cloud, the initiation of the ground vortex was examined for each of the approach profiles. Figure 3.25 shows the combination of normalized height, h/D, and normalized advance ratio, $\mu^\star$, at which the vortex wake is impinging on the ground directly beneath the rotor hub for each approach calculated during the optimization. Although the wake may impinge upon the ground at longitudinal locations aft of the main
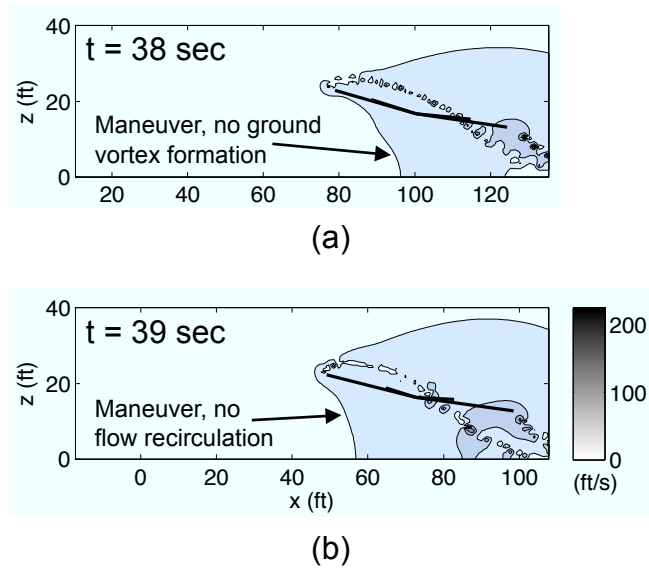
Figure 3.24: Instantaneous realizations of the flow velocity magnitudes in a longitudinal plane through the flow field for $\mathbf{X}_9$ at (a) 38 s and (b) 39 s into the approach.
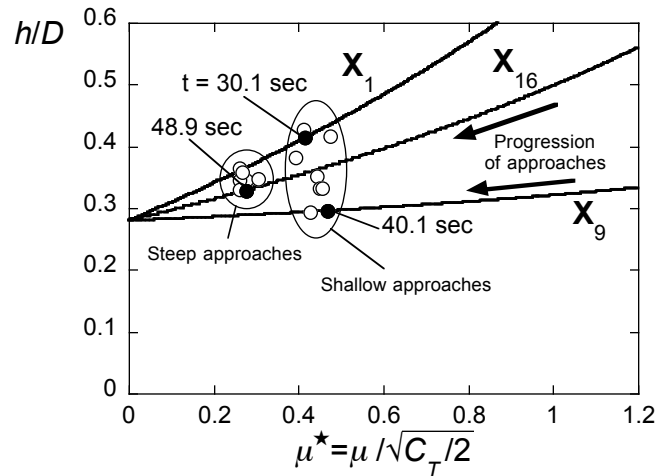
Figure 3.25: Flight conditions for the instant at which the vortex wake is impinging on the ground directly beneath the rotor hub. Overlaid on the axes are the baseline, $\mathbf{X}_1$, local (shallow) optimum, $\mathbf{X}_9$, and global (steep) optimum, $\mathbf{X}_{16}$, approach profiles.

rotor hub position early in the approach (i.e., when the rotor is operating at higher advance ratios), the wake skew angle is reduced as the rotor advance ratio decreases over the course of the approach. This longitudinal deceleration of the rotor causes the location of wake impingement on the ground relative to the rotor hub to move forward. A ground vortex typically forms just after the longitudinal location of wake impingement approaches the main rotor hub. The approach profiles for the baseline, shallow optimum, and steep optimum cases are overlaid on the axes, and solid markers identify these three approaches for clarity.

Figure 3.26 shows instantaneous distributions of the velocity magnitudes in a longitudinal plane through the flow field for the moment at which the wake is impinging on the ground directly beneath the main rotor hub for the baseline, shallow optimum, and steep optimum cases. The concentrated bundling of the wake that occurs as it impinges on the ground will develop into a ground vortex and convect forward from the rotor, as shown previously in Figs. 3.19 and 3.20. Notice that, although these three approaches are drastically different, the flow fields in Fig. 3.26 show remarkable similarity.

Notice in Fig. 3.25 that the flight conditions for which the wake impinges on the ground directly beneath the rotor hub show clear trends for shallow and steep approach angles, i.e., that the nondimensional heights and velocities appear in two fairly distinct clusters. Figure 3.27 shows the approaches corresponding to each of these clusters in more detail. The normalized heights and velocities corresponding to all of the shallow and all of the steep approaches are plotted in Fig. 3.27(a) and (b), respectively. By marking the conditions before and after the wake impingement location reaches the same longitudinal

Baseline

t = 30.1 sec

Impinging wake below
rotor hub, will form
ground vortex

(a)

Local (shallow) optimum

t = 40.1 sec

Impinging wake below
rotor hub, will form
ground vortex

(b)

Global (steep) optimum

t = 48.9 sec

Impinging wake below
rotor hub, will form
ground vortex

(ft/s)

(c)
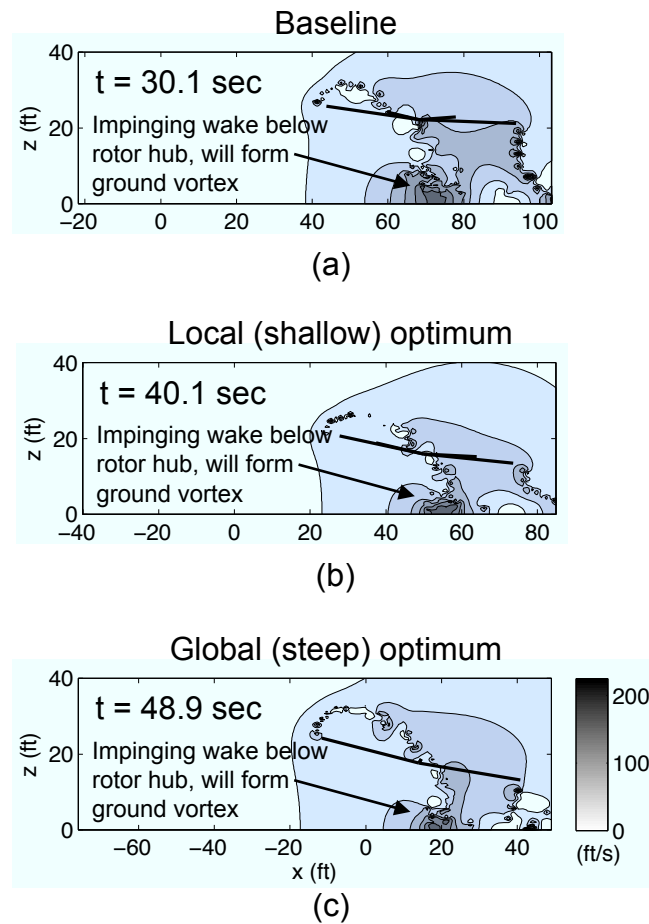
Figure 3.26: Instantaneous realizations of the velocity magnitudes in a longitudinal plane through the flow field for the moment at which the wake is impinging on the ground directly beneath the main rotor hub for the (a) baseline, $\mathbf{X}_1$, (b) local (shallow) optimum, $\mathbf{X}_9$, and (c) global (steep) optimum, $\mathbf{X}_{16}$, approach profiles.

Shallow approaches

Wake trails rotor in direction of flight

Ground vortex forms and convects forward

Progression of approaches

Approximate flight conditions for ground vortex formation

h/D

$\mu^{\star} = \mu / \sqrt{C_T/2}$

(a)

Steep approaches

Wake trails rotor in direction of flight

Ground vortex forms and convects forward

Progression of approaches

Approximate flight conditions for ground vortex formation

h/D

$\mu^{\star} = \mu / \sqrt{C_T/2}$

(b)

Figure 3.27: Flight conditions for the instant at which the vortex wake is impinging on the ground directly beneath the rotor hub for (a) shallow and (b) steep approach profiles.

position as the main rotor hub, approximate boundary lines begin to emerge for both types of approaches. Prior to crossing these boundaries, the wake trails behind the rotor in the direction of flight because of the larger wake skew angles at high values of $\mu^\star$. As an approach-to-landing maneuver is continued beyond the conditions marked by the boundaries, the wake skew angle becomes smaller, a ground vortex forms, and brownout conditions are likely to develop quickly (as illustrated in Figs. 3.19 and 3.20). As such, a pilot who is executing an approach over loose dust may need to expedite his/her landing upon entering these flight regimes.

The results in Fig. 3.28 are similar to Fig. 3.27, but they explicitly relate the flight conditions conducive to ground vortex formation with the time at which brownout conditions are first encountered. This instant is mathematically defined as the time at which $b(\mathbf{X}, t)$ first becomes nonzero; see Eq. (2.79), i.e., the time at which even the "best region" of the FOV will exhibit some obscuration in the simulation. Flight in brownout conditions is depicted by a dashed line in Fig. 3.28, and it is apparent that the onset of brownout conditions quickly follows the entry into flight conditions within which a ground vortex is likely to form. The close link between brownout and ground vortex formation also suggests that it might be possible to use the latter as a proxy for the former when trying to develop brownout mitigation strategies, i.e., that useful mitigation information could be obtained from wake geometry considerations alone and without the dust cloud modeling.

Figure 3.29 shows four randomly generated approach profiles superimposed on the ground vortex boundaries of Figs. 3.27–3.28. The circles on each trajectory mark the instant at which the wake impinges on the ground directly beneath the rotor hub. The
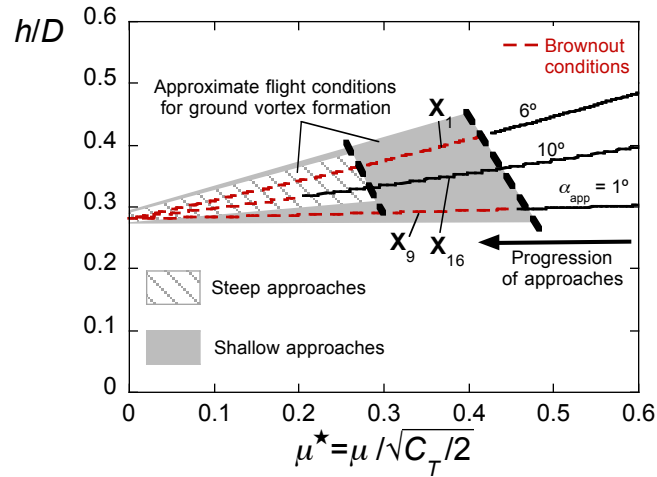
Figure 3.28: The baseline, $\mathbf{X}_1$, local (shallow) optimum, $\mathbf{X}_9$, and global (steep) optimum, $\mathbf{X}_{16}$, approach profiles plotted against the approximate flight conditions for ground vortex formation.
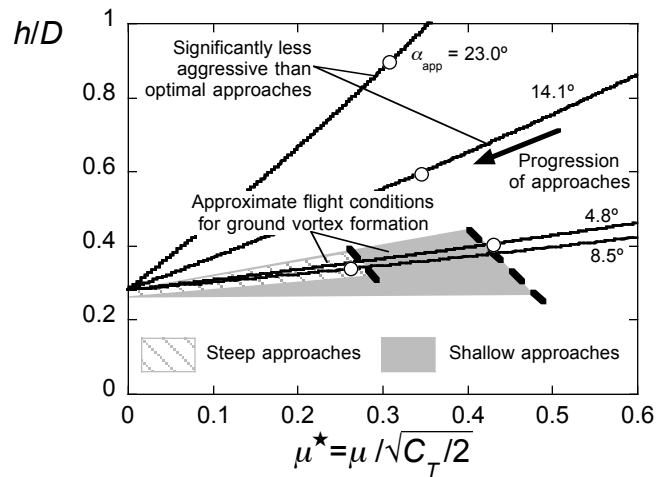
Figure 3.29: Normalized height and normalized advanced ratio for the instant at which the vortex wake is impinging on the ground directly beneath the rotor hub for four randomly-generated approach profiles.

two approaches with $\alpha_{app} = 4.8°$ and $\alpha_{app} = 8.5°$ correspond to shallow (i.e., outrun the developing cloud), and steep (i.e., delay wake impingement on the ground) strategies, respectively. For these two approaches, the instants at which the wake impingement location reaches the same longitudinal position as the main rotor hub are consistent with the boundaries of Figs. 3.27 and 3.28. The other two trajectories, with $\alpha_{app} = 14.1°$ and $\alpha_{app} = 23.0°$, are inconclusive in the sense that the times at which the wake impingement location reaches the same longitudinal position as the main rotor hub are well outside the ground vortex formation regions that are identified in Figs. 3.27–3.28. However, it is conceivable that at least one dashed line could be extended upward and to the left in the figure to provide a predictive boundary for these two trajectories as well.

Upon further examination, it was determined that these two approach profiles represented significantly less aggressive maneuvers that the optimal approaches, and this may also play a role. Clearly, additional simulations would be required to explore the ground vortex development boundaries for higher values of h/D at low $\mu^\star$. This is recommended as future work.

Converting the nondimensional coordinates of Figs. 3.27–3.29 to actual values of height and velocity for the helicopter configuration used in the present study results in the Height-Velocity (H-V) representation of Fig. 3.30, which could be seen as an initial step toward the formal development of operational criteria for brownout mitigation. The regions identified on the diagram would be those where a ground vortex would be expected to form and quickly trigger brownout conditions. While clearly unavoidable, flight within the shaded regions should be as short as possible. The dashed lines that complete the hy-
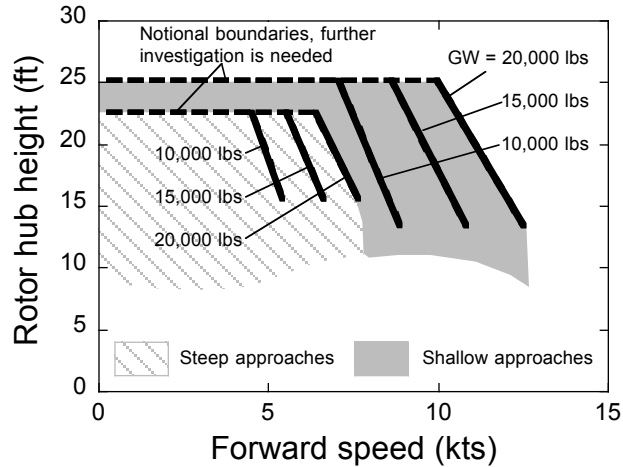
Figure 3.30: A notional H-V diagram for brownout approaches for the helicopter used in the present study.

pothetical brownout H-V diagram are purely notional because there are insufficient data upon which to base better suggestions.

While Fig. 3.30 is based on extensive simulation and solid first-principles physical arguments, a considerable amount of additional research needs to be carried out to determine whether the boundaries in the figure have general validity, how the brownout regions extend beyond the range of heights and velocities considered in the present study, and whether an H-V representation is the best way to draw useful operational brownout boundaries. This research should certainly include piloted simulation, and possibly validation with actual flight test. Even from a pure simulation standpoint, it should be remembered that the present study is based on several significant assumptions, including that: (i) only the main rotor is modeled with no fuselage or tail rotor, (ii) the wake is modeled using a FVM, which is an inviscid method that only approximately captures the physics of ground vortex formation, (iii) the formulation of the approach profile is such that the motion of the rotor hub is prescribed, and blade pitch controls and tip-path-plane

168

motion are based on assumptions on the time-history of rotor thrust (and, therefore, are not necessarily those that an actual pilot would command). Finally, the representation of Fig. 3.30 does not include any information on the severity of the brownout and the expected Usable Cue Environment levels (which would also depend on the characteristics of the sediment bed and on the environmental conditions).

Chapter 4

Brownout Mitigation Through Main Rotor Design

The study presented in Chapter 3 clearly demonstrated the potential for brownout mitigation by trajectory optimization. Implicit in this study, however, was a philosophy that attempted to minimize the effects of brownout *for a given helicopter*. A reasonable follow-on question, however, is whether specific design strategies may be developed to produce rotorcraft with more benign brownout characteristics.

The general objective of the present chapter, therefore, is to propose and demonstrate, through simulation, a systematic procedure to optimize a rotor for brownout mitigation. The specific objectives are:

1. To present a systematic brownout mitigation procedure based on rotor design optimization that incorporates mixed continuous (i.e., blade chord, rotor radius, blade twist rate) and integer (i.e., number of blades) design variables.

2. To present the results of a brownout mitigation study that highlight the mathematical properties of the proposed optimization procedure and the key physical mechanisms involved in the mitigation process.

3. To demonstrate methods for extracting system-level preliminary design guidelines from the optimization data.

4.1 Optimization Methodology

In the present section, brownout mitigation is formulated mathematically as a numerical optimization problem and cast into nonlinear mathematical programming form. Therefore, the procedure consists of finding the value of a vector of design variables, $\mathbf{X}^{4b}$, such that a scalar objective function, $B(\mathbf{X}^{4b})$, is minimized, i.e.,

$$B(\mathbf{X}^{4b}) \rightarrow \min \tag{4.1}$$

subject to:

behavior constraints $\qquad g_j(\mathbf{X}^{4b}) \leq 0 \quad j = 1, \ldots, m \tag{4.2}$

side constraints $\qquad \mathbf{X}^{4b}_{\min} \leq \mathbf{X}^{4b} \leq \mathbf{X}^{4b}_{\max} \tag{4.3}$

Notice that the "4b" superscript denotes a 4-bladed main rotor design. This notation is introduced at this point for consistency with later portions of this chapter, although it should be noted that all rotor designs considered in the present optimization study will be 4-bladed.

4.1.1 Design Vector, $\mathbf{X}^{4b}$

The vector $\mathbf{X}^{4b}$ of design variables is defined as

$$\mathbf{X}^{4b} = \left\{ \begin{array}{c} x_1 \\ x_2 \\ x_3 \end{array} \right\} = \left\{ \begin{array}{c} c \\ R \\ \theta_{tw} \end{array} \right\} \tag{4.4}$$

where c, R, and θ_{tw} are, respectively the blade chord, rotor radius, and effective linear blade twist rate. The baseline design is $\mathbf{X}_1^{4b} = [c_1 \ R_1 \ \theta_{\text{tw},1}]^T = [1.9 \text{ ft} \ 26.8 \text{ ft} \ -18°]^T$.

All the design variables in the present study are subject to side constraints using Eq. (4.3). The rotor radius, R, is constrained as

$$0.9R_1 \leq R \leq 1.1R_1 \tag{4.5}$$

where R_1 is the initial, baseline value. The blade twist rate was similarly constrained as

$$0.9\theta_{\text{tw},1} \leq \theta_{\text{tw}} \leq 1.1\theta_{\text{tw},1} \tag{4.6}$$

where $\theta_{\text{tw},1}$ is the baseline value. The blade chord, c, was approximately constrained as

$$0.5c_1 \leq c \leq 1.5c_1 \tag{4.7}$$

where c_1 is the initial, baseline value. Notice that the constraints on blade chord are more relaxed than those on the rotor radius and blade twist rate. The relaxed constraints were chosen to accommodate the future inclusion of the number of blades, N_b, as a design variable (recall that, for the present study, $N_b = 4$). More specifically, the blade chord constraints were formulated as

$$c_1^{6b} - \Delta c \leq c \leq c_1^{3b} + \Delta c \tag{4.8}$$

where c_1^{3b} and c_1^{6b} are chord values that correspond to the same solidity, σ, as the baseline

rotor design for 3-bladed and 6-bladed rotor designs with radius R_1, respectively, and where $\Delta c = 0.1 c_1^{3b}$. In dimensional terms, the side constraints are

$$1.0 \text{ ft} \leq c \leq 2.8 \text{ ft} \tag{4.9}$$

$$24.1 \text{ ft} \leq R \leq 29.5 \text{ ft} \tag{4.10}$$

$$16.2° \leq \theta_{\text{tw},1} \leq 19.8° \tag{4.11}$$

4.1.2 Objective Function, $B(\mathbf{X}^{4b})$

The brownout objective function, $B(\mathbf{X}^{4b})$, has been described in detail in Section 2.3 and is mathematically defined as

$$B(\mathbf{X}^{4b}) = \int_{t_1}^{t_2} b(\mathbf{X}^{4b}, t) dt \tag{2.80}$$

where t_1 is the starting time and t_2 is the ending time of the maneuver and the integrand is

$$b(\mathbf{X}^{4b}, t) = \min \left[\sum_{\phi_P = i}^{i+25°} \sum_{\theta_P = j}^{j+40°} n_P(\phi_P, \theta_P, t) \right] \tag{2.79}$$

$$\text{for} \quad \begin{array}{c} -50° \leq i \leq -20° \\ -90° \leq j \leq 50° \end{array}$$

where $n_P(\phi_P, \theta_P, t)$ is the number of dust particles in the one-degree solid angle centered at ϕ_P and θ_P at time t, and the values selected for i and j restrict the scan area to the "critical region for visual cues" that was identified in Fig. 2.30

4.1.3 Behavior Constraint, $g(\mathbf{X}^{4b})$

The only behavior constraint placed on the design requires that the blade loading coefficient, C_T/σ, be less than or equal to its baseline value, $(C_T/\sigma)_1$, to prevent designs that might compromise the propulsive and maneuver margins of the rotor. This constraint is written as

$$g(\mathbf{X}^{4b}) = \frac{C_T/\sigma}{(C_T/\sigma)_1} - 1 \le 0 \tag{4.12}$$

4.1.4 Approximate Problem Formulation

Because of the high computational cost of a brownout simulation, the optimization problem cannot be solved by directly connecting the simulation and the optimizer. Instead, the baseline optimization problem is converted into a sequence of computationally inexpensive approximate optimization problems in which the objective function and behavior constraint are replaced by approximations that are updated at each step of the sequence. These approximations may have multiple minima within the design space, so they are solved using a Genetic Algorithm (GA).

If the GA optimizer were directly connected to the simulation, the computational cost would be prohibitive. Consider, for example, that a typical value for the number of chromosomes in an initial population is 10 times the number of design variables. A reasonable initial population, in this case, would therefore consist of 40 chromosomes. The "fitness" (i.e., the objective function value) for each chromosome is then calculated, parents are selected, and a new generation is created. Typically the new generation consists of the same number of chromosomes as the previous, meaning that each generation would

consist of 40 new chromosomes and require 40 more objective function evaluations. In the present study, a reasonable estimate for the computational cost of each function evaluation is approximately one day, meaning that each generation in the procedure would take over a month to populate. In practice, it would be expected for the procedure to take tens of generations to converge. In formulating the optimization as an approximate problem, however, the optimizer acts on the approximate objective function and can evaluate tens of generations in a matter of seconds.

While a variety of approximating functions may be used, the approach of the present work is to replace the objective function, $B(\mathbf{X}^{4b})$, by an approximation based on a Radial Basis Function (RBF) that is generated from the exact objective function evaluations. A general equation for the RBF-based approximate objective function is given in Ref. 131, i.e.,

$$B_{\text{app}}(\mathbf{X}^{4b}) = \sum_{i=1}^{n} \lambda_i \phi \left(||\mathbf{X}^{4b} - \mathbf{X}_i^{4b}|| \right) + p(\mathbf{X}^{4b}) \tag{4.13}$$

where $|| \cdot ||$ is the Euclidean norm, λ is a n-element vector of RBF coefficients where n is the number of designs that have been evaluated exactly, $p(\mathbf{X}^{4b})$ is a low-degree polynomial (typically linear or quadratic), ϕ is a real-valued function called the basic function (which can take many forms), and $\mathbf{X}_i^{4b}$ for $i = 1, ..., n$ is the collection of designs that have been evaluated exactly. In the present study, $p(\mathbf{X}^{4b})$ is linear, i.e.,

$$p(\mathbf{X}^{4b}) = c_0 + c_1 \mathbf{X}^{4b} \tag{4.14}$$

where c_1 is a d-element vector where d is the number of dimensions of the design vector,

$\mathbf{X}^{4b}$, and the basic function is a multiquadric, i.e.,

$$\phi\left(||\mathbf{X}^{4b} - \mathbf{X}_i^{4b}||\right) = \sqrt{1 + \left(\varepsilon\left(||\mathbf{X}^{4b} - \mathbf{X}_i^{4b}||\right)\right)^2} \qquad (4.15)$$

where ε is the RBF constant. The unknowns λ, c_0, c_1, and ε are solved to fit the known, exact objective function values.

The same procedure could be used to approximate the behavior constraint, Eq. (4.12), but a more accurate approximation can be obtained using intermediate design variables. Recall that C_T/σ is a function of radius and chord, i.e.,

$$\frac{C_T}{\sigma} = \frac{T/\left(\rho\pi R^2 \Omega^2 R^2\right)}{(N_b c R)/(\pi R^2)} = \frac{T\pi R}{N_b c \rho \pi \Omega^2 R^4} = f\left(\frac{1}{cR^3}\right) \qquad (4.16)$$

such that C_T/σ is a linear function of an intermediate variable $y = 1/cR^3$. An exact fit to the constraint function can therefore be achieved using

$$g_{\text{app}}(y) = p(y) \qquad (4.17)$$

where $p(y)$ is linear, i.e., the first term in the general equation for the RBF-based approximate constraint function is zero.

It is prudent to impose move limits on the design when formulating the optimization as an approximate problem. In the present study, each new design cannot traverse more than 20% of the design space (covering rotor radius, blade chord, and blade twist ratio) in

176

a single optimization step, i.e.,

$$-0.2\left(R_{\max}-R_{\min}\right) \leq R_k - R_{k-1} \leq 0.2\left(R_{\max}-R_{\min}\right) \tag{4.18}$$

$$-0.2\left(c_{\max}-c_{\min}\right) \leq c_k - c_{k-1} \leq 0.2\left(c_{\max}-c_{\min}\right) \tag{4.19}$$

$$-0.2\left(\theta_{\mathrm{tw,max}}-\theta_{\mathrm{tw,min}}\right) \leq \theta_{\mathrm{tw},k} - \theta_{\mathrm{tw},k-1} \leq 0.2\left(\theta_{\mathrm{tw,max}}-\theta_{\mathrm{tw,min}}\right) \tag{4.20}$$

4.1.5 Additional Designs

To improve the global convergence characteristics of the methodology, additional designs are generated during the course of the optimization based on the maximization of the following objective function

$$F(\mathbf{X}^{4\mathrm{b}}) = \min_{\mathbf{X}_k^{4\mathrm{b}} \in \mathbf{X}_{\mathrm{all}}^{4\mathrm{b}}} \left(\left\|\frac{\mathbf{X}^{4\mathrm{b}} - \mathbf{X}_k^{4\mathrm{b}}}{\mathbf{X}_{\max}^{4\mathrm{b}} - \mathbf{X}_{\min}^{4\mathrm{b}}}\right\|\right) \to \max \tag{4.21}$$

The goal of the procedure is to select a new design, $\mathbf{X}^{4\mathrm{b}}$, that maximizes the nondimensionalized distance from the nearest design, $\mathbf{X}_k^{4\mathrm{b}}$, of the entire inventory of designs for which the objective function has been solved exactly, $\mathbf{X}_{\mathrm{all}}^{4\mathrm{b}}$.

The objective, $F(\mathbf{X}^{4\mathrm{b}})$, is maximized subject to the same side constraints and behavior constraint as the baseline optimization, but it is not subjected to any move limits. The resulting optimization can have multiple minima, therefore, it is also solved using a GA. Because $F(\mathbf{X}^{4\mathrm{b}})$ is computationally simple, the GA solution is still rapid. The designs computed in this way are not necessarily better designs. However, they can improve the mathematical properties of the overall optimization by improving the accuracy of the

approximate objective function and improving the global convergence characteristics.

4.1.6   Summary of the Optimization Procedure

In summary, the computational procedure for brownout mitigation consists of the following steps:

1. Compute the objective function, $B(\mathbf{X}^{4b})$, and constraint, $g(\mathbf{X}^{4b})$, for a baseline and N additional designs. The initial designs need not be close and may be infeasible.

2. Compute the approximations to objective, $B_{\mathrm{app}}(\mathbf{X}^{4b})$, and constraint, $g_{\mathrm{app}}(\mathbf{X}^{4b})$.

3. Solve the approximate optimization problem:

   Find $\mathbf{X}^{4b*}$ such that $B_{\mathrm{app}}(\mathbf{X}^{4b*}) \to \min$

   Subject to:

<u>Behavior Constraint</u>

$$g_{\mathrm{app}}(\mathbf{X}^{4b}) \leq 0$$

<u>Side Constraints</u>

$$0.9 R_1 \leq R \leq 1.1 R_1$$

$$c_1^{6b} - \Delta c \leq c \leq c_1^{3b} + \Delta c$$

$$0.9 \theta_{\mathrm{tw},1} \leq \theta_{\mathrm{tw}} \leq 1.1 \theta_{\mathrm{tw},1}$$

<u>Move Limits</u>

$$-0.2\,(R_{\max} - R_{\min}) \le R_k - R_{k-1} \le 0.2\,(R_{\max} - R_{\min})$$

$$-0.2\,(c_{\max} - c_{\min}) \le c_k - c_{k-1} \le 0.2\,(c_{\max} - c_{\min})$$

$$-0.2\,(\theta_{\text{tw,max}} - \theta_{\text{tw,min}}) \le \theta_k - \theta_{k-1} \le 0.2\,(\theta_{\text{tw,max}} - \theta_{\text{tw,min}})$$

and let $\mathbf{X}^{4b}_{k+1}$ be the optimum for the approximate problem.

4. Compute $B(\mathbf{X}^{4b}_{k+1})$ and $g(\mathbf{X}^{4b}_{k+1})$. If: (i) the design is feasible, (ii) the new design, $\mathbf{X}^{4b}_{k+1}$, is close to the previous design, $\mathbf{X}^{4b}_{k}$, within a specified tolerance, and (iii) the objective function, $B(\mathbf{X}^{4b}_{k+1})$, is also close to $B(\mathbf{X}^{4b}_{k})$ within a specified tolerance, assume that the sequence of solutions of the approximate problems has converged to the solution of the original optimization problem, and terminate the procedure. Otherwise, add the solution, $\mathbf{X}^{4b}_{k+1}$, of the approximate optimization problem to the current solution set, update the approximations, and repeat Step 2. The optimization procedure can also be terminated early if a sufficient reduction of the objective function, $B(\mathbf{X}^{4b})$, has been achieved.

5. For every two executions of Step 2, compute an additional design based on Eq. (4.21).

There is some flexibility in the procedure summarized above. For example, if multiple computers are available to perform brownout calculations for different designs, and they complete the calculations at different times, the approximations can be constructed with whatever designs are available at that time. Such procedural modifications do not affect the overall optimization in any significant way.

Similarly, if designs are available from previous optimizations, or are formulated outside the optimization procedure (perhaps they are available from previous parametric studies, or are simply formulated to take advantage of computers that are idle at the time), they can all be used in the optimization. While not all designs may directly represent improvements, they all contribute to improving the accuracy of the approximations to the objective function and behavior constraints. In this sense, the procedure is very robust.

4.1.7 Sizing the Brownout Cloud Model

Because of computational considerations, the present study required a "design model" rather than a comprehensive "analysis model" to ensure efficient solution of the optimization problem. As such, the proper sizing of the brownout simulation (through the number of particle layers in the sediment bed) was examined in a sensitivity study. While maximizing the number of particle layers certainly maximizes the fidelity of the simulation and may be necessary for a detailed analysis of the finer details of the brownout cloud, it simultaneously increases the computational and file storage cost of each objective function evaluation. It is, therefore, desirable to select a sediment bed depth that provides only enough particles to achieve consistent relative comparisons between competing rotor designs. To this end, a preliminary sensitivity study was conducted to determine a suitable number of particle layers for the sediment bed.

To examine these effects, the number of layers of particles in the initial sediment bed was successively increased (the time between particle layer "activation" was adjusted accordingly to prevent all the particle layers from being entrained at nearly the same

instant), and the objective function values for two rotor designs (one 3-bladed and one 6-bladed, $B(\mathbf{X}^{3b})$ and $B(\mathbf{X}^{6b})$, respectively) were computed. The C_T/σ of the rotor designs was matched. A relative comparison of the brownout severity between the two rotor designs was calculated, $B(\mathbf{X}^{3b})/B(\mathbf{X}^{6b})$. The number of particle layers in the sediment bed ranged from 11 to 49, at which point the computational cost (i.e., run time), the memory requirements for tracking the particles, and the file storage costs (well over 100 GB per evaluation) became prohibitive. The comparison of brownout severity at 49 particle layers was assumed to be the most representative, and the relative error for other sediment bed depths was calculated, i.e.,

$$\text{Relative Error} = \left| \frac{\left(\frac{B(\mathbf{X}^{3b})}{B(\mathbf{X}^{6b})}\right)_{n \text{ layers}} - \left(\frac{B(\mathbf{X}^{3b})}{B(\mathbf{X}^{6b})}\right)_{49 \text{ layers}}}{\left(\frac{B(\mathbf{X}^{3b})}{B(\mathbf{X}^{6b})}\right)_{49 \text{ layers}}} \right| \tag{4.22}$$

An assessment of the relative storage cost versus the relative error for varying sediment bed depths is shown in Fig. 4.1, and it is apparent that 20–25 particle layers provides a reasonable trade between storage cost and simulation fidelity. To ensure that the simulations were of suitable fidelity, however, 35 particle layers was chosen as the sediment bed depth for the present study. Although the storage cost is perhaps less important than the computational cost and memory considerations, it is used as the basis for comparison in this case because it is unaffected by any residual workload on the machine.

4.1.8 Assumptions and Limitations

A number of key assumptions are included in the present work:
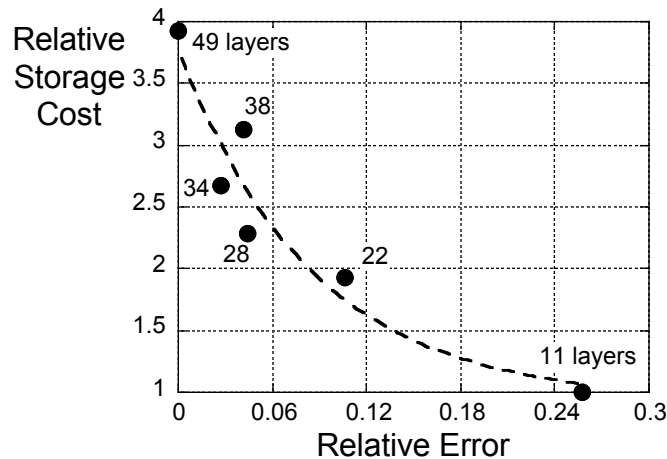
Figure 4.1: Relative storage cost versus relative error for varying sediment bed depths.

1. Only the main rotor is modeled (i.e., the effects of the fuselage and tail rotor are ignored), and the flow is modeled using an inviscid method (i.e., a FVM).

2. From a flight dynamics perspective, the formulation of the approach profile involves only a simple prescription of the linear motion of the rotor. The angular motion, i.e., Eq. (3.11), is only an approximation of the motion that would result from the prescribed linear motion.

3. The rotor controls at each time step are determined for a prescribed thrust (i.e., there is no pilot model and no inverse simulation procedure to determine the control positions for the given maneuver).

4. From the standpoint of the dust cloud simulation, the brownout model assumes a one-way coupling of the air and dust particles (i.e., the air affects the dust particles but the particles do not have an impact on the fluid flow).

5. The dust cloud simulation model includes only monodisperse dust particles, and the

total number of particles in the initial sediment bed is, in comparison with an actual brownout cloud, realtively small (although the sensitivity study indicated this was sufficient for the present analysis).

4.2 Results

This section presents the results of a brownout mitigation study for a medium-lift, single main rotor helicopter executing a visual approach to landing. In the present case, mitigation strategies are developed through main rotor design, i.e., the specifics of the approach-to-landing profile are unchanged. The baseline main rotor design includes four rectangular planform blades with a 26.8 ft radius, 1.9 ft chord, and $18°$ of linear nose-down twist. Only the main rotor is modeled.

Much of the simulation work was performed on an Apple MacPro work station, and the cloud projection and assessment routines were parallelized via MPI (Message Passing Interface). The dust cloud model was executed on a custom machine with a NVIDIA Tesla C2050 GPU, and it was parallelized for GPU execution using the CUDA parallel computing architecture. Each objective function evaluation required approximately 12–48 hours (the exact time depended on the particulars of the simulation and the computing load at the time) from the initial setup to the point that the objective function could be calculated for the brownout cloud. Each case required approximately 100 GB of disk storage space.
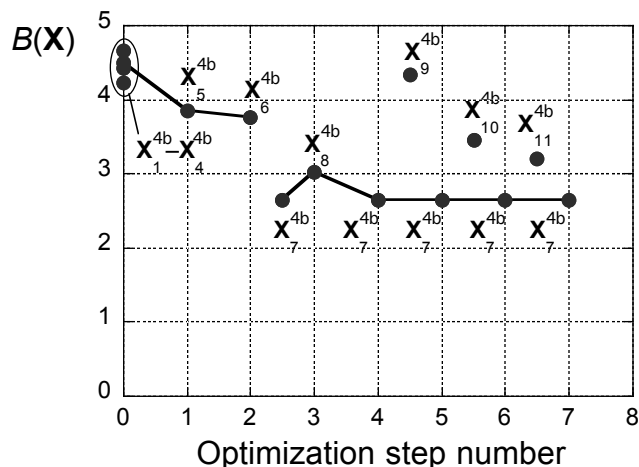
Figure 4.2: Optimization history, i.e., objective function value versus optimization step number.

4.2.1 Optimization Results

A summary of the progression of the optimization procedure is given in Fig. 4.2, and two-dimensional contour maps through the three-dimensional approximate objective function, $B_{\text{app}}(\mathbf{X}^{4b})$, are shown in Figs. 4.3–4.9. Notice that the designs evaluated over the course of the procedures are depicted in the contour maps as circles and the optimal designs are denoted by diamonds. Only three values are shown for θ_{tw}, and the designs are plotted for the closest θ_{tw} value. In some instances, multiple designs may be overlaid in this representation if they have the same values for c and R, and similar values for θ_{tw}. A listing of all of the function evaluations is provided in Table 4.1.

The rotor designs described by $\mathbf{X}_1^{4b}$–$\mathbf{X}_4^{4b}$ were the initial runs needed to explore the design space before beginning any formal optimization steps. The rotor designs described by $\mathbf{X}_5^{4b}$–$\mathbf{X}_6^{4b}$ (i.e., optimization steps 1 and 2) show the initial progress of the optimization procedure, and they clearly resulted in a reduction of the objective function. It was apparent that the optimization methodology was seeking to reduce blade chord, c, increase
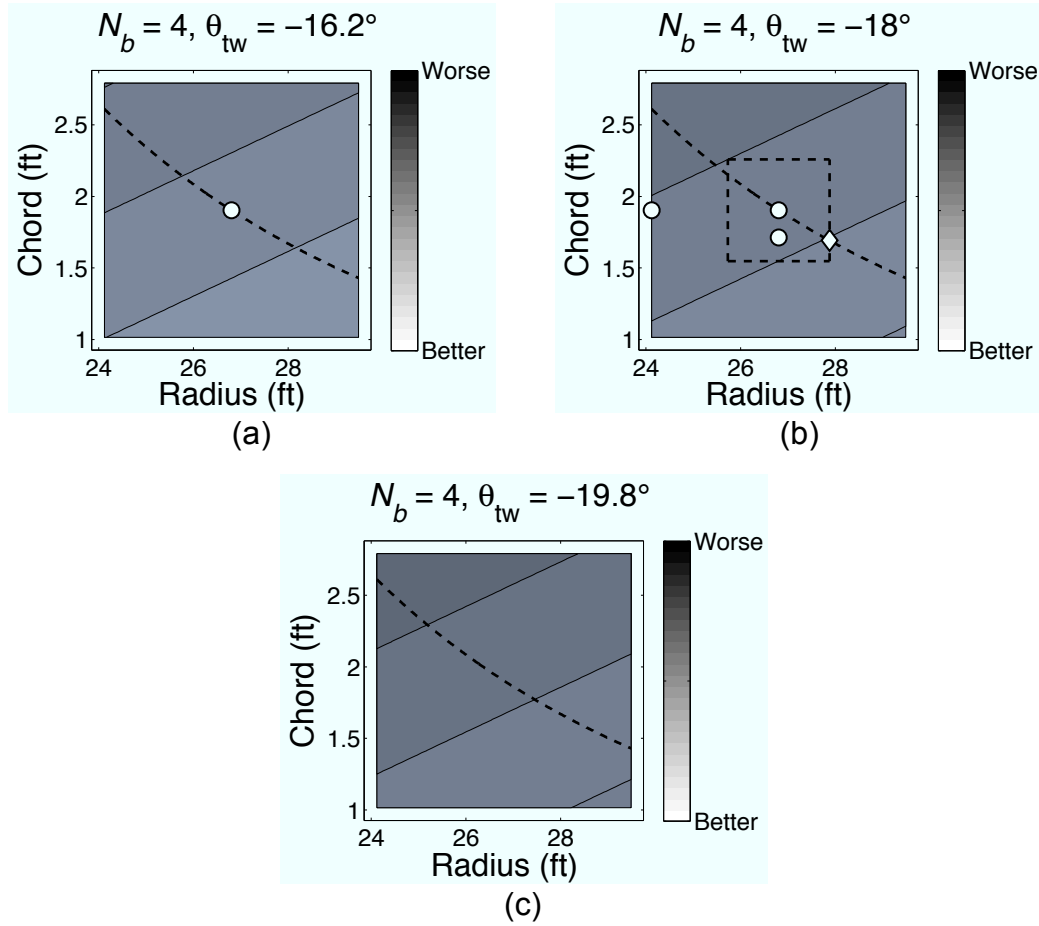
Figure 4.3: Two-dimensional contour maps through the three-dimensional approximate objective function, $B_{\text{app}}(\mathbf{X}^{4b})$, for the first optimization step. Move limits are shown as dashed lines, and the region of the design space that satisfies the behavior constraint on C_T/σ is above the curved dashed line.
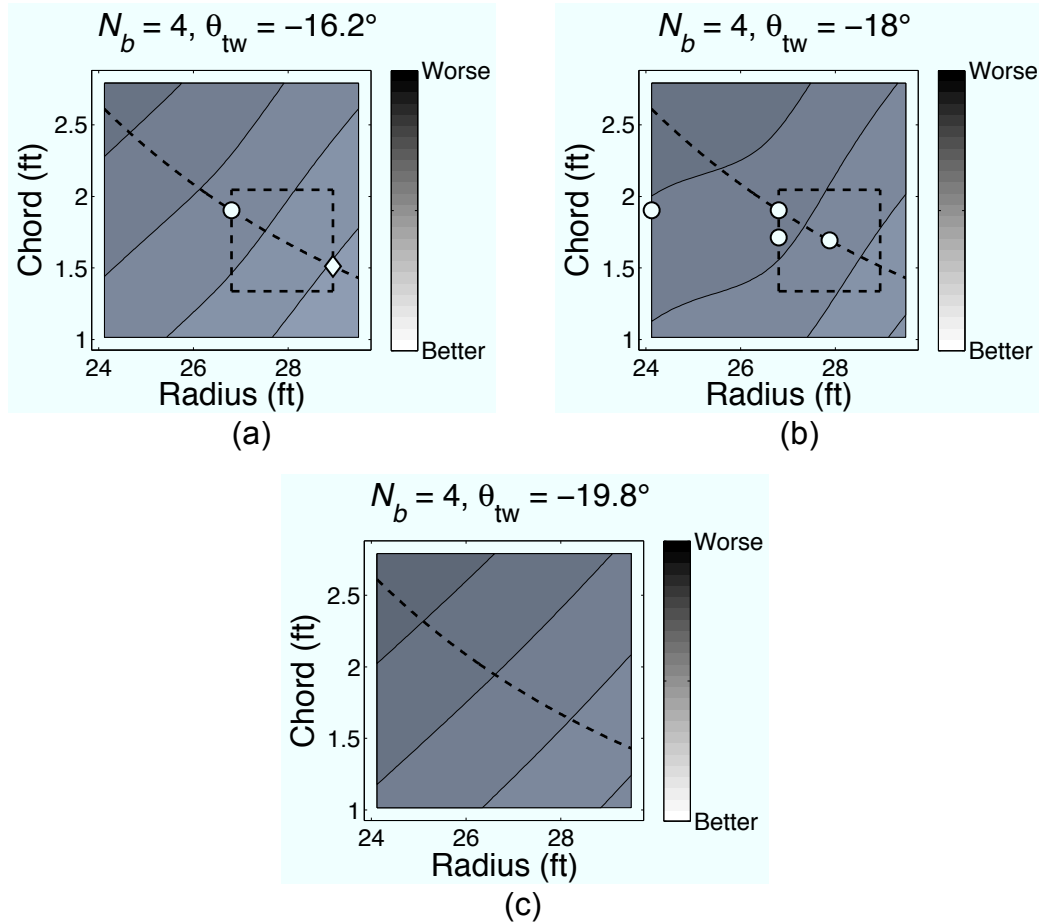
Figure 4.4: Two-dimensional contour maps through the three-dimensional approximate objective function, $B_{\mathrm{app}}(\mathbf{X}^{4\mathrm{b}})$, for the second optimization step. Move limits are shown as dashed lines, and the region of the design space that satisfies the behavior constraint on C_T/σ is above the curved dashed line.
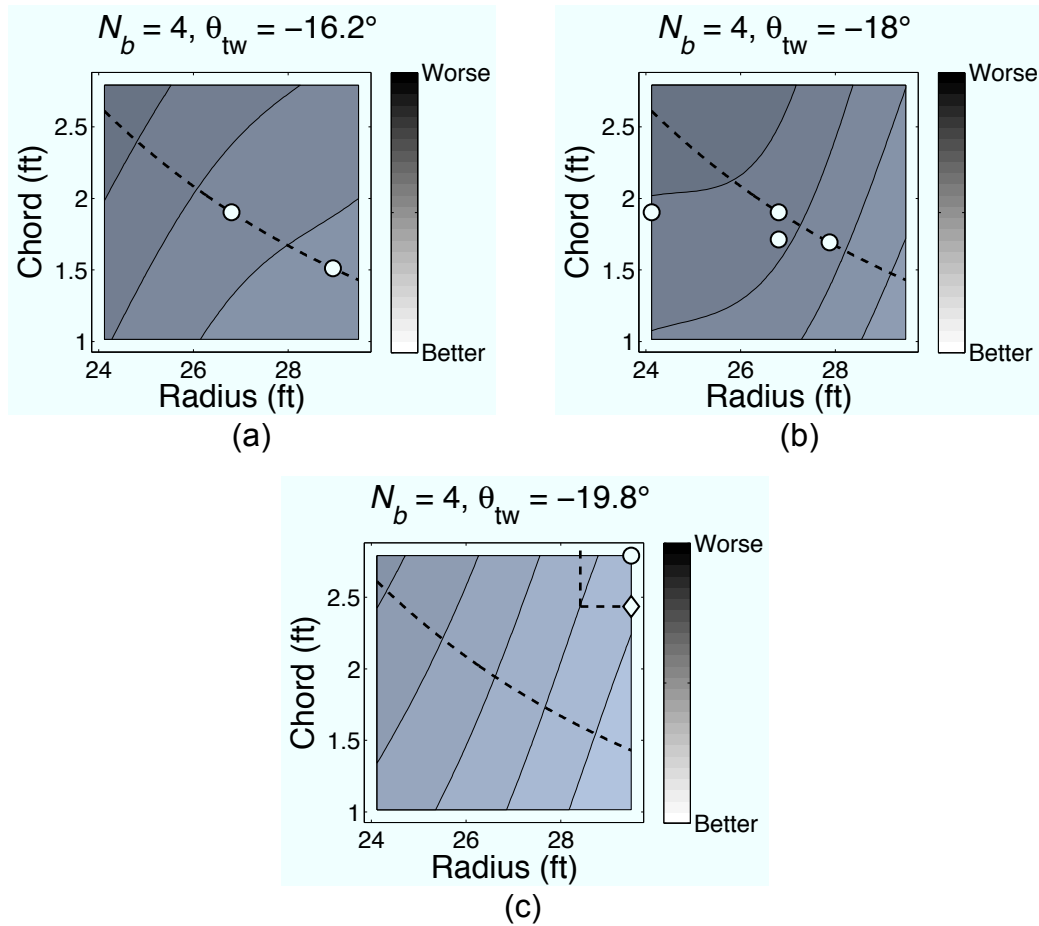
Figure 4.5: Two-dimensional contour maps through the three-dimensional approximate objective function, $B_{\text{app}}(\mathbf{X}^{4b})$, for the third optimization step. Move limits are shown as dashed lines, and the region of the design space that satisfies the behavior constraint on C_T/σ is above the curved dashed line.
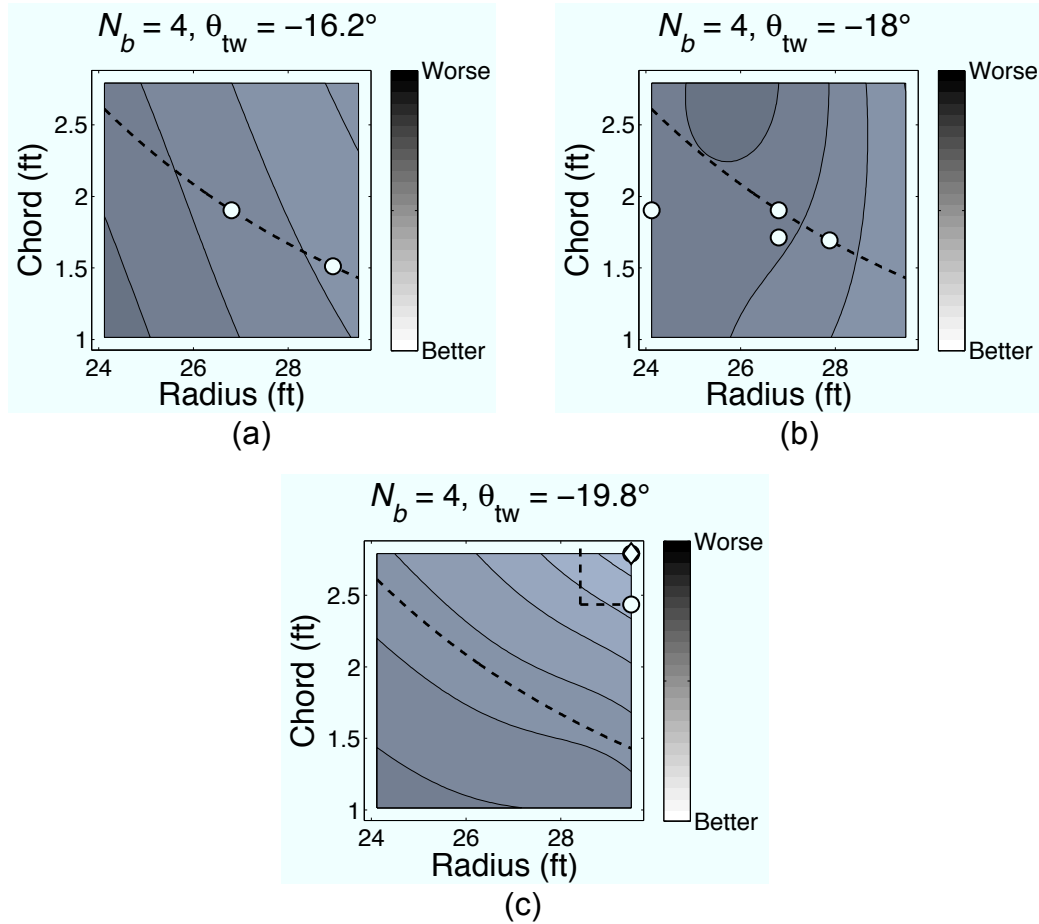
Figure 4.6: Two-dimensional contour maps through the three-dimensional approximate objective function, $B_{app}(\mathbf{X}^{4b})$, for the fourth optimization step. Move limits are shown as dashed lines, and the region of the design space that satisfies the behavior constraint on C_T/σ is above the curved dashed line.
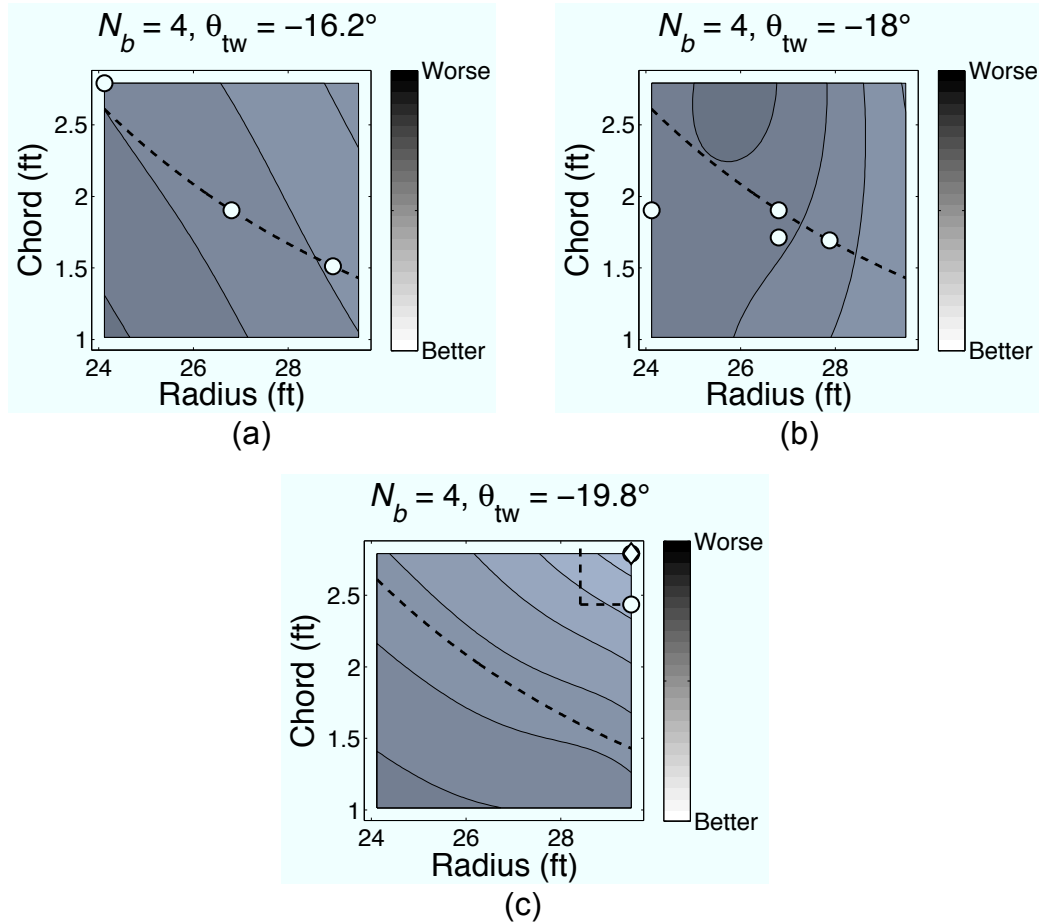
Figure 4.7: Two-dimensional contour maps through the three-dimensional approximate objective function, $B_{\text{app}}(\mathbf{X}^{4b})$, for the fifth optimization step. Move limits are shown as dashed lines, and the region of the design space that satisfies the behavior constraint on C_T/σ is above the curved dashed line.
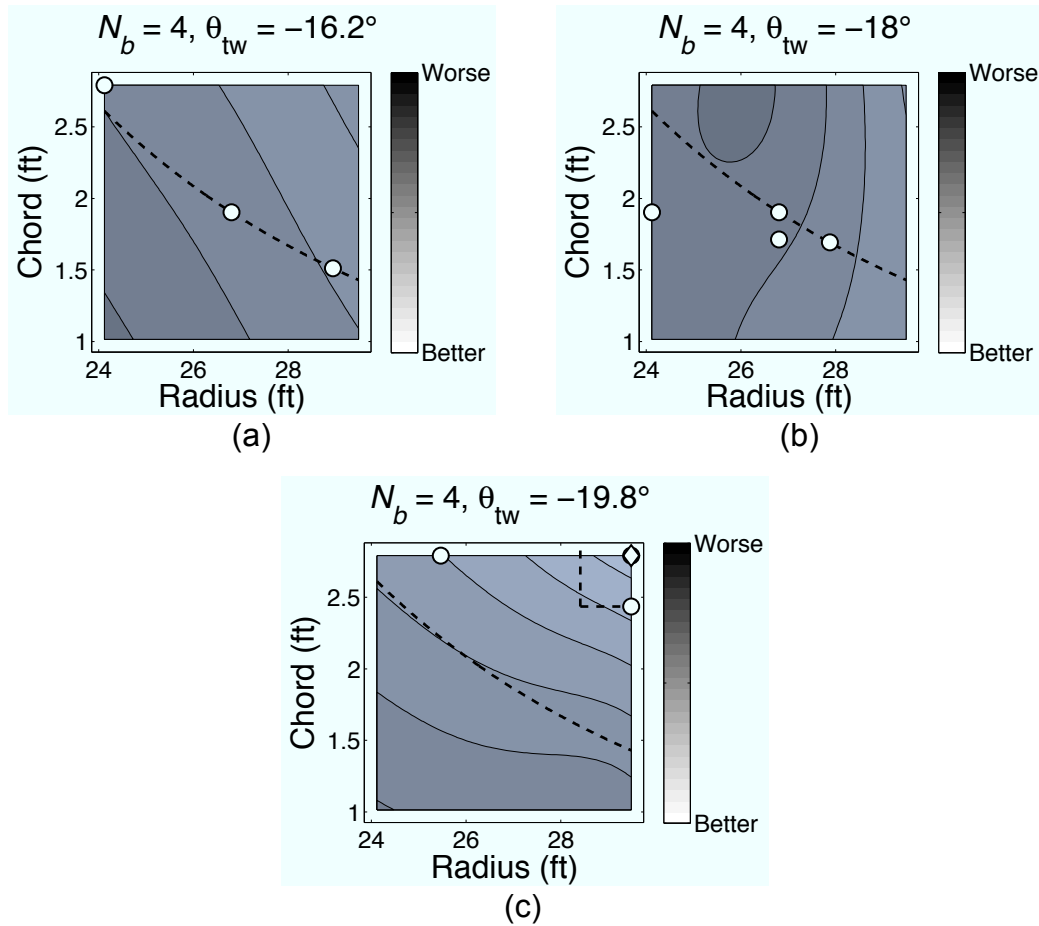
Figure 4.8: Two-dimensional contour maps through the three-dimensional approximate objective function, $B_{\mathrm{app}}(\mathbf{X}^{4b})$, for the sixth optimization step. Move limits are shown as dashed lines, and the region of the design space that satisfies the behavior constraint on C_T/σ is above the curved dashed line.
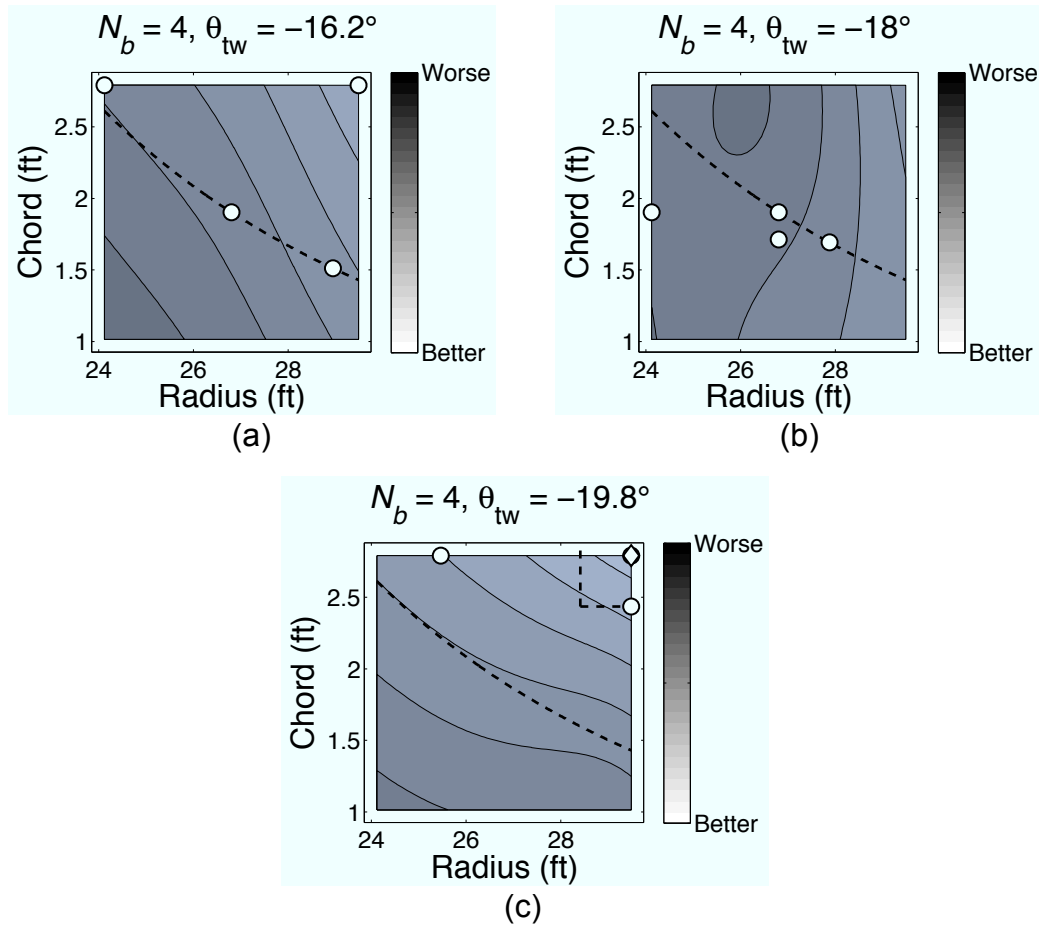
Figure 4.9: Two-dimensional contour maps through the three-dimensional approximate objective function, $B_{\mathrm{app}}(\mathbf{X}^{4b})$, for the seventh optimization step. Move limits are shown as dashed lines, and the region of the design space that satisfies the behavior constraint on C_T/σ is above the curved dashed line.

Table 4.1: Function evaluations for the 4-bladed rotor design optimization.

Optimization Step	Rotor design, $\mathbf{X}^{4b} = [c_1 \ R_1 \ \theta_{tw,1}]^T$	Function Value, $B(\mathbf{X}^{4b})$
0	$\mathbf{X}_1^{4b} = [1.9 \text{ ft } 26.8 \text{ ft } -18.0°]^T$	450.1
0	$\mathbf{X}_2^{4b} = [1.9 \text{ ft } 24.1 \text{ ft } -18.0°]^T$	465.0
0	$\mathbf{X}_3^{4b} = [1.7 \text{ ft } 26.8 \text{ ft } -18.0°]^T$	443.3
0	$\mathbf{X}_4^{4b} = [1.9 \text{ ft } 26.8 \text{ ft } -16.2°]^T$	423.2
1	$\mathbf{X}_5^{4b} = [1.7 \text{ ft } 27.9 \text{ ft } -17.3°]^T$	385.3
2	$\mathbf{X}_6^{4b} = [1.5 \text{ ft } 28.9 \text{ ft } -17.0°]^T$	376.4
additional design	$\mathbf{X}_7^{4b} = [2.8 \text{ ft } 29.5 \text{ ft } -19.8°]^T$	264.7
3	$\mathbf{X}_8^{4b} = [2.4 \text{ ft } 29.5 \text{ ft } -19.8°]^T$	302.2
4	$\mathbf{X}_7^{4b} = [2.8 \text{ ft } 29.5 \text{ ft } -19.8°]^T$	264.7
additional design	$\mathbf{X}_9^{4b} = [2.8 \text{ ft } 24.1 \text{ ft } -16.2°]^T$	433.0
5	$\mathbf{X}_7^{4b} = [2.8 \text{ ft } 29.5 \text{ ft } -19.8°]^T$	264.7
additional design	$\mathbf{X}_{10}^{4b} = [2.8 \text{ ft } 25.5 \text{ ft } -19.8°]^T$	344.9
6	$\mathbf{X}_7^{4b} = [2.8 \text{ ft } 29.5 \text{ ft } -19.8°]^T$	264.7
additional design	$\mathbf{X}_{11}^{4b} = [2.8 \text{ ft } 29.5 \text{ ft } -16.6°]^T$	319.6
7	$\mathbf{X}_7^{4b} = [2.8 \text{ ft } 29.5 \text{ ft } -19.8°]^T$	264.7

rotor radius, R, and reduce blade twist rate, θ_{tw}; see Figs. 4.3 and 4.4. Notice also from Figs. 4.3 and 4.4 that the C_T/σ constraint was active. Design $\mathbf{X}_7^{4b}$, however, was the result of an "additional design" optimization step that showed significant improvement over $\mathbf{X}_6^{4b}$. Notice that the side constraints were active for $\mathbf{X}_7^{4b}$, i.e.,

$$\mathbf{X}_7^{4b} = [2.8 \text{ ft } 29.5 \text{ ft } -19.8°]^T = [c_{min} \ R_{max} \ \theta_{tw,max}]^T \qquad (4.23)$$

and the associated C_T/σ was the lowest possible value that could be achieved within the allowable design space.

After one more optimization step, which led to $\mathbf{X}_8^{4b}$ (see Fig. 4.5), the optimization methodology converged on design $\mathbf{X}_7^{4b}$; see Fig. 4.6. To ensure that the method had converged, additional designs $\mathbf{X}_9^{4b}$–$\mathbf{X}_{11}^{4b}$ were evaluated. After each of these additional

designs, however, the methodology returned to $\mathbf{X}_7^{4b}$ as its optimum; see Figs. 4.7–4.9.

Notice that, in comparison with the objective function approximations presented in Section 3.2.1, the objective function approximations in Figs. 4.3–4.9 were much less prone to drastic changes between optimization steps. This observation indicates that the RBF-based approximation to the objective function may be better suited than the second-order Taylor series expansion for brownout-related optimization problems (at least under the assumptions made in the present work).

4.2.2   Verifying Convergence

Although the optimization procedure had returned the same optimum design in four successive iterations (see Fig. 4.2), it was desirable to perform a more rigorous verification that the methodology had, in fact, converged to an optimum. Such a verification is not necessarily straightforward, and two separate verification procedures were examined.

In the first instance, the convergence of the optimization methodology may be questionable if large regions of the design space have gone unexamined by an exact objective function evaluation. Although the use of "additional designs" within the optimization procedure sought to ensure that the design space would be explored as thoroughly as possible, the potential still existed that rapid convergence to an optimum would result in large regions of the design space remaining unexplored. Because of this potential issue, a series of additional designs, $\mathbf{X}_{12}^{4b}$–$\mathbf{X}_{21}^{4b}$, were evaluated to ensure that the design space was explored to a suitable degree. These designs are shown in Table 4.2.

Each additional design was solved in accordance with Eq. (4.21). Recall that the

Table 4.2: Function evaluations for verifying the convergence of the 4-bladed rotor design optimization.

Optimization Step	Rotor design, $\mathbf{X}^{4b} = [c_1 \; R_1 \; \theta_{tw,1}]^T$	Function Value, $B(\mathbf{X}^{4b})$
additional design	$\mathbf{X}_{12}^{4b} = [2.8 \text{ ft } 26.7 \text{ ft } -17.2°]^T$	403.5
additional design	$\mathbf{X}_{13}^{4b} = [2.5 \text{ ft } 28.7 \text{ ft } -18.1°]^T$	341.3
additional design	$\mathbf{X}_{14}^{4b} = [1.4 \text{ ft } 29.5 \text{ ft } -19.1°]^T$	361.1
additional design	$\mathbf{X}_{15}^{4b} = [1.9 \text{ ft } 27.3 \text{ ft } -19.8°]^T$	339.0
additional design	$\mathbf{X}_{16}^{4b} = [2.1 \text{ ft } 29.5 \text{ ft } -16.2°]^T$	325.3
additional design	$\mathbf{X}_{17}^{4b} = [2.8 \text{ ft } 24.4 \text{ ft } -18.1°]^T$	411.4
additional design	$\mathbf{X}_{18}^{4b} = [2.3 \text{ ft } 25.1 \text{ ft } -17.1°]^T$	410.0
additional design	$\mathbf{X}_{19}^{4b} = [2.5 \text{ ft } 27.8 \text{ ft } -16.2°]^T$	369.3
additional design	$\mathbf{X}_{20}^{4b} = [2.6 \text{ ft } 26.6 \text{ ft } -18.6°]^T$	363.2
additional design	$\mathbf{X}_{21}^{4b} = [2.3 \text{ ft } 27.6 \text{ ft } -17.3°]^T$	406.4
8	$\mathbf{X}_{7}^{4b} = [2.8 \text{ ft } 29.5 \text{ ft } -19.8°]^T$	264.7

outcome of this process is a design that is most different (i.e., furthest from) the other designs that have been evaluated previously. Figure 4.10 shows the results of this procedure, which was continued until $F(\mathbf{X}^{4b}) \leq 0.33$. Figures 4.11–4.20 show two-dimensional contour maps through the three-dimensional "additional design" objective function, $F(\mathbf{X}^{4b})$. Once again, the designs evaluated over the course of the procedures are shown in the contour maps as circles and the optimal designs (i.e., optimal in terms of the "additional design" objective) are denoted by diamonds.

Another form of verification may be derived from a mathematical assessment that the approximate objective function is not changing significantly between function evaluations. If the approximate objective function is not likely to change with the addition of more design evaluations, it stands to reason that the optimum of that approximate objective function is not likely to change, and the method may be considered to have converged.
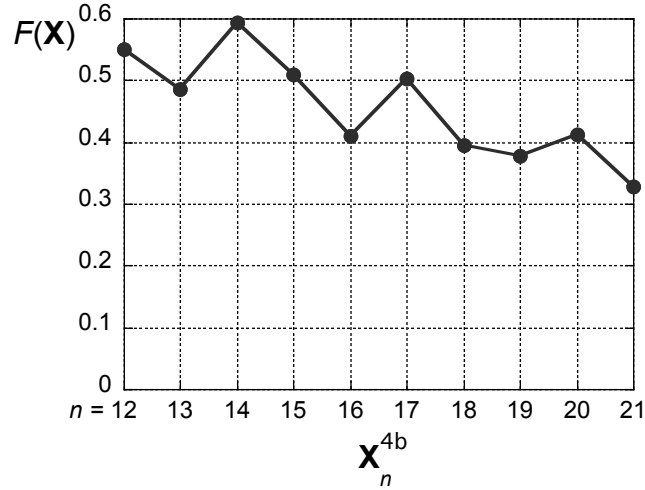
Figure 4.10: The "additional design" objective, $F(\mathbf{X}^{4b})$, for the designs generated for convergence verification, $\mathbf{X}^{4b}_{12}$–$\mathbf{X}^{4b}_{21}$.

To this end, a convergence tolerance was defined, i.e.,

$$\varepsilon_{\text{conv}} = \frac{\sum\limits_{i=1}^{m} \left| \dfrac{B^k_{\text{app}}(\mathbf{Y}_i) - B^{k-1}_{\text{app}}(\mathbf{Y}_i)}{B^k_{\text{app}}(\mathbf{Y}_i)} \right|}{m} \tag{4.24}$$

where B^k_{app} is the approximate objective function that is constructed using designs $\mathbf{X}^{4b}_1$–$\mathbf{X}^{4b}_k$, and $\mathbf{Y}$ is a matrix that contains a uniform m-point mesh over the entire design space. In the present study, $m = 125$. In essence, $\varepsilon_{\text{conv}}$ is a mean measure of the percent change in the approximate objective function as each new function evaluation is calculated. The variation of $\varepsilon_{\text{conv}}$ with the total number of design evaluations, k, is shown in Fig. 4.21. Notice that the values for $\varepsilon_{\text{conv}}$ reduce to approximately 1–2% as k increases beyond 13, indicating that the approximate objective function is virtually unchanged with each successive function evaluation.

In the present study, a final check on the convergence of the method involved an

195
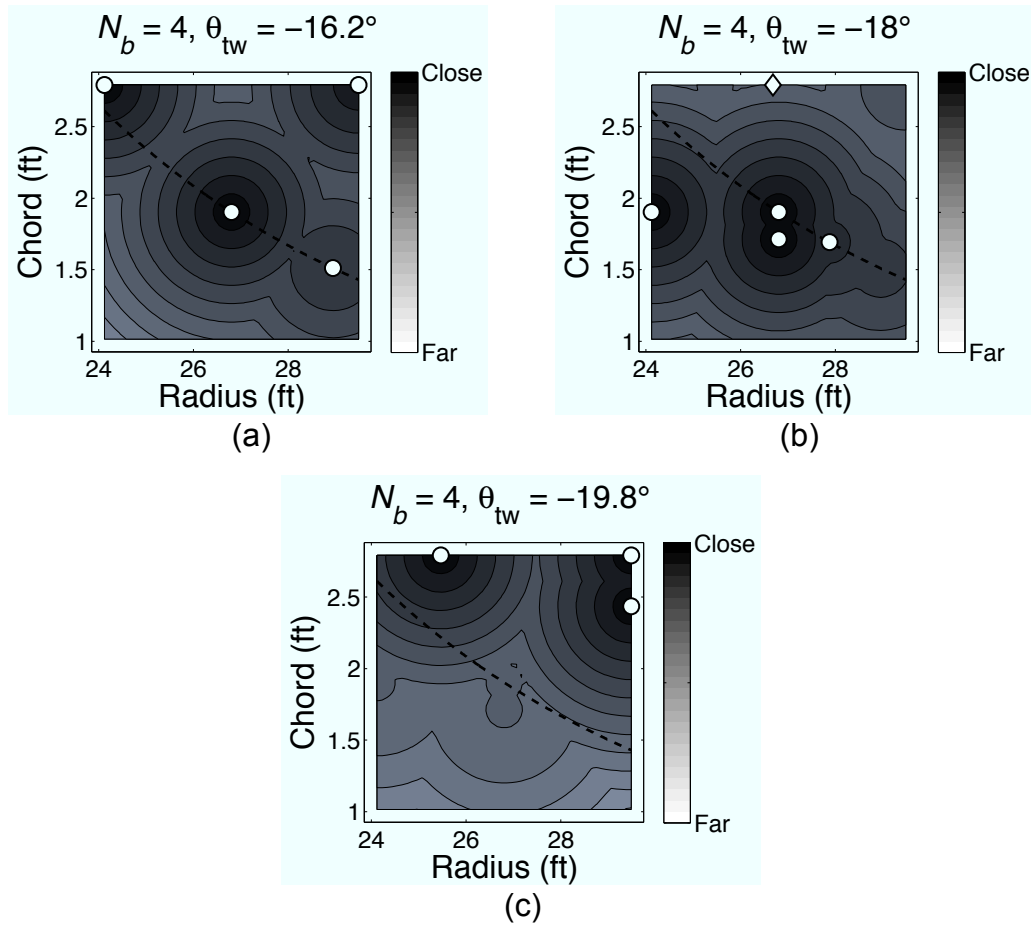
Figure 4.11: Two-dimensional contour maps through the three-dimensional objective function for selecting additional designs, $F(\mathbf{X}^{4\mathrm{b}})$, for the first step to ensure convergence. The region of the design space that satisfies the behavior constraint on C_T/σ is above the curved dashed line.
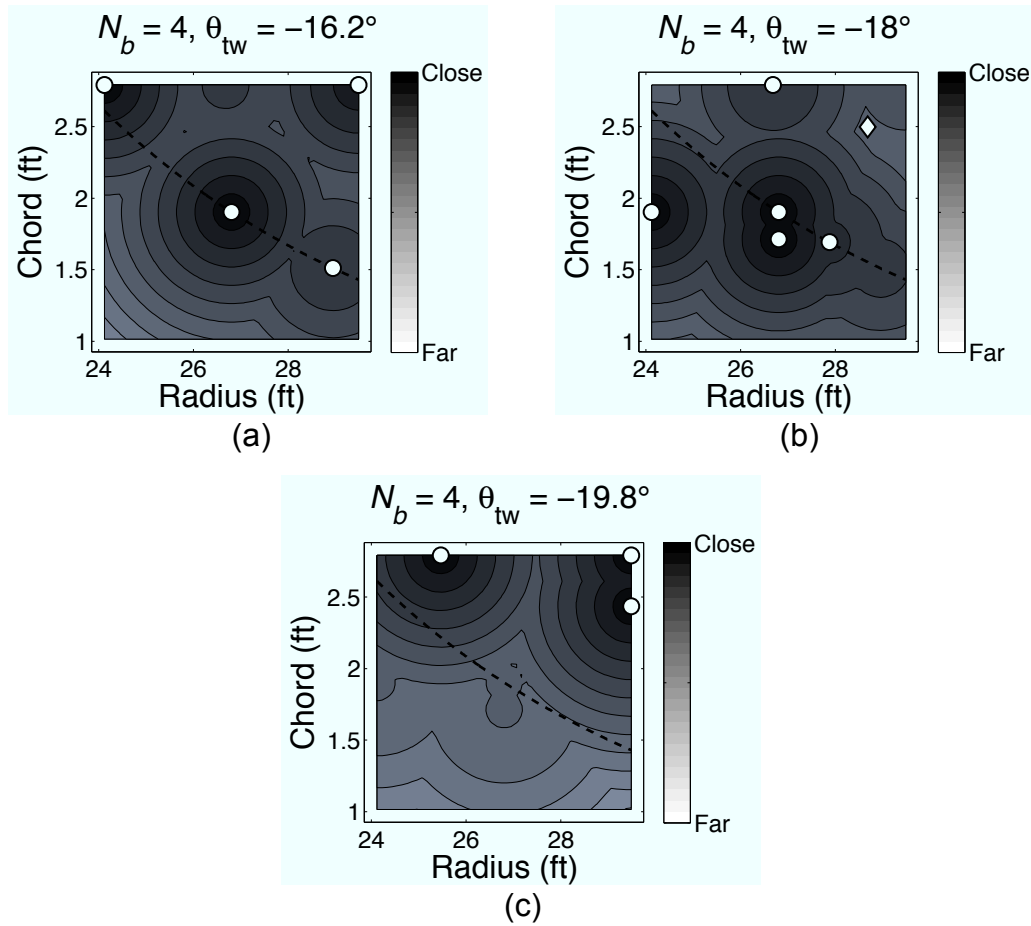
Figure 4.12: Two-dimensional contour maps through the three-dimensional objective function for selecting additional designs, $F(\mathbf{X}^{4b})$, for the second step to ensure convergence. The region of the design space that satisfies the behavior constraint on C_T/σ is above the curved dashed line.
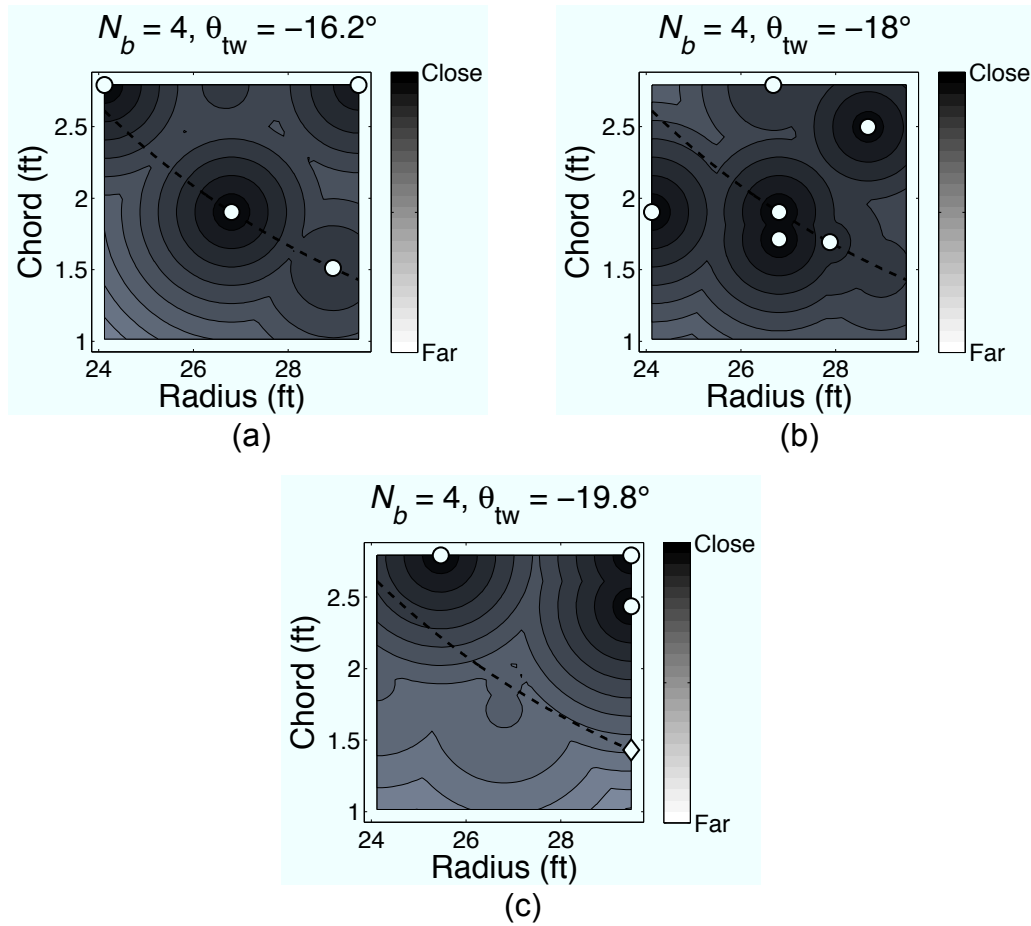
Figure 4.13: Two-dimensional contour maps through the three-dimensional objective function for selecting additional designs, $F(\mathbf{X}^{4b})$, for the third step to ensure convergence. The region of the design space that satisfies the behavior constraint on C_T/σ is above the curved dashed line.
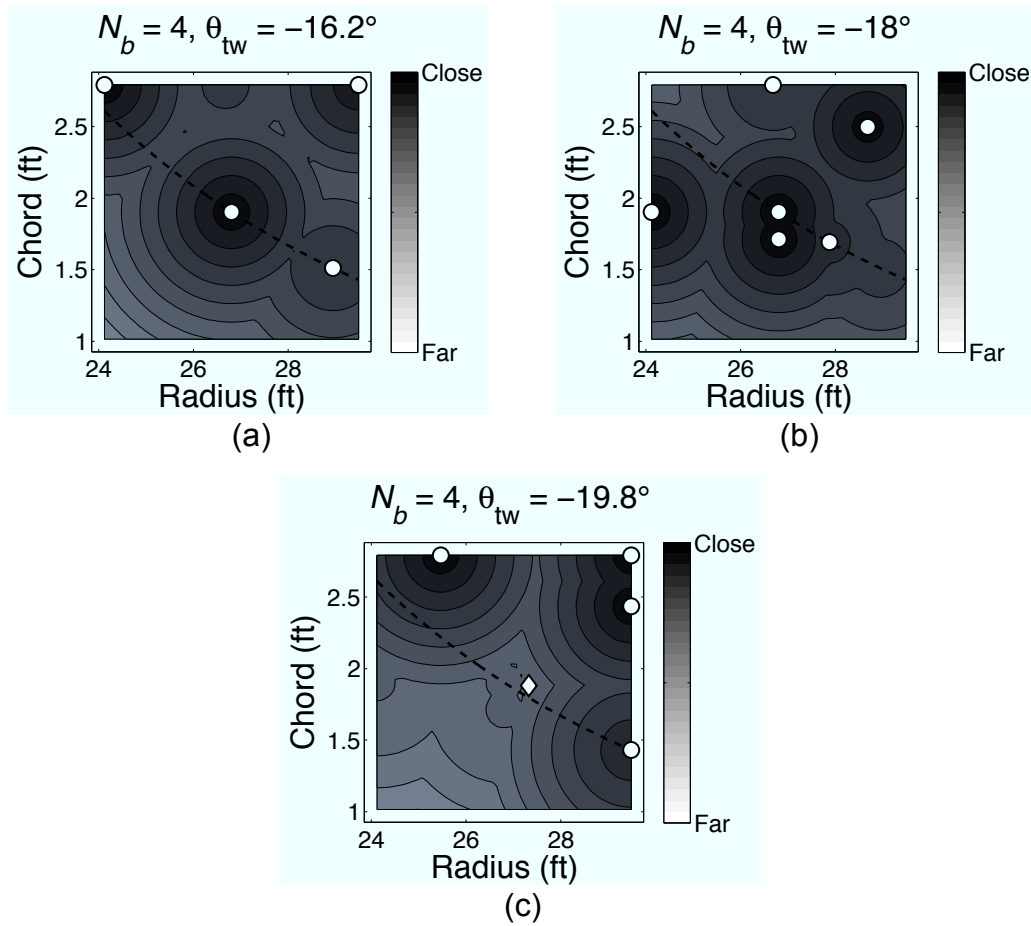
Figure 4.14: Two-dimensional contour maps through the three-dimensional objective function for selecting additional designs, $F(\mathbf{X}^{4b})$, for the fourth step to ensure convergence. The region of the design space that satisfies the behavior constraint on C_T/σ is above the curved dashed line.
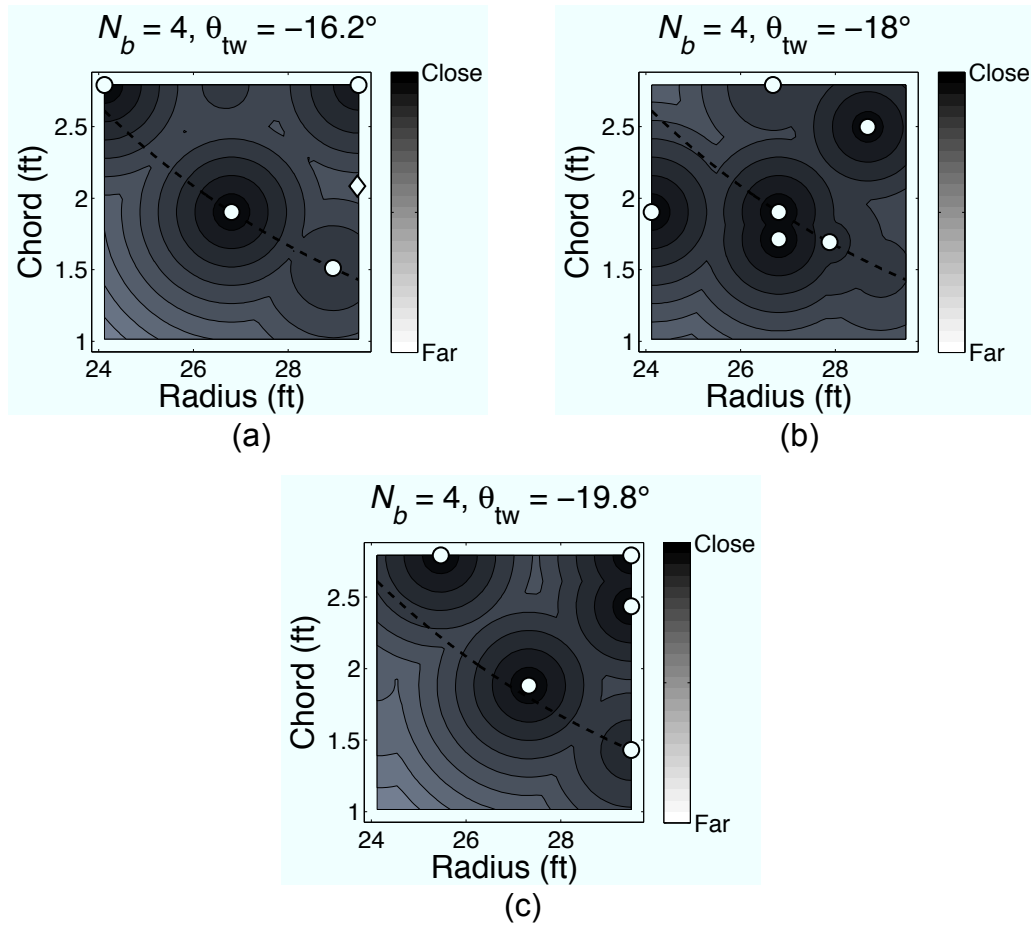
Figure 4.15: Two-dimensional contour maps through the three-dimensional objective function for selecting additional designs, $F(\mathbf{X}^{4b})$, for the fifth step to ensure convergence. The region of the design space that satisfies the behavior constraint on C_T/σ is above the curved dashed line.
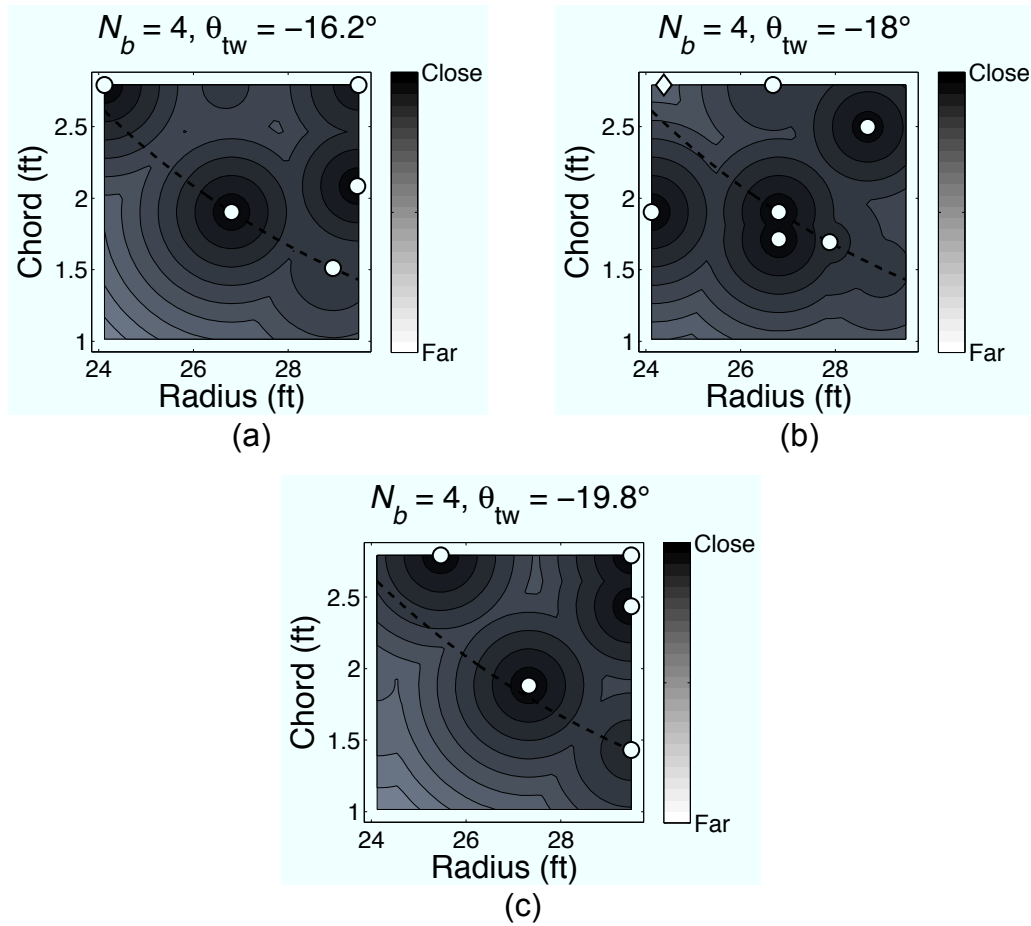
Figure 4.16: Two-dimensional contour maps through the three-dimensional objective function for selecting additional designs, $F(\mathbf{X}^{4b})$, for the sixth step to ensure convergence. The region of the design space that satisfies the behavior constraint on C_T/σ is above the curved dashed line.
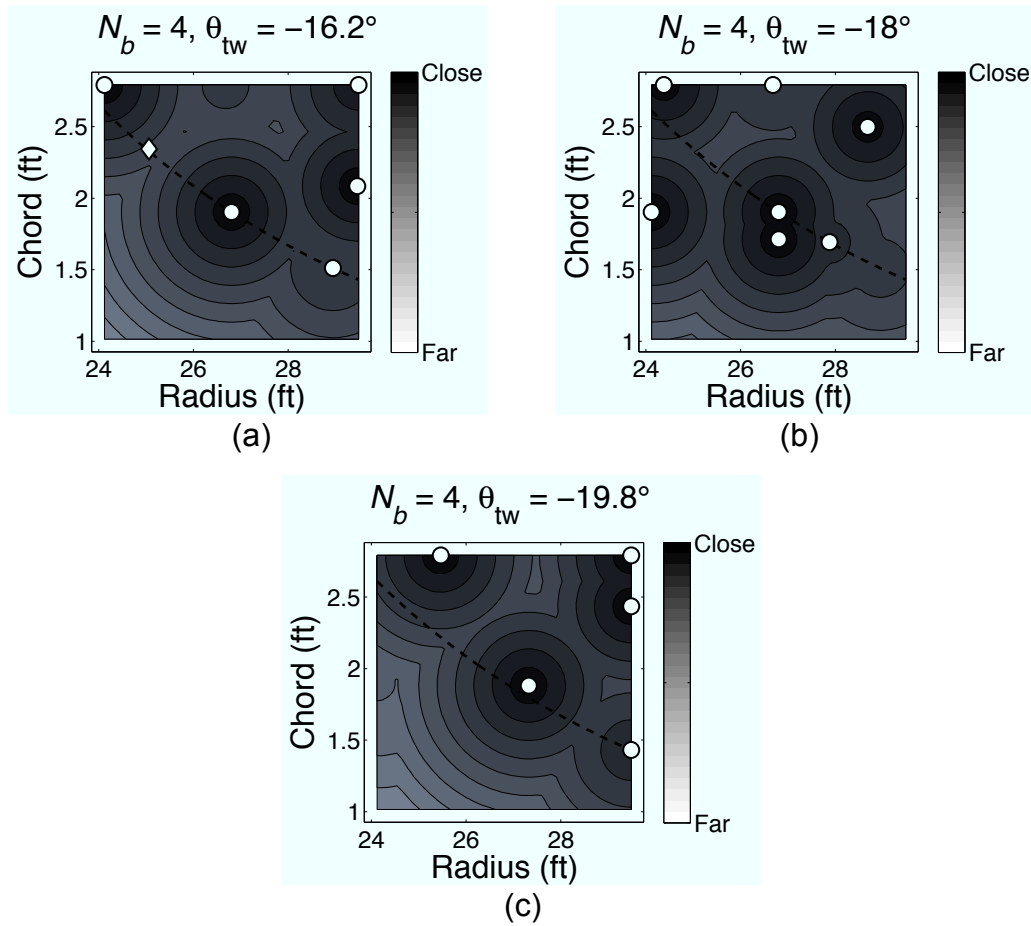
Figure 4.17: Two-dimensional contour maps through the three-dimensional objective function for selecting additional designs, $F(\mathbf{X}^{4b})$, for the seventh step to ensure convergence. The region of the design space that satisfies the behavior constraint on C_T/σ is above the curved dashed line.
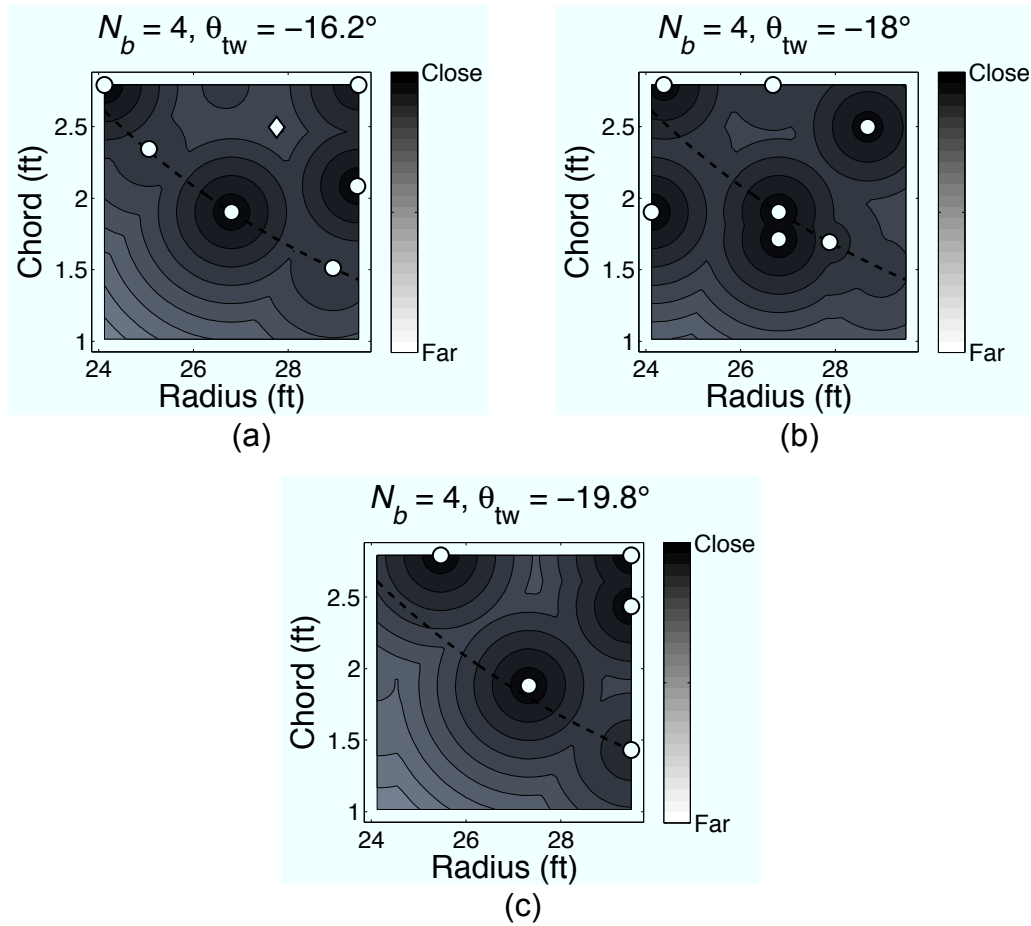
Figure 4.18: Two-dimensional contour maps through the three-dimensional objective function for selecting additional designs, $F(\mathbf{X}^{4b})$, for the eighth step to ensure convergence. The region of the design space that satisfies the behavior constraint on C_T/σ is above the curved dashed line.
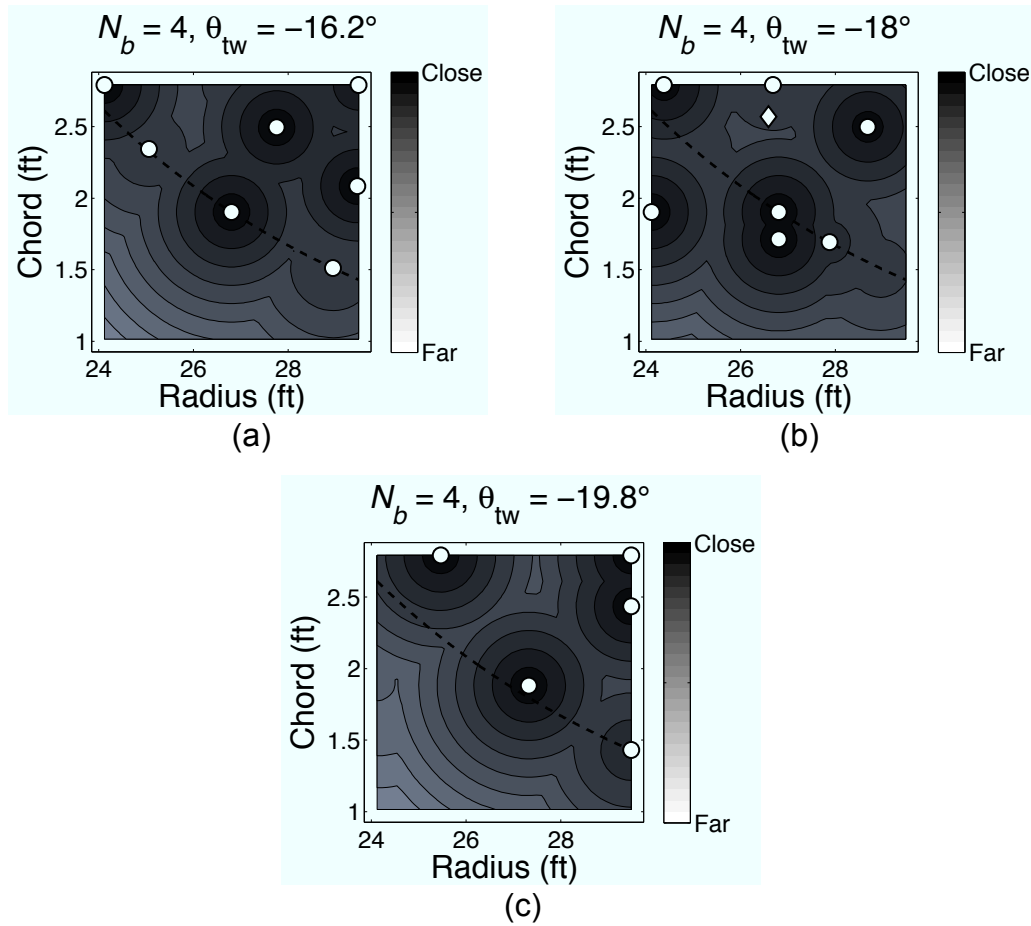
Figure 4.19: Two-dimensional contour maps through the three-dimensional objective function for selecting additional designs, $F(\mathbf{X}^{4b})$, for the ninth step to ensure convergence. The region of the design space that satisfies the behavior constraint on C_T/σ is above the curved dashed line.
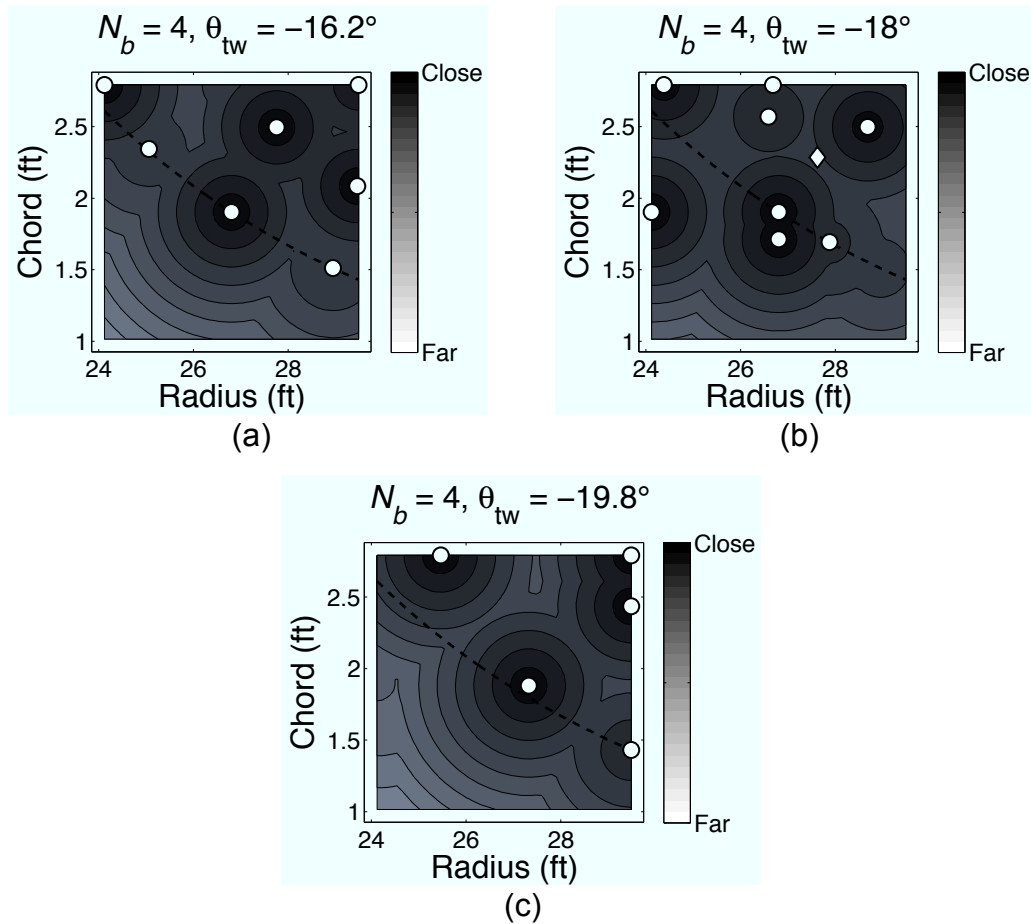
Figure 4.20: Two-dimensional contour maps through the three-dimensional objective function for selecting additional designs, $F(\mathbf{X}^{4b})$, for the tenth step to ensure convergence. The region of the design space that satisfies the behavior constraint on C_T/σ is above the curved dashed line.
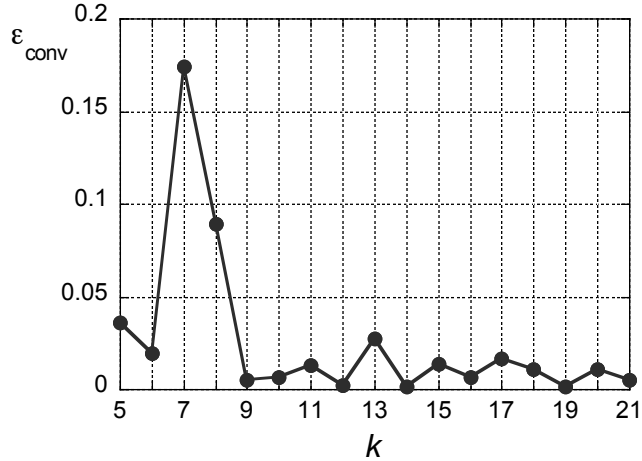
Figure 4.21: Convergence tolerance, $\varepsilon_{\text{conv}}$, versus total number of design evaluations, k.

eighth optimization step, in which the approximate objective function was constructed from designs $\mathbf{X}_1^{4b}$–$\mathbf{X}_{21}^{4b}$. This check resulted in the selection of $\mathbf{X}_7^{4b}$ as the optimum design once again, and it was determined that the method had truly converged, i.e., $\mathbf{X}_7^{4b} = \mathbf{X}^{4b*}$.

A summary of the progression of the overall optimization procedure, including the convergence verification, is shown in Fig. 4.22, and two-dimensional contour maps through the three-dimensional approximate objective function, $B_{\text{app}}(\mathbf{X}^{4b})$, for the eighth and final optimization step are shown in Fig. 4.23.
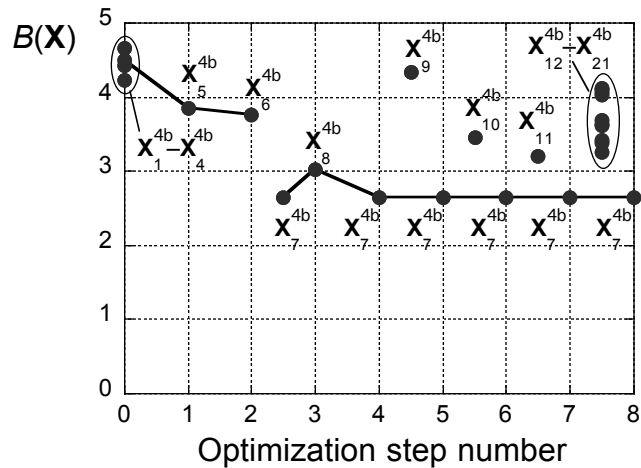
Figure 4.22: Optimization history, i.e., objective function value versus optimization step number.
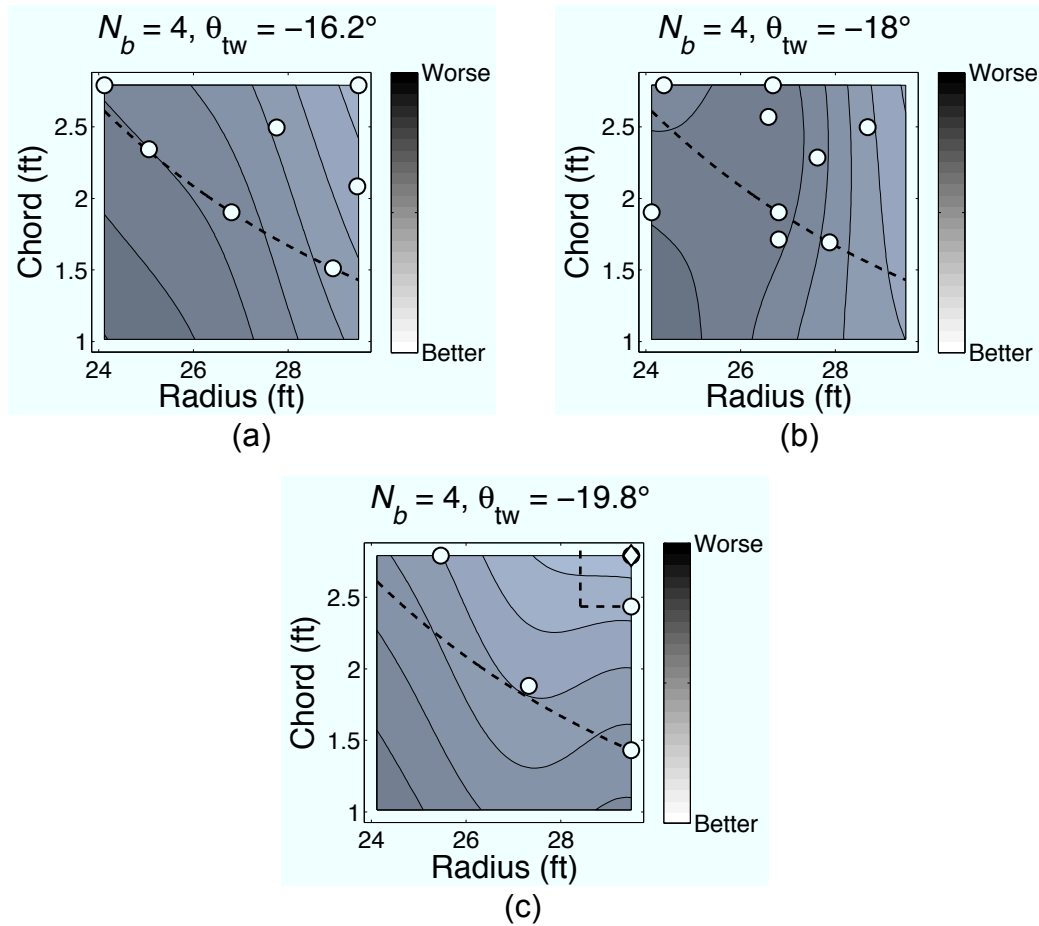
Figure 4.23: Two-dimensional contour maps through the three-dimensional approximate objective function, $B_{\text{app}}(\mathbf{X}^{4b})$, for the eighth optimization step. Move limits are shown as dashed lines, and the region of the design space that satisfies the behavior constraint on C_T/σ is above the curved dashed line.

4.2.3 Physical Interpretation of the Results

To gain a better understanding of the physical mechanisms at play within the present study, the flow fields resulting from the baseline, $\mathbf{X}_1^{4b}$, and optimum, $\mathbf{X}^{4b*}$, designs were examined in detail. Figure 4.24 shows instantaneous realizations of the flow velocities and cloud development in a longitudinal plane passing through the rotor hub.

It is instructive to first consider only the flow field. Examining the baseline case, i.e., Fig. 4.24(a)–(d), it is apparent that the blade tip vortices, seen as concentrated regions of high velocity in the plane, impinge upon the ground and interact with each other to form a "super-vortex" or ground vortex, as noted in prior research (Refs. 9, 42, 44). The ground vortex begins to form beneath the forward half of the rotor disk, Fig. 4.24(a), and convects forward, Fig. 4.24(b)–(c), as the rotor continues to its hover position. Once the ground vortex has convected forward and restructured, the flow field is more representative of that of steady in-ground-effect (IGE) hover, Fig. 4.24(d), in which the blade tip vortices convect along the slipstream boundary, impinge upon the ground, and spread outward.

In examining Fig. 4.24, it is apparent that the initial uplift of sediment particles can primarily be attributed to the ground vortex. This observation is reasonable because the ground vortex contains multiple individual tip vortices that interact to form concentrated regions of circulation and higher local velocities that are directly responsible for mobilizing and uplifting large amounts of dust. Figure 4.24 shows a comparison of the flow fields and brownout clouds for the baseline design, Fig. 4.24(a)–(d), and optimum design, Fig. 4.24(e)–(h).

Figures 4.24(a) and (e) show the instant at which the vortex wake first impinges
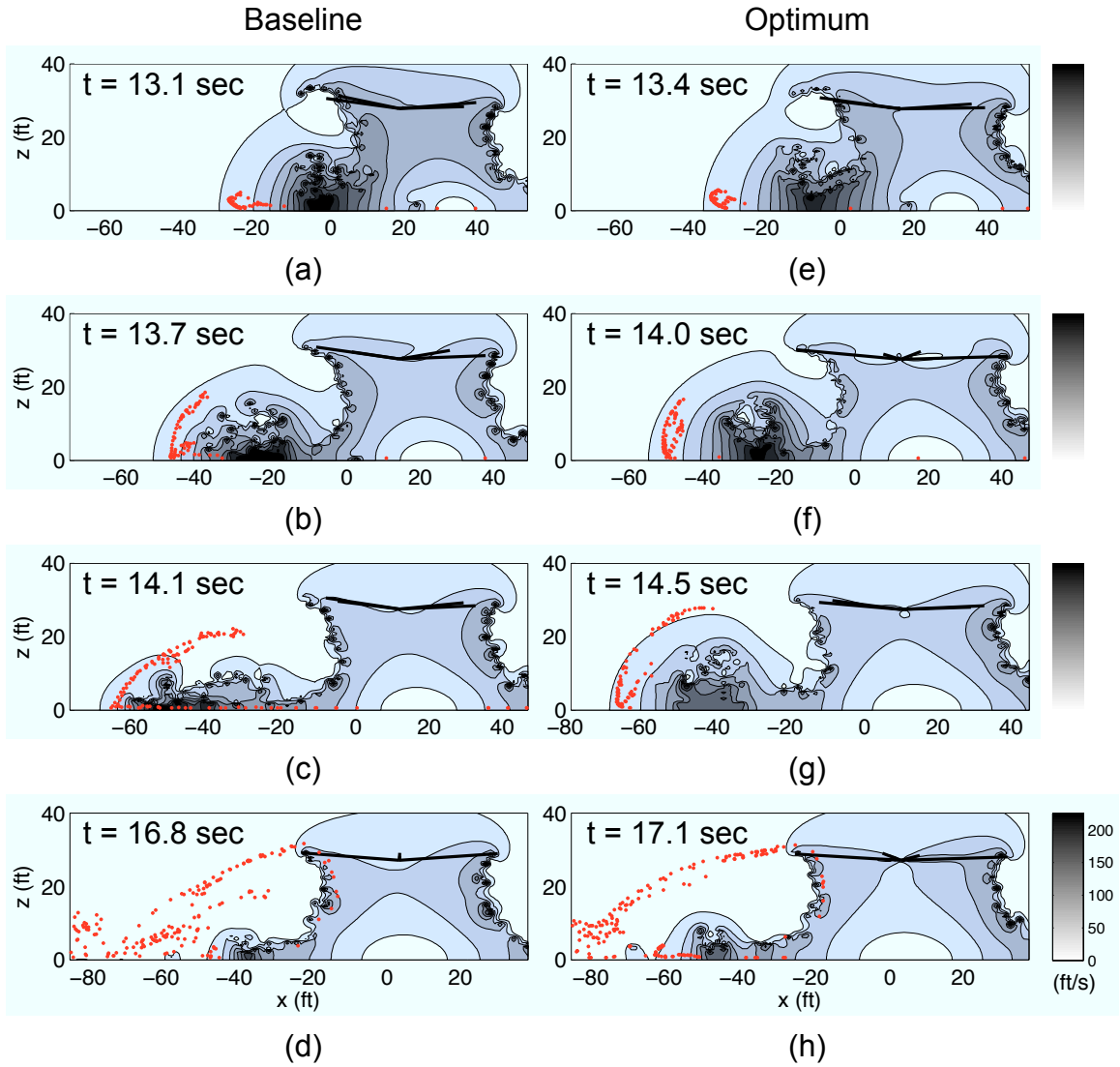
Figure 4.24: Instantaneous realizations of the flow velocity magnitudes and developing cloud in a longitudinal plane through the flow field for (a)–(d) the baseline and (e)–(h) the optimum designs.

on the ground and forms a ground vortex for the baseline and optimum cases. As the ground vortex convects forward, it tends to trap dust and uplift it into the flow field; see Fig. 4.24(b) and (f). The ground vortex continues to entrain the dust particles into more quiescent regions of the flow field as it convects further away from the rotor and begins to undergo a restructuring; see Fig. 4.24(c) and (g). Notice that the ground vortex clearly restructures at this stage for the baseline rotor design, Fig. 4.24(c), although it maintains a more coherent ground vortex structure for the optimum rotor design, Fig. 4.24(g). Notice also that the shapes of the the developing clouds are quite different at this stage; the baseline design entrains dust particles to lower heights and at closer distances to the rotor versus the optimum design.

The dust particles may, some time after being suspended, be reingested through the rotor disk, leading to a phenomenon known as reingestion bombardment; see Fig. 4.24(d) and (h). Reingestion bombardment precipitates a sharp increase in the volume and severity of the developing brownout cloud (Ref. 7).

Although an examination of the key physical mechanisms in the formation of the brownout cloud for the baseline and optimum rotor designs reveals some general insight into the role of the ground vortex in the brownout cloud development, the differences between the two designs are nuanced. A comparison of the time-history of particle entrainment for the baseline and optimum cases, however, provides additional insight.

Figure 4.25 shows $b(\mathbf{X})$ as a function of time for $\mathbf{X}_1^{4b}$ and $\mathbf{X}^{4b*}$. Recall that $b(\mathbf{X})$ indicates the particle count in the "best" region of a pilot's FOV at a given instant in time (Eq. 2.79) and is integrated over the duration of the maneuver to calculate the objective

210
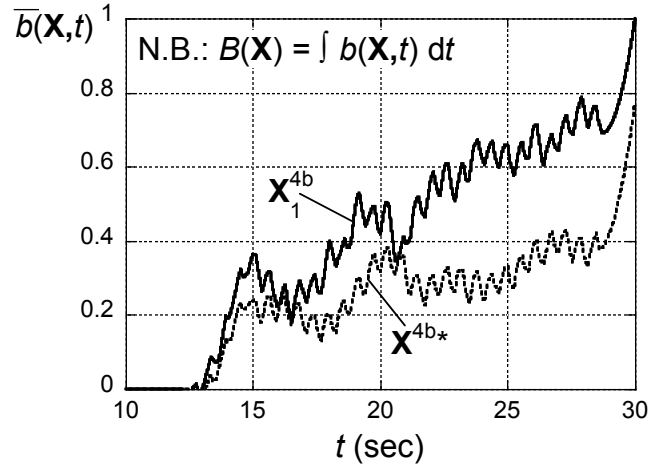
Figure 4.25: $\bar{b}(\mathbf{X})$ versus time for the baseline and optimum rotor designs.

function (Eq. 2.80). For clarity, $b(\mathbf{X})$ has been normalized and smoothed, i.e., $\bar{b}(\mathbf{X})$. The plot clearly shows that, although the brownout clouds develop at approximately the same time for both rotor designs (i.e., approximately 13–14 s into the simulation), the number of particles in the "best" region of the pilot's FOV is typically lower for $\mathbf{X}^{4b*}$ at all times during the maneuver.

4.3   The Effect of N_b: Optimization Methodologies

The addition of the number of blades, N_b, as a design variable makes the optimization a Mixed Integer Non-Linear Programming (MINLP) problem. As discussed in Section 2.2, optimization problems that take on mixed continuous and discrete/integer variables tend to be more complicated than problems using only continuous variables. In the present study, two approaches were evaluated to determine their efficacy in accommodating the addition of N_b as a design variable:

1. A series of three-design-variable (3DV) optimizations to examine the potential for

utilizing the Branch-and-Bound (B&B) algorithm to solve the overall four-design-variable (4DV) problem.

2. A single 4DV optimization.

4.3.1 Formulation as a MINLP Problem

The addition of N_b as a design variable results in a MINLP problem. In a general sense, the overall optimization procedure still consists of finding the value of a vector $\mathbf{X}$ of design variables such that a scalar objective function $B(\mathbf{X})$ is minimized, i.e.,

$$B(\mathbf{X}) \rightarrow \min \qquad (4.25)$$

subject to:

behavior constraints $\qquad g_j(\mathbf{X}) \leq 0 \quad j = 1, \ldots, m \qquad (4.26)$

side constraints $\qquad \mathbf{X}_{\min} \leq \mathbf{X} \leq \mathbf{X}_{\max} \qquad (4.27)$

and $\qquad x_i = \text{discrete for some } i \qquad (4.28)$

where x_i is the i-th component of the design vector $\mathbf{X}$. Notice that the only difference between the present formulation and that presented in Section 4.1 is the addition of a discrete design variable, i.e., Eq. (4.28).

With the addition of N_b as a design variable, $\mathbf{X}$ becomes

$$\mathbf{X} = \left\{ \begin{array}{c} x_1 \\ x_2 \\ x_3 \\ x_4 \end{array} \right\} = \left\{ \begin{array}{c} N_b \\ c \\ R \\ \theta_{\text{tw}} \end{array} \right\} \tag{4.29}$$

where N_b is constrained to the following integer values, i.e., $N_b = 3, 4, 5,$ or 6. Move limits are not imposed on N_b.

As N_b is included as a variable, the behavior constraint on C_T/σ is best expressed as a linear function of the intermediate variable $y_2 = 1/N_b c R^3$. An exact fit to the constraint function can therefore be achieved using

$$g_{\text{app}}(y_2) = p(y_2) \tag{4.30}$$

where $p(y_2)$ is linear.

4.3.2 Three-Design-Variable (3DV) Optimizations for $N_b = 3, 4, 5, 6$

As a preliminary step to utilizing the Branch & Bound algorithm (B&B), independent optimization procedures were performed for $N_b = 3, 5, 6$ (in addition to the optimization for $N_b = 4$ that was presented in Section 4.2.1). The procedure for these three new optimizations was identical to the one described previously in Section 4.1. The chord value for each baseline design was modified so that all baseline rotor designs had the

same rotor solidity, σ, as the baseline from the 4-bladed design optimization, i.e.,

$$\mathbf{X}_1^{3b} = [2.5 \text{ ft} \ 26.8 \text{ ft} \ 18°]^T \tag{4.31}$$

$$\mathbf{X}_1^{4b} = [1.9 \text{ ft} \ 26.8 \text{ ft} \ 18°]^T \tag{4.32}$$

$$\mathbf{X}_1^{5b} = [1.5 \text{ ft} \ 26.8 \text{ ft} \ 18°]^T \tag{4.33}$$

$$\mathbf{X}_1^{6b} = [1.3 \text{ ft} \ 26.8 \text{ ft} \ 18°]^T \tag{4.34}$$

For the purposes of the present study, convergence of the method was defined by satisfying two conditions:

1. The optimum design of a given step is determined to be a design that has already been evaluated.

2. The convergence tolerance defined by Eq. (4.24) is below a set threshold, i.e., $\epsilon_{\text{conv}} \leq 0.02$.

Within the context of B&B, formulating four separate design optimizations is the equivalent of breaking the original 4DV optimization problem into four distinct 3DV sub-problems. Recall from Section 2.2.3 that B&B seeks to "fathom" or "prune" branches of sub-problems by taking advantage of some knowledge that solutions to one of the sub-problems are always better than solutions to one of the other sub-problems. For the example problem in Section 2.2.3, such assessments were made easier by two key properties:

1. The optimization problem was linear, and linear problems always have optima that reside on its constraints.

2. As the original optimization problem was branched into sub-problems, each sub-problem was solved exactly.

For the present case, the overall optimization problem was likely to be nonlinear (based upon the results presented in Section 4.2.1). Furthermore, the optimizations were to be formulated as approximate problems because of the high computational cost of each function evaluation. These considerations led to the efficacy of B&B being highly questionable for the present work. As such, the present study was intended to be an initial investigation into the utility of B&B for the problem rather than a direct application of the B&B algorithm.

4.3.3 Four-Design-Variable (4DV) Optimization (N_b as variable)

As discussed in Section 2.2.2, Genetic Algorithms (GA) possess the ability to solve optimization problems in which the variables take on a mix of continuous and discrete values (i.e., MINLP problems). As such, the basic problem formulation provided in Eqs. 4.25–4.28 may be solved through the use of GA without any additional algorithms (e.g., B&B). In the present study, an optimization with all four design variables, including the integer-only N_b, was performed in parallel with the four separate 3DV optimization studies described in Section 4.3.2. The 4DV optimization was again formulated as an approximate problem, and the "additional design" procedure was again used to improve the global convergence characteristics of the method.

In summary, the computational procedure for the 4DV brownout mitigation study consists of the following steps:

1. Compute the objective function, $B(\mathbf{X})$, and constraint, $g(\mathbf{X})$, for a baseline and N additional designs. The initial designs need not be close and may be infeasible.

2. Compute the approximations to objective, $B_{\text{app}}(\mathbf{X})$, and constraint, $g_{\text{app}}(\mathbf{X})$.

3. Solve the approximate optimization problem:

   Find $\mathbf{X}^*$ such that $B_{\text{app}}(\mathbf{X}^*) \to \min$

   Subject to:

<div align="center">

Behavior Constraint

$$g_{\text{app}}(\mathbf{X}) \leq 0$$

Side Constraints

$$0.9R_1 \leq R \leq 1.1R_1$$

$$c_1^{6b} - \Delta c \leq c \leq c_1^{3b} + \Delta c$$

$$0.9\theta_{\text{tw},1} \leq \theta_{\text{tw}} \leq 1.1\theta_{\text{tw},1}$$

Move Limits

$$-0.2\left(R_{\text{max}} - R_{\text{min}}\right) \leq R_k - R_{k-1} \leq 0.2\left(R_{\text{max}} - R_{\text{min}}\right)$$

$$-0.2\left(c_{\text{max}} - c_{\text{min}}\right) \leq c_k - c_{k-1} \leq 0.2\left(c_{\text{max}} - c_{\text{min}}\right)$$

$$-0.2\left(\theta_{\text{tw},\text{max}} - \theta_{\text{tw},\text{min}}\right) \leq \theta_k - \theta_{k-1} \leq 0.2\left(\theta_{\text{tw},\text{max}} - \theta_{\text{tw},\text{min}}\right)$$

Integer Constraint

$$3 \leq N_b \leq 6, \; N_b \text{ is integer only}$$

</div>

   and let $\mathbf{X}_{k+1}$ be the optimum for the approximate problem.

4. Compute $B(\mathbf{X}_{k+1})$ and $g(\mathbf{X}_{k+1})$. If: (i) the design is feasible, (ii) the new design, $\mathbf{X}_{k+1}$, is close to the previous design, $\mathbf{X}_k$, within a specified tolerance, (iii) the objective function, $B(\mathbf{X}_{k+1})$, is also close to $B(\mathbf{X}_k)$ within a specified tolerance, and (iv) the convergence tolerance is satisfied, i.e., $\varepsilon_{\text{conv}} \leq 0.02$, assume that the sequence of solutions of the approximate problems has converged to the solution of the original optimization problem, and terminate the procedure. Otherwise, add the solution, $\mathbf{X}_{k+1}$, of the approximate optimization problem to the current solution set, update the approximations, and repeat Step 2. The optimization procedure can also be terminated early if a sufficient reduction of the objective function, $B(\mathbf{X})$, has been achieved.

5. For every two executions of Step 2, compute an additional design using Eq. (4.21).

4.4 The Effect of N_b: Results

The key analysis parameters of the present studies are identical to those outlined in Section 4.2. Notice that the formulation of separate, independent optimization studies allowed for much of the computational work to be performed concurrently, i.e., because the 3DV and 4DV optimization studies did not necessarily require the interchange of information, cases from the various studies were able to be run simultaneously. At the same time, if the 4DV optimization study required the computation of a design that had already been evaluated in one of the 3DV optimization studies (or vice-versa), the formulation of the studies as approximate optimizations required that the design need only be computed once. For these reasons, the separate optimization studies were simultaneously executed

217

much more efficiently than they could have been performed serially. This latter point highlights a key advantage of formulating the studies as approximate optimizations.

4.4.1 Optimization Results

Three-Design-Variable (3DV) Optimizations for $N_b = 3, 4, 5, 6$

A summary of the progress of each of the 3DV optimization studies is shown in Fig. 4.26, and listings of all of the exact function evaluations for the $N_b = 3, 5, 6$ studies are provided in Tables 4.3–4.5, respectively (the function evaluations for $N_b = 4$ have been given in Tables 4.1 and 4.2). In each case, the procedure begins with the evaluation of an initial inventory of designs consisting of a baseline plus perturbations in R, c, and θ_{tw}. The initial designs are given by optimization step "zero" in Fig. 4.26.

Notice that each optimization step does not necessarily result in an improvement in the objective function (e.g., steps one to two for the 3-bladed designs). This outcome occurs when the approximate objective function value at the next optimization step predicts improvement (i.e., $B_{app}(\mathbf{X}_{k+1}) < B(\mathbf{X}_k)$), but no improvement is seen when the objective function value is evaluated exactly (i.e., $B(\mathbf{X}_{k+1}) > B(\mathbf{X}_k)$).

Additional designs were incorporated after every two optimization steps, and these design are shown in Fig. 4.26 at "half-steps." Notice that the additional designs play a pivotal role in the progression of the optimization. This point can be seen in the results of Fig. 4.26, as the 4- and 5-bladed design optimization paths both include additional designs between the second and third optimization steps, and the 6-bladed design optimization path includes an additional design between the fourth and fifth steps.
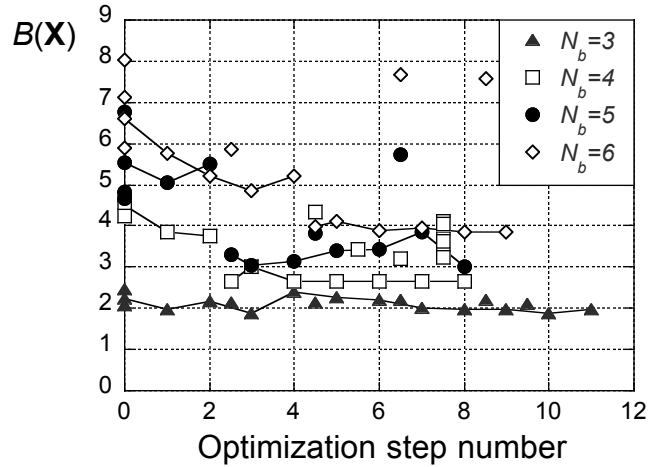
Figure 4.26: Optimization history, i.e., objective function value versus optimization step number for each of the four 3DV optimization studies..

Table 4.3: Function evaluations for the 3-bladed rotor design optimization.

Optimization Step	Rotor design, $\mathbf{X}^{3b} = [c_1 \ R_1 \ \theta_{tw,1}]^T$	Function Value, $B(\mathbf{X})$
0	$\mathbf{X}_1^{3b} = [2.5 \text{ ft } 26.8 \text{ ft } -18.0°]^T$	223.7
0	$\mathbf{X}_2^{3b} = [2.5 \text{ ft } 29.5 \text{ ft } -18.0°]^T$	206.0
0	$\mathbf{X}_3^{3b} = [2.3 \text{ ft } 26.8 \text{ ft } -18.0°]^T$	205.9
0	$\mathbf{X}_4^{3b} = [2.5 \text{ ft } 26.8 \text{ ft } -16.2°]^T$	246.0
1	$\mathbf{X}_5^{3b} = [2.3 \text{ ft } 27.9 \text{ ft } -18.7°]^T$	198.1
2	$\mathbf{X}_6^{3b} = [2.0 \text{ ft } 28.9 \text{ ft } -19.4°]^T$	217.8
additional design	$\mathbf{X}_7^{3b} = [1.9 \text{ ft } 29.5 \text{ ft } -16.2°]^T$	214.9
3	$\mathbf{X}_8^{3b} = [2.0 \text{ ft } 28.9 \text{ ft } -18.1°]^T$	187.9
4	$\mathbf{X}_9^{3b} = [1.9 \text{ ft } 29.5 \text{ ft } -17.8°]^T$	239.5
additional design	$\mathbf{X}_{10}^{3b} = [2.8 \text{ ft } 29.4 \text{ ft } -16.3°]^T$	212.6
5	$\mathbf{X}_{11}^{3b} = [2.0 \text{ ft } 29.2 \text{ ft } -18.4°]^T$	227.7
6	$\mathbf{X}_{12}^{3b} = [2.1 \text{ ft } 28.4 \text{ ft } -18.1°]^T$	218.9
additional design	$\mathbf{X}_{13}^{3b} = [2.8 \text{ ft } 27.9 \text{ ft } -17.1°]^T$	221.7
7	$\mathbf{X}_{14}^{3b} = [2.3 \text{ ft } 27.9 \text{ ft } -18.9°]^T$	201.7
8	$\mathbf{X}_5^{3b} = [2.3 \text{ ft } 27.9 \text{ ft } -18.7°]^T$	198.1
additional design	$\mathbf{X}_{15}^{3b} = [2.8 \text{ ft } 26.0 \text{ ft } -19.8°]^T$	218.7
9	$\mathbf{X}_5^{3b} = [2.3 \text{ ft } 27.9 \text{ ft } -18.7°]^T$	198.1
additional design	$\mathbf{X}_{16}^{3b} = [2.8 \text{ ft } 29.5 \text{ ft } -19.8°]^T$	211.3
10	$\mathbf{X}_{17}^{3b} = [2.0 \text{ ft } 29.2 \text{ ft } -18.1°]^T$	189.4
11	$\mathbf{X}_5^{3b} = [2.3 \text{ ft } 27.9 \text{ ft } -18.7°]^T$	198.1

Table 4.4: Function evaluations for the 5-bladed rotor design optimization.

Optimization Step	Rotor design, $\mathbf{X}^{5b} = [c_1 \ R_1 \ \theta_{tw,1}]^T$	Function Value, $B(\mathbf{X})$
0	$\mathbf{X}_1^{5b} = [1.5 \text{ ft } 26.8 \text{ ft } -18.0°]^T$	552.6
0	$\mathbf{X}_2^{5b} = [1.5 \text{ ft } 24.1 \text{ ft } -18.0°]^T$	678.1
0	$\mathbf{X}_3^{5b} = [1.4 \text{ ft } 26.8 \text{ ft } -18.0°]^T$	482.6
0	$\mathbf{X}_4^{5b} = [1.5 \text{ ft } 26.8 \text{ ft } -16.2°]^T$	466.9
1	$\mathbf{X}_5^{5b} = [1.4 \text{ ft } 27.9 \text{ ft } -17.3°]^T$	504.9
2	$\mathbf{X}_6^{5b} = [1.4 \text{ ft } 27.9 \text{ ft } -16.2°]^T$	550.7
additional design	$\mathbf{X}_7^{5b} = [2.8 \text{ ft } 29.5 \text{ ft } -19.8°]^T$	331.6
3	$\mathbf{X}_8^{5b} = [2.4 \text{ ft } 29.5 \text{ ft } -19.8°]^T$	304.0
4	$\mathbf{X}_9^{5b} = [2.1 \text{ ft } 29.5 \text{ ft } -19.8°]^T$	314.8
additional design	$\mathbf{X}_{10}^{5b} = [2.8 \text{ ft } 29.5 \text{ ft } -16.7°]^T$	383.7
5	$\mathbf{X}_{11}^{5b} = [2.6 \text{ ft } 29.5 \text{ ft } -19.8°]^T$	341.1
6	$\mathbf{X}_{12}^{5b} = [2.4 \text{ ft } 29.5 \text{ ft } -19.8°]^T$	344.6
additional design	$\mathbf{X}_{13}^{5b} = [2.8 \text{ ft } 24.1 \text{ ft } -16.2°]^T$	572.2
7	$\mathbf{X}_{14}^{5b} = [2.1 \text{ ft } 28.4 \text{ ft } -19.8°]^T$	385.0
8	$\mathbf{X}_{15}^{5b} = [2.6 \text{ ft } 29.5 \text{ ft } -19.8°]^T$	300.1

Table 4.5: Function evaluations for the 6-bladed rotor design optimization.

Optimization Step	Rotor design, $\mathbf{X}^{6b} = [c_1 \ R_1 \ \theta_{tw,1}]^T$	Function Value, $B(\mathbf{X})$
0	$\mathbf{X}_1^{6b} = [1.3 \text{ ft } 26.8 \text{ ft } -18.0°]^T$	660.7
0	$\mathbf{X}_2^{6b} = [1.3 \text{ ft } 24.1 \text{ ft } -18.0°]^T$	804.2
0	$\mathbf{X}_3^{6b} = [1.1 \text{ ft } 26.8 \text{ ft } -18.0°]^T$	713.7
0	$\mathbf{X}_4^{6b} = [1.3 \text{ ft } 26.8 \text{ ft } -16.2°]^T$	590.9
1	$\mathbf{X}_5^{6b} = [1.6 \text{ ft } 27.9 \text{ ft } -17.3°]^T$	576.6
2	$\mathbf{X}_6^{6b} = [2.0 \text{ ft } 28.9 \text{ ft } -16.6°]^T$	521.2
additional design	$\mathbf{X}_7^{6b} = [2.8 \text{ ft } 25.5 \text{ ft } -19.8°]^T$	586.6
3	$\mathbf{X}_8^{6b} = [2.3 \text{ ft } 27.9 \text{ ft } -16.2°]^T$	485.0
4	$\mathbf{X}_9^{6b} = [2.7 \text{ ft } 26.8 \text{ ft } -16.9°]^T$	521.7
additional design	$\mathbf{X}_{10}^{6b} = [2.2 \text{ ft } 29.5 \text{ ft } -19.8°]^T$	399.4
5	$\mathbf{X}_{11}^{6b} = [2.5 \text{ ft } 29.5 \text{ ft } -19.1°]^T$	412.8
6	$\mathbf{X}_{12}^{6b} = [2.5 \text{ ft } 29.5 \text{ ft } -19.8°]^T$	387.3
additional design	$\mathbf{X}_{13}^{6b} = [2.0 \text{ ft } 24.1 \text{ ft } -16.2°]^T$	767.3
7	$\mathbf{X}_{14}^{6b} = [2.8 \text{ ft } 29.5 \text{ ft } -19.1°]^T$	394.8
8	$\mathbf{X}_{15}^{6b} = [2.8 \text{ ft } 29.5 \text{ ft } -19.8°]^T$	384.8
additional design	$\mathbf{X}_{16}^{6b} = [1.8 \text{ ft } 24.1 \text{ ft } -19.8°]^T$	758.2
9	$\mathbf{X}_{15}^{6b} = [2.8 \text{ ft } 29.5 \text{ ft } -19.8°]^T$	384.8

Two-dimensional contour maps through the three-dimensional approximate objective function, $B_{app}(\mathbf{X})$, for the final optimization steps from the $N_b = 3, 5, 6$ studies are shown in Figs. 4.27–4.29, respectively (see Fig. 4.23 for the $N_b = 4$ study). The designs evaluated over the course of the procedures are depicted in the contour maps as circles and optimal designs are denoted by diamonds. The designs are plotted for the closest θ_{tw} value, and multiple designs may be overlaid in this representation if they have the same values for N_b, c, and R and similar values for θ_{tw}. Notice also that the contour plots are empty in regions where $B_{app}(\mathbf{X}) < 0$.

The convergence tolerances for the $N_b = 3, 5, 6$ studies are shown in Figs. 4.30(a)–(c), respectively (see Fig. 4.21 for the $N_b = 4$ study). Notice that the convergence tolerance was eventually satisfied, i.e., $\varepsilon_{conv} \leq 0.02$, for $N_b = 3, 4, 6$, although it was never satisfied for $N_b = 5$. Indeed, the convergence tolerance for the $N_b = 5$ study was as much as two orders of magnitude larger than those for $N_b = 3, 4, 6$ for commensurate numbers of design evaluations. This finding indicates that, even after a relatively large number of function evaluations were computed, the approximate objective function for the 5-bladed design optimization still exhibited drastic variations in its approximate objective function between optimization steps. As such, the optimization methodology struggled to converge to an optimum design. However, it still succeeded in identifying designs with significant improvement over the baseline.
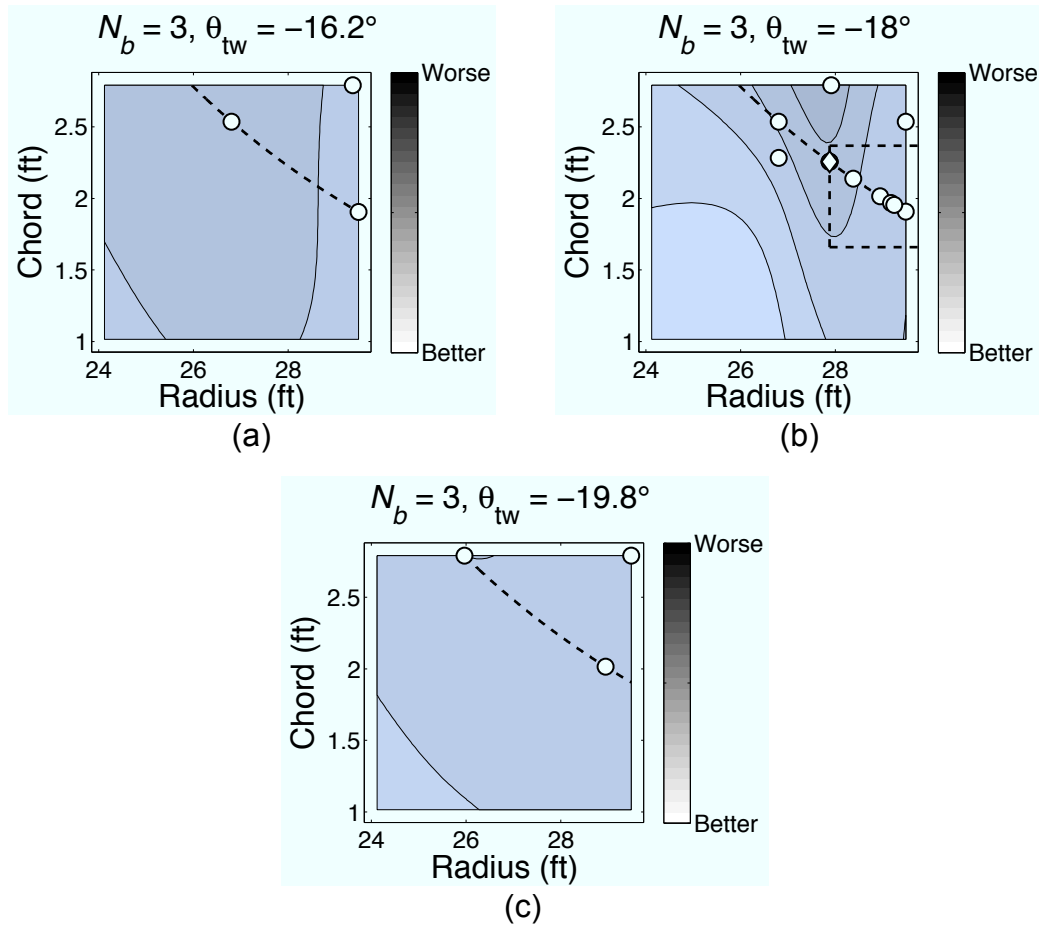
Figure 4.27: Two-dimensional contour maps through the three-dimensional approximate objective function, $B_{\text{app}}(\mathbf{X}^{3b})$, for the eleventh (and final) optimization step. Move limits are shown as dashed lines, and the region of the design space that satisfies the behavior constraint on C_T/σ is above the curved dashed line.
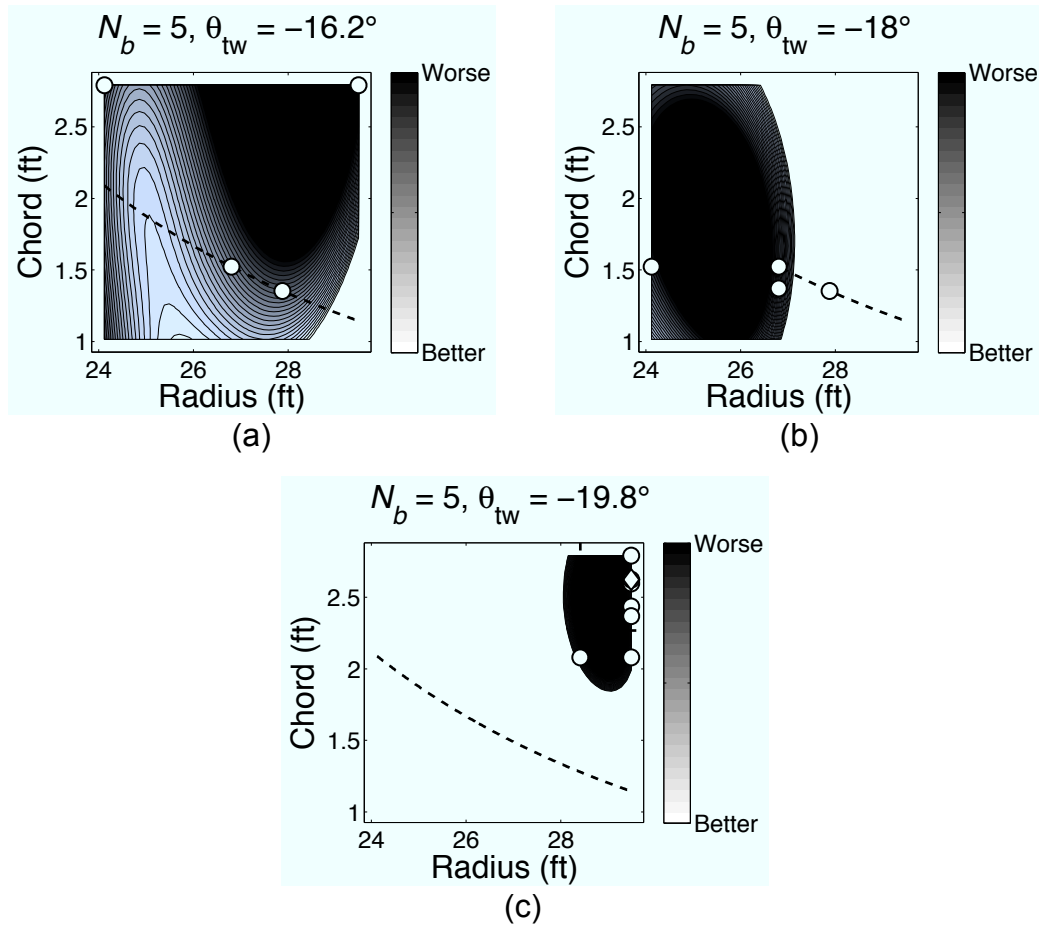
Figure 4.28: Two-dimensional contour maps through the three-dimensional approximate objective function, $B_{app}(\mathbf{X}^{5b})$, for the eighth (and final) optimization step. Move limits are shown as dashed lines, and the region of the design space that satisfies the behavior constraint on C_T/σ is above the curved dashed line.
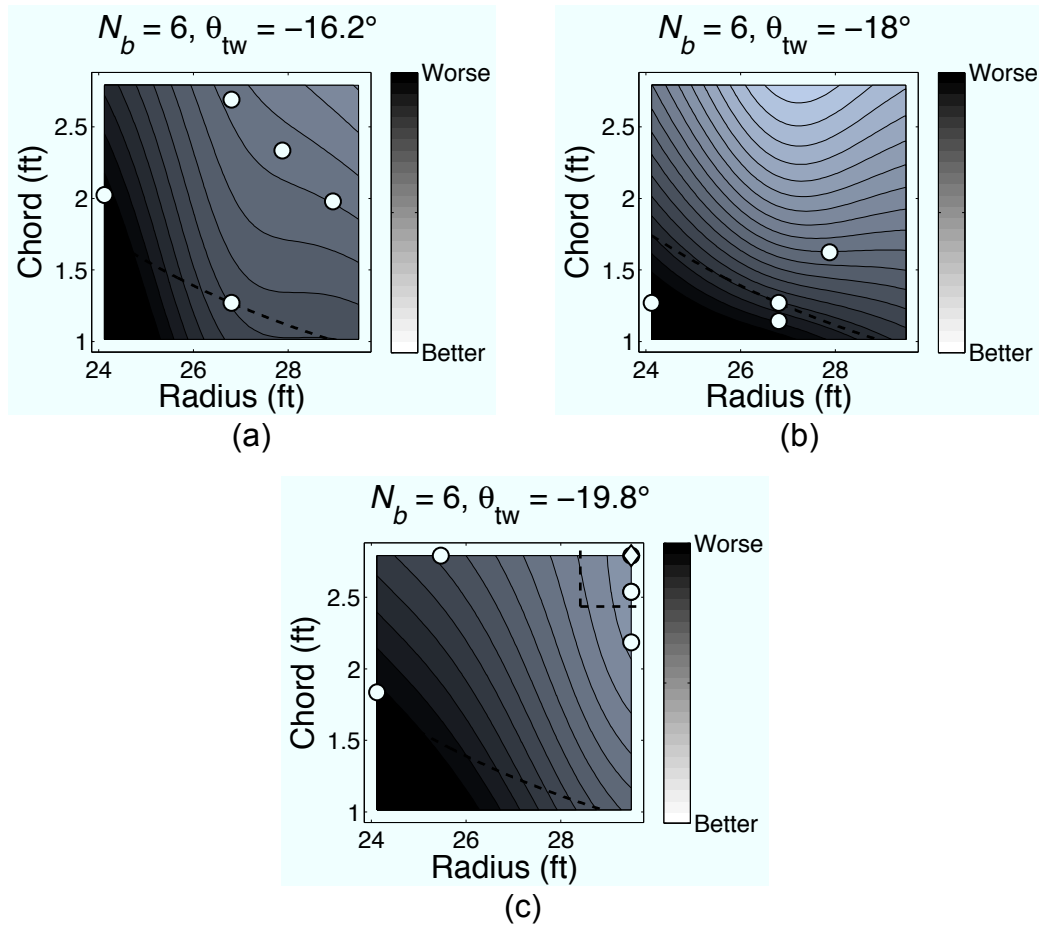
Figure 4.29: Two-dimensional contour maps through the three-dimensional approximate objective function, $B_{\mathrm{app}}(\mathbf{X}^{6b})$, for the ninth (and final) optimization step. Move limits are shown as dashed lines, and the region of the design space that satisfies the behavior constraint on C_T/σ is above the curved dashed line.
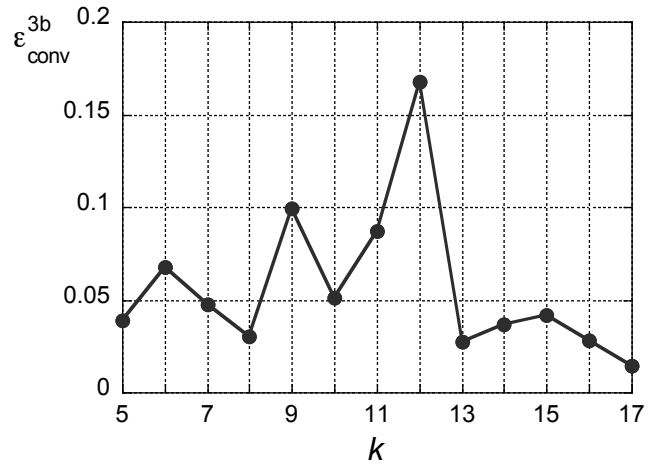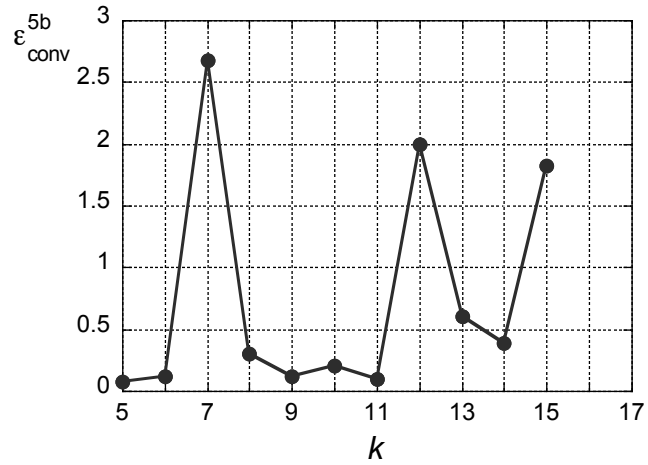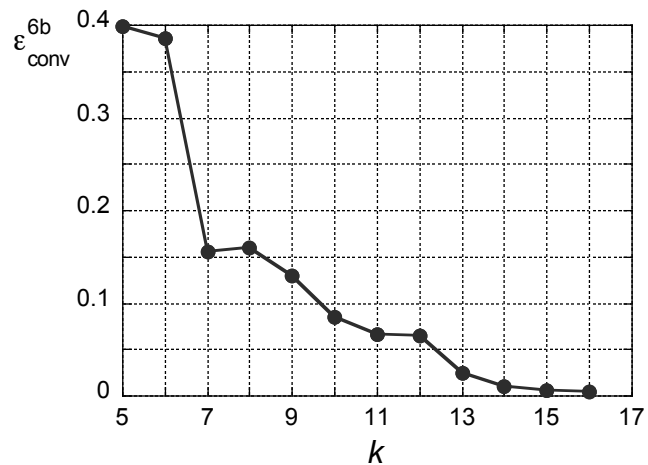
Figure 4.30: Convergence tolerance, ε_{conv}, versus total number of design evaluations, k, for (a) $N_b = 3$, (b) $N_b = 5$, and (c) $N_b = 6$.

The best designs for each of the 3DV studies were determined to be:

$$\mathbf{X}^{3b*} = \mathbf{X}_8^{3b} = [2.0\text{ ft }\ 28.9\text{ ft }\ -18.1°]^T \tag{4.35}$$

$$\mathbf{X}^{4b*} = \mathbf{X}_7^{4b} = [2.8\text{ ft }\ 29.5\text{ ft }\ -19.8°]^T \tag{4.36}$$

$$\mathbf{X}^{5b*} = \mathbf{X}_{15}^{5b} = [2.6\text{ ft }\ 29.5\text{ ft }\ -19.8°]^T \tag{4.37}$$

$$\mathbf{X}^{5b*} = \mathbf{X}_{15}^{6b} = [2.8\text{ ft }\ 29.5\text{ ft }\ -19.8°]^T \tag{4.38}$$

However, the methodology only truly "converged" for $N_b = 4$ and 6. For $N_b = 5$, the drastic variations in the approximate objective function prevented the optimization methodology from converging. For the case of $N_b = 3$, however, the optimization methodology repeatedly tried to converge to designs that were practically equivalent to $\mathbf{X}_5^{3b}$ (i.e., varying by only hundredths of an inch or hundredths of a degree in geometry) even though $\mathbf{X}_8^{3b}$ was marginally "better" than $\mathbf{X}_5^{3b}$. Although the $N_b = 3$ optimization did not formally "converge," it clearly resulted in a preferred region of the design space; notice the many designs that were evaluated along the C_T/σ constraint in Fig 4.27(b). For $N_b = 4, 6$, the optimization methodology converged to nearly identical solutions. In both instances, the optimization methodology sought to reduce blade chord, c, increase rotor radius, R, and increase blade twist rate, θ_{tw}; see Figs 4.23 and 4.29. The side constraints on all three design variables were active, and the associated C_T/σ was, therefore, the lowest possible value that could be achieved within the allowable design space.

On the basis of the 3DV optimization studies, the objective function appears to be strongly nonconvex over large portions of the design space for each study. This prop-

erty would make the B&B algorithm, as formulated in Ref. 96, unlikely to provide much benefit. This particular formulation for the B&B algorithm involves the direct linking between the optimizer and a linear objective function, and results in the solution of a sequence of linear programming (LP) problems. One benefit to this formulation is that LP problems always have optima that reside on constraints, so intermediate solutions are guaranteed to have integer values for the number of blades. To apply a similar methodology in the present study, the objective function would be approximated as a linear function and would subsequently be optimized as a MILP problem. For the present case, the objective function clearly could not reliably be approximated as a linear function. Although this particular formulation of the B&B algorithm will not work, some other formulation of may be possible if it can be demonstrated that designs with a given number of blades are always better than designs with a different number of blades. The results, however, indicated that it would be difficult to make such a claim.

This latter point can be seen in Fig. 4.31, which shows the full inventory of exact objective function values from the 3DV studies as a function of the number of blades. Although a clear trend emerges that fewer blades generally result in lower objective function values (and, therefore, less severe brownout clouds), the significant overlap between the objective function values for designs with different numbers of blades would pose challenges in the application of the B&B algorithm for this optimization problem.

227
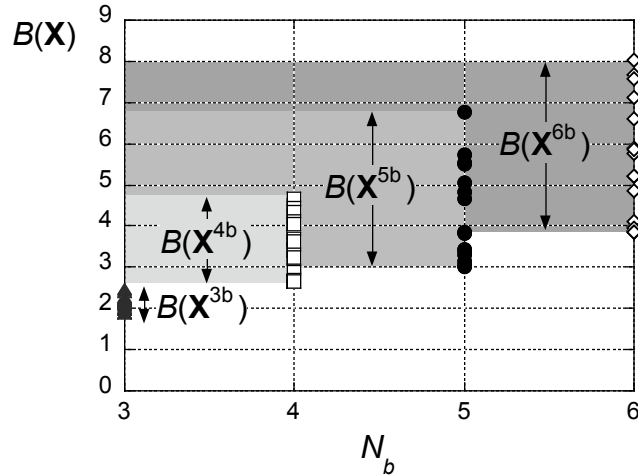
Figure 4.31: Objective function value versus number of blades for all designs in each of the four 3DV optimization studies.

Four-Design-Variable (4DV) Optimization (N_b as a variable)

A summary of the progress of the 4DV optimization study is shown in Fig. 4.32, and a listing of all of the exact function evaluations from the study is given in Table 4.6. The procedure once again begins with the evaluation of a preliminary inventory of designs. Seven initial designs are given by optimization step "zero" in Fig. 4.32 and were selected as follows: (i) the baseline design (with four blades), (ii) three designs, each defined by perturbing R, c, or θ_{tw} by ten percent (again, for four blades), and (iii) three designs, each defined by matching the baseline C_T and σ for three, five, and six blades. The optimization procedure could have commenced with just five initial designs, i.e., a baseline plus perturbations in R, c, θ_{tw}, and N_b. Nevertheless, the extra two designs were incorporated to increase the available information with respect to N_b at the outset.

The 4DV optimization procedure executed 14 steps, and it had a clear preference for 3-bladed rotor designs. In other words, it appears that the optimizer has effectively "fathomed" (to use the terminology of B&B) designs with four, five, or six blades on

228

Table 4.6: Function evaluations for the 4DV rotor design optimization.

Optimization Step	Rotor design, $\mathbf{X} = [N_b \ \ c_1 \ \ R_1 \ \ \theta_{\text{tw},1}]^T$	Function Value, $B(\mathbf{X})$
0	$\mathbf{X}_1 = [3 \ \ 2.5 \text{ ft} \ \ 26.8 \text{ ft} \ \ -18.0°]^T$	223.7
0	$\mathbf{X}_2 = [4 \ \ 1.9 \text{ ft} \ \ 26.8 \text{ ft} \ \ -18.0°]^T$	450.1
0	$\mathbf{X}_3 = [4 \ \ 1.9 \text{ ft} \ \ 24.1 \text{ ft} \ \ -18.0°]^T$	465.0
0	$\mathbf{X}_4 = [4 \ \ 1.7 \text{ ft} \ \ 26.8 \text{ ft} \ \ -18.0°]^T$	443.3
0	$\mathbf{X}_5 = [4 \ \ 1.9 \text{ ft} \ \ 26.8 \text{ ft} \ \ -16.2°]^T$	423.2
0	$\mathbf{X}_6 = [5 \ \ 1.5 \text{ ft} \ \ 26.8 \text{ ft} \ \ -18.0°]^T$	552.6
0	$\mathbf{X}_7 = [6 \ \ 1.3 \text{ ft} \ \ 26.8 \text{ ft} \ \ -18.0°]^T$	660.7
1	$\mathbf{X}_8 = [3 \ \ 2.3 \text{ ft} \ \ 27.9 \text{ ft} \ \ -18.7°]^T$	198.1
2	$\mathbf{X}_9 = [3 \ \ 2.0 \text{ ft} \ \ 28.9 \text{ ft} \ \ -19.4°]^T$	235.4
additional design	$\mathbf{X}_{10} = [6 \ \ 2.8 \text{ ft} \ \ 24.1 \text{ ft} \ \ -16.2°]^T$	765.6
3	$\mathbf{X}_{11} = [3 \ \ 2.0 \text{ ft} \ \ 28.9 \text{ ft} \ \ -18.4°]^T$	223.8
4	$\mathbf{X}_{12} = [3 \ \ 2.5 \text{ ft} \ \ 27.0 \text{ ft} \ \ -18.8°]^T$	215.8
additional design	$\mathbf{X}_{13} = [5 \ \ 2.8 \text{ ft} \ \ 29.5 \text{ ft} \ \ -17.1°]^T$	374.5
5	$\mathbf{X}_{14} = [3 \ \ 2.2 \text{ ft} \ \ 28.3 \text{ ft} \ \ -18.8°]^T$	221.5
6	$\mathbf{X}_{15} = [3 \ \ 2.3 \text{ ft} \ \ 27.6 \text{ ft} \ \ -18.4°]^T$	230.2
additional design	$\mathbf{X}_{16} = [4 \ \ 2.8 \text{ ft} \ \ 24.4 \text{ ft} \ \ -16.4°]^T$	467.0
7	$\mathbf{X}_{17} = [3 \ \ 2.4 \text{ ft} \ \ 27.5 \text{ ft} \ \ -18.9°]^T$	239.5
8	$\mathbf{X}_{18} = [3 \ \ 2.0 \text{ ft} \ \ 28.9 \text{ ft} \ \ -18.0°]^T$	220.4
additional design	$\mathbf{X}_{19} = [6 \ \ 1.7 \text{ ft} \ \ 29.5 \text{ ft} \ \ -16.2°]^T$	453.0
9	$\mathbf{X}_{20} = [3 \ \ 2.3 \text{ ft} \ \ 27.6 \text{ ft} \ \ -18.7°]^T$	238.1
10	$\mathbf{X}_{21} = [3 \ \ 2.6 \text{ ft} \ \ 26.8 \text{ ft} \ \ -19.4°]^T$	205.9
additional design	$\mathbf{X}_{22} = [3 \ \ 2.8 \text{ ft} \ \ 29.5 \text{ ft} \ \ -16.2°]^T$	213.1
11	$\mathbf{X}_{23} = [3 \ \ 2.2 \text{ ft} \ \ 28.2 \text{ ft} \ \ -18.2°]^T$	200.5
12	$\mathbf{X}_{24} = [3 \ \ 2.6 \text{ ft} \ \ 26.8 \text{ ft} \ \ -19.0°]^T$	197.8
additional design	$\mathbf{X}_{25} = [3 \ \ 2.8 \text{ ft} \ \ 26.6 \text{ ft} \ \ -16.2°]^T$	242.5
13	$\mathbf{X}_{26} = [3 \ \ 2.8 \text{ ft} \ \ 26.0 \text{ ft} \ \ -18.8°]^T$	232.9
14	$\mathbf{X}_{27} = [3 \ \ 2.3 \text{ ft} \ \ 27.9 \text{ ft} \ \ -19.7°]^T$	232.8
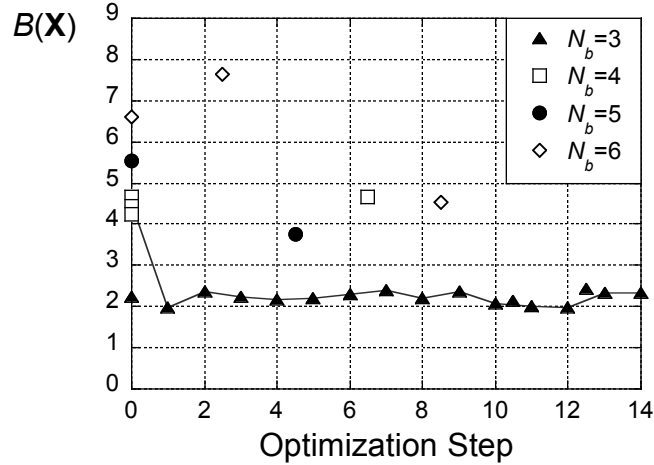
Figure 4.32: Optimization history, i.e., objective function value versus optimization step number for each of the four 3DV optimization studies..

its own, although the infusion of additional designs served to periodically confirm that it should continue on its present search direction. The additional designs are shown in Fig. 4.32 at "half-steps." Because these additional designs never resulted in improvement to the objective function, the optimization path, which is represented by a solid line in Fig. 4.32, only includes true optimization steps.

Two-dimensional contour maps through the four-dimensional approximate objective function, $B_{\mathrm{app}}(\mathbf{X})$, for the final optimization step, are shown in Figs. 4.33–4.36 for $N_b = 3$–6, respectively. The designs evaluated over the course of the procedure are depicted in the contour maps as circles, and the optimal design is denoted by a diamond in Fig. 4.33(b). The designs are plotted for the closest θ_{tw} value, and multiple designs may be overlaid in this representation if they have the same values for N_b, c, and R and similar values for θ_{tw}.

The convergence tolerance for the 4DV study is shown in Fig. 4.37, and it clearly varied as a function of the total number of design evaluations. This finding indicates that,

230
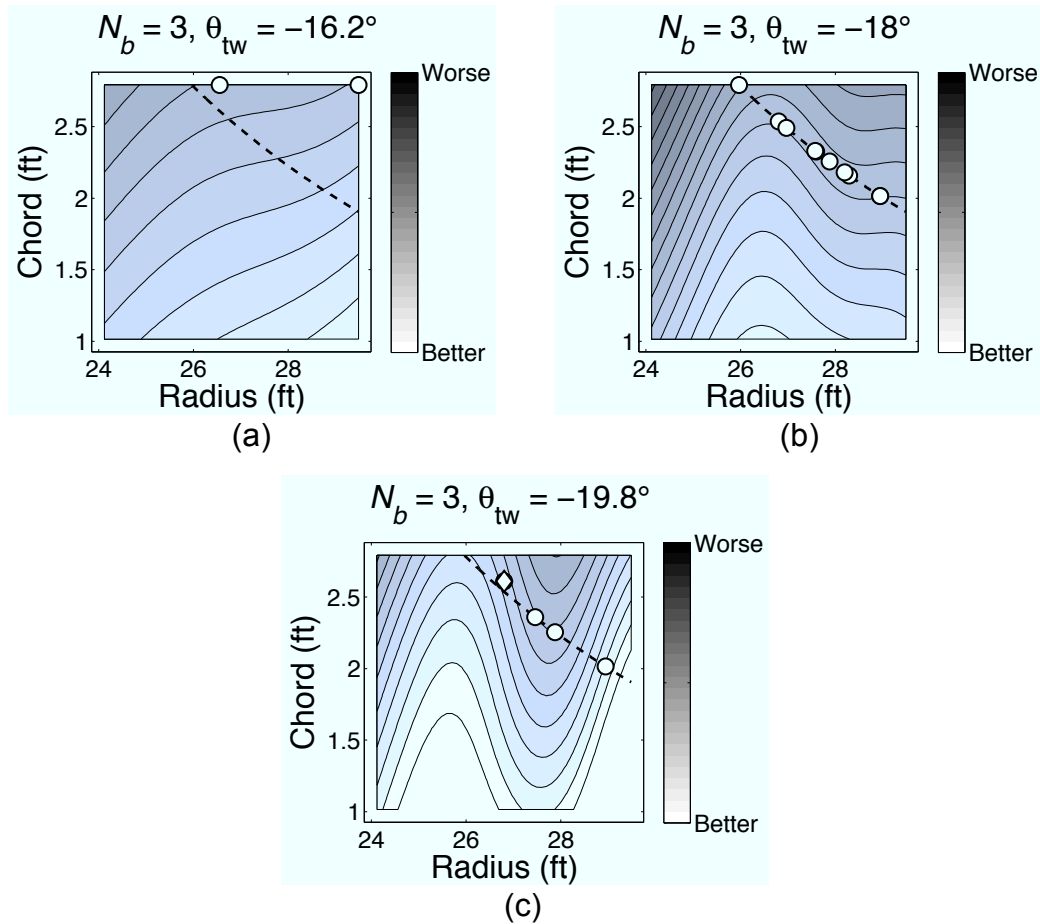
Figure 4.33: Two-dimensional contour maps through the three-dimensional approximate objective function, $B_{app}(\mathbf{X})$, for $N_b = 3$. Move limits are shown as dashed lines, and the region of the design space that satisfies the behavior constraint on C_T/σ is above the curved dashed line.
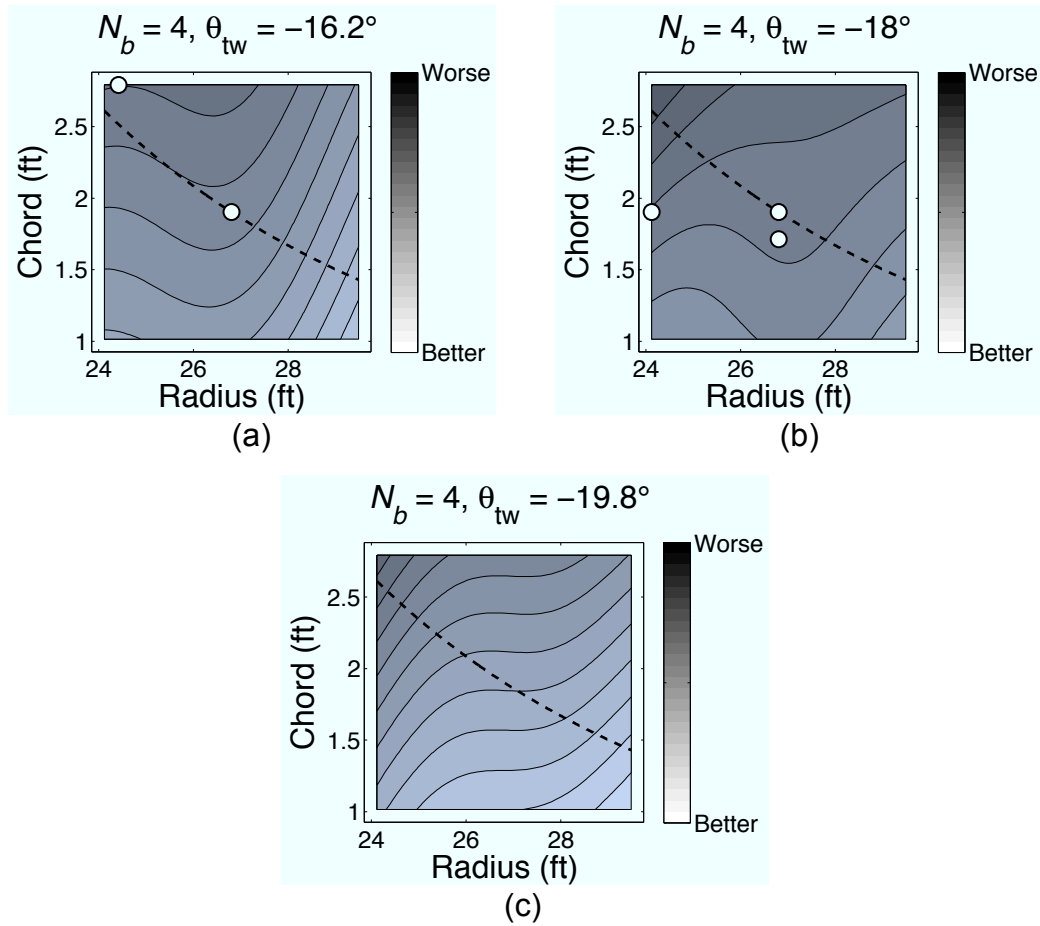
Figure 4.34: Two-dimensional contour maps through the three-dimensional approximate objective function, $B_{\text{app}}(\mathbf{X})$, for $N_b = 4$. Move limits are shown as dashed lines, and the region of the design space that satisfies the behavior constraint on C_T/σ is above the curved dashed line.
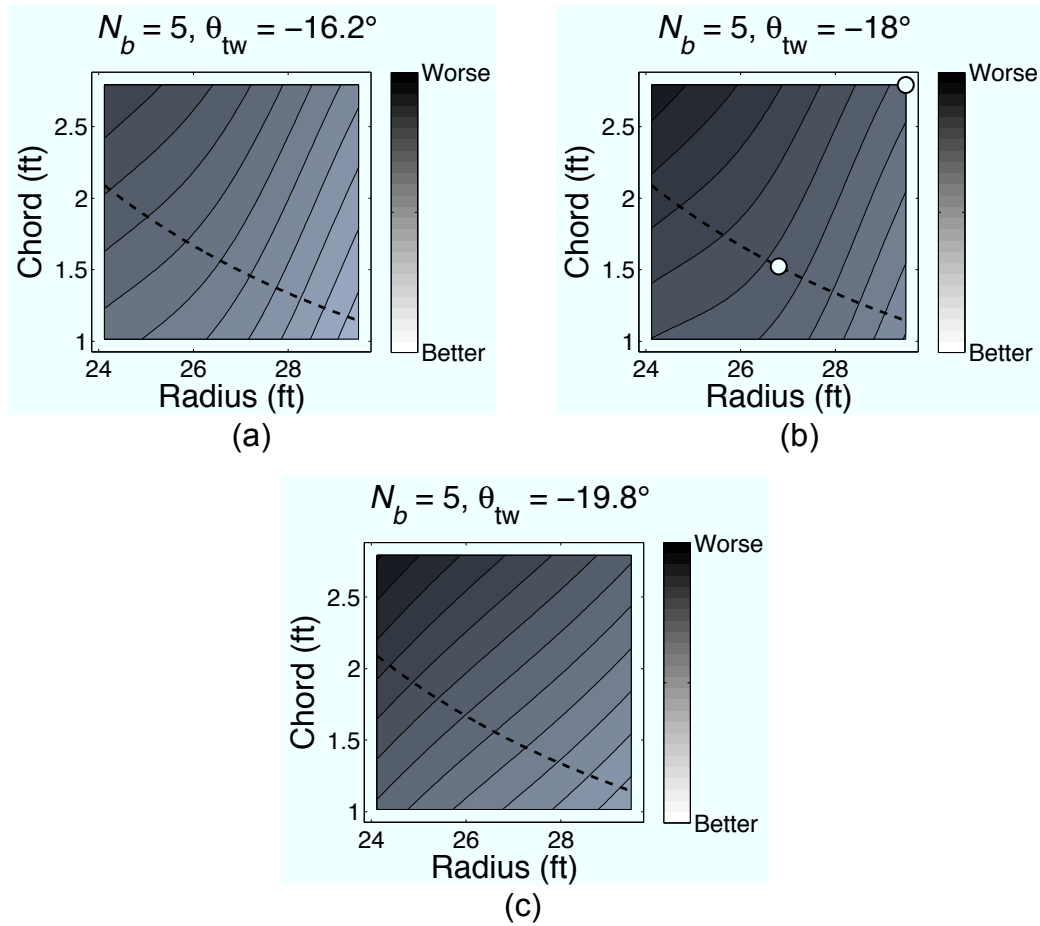
Figure 4.35: Two-dimensional contour maps through the three-dimensional approximate objective function, $B_{\text{app}}(\mathbf{X})$, for $N_b = 5$. Move limits are shown as dashed lines, and the region of the design space that satisfies the behavior constraint on C_T/σ is above the curved dashed line.
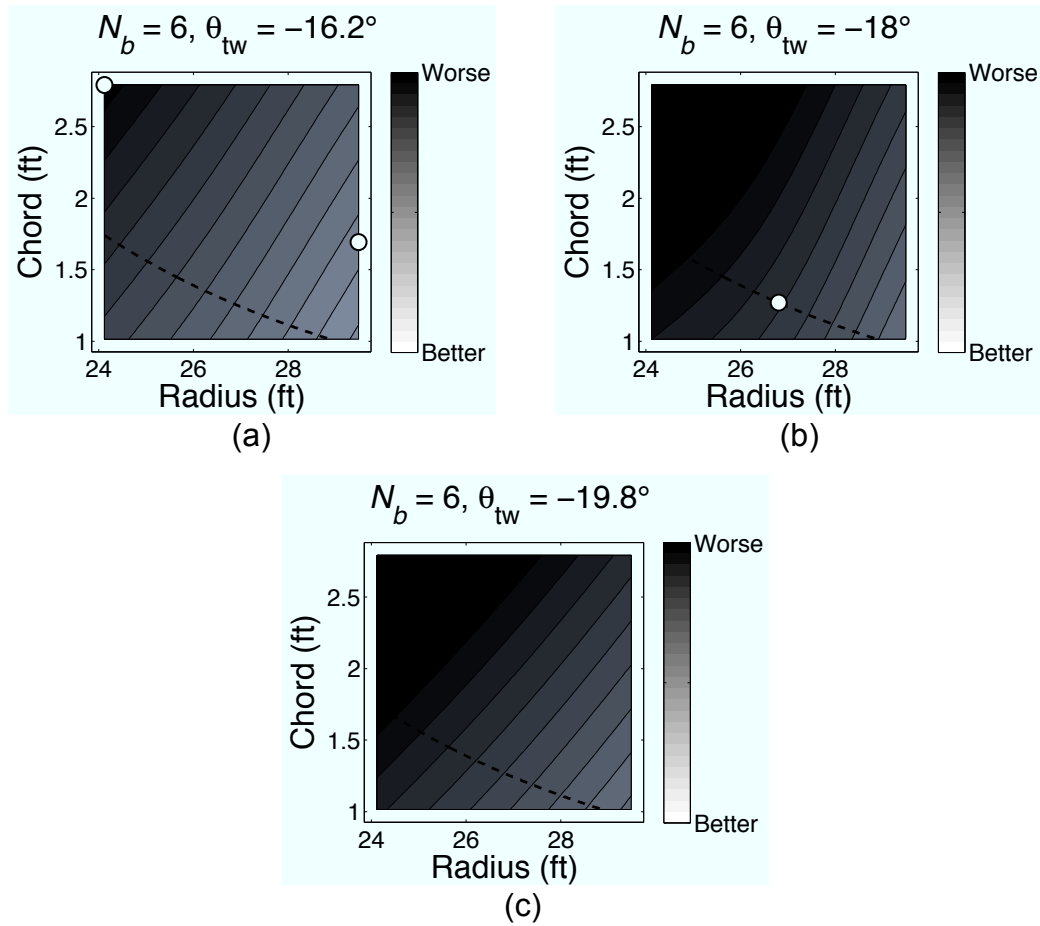
Figure 4.36: Two-dimensional contour maps through the three-dimensional approximate objective function, $B_{app}(\mathbf{X})$, for $N_b = 6$. Move limits are shown as dashed lines, and the region of the design space that satisfies the behavior constraint on C_T/σ is above the curved dashed line.
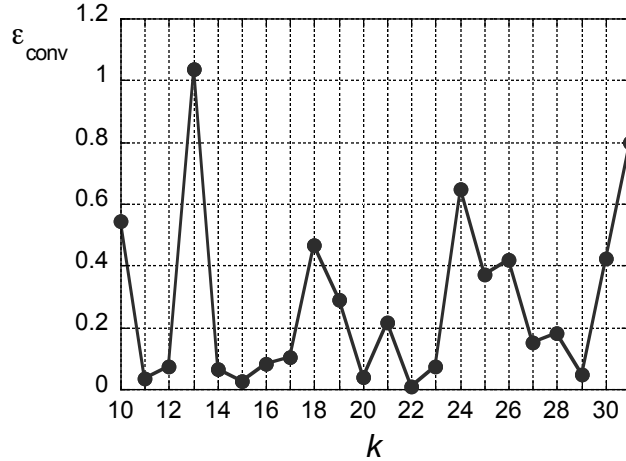
Figure 4.37: Convergence tolerance, $\varepsilon_{\mathrm{conv}}$, versus total number of design evaluations, k.

even after a relatively large number of function evaluations were computed, the approximate objective function for the 4DV optimization study still exhibited drastic variations in its approximate objective function between optimization steps. This being the case, the optimization methodology struggled to converge to an optimum design, although it succeeded in identifying designs with significant improvement over the baseline.

The best design from the 4DV study was determined to be:

$$\mathbf{X}^* = \mathbf{X}_{24} = [3 \ \ 2.6 \text{ ft} \ \ 26.8 \text{ ft} \ \ -19.0°]^T \tag{4.39}$$

This particular design is noticeably different from the overall optimum from the 3DV studies, $\mathbf{X}^{3b*} = \mathbf{X}_8^{3b} = [2.0 \text{ ft} \ \ 28.9 \text{ ft} \ \ -18.1°]^T$, and the lack of convergence between the studies is likely attributable to the nonconvexity of the objective function. In fact, the 4DV study included a design that varied from $\mathbf{X}^{3b*}$ by only tenths of an inch in radius and chord and about a tenth of a degree in twist rate, yet it was unable to converge to the same optimum. Despite their inability to converge to the same optimum, the objective

function values of the optimal designs from the 3DV and 4DV studies varied only by approximately 4%.

4.4.2   Interpretation of the Results

Physical Mechanisms

The key physical mechanisms in the brownout cloud development were again examined to gain a better understanding of the problem. Figure 4.38 shows instantaneous realizations of the flow velocities and cloud development in a longitudinal plane through the flow field for the 4-bladed optimum, $\mathbf{X}^{4b*}$, and the 3-bladed optimum, $\mathbf{X}^{3b*}$. As seen in the 4-bladed design optimization results, it was once again apparent that the initial uplift of particles could primarily be attributed to the ground vortex. It is interesting to notice, however, that the rate and geometry of the brownout cloud development can vary significantly, depending on the characteristics of the flow field.

A comparison of the flow fields and brownout clouds for the 4-bladed optimum design, Fig. 4.38(a)–(d), and the 3-bladed optimum design, Fig. 4.38(e)–(h), reveals some interesting differences. Figures 4.38(a) and (e) depict the instant for the baseline and optimum cases at which the vortex wake first impinges on the ground and forms a ground vortex. Notice that this stage occurs about a second and a half later into the approach for the 3-bladed optimum rotor design than for the 4-bladed optimum design. As the ground vortex convects forward, it tends to trap dust and uplift it into the flow field; see Fig. 4.38(b) and (f). Notice again that this stage occurs earlier in the approach for the 4-bladed optimum rotor design than for the 3-bladed optimum design. Furthermore, the

236

geometry of the developing cloud differs. Although the dust particles are, in both cases, uplifted to heights 15–20 ft above the ground, they are in closer proximity to the main rotor for the 4-bladed optimum rotor design.

The ground vortex continues to entrain the dust particles into more quiescent regions of the flow field as it convects further away from the rotor and begins to undergo a restructuring; see Fig. 4.38(c) and (g). Again, this stage occurs earlier in the approach for the 4-bladed optimum rotor design. The differences in cloud geometry appear to be even more pronounced at this stage because the 4-bladed rotor optimum design entrains dust particles at closer distances to the rotor versus the 3-bladed optimum design. The dust particles may, after some time, be reingested through the rotor disk, leading to reingestion bombardment; see Fig. 4.38(d) and (h). Reingestion bombardment precipitates a sharp increase in the volume and severity of the developing brownout cloud and occurs approximately five seconds later for the 3-bladed optimum rotor design than it does for the 4-bladed optimum design. In the context of a brownout landing, this five second difference could make the difference between a safe landing and a mishap.

A comparison of all four optimal rotor designs from the 3DV studies provides further insight. Figure 4.39 shows $b(\mathbf{X})$ as a function of time for $\mathbf{X}^{3b*}$, $\mathbf{X}^{4b*}$, $\mathbf{X}^{5b*}$, and $\mathbf{X}^{6b*}$. Recall that $b(\mathbf{X})$ indicates the particle count in the "best" region of a pilot's FOV at a given instant in time (Eq. 2.79) and is integrated over the duration of the maneuver to calculate the objective function (Eq. 2.80). For clarity, $b(\mathbf{X})$ has been normalized and smoothed, i.e., $\bar{b}(\mathbf{X})$. The plot clearly shows that the cloud develops earlier for designs with more blades. Furthermore, the number of particles in the "best" region of the pilot's FOV is
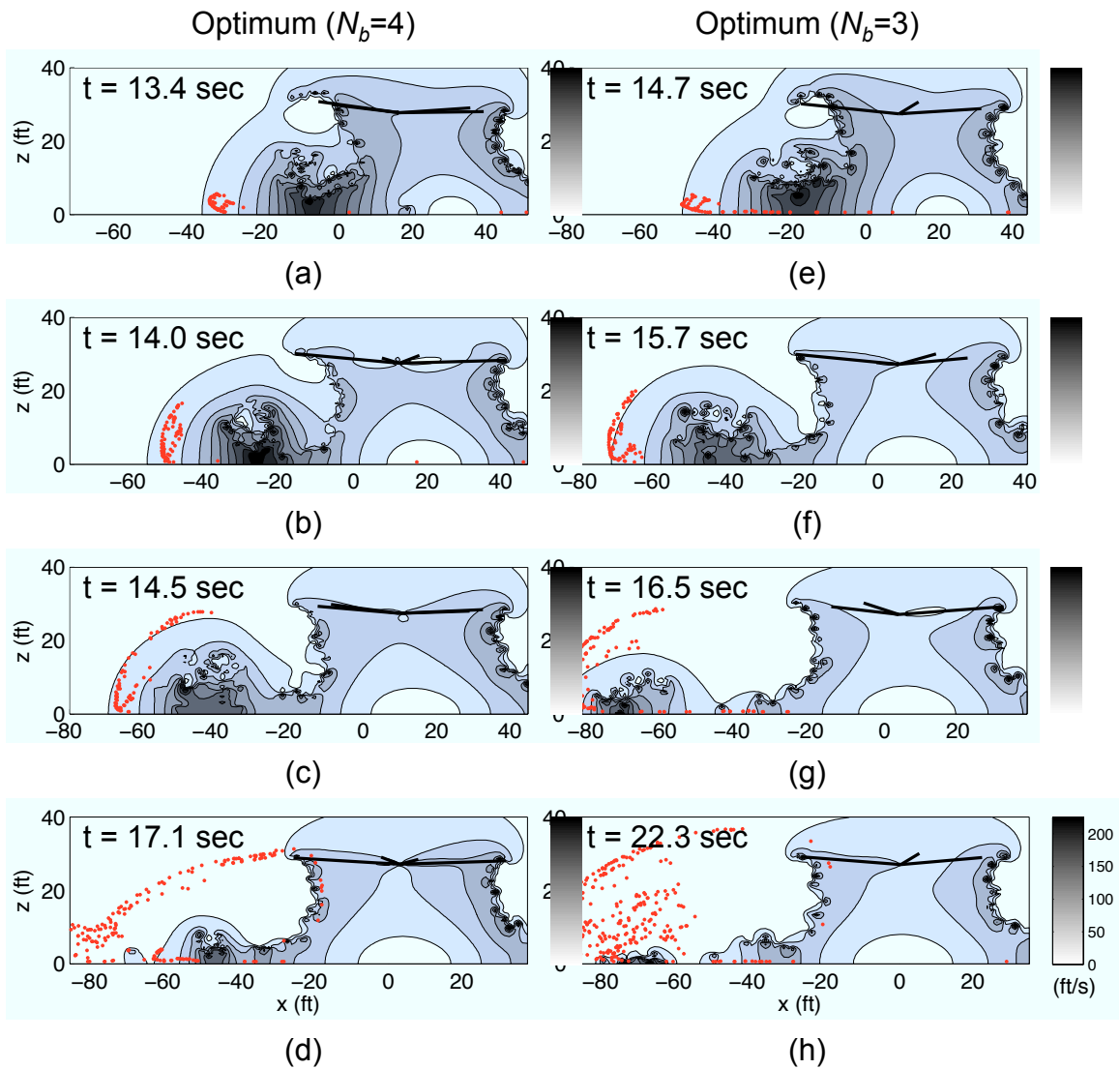
Figure 4.38: Instantaneous realizations of the flow velocity magnitudes and developing cloud in a longitudinal plane through the flow field for (a)–(d) the optimum 4-bladed design and (e)–(h) the optimum 3-bladed design.
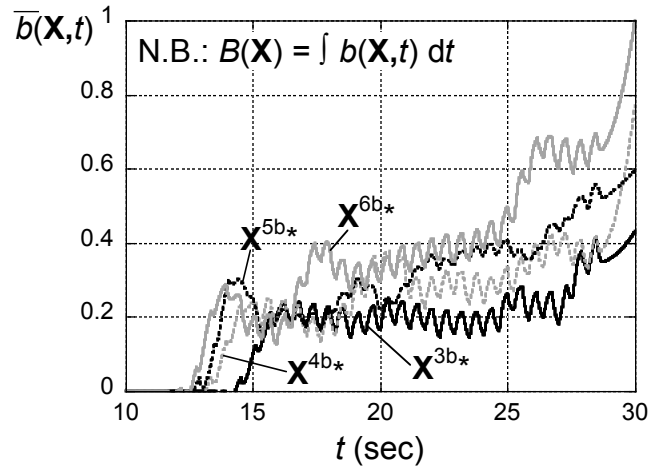
Figure 4.39: $\bar{b}(\mathbf{X})$ versus time for the optimum rotor designs from each of the 3DV optimization studies.

typically lower for fewer blades (and at all times), though this trend is less well-defined for the 4-bladed and 5-bladed rotor designs.

Design Guidelines

A benefit of the optimization procedure is that it generates a wealth of information that goes beyond the determination of a theoretical "optimum" rotor design. For example, the inventory of designs evaluated over the course of the optimization procedure provides a basis for generating parametric curves, similar to those that are oftentimes generated by parametric studies in the preliminary design process.

In the first instance, Fig. 4.40 shows relationships between the "primitive" design variables (i.e., blade chord, rotor radius, blade twist rate, and number of blades) and brownout severity (i.e., the approximate objective function, $B_{\mathrm{app}}(\mathbf{X})$) by varying each of the variables individually while holding the other variables fixed. The approximate objective function was created from all of the designs that had been evaluated, including
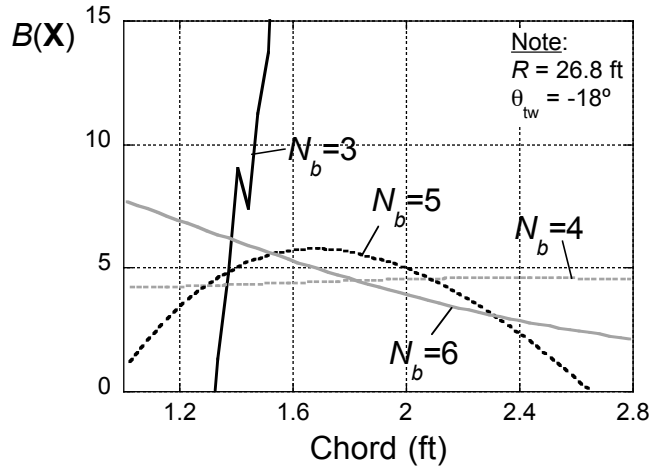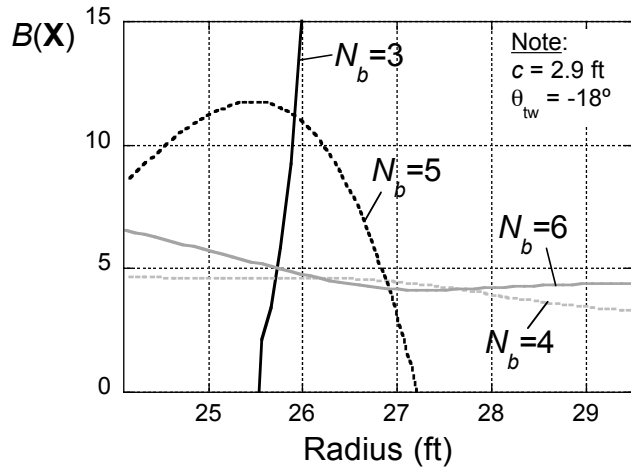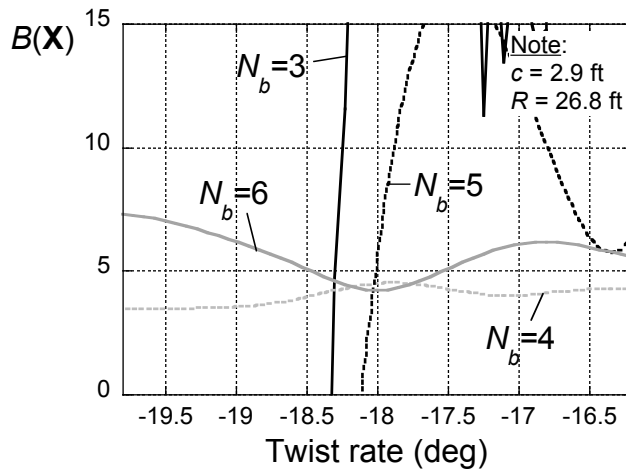
Figure 4.40: Parametric study "primitives" based on the approximate objective function, $B(\mathbf{X})$, for (a) blade chord, (b) rotor radius, and (c) blade twist rate.

those from all four 3DV studies as well as the 4DV study. It must be noted, however, that these relationships are only as good as the approximating function, and they are further prone to drastic changes depending on the values chosen for the variables that are held fixed.

Alternatively, relationships for the "primitive" design variables may be derived by fitting a quadratic polynomial to the exact objective function evaluations. Such results are shown in Fig. 4.41. First, consider the trend line shown for $N_b = 3$ in Fig. 4.41(a). The triangles represent the exact objective function values calculated for all the 3-bladed designs as a function of blade chord, and the trend line is a quadratic polynomial fit to those data. Similar trend lines may be plotted for $N_b = 4, 5, 6$. The procedure is repeated for rotor radius in Fig. 4.41(b), and blade twist rate in Fig. 4.41(c). Notice that each plot only shows the effects of two design variables (e.g., Fig. 4.41(a) shows the effects of just N_b and c on brownout severity; R and θ_{tw} are ignored). Although care must be exercised in selecting a suitable function to fit the data, the results of this procedure provide more general design guidelines than those presented in Fig. 4.40.

Notice also that, while the overall optimization methodologies selected various configurations of blade number, blade chord, blade twist rate, and rotor radius over the course of the present work, many other system-level design parameters were varied in the process. Some of these design parameters include:

1. Thrust coefficient, $C_T = T/\rho A (\Omega R)^2$.

2. Rotor solidity, $\sigma = N_b c / \pi R$.

3. Blade loading coefficient, C_T / σ.
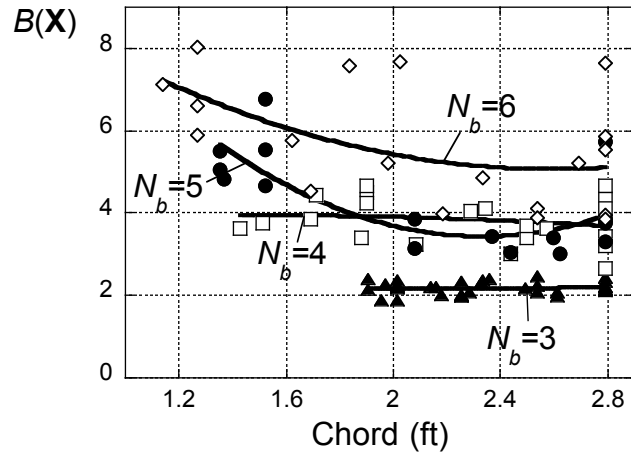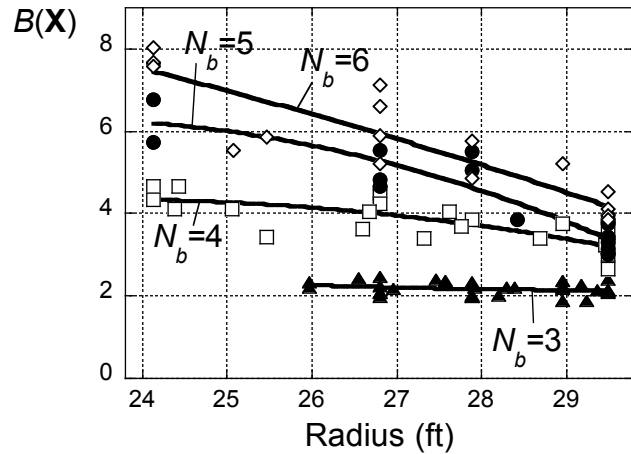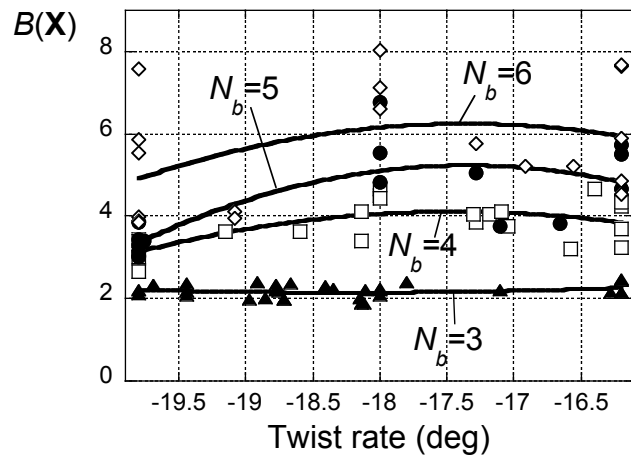
Figure 4.41: Parametric study "primitives" based on second-order polynomial fits for (a) blade chord, (b) rotor radius, and (c) blade twist rate.

4. Wake frequency, $\Omega_s = N_r N_b \Omega$ (Ref. 9).

5. Normalized wake-reduced frequency, $k_s = \Omega_s c / 2\Omega R$ (Ref. 9).

6. Blade tip vortex strength, $\Gamma_v \approx k(C_T/\sigma)(\Omega R)c$.

7. Total wake strength, $\Gamma_w = N_r N_b \Gamma_v$.

8. Disk loading, $DL = T/A$.

9. Average downwash velocity, $w = 2\sqrt{T/2\rho A}$.

It should be noted that some of these parameters may tend to simplify the complex physics at play in the problem. For example, the expression for blade tip vortex strength is strictly valid for an "ideal" rotor operating in hover. While this expression gives an approximation of the strength of the blade tip vortex filaments that are trailed into the rotor wake, the ultimate strength of a blade tip vortex as it impinges on the ground is affected by the instantaneous blade lift. While the use of these parameters may be a simplification of the physics, they do provide a quantitative basis for comparison between the primary features of competing designs.

Figure 4.42 shows similar trend lines to those presented in Fig. 4.41, although for three system-level design parameters rather than the "primitives" shown in Fig. 4.41. In particular, Fig. 4.42 shows the relationship of brownout severity (i.e., objective function value) to (a) disk loading, DL, (b) wake-reduced frequency, k_s, and (c) tip vortex strength, Γ_v.

Figure 4.42(a) indicates that the objective function has been reduced, and hence brownout severity may be reduced, by decreasing the disk loading for a given number

of blades. This result is in direct contradiction with claims in the literature that a high disk loading results in more benign brownout signatures. A physical explanation for this result may be made by citing the fact that DL is directly related to the average downwash velocity, w, which may be considered to be a reasonable first-order approximation to the expected maximum average groundwash velocity during landing or takeoff operations (Ref. 9). Furthermore, it is interesting to notice that the results in Fig. 4.42(a) clearly indicate that the rotor disk loading alone is not a strong indicator of brownout severity.

Although Fig. 4.42(b) indicates that it is more difficult to identify a clear relationship between the wake-reduced frequency, k_s, and brownout severity, it is interesting to notice that the trend lines exhibit clear minima depending on the number of blades. This result indicates that there may be an optimal blade tip speed for a given rotor design for brownout mitigation. This result is potentially of a high practical significance, because it implies that it may be possible to mitigate brownout through the variation of the blade tip speed during the final stages of a brownout approach.

Finally, Fig. 4.42(c) indicates that the objective function may be reduced (and brownout severity, likewise, reduced) by minimizing the strength of the individual tip vortices (for constant N_b). It is interesting to notice, however, that the sensitivity of the brownout severity to tip vortex strength appears to be strongly linked to the number of blades. For example, the objective function is much more sensitive to the strengths of the individual tip vortices for 6-bladed designs than for 3-bladed designs. This result implies that the strength of the individual vortices (at least within some range) is secondary to the interactions between the tip vortices in affecting brownout severity. Notice that the
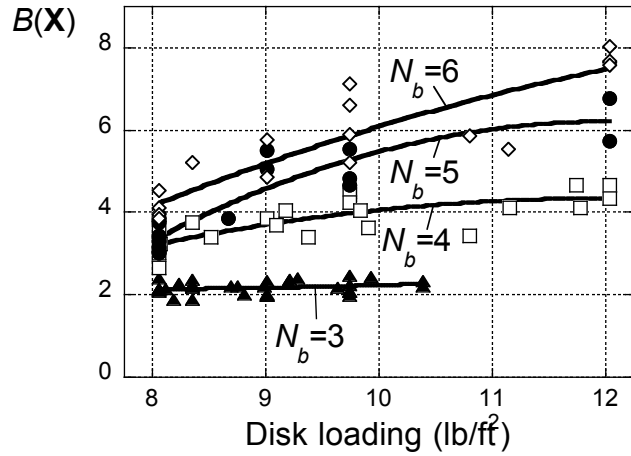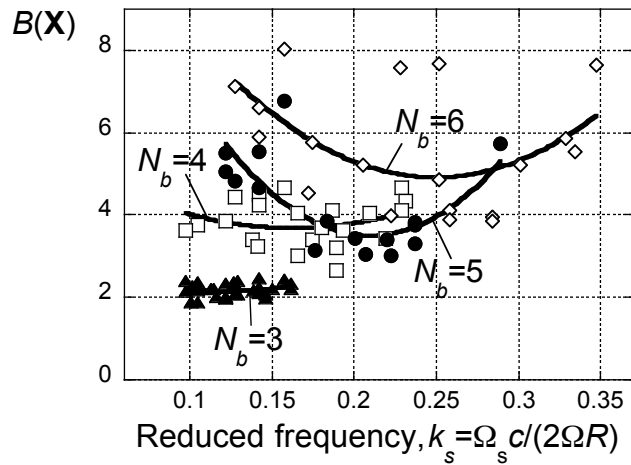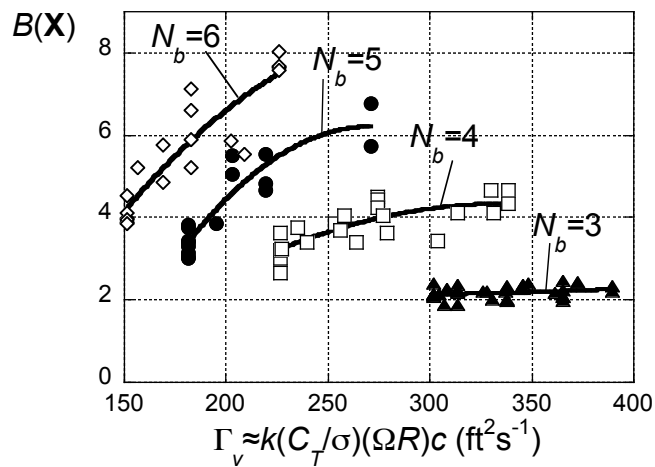
Figure 4.42: Parametric studies of (a) disk loading, *DL*, (b) wake-reduced frequency, k_s, and (c) tip vortex strength, Γ_v.

details of the unsteady boundary layer and turbulence spectra, although not considered

in this simulation methodology, may also affect the development of the brownout cloud.

The results must be considered in this context.

Part II

Brownout Characterization

Chapter 5

Measurements of the Visual Degradation Caused by a Brownout Cloud

A number of methods for characterizing brownout were cited in Chapter 1, although it was noted that none of these methods have been based upon quantitative measures of the visual obscuration that a pilot experiences as a result of the brownout cloud. As such, the approach of the present work is to propose a method for characterizing the severity of a brownout cloud by its optical properties, specifically by the ways in which the dust in the cloud absorbs and scatters incident light.

In the first instance, the efficacy of the Modulation Transfer Function (MTF) in characterizing brownout was examined in two flight test campaigns. The specific goals of these tests were:

1. To adapt existing optics test techniques for the purposes of extracting MTF measurements from rotorcraft flight testing in brownout conditions.

2. To report MTF measurements obtained from brownout flight testing.

3. To develop image processing techniques for automating MTF extraction.

4. To explore new methods for interpreting the temporal and spatial variations of the brownout cloud to provide insight into the cloud's development.

5. To determine practical guidelines for future MTF testing (e.g., camera selection, optical target design, etc.).
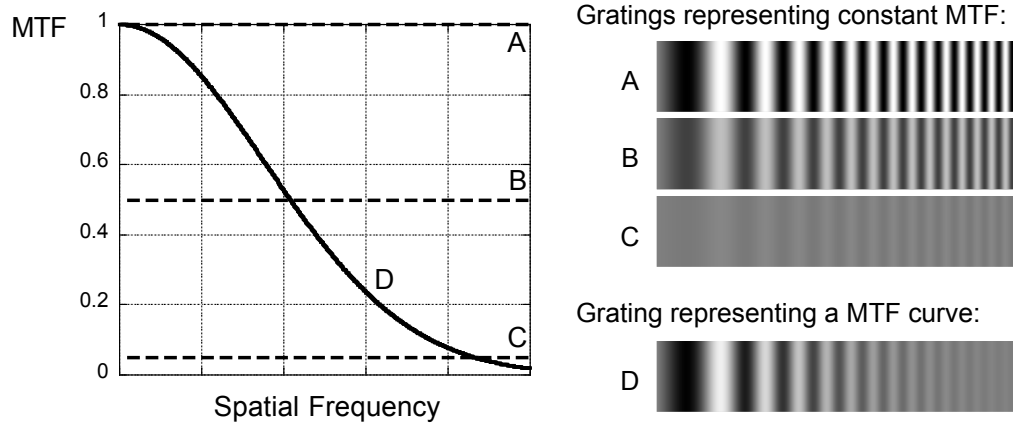
Figure 5.1: MTF axes with constant-MTF lines A–C and representative MTF curve D, with corresponding increasing-frequency sine-wave gratings.

5.1 The Modulation Transfer Function (MTF)

The Modulation Transfer Function (MTF) is a measure of the loss of contrast and resolution caused by an optical medium. Representative MTF axes are shown in Fig. 5.1. Dashed lines of constant MTF (labeled A through C) represent constant contrast at all spatial frequencies, as depicted by the increasing-frequency sine-wave gratings A through C. Note that MTF $= 1$ corresponds to 100% contrast, MTF $= 0.5$ corresponds to 50% contrast, and so forth. In reality, the MTF will vary with spatial frequency, as given by curve D in Fig. 5.1. This result corresponds to a reduction in contrast with increasing spatial frequency, as given by grating D.

In linear optics, the image irradiance (H_i, the radiant power per unit area perceived by the imaging device) can be described by the convolution of the object irradiance (H_o, the irradiance of the object being viewed) with the Point Spread Function (PSF), i.e.,

$$H_i\left(x',y'\right) = \int_{-\infty}^{\infty}\int_{-\infty}^{\infty} H_o\left(x,y\right)s\left(x'-x,y'-y\right)dx\,dy \qquad (5.1)$$
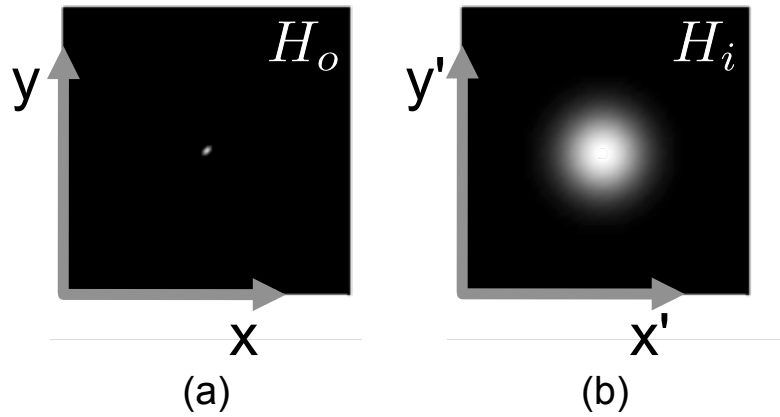
Figure 5.2: The Point Spread Function (PSF).

where (x', y') describes coordinates in the image plane, (x, y) describes coordinates in the object plane, and $s(x', y')$ is the PSF, which describes the spreading of irradiance of a point image. An example of the PSF is shown in Fig. 5.2, in which the object is a single point that is spread by a two-dimensional Gaussian PSF to yield the image. The figure could represent the behavior of a hypothetical optical instrument, such as a camera lens or a telescope. From a practical standpoint, the PSF is a result of the combination of effects from all components of the imaging *system*, where *system* is inclusive of everything from the imaging equipment to the environment through which the image is transmitted.

The Optical Transfer Function (OTF) is defined as the Fourier transform of the PSF, scaled to provide a maximum value of unity,i.e.,

$$
\mathrm{OTF} = \frac{\int_{-\infty}^{\infty} \int_{-\infty}^{\infty} s(x', y') \exp\left\{-j\left(\omega_x x' + \omega_y y'\right)\right\} dx' \, dy'}{\int_{-\infty}^{\infty} \int_{-\infty}^{\infty} s(x', y') \, dx' \, dy'}
$$

$$
= \frac{S(\omega_x, \omega_y)}{S(0,0)} = \mathrm{MTF} \exp(j\mathrm{PTF}) \tag{5.2}
$$

where PTF is the Phase Transfer Function (which is not as important as the MTF in describing resolution, Ref. 84) and $S(\omega_x, \omega_y)$ is the Fourier transform of the PSF, in terms of spatial frequency, ω. It should be noted that, although the dividing by $S(0,0)$ normalizes the resulting MTF curve to a maximum value of unity, it is not uncommon for multiple MTF curves to be normalized to a common baseline for the purposes of relative comparison.

A conceptual analogy can be drawn between the OTF and the transfer function of a mechanical system, in which case the irradiance of the object (e.g., the ground, the sky, mountains, trees, etc.) corresponds to the forcing function, and the irradiance in the image plane (e.g., the pilot retina or the focal plane of a camcorder) corresponds to the mechanical system output. Measuring the MTF, then, is analogous to extracting the magnitude of the frequency response of a mechanical system through nonparametric system identification techniques.

The role of the frequency sweep input for mechanical systems is taken by appropriate test patterns, as shown in Fig. 5.3. While a variety of patterns may be utilized, they generally consist of alternating black and white regions with varying spatial frequency. The spatial frequency can be defined as the number of black/white cycles per degree subtended in the field of view of the imaging system. The patterns conceptually closest to a frequency sweep are those in which the frequency increases linearly along some dimensions, such as the Siemens star, Fig. 5.3(c), where the frequency increases by moving toward the center of the star.
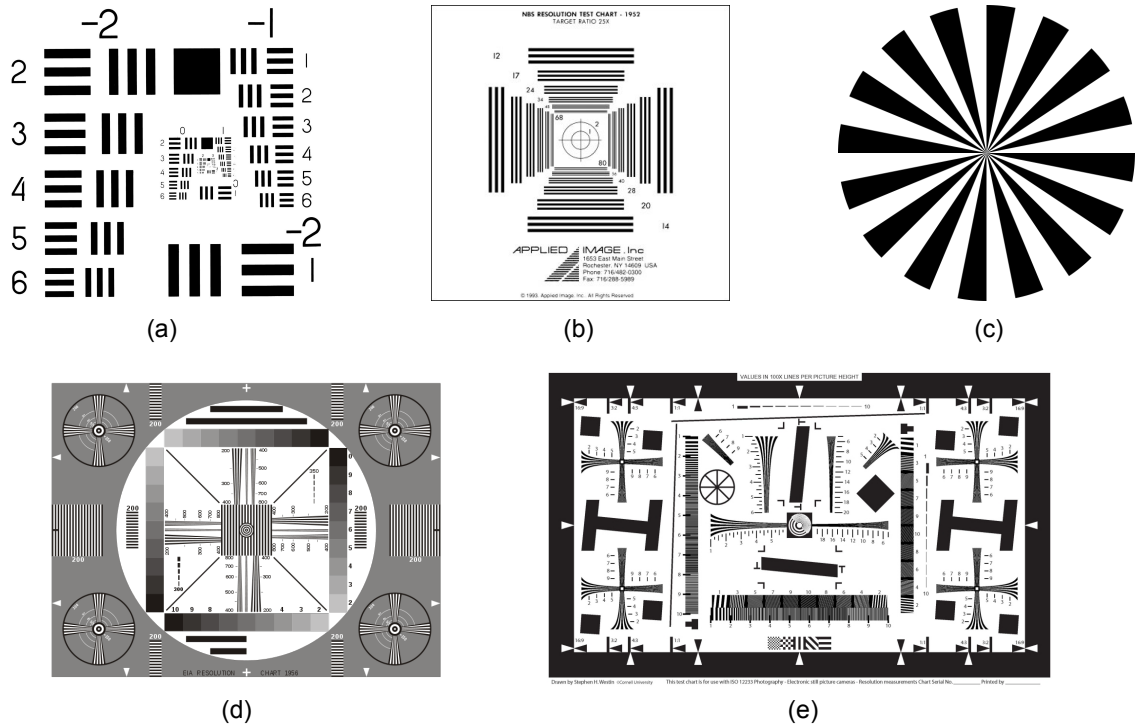
Figure 5.3: Typical test patterns: (a) USAF 1951, (b) NBS, (c) Siemens Star, (d) EIA, and (e) ISO 12233 resolution charts.

5.2 Proof of Concept Testing

An initial brownout flight testing campaign afforded a unique opportunity to perform proof-of-concept MTF testing in actual brownout conditions. For these tests, a utility helicopter was flown over a desert surface in a sequence of approaches. Specially-designed test targets were fabricated. Images were recorded, as seen through the developing brownout cloud, from two vantage points. Two methods for MTF extraction were adapted from prior optics research to calculate MTFs along optical paths through the brownout cloud, and methods for automating the MTF extraction process were examined. The present study provided not only a proof-of-concept for the use of the MTF in characterizing brownout, but also important practical information on how to perform such

252

tests in the future (e.g., which methods work best, what equipment is necessary, how test patterns should be designed, where test patterns should be positioned, etc.).

5.2.1   Test Methodology

Two methods are presented for calculating the MTF of a brownout cloud from flight tests: (i) square wave response and (ii) edge response. In the present study, each of these methods is utilized in the analysis of data from two viewpoints: (i) outside the brownout cloud, looking in, toward an optical target placed on the helicopter, and (ii) inside the brownout cloud, looking out, toward an optical target placed on the ground. Results are presented for each case, and practical limitations are discussed.

Square-Wave Response Method

The square-wave response method involves the calculation of the contrast degradation of test patterns such as those shown previously in Fig. 5.3. This method has been used extensively in the optics community to characterize imaging systems (Ref. 84). Its primary strengths include intuitiveness and ease of calculation. This procedure does not yield the MTF, but rather the closely related Modulation *Contrast* Function. The discussion will continue to be in terms of the MTF, however, because the square-wave response is often used as a surrogate (Refs. 76, 84).

The first step is the design of a suitable test pattern to span a range of spatial frequencies. For the brownout testing of the present study, two test patterns were designed (see Fig. 5.4). The sharp black-white transitions of each portion of a test pattern can be
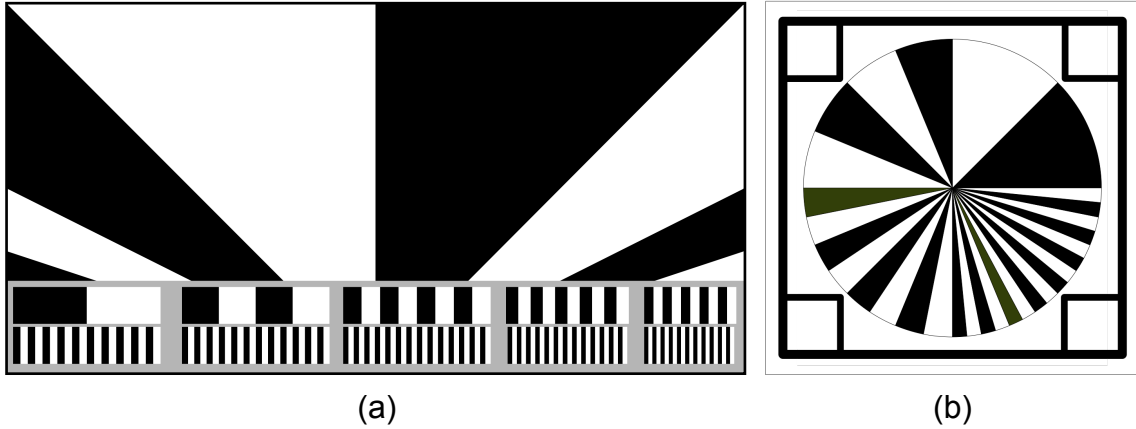
Figure 5.4: Test patterns utilized for brownout testing: (a) the "ground target", and (b) the "aircraft target."

considered as square-wave input signals at specific spatial frequencies (versus sine-wave inputs, which would rigorously yield the MTF, and which would transition between black and white through continuous shades of gray).

For the ground-based test pattern (shown in Fig. 5.4(a), and referred to as the "ground target"), the upper portion of the target features a radial design such that the the spatial frequency increases from one horizontal cycle per pattern width at the top to four horizontal cycles per pattern width at the bottom of the radial portion of the pattern. Beneath the radial portion, ten constant frequency "blocks" are positioned, with spatial frequencies ranging from five to 90 cycles per pattern width. To calculate the angular spatial frequency in the top portion of the target, then, the only required information is the angular size of the pattern width in the field of view. For example, if the width of the pattern subtends $10°$ in the field of view of the camera, the top of the pattern would correspond to a spatial frequency of 1 cycle/pattern width $\times$ 1 pattern width/$10° = 0.1$ cycles per degree. Similarly, a modified Siemens star (shown in Fig. 5.4(b) and referred to as the "aircraft target") was chosen as a test pattern to be applied to the side of the aircraft. Each quadrant

of the pattern contains a different range of spatial frequencies, and the alternating wedges result in increasing spatial frequencies as the center of the pattern is approached.

To calculate the MTF in a given image, the contrast in the test pattern was evaluated at a variety of spatial frequencies. An example is given in Fig. 5.5, in which the contrast in the ground target is evaluated at 12 spatial frequencies (labeled 'a' through 'l'). In the example, two of the frequencies are measured from the top portion of the test pattern, and 10 of the frequencies are measured from the blocks at the bottom of the test pattern. For each spatial frequency, the contrast between black and white is quantified and plotted. In practice, the contrast of the test pattern is attenuated as the brownout cloud develops between the imaging system and the test pattern, and a degraded image is captured by the imaging system. This results in a decrease in the magnitude of the response shown in the MTF plot, as well as a drop-off in MTF that will occur at higher spatial frequencies. Although this method is easy to understand and implement, significant noise can be introduced into the measurements by non-uniformities in the brownout cloud density over the area of the optical target.

Edge Response Method

Another method for calculation of the MTF consists of analyzing the black-white transition of a single edge (Refs. 78, 84), rather than a full optical pattern. The primary strength of this method is its broad applicability because it eliminates the need for a prefabricated test pattern. In fact, the method can be implemented on any edge in the visual scene that exhibits sufficient contrast. In comparison with the square-wave response
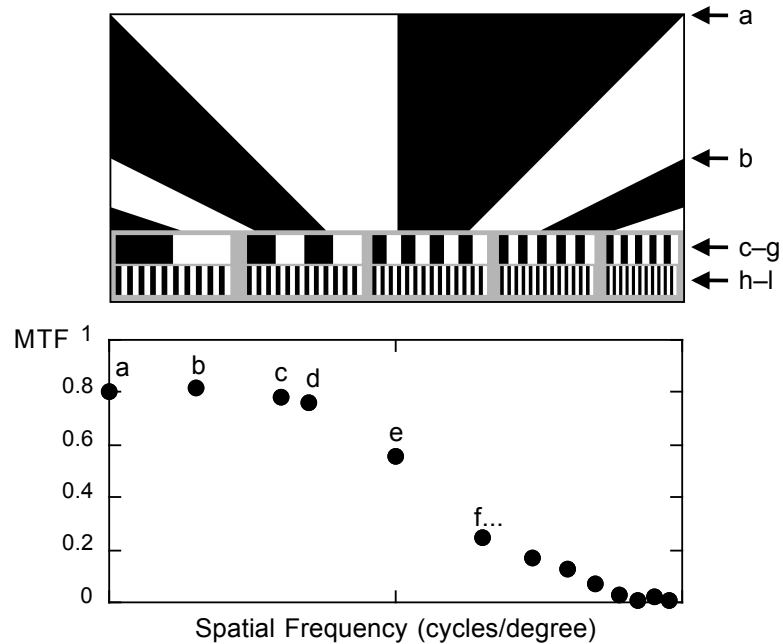
Figure 5.5: Schematic of the basic methodology for calculating the MTF using the square-wave response.

method, which can only yield MTF measurements for a small portion of the camera FOV (i.e., the MTF is obtained only for the direct path between the camera and the target), the edge response method can be used to calculate the MTF anywhere in the camera FOV that contains a suitable edge. The edge response method can even be used to calculate MTFs for multiple regions of the same frame, thus providing a unique capability to characterize the spatial variation of the brownout cloud. Another advantage to the edge response method is its ability to determine MTF values over the full range of spatial frequencies, whereas the square-wave response will only yield measurements at the spatial frequencies contained in the test pattern. Although the complexity of the post-processing is greater than for the square-wave response method, the calculations can still be performed with relatively low computational cost.

An overview of the edge response method is given in Fig. 5.6. For a given edge,

such as the one shown in Fig. 5.6(a), a mathematical "Edge Response Function" (ERF) can be defined as the grayscale level variation (or "response") along a line normal to the edge of interest. Notice that, for a typical edge, there is some distance over which the transition from dark to light occurs. The ERF is then approximated by a suitably-scaled Gaussian Cumulative Distribution Function (CDF), as shown in Fig. 5.6(b). This fitting process can be automated by defining the limits of the "edge" region as the points at which a rolling average of the grayscale response converges to a consistent value. Variations from image noise can be minimized by averaging the edge response over multiple closely-spaced (e.g., separated by a few pixels) parallel lines that are normal to the edge.

The derivative of the ERF gives the edge spread function, ESF, i.e.,

$$\frac{d}{dx}\text{ERF}(x) = \text{ESF}(x) \tag{5.3}$$

as shown in Fig. 5.6(c). The maximum value of the ESF corresponds to the location that is most likely the "true edge," though the edge is spread out because of imperfections in the imaging system.

It is apparent that the ESF, also referred to as the "Line Spread Function" (LSF) is the one-dimensional analogue to the two-dimensional PSF in Eq. 5.2. Similarly, then, the Fourier transform of the ESF yields the MTF, i.e.,

$$\mathcal{F}[\text{ESF}(x)] = \text{MTF}(\omega_x) \tag{5.4}$$

as shown in Fig. 5.6(d).
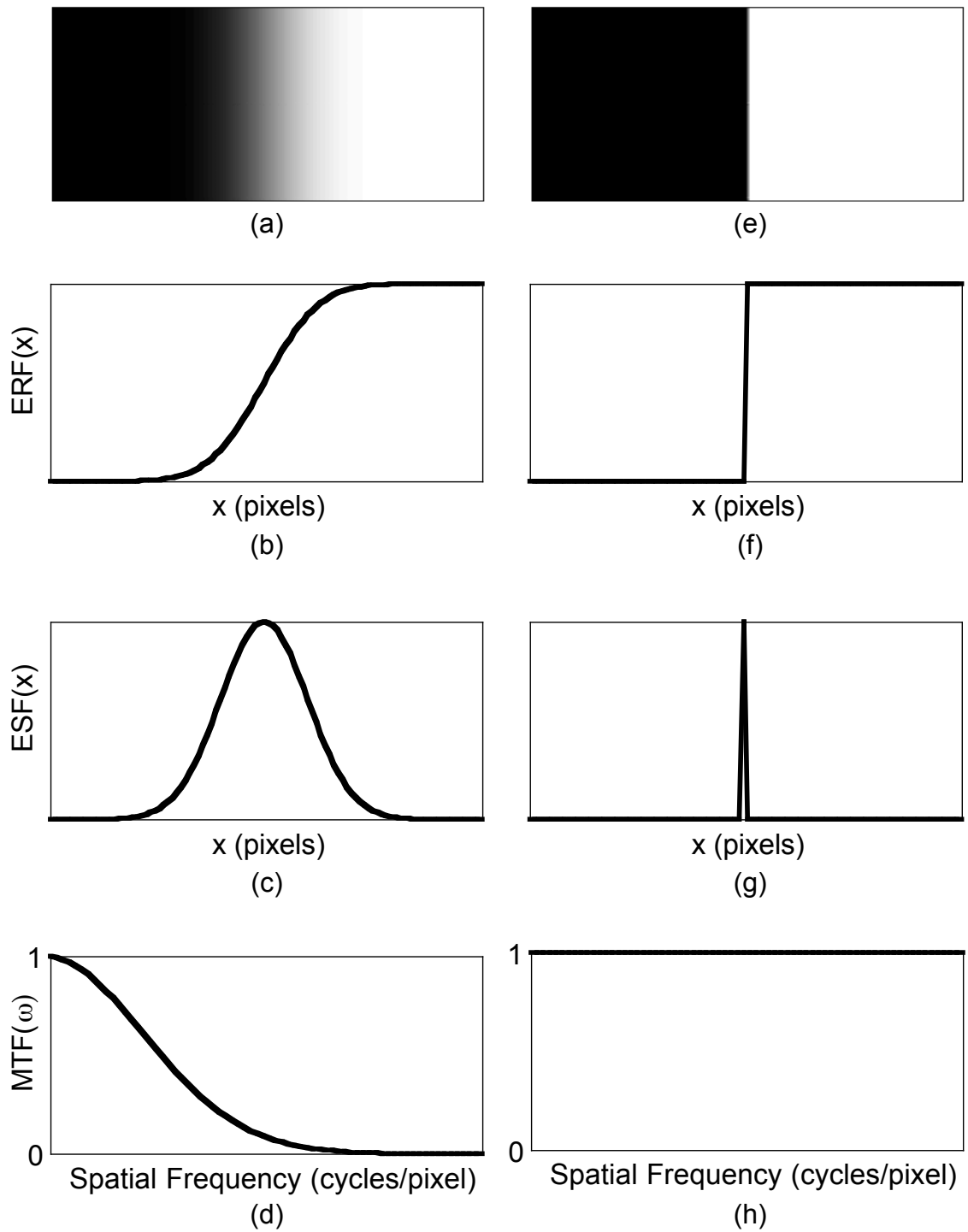
Figure 5.6: Basic methodology for calculating the MTF using the edge response.

It is instructive to consider an idealized case. A "perfectly sharp" edge is depicted in Fig. 5.6(e). The ERF of this edge, Fig. 5.6(f), is a step function, and the ESF, which is the derivative of the ERF, is an impulse, Fig. 5.6(g). This result can be interpreted to mean that the edge is not artificially spread in the image, as it was in Fig. 5.6(a). Taking the Fourier transform of the ESF, in this case, yields a MTF equal to one across all spatial frequencies, as shown in Fig. 5.6(h), meaning that all spatial frequencies can be discerned without loss of contrast. In other words, infinitely high spatial frequencies (i.e., infinitely fine-grained detail) can be resolved if the edges are "perfectly sharp."

There are a number of key considerations in employing the edge response method. First, the resolution of the camera plays a critical role in that it provides a practical limitation to the MTF measurements. It can be shown (Ref. 84) that a best case OTF for an imaging system is a normalized Fourier transform of the pixel shape. For a square pixel of width of a, the Fourier transform is, by definition, $\text{sinc}(2\pi\omega_x a)$. Note that, although a sinc function is defined for infinitely high spatial frequencies, any values that extend beyond the spatial frequency corresponding to the first zero, which occurs at $\omega_x = (2a)^{-1}$, should be considered "false resolution," because they are not physically possible and would imply pixel dimensions smaller than the actual size (Ref. 84). Consequently, smaller pixels result in larger spatial-frequency bandwidths.

Another important consideration is the quality of the edge. For example, using the edge of an object that has some curvature or texture can cause the effect of lighting location and intensity to strongly impact the MTF measurements. A final consideration is the importance of sampling normal to the edge. If the edge response is taken at an angle

that is not perpendicular to the edge, the ERF will be artificially spread out over a larger number of pixels, leading to erroneous MTF calculations.

5.2.2   Results

Calculating MTF from Flight Test

A 20 inch-by-20 inch Siemens star, Fig. 5.4(b), was placed on a helicopter cabin door, and filmed in high-definition video, at 30 frames-per-second with a Canon VIXIA HFS10 camcorder from a distance of approximately 500 ft. Each video frame was saved as a 1920-by-1080 pixel bitmap in 24-bit RGB color and then converted into 8-bit grayscale, with gray levels from 0 (black) to 255 (white). Portions from three frames of the video are shown in Fig. 5.7. They correspond to three successive instants of an approach, i.e., $T_1 < T_2 < T_3$. The frame at T_1 was taken prior to the descent by the helicopter into the brownout cloud.

For each frame, the contrast between the black-and-white wedges in the aircraft target was evaluated at 17 different locations, i.e., the 17 line segments shown in Fig. 5.8(a). For each of these locations, a line segment was identified to span the black/white wedges, and the spatial frequency for each segment was calculated by dividing the number of black/white cycles by the angle subtended in the camera FOV. The grayscale values of the pixels along each segment were obtained, and an averaging technique was then used to determine the mean "black" and "white" response. The contrast was calculated as the difference between the two values; see Fig. 5.8(b).

MTFs corresponding to the frames of Fig. 5.7 are shown in Fig. 5.9. The MTF

(a)

(b)

(c)
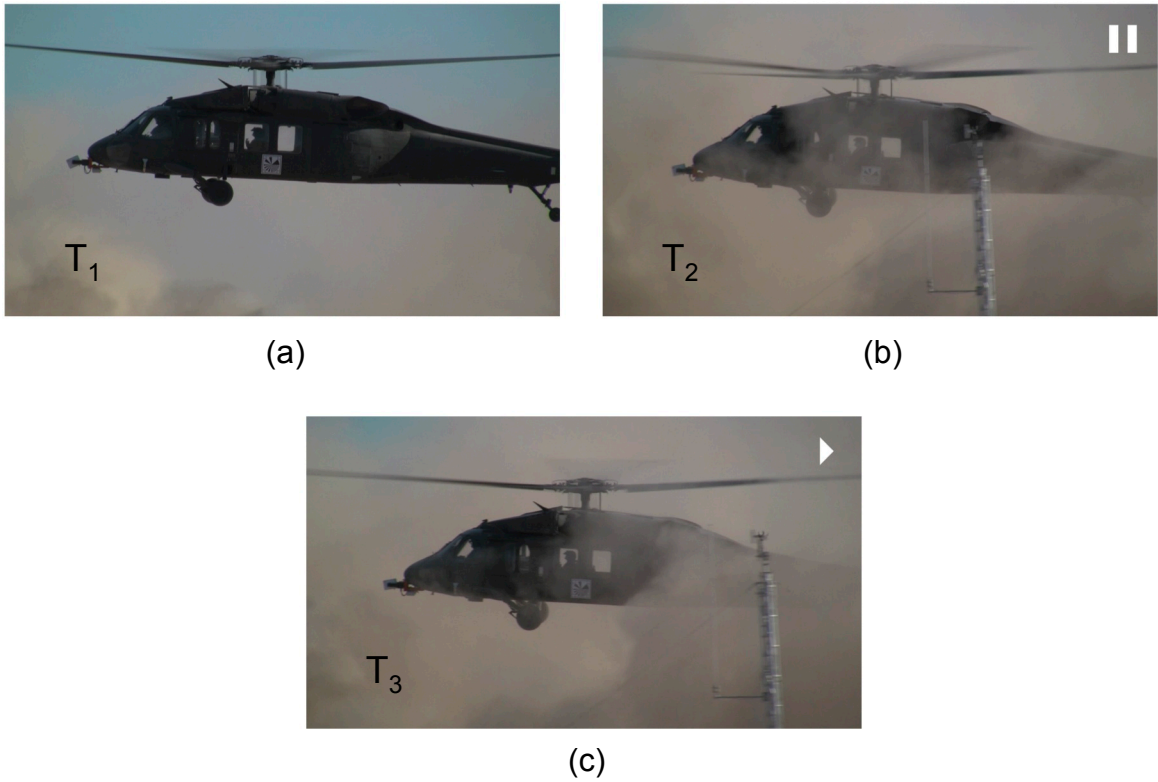
Figure 5.7: The modified Siemens star test pattern placement on the side of the aircraft and three frames from a video recording of the same approach, spanning less than two seconds; $T_1 < T_2 < T_3$.

(a)

(b)
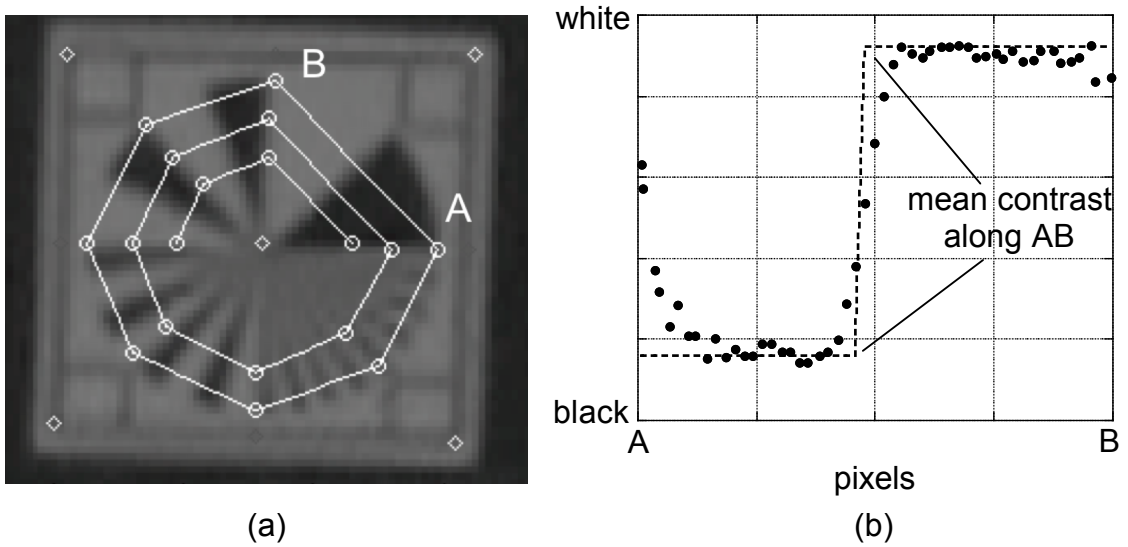
Figure 5.8: Illustrative calculation of contrast response for a given line segment of the target.
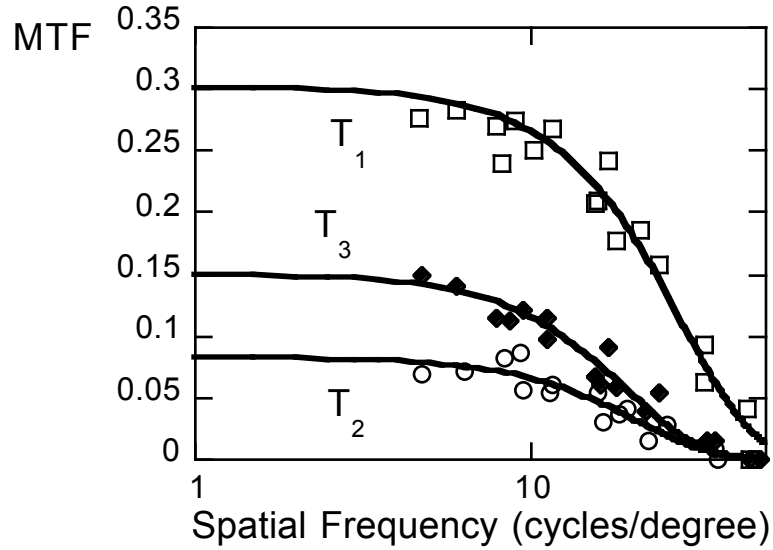
Figure 5.9: Modulation Transfer Functions calculated by the square-wave response method, corresponding to the three frames of Fig. 5.7.

curves are normalized so that a value of unity is representative of the contrast between "true black" (i.e. "0" in 8-bit grayscale) and "true white" (i.e., "255" in 8-bit grayscale). Because of the combined effects of background irradiance, atmospheric turbulence, camcorder characteristics, and the brownout cloud (at T_2 and T_3), the maximum MTF values are less than unity. MTF curves are calculated as a least-squares fit to the data. Each curve is of the form of the classical aerosol MTF (Ref. 85), i.e.,

$$\text{MTF}(\omega) = \begin{cases} \exp\left[-A_a L - S_a L \left(\dfrac{\omega}{\omega_c}\right)^2\right] & \omega \leq \omega_c \\[2ex] \exp\left[-(A_a + S_a)L\right] & \omega > \omega_c \end{cases}, \tag{5.5}$$

where A_a is the absorption coefficient, S_a is the scattering coefficient, L is the optical path length, ω is the spatial frequency, and ω_c is the cutoff frequency (the spatial frequency above which the MTF no longer degrades).
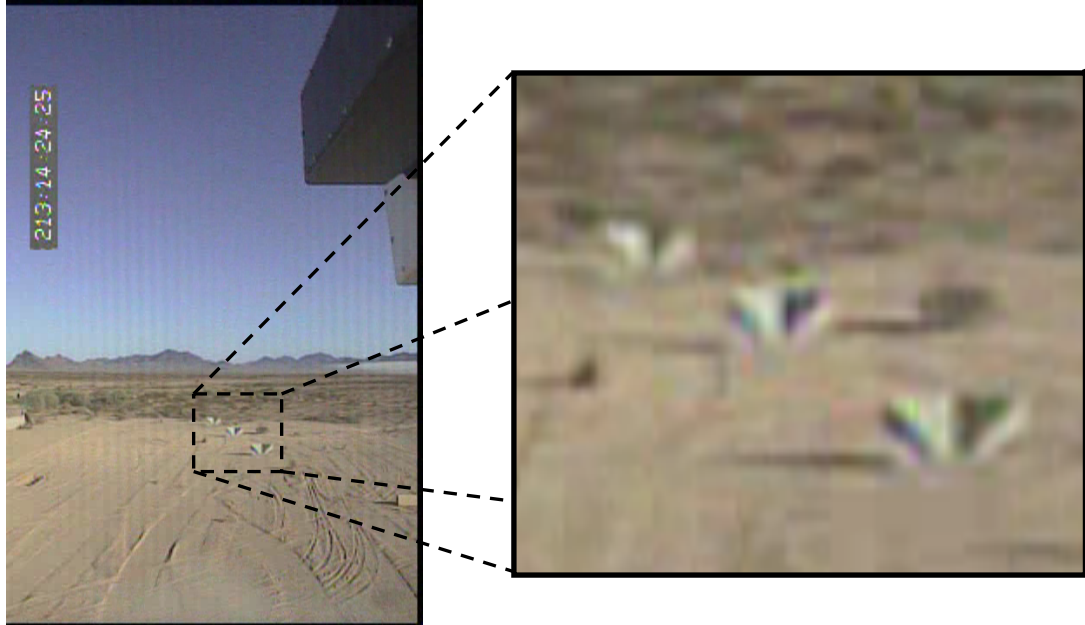
Figure 5.10: Billboard resolution targets placed forward of the landing zone, as viewed from a nose-mounted camera.

To calculate the MTF of the brownout cloud from inside, looking out, a set of three 4- by 8-foot "ground targets," as shown in Fig. 5.4(a), were placed forward of the landing zone. These targets were filmed using a Hitachi KP-D20AU video camera that was mounted to the nose of the helicopter. The same algorithm discussed for the aircraft target was used, but the combination of target distance and camera resolution was such that the test patterns could not be well resolved, particularly the high-frequency regions in the lower portion of the target (see Fig. 5.10). Each frame of the video consisted of 480-by-720 pixels, giving only one-sixth of the resolution that was captured in the aircraft target video.

To compare the edge response method with the square-wave response method, MTF measurements were performed using the same frames given in Fig. 5.7. To calculate the MTF of the brownout cloud from the outside, looking in toward the Siemens star, the edge
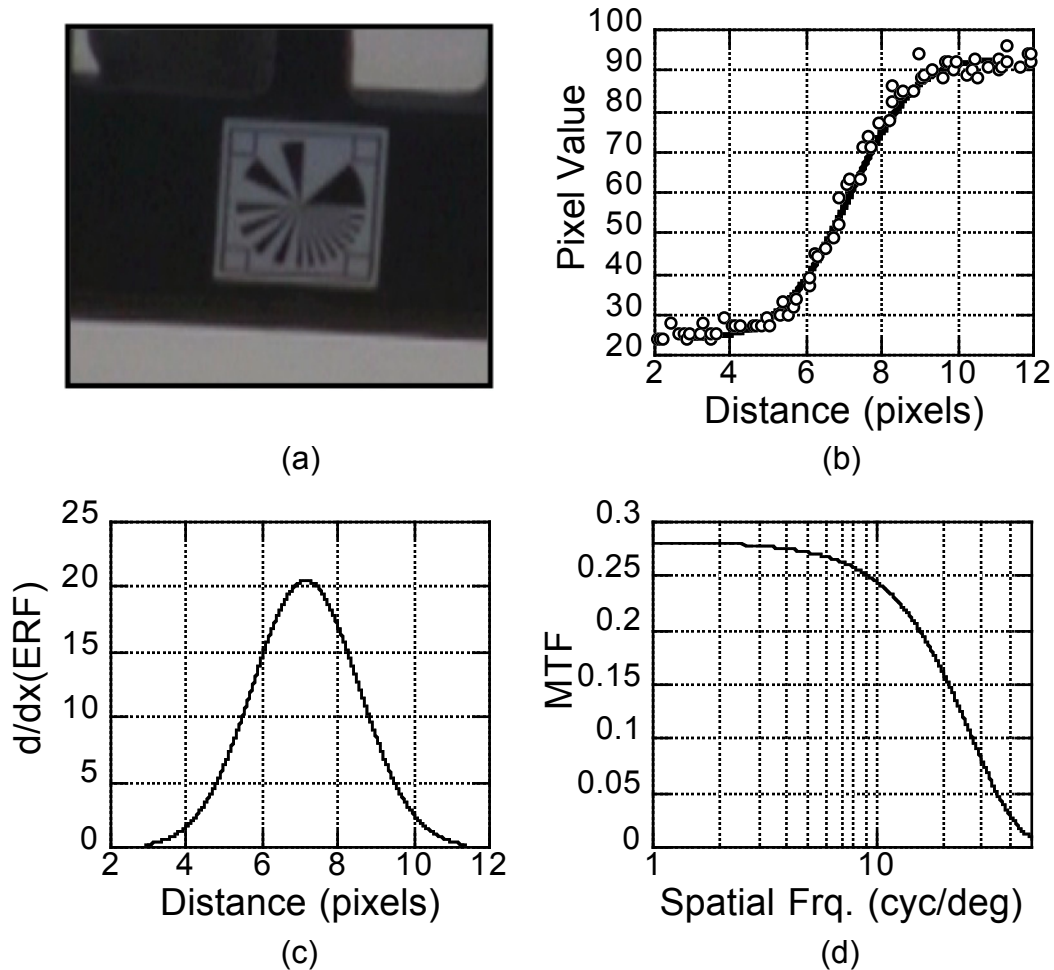
Figure 5.11: Edge response method for MTF calculation.

along the largest wedges was used, as shown for a representative case in Fig. 5.11. Using

the methods previously described, the ERF, ESF, and MTF were extracted. The MTF

curves were normalized so that a value of unity is representative of the contrast between

"true black" and "true white." The results are shown in Fig. 5.12 and are compared with

the square-wave results in Fig. 5.13.

The edge response method was likewise utilized to calculate the MTF of one of

the ground targets, and results are shown in Fig. 5.14. The lower spatial frequencies

are strongly attenuated (as compared with Fig. 5.12), illustrating a fundamental limi-
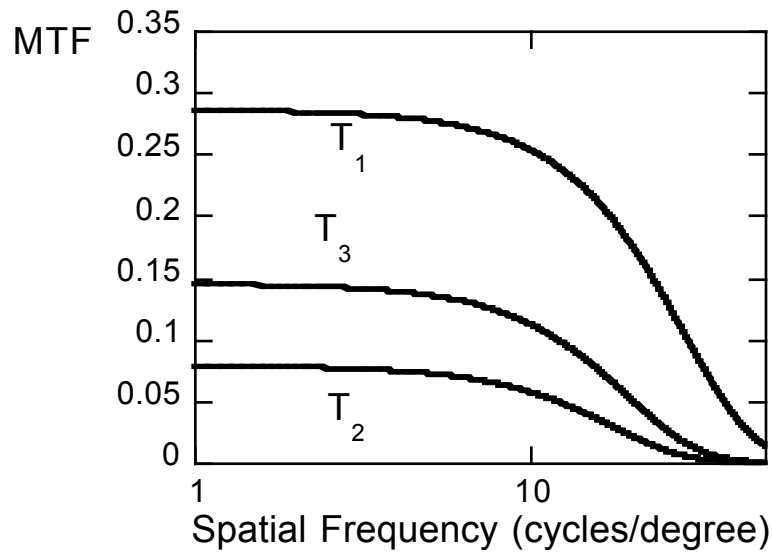
Figure 5.12: Modulation Transfer Functions calculated by the edge response method, corresponding to the three frames of Fig. 5.7.
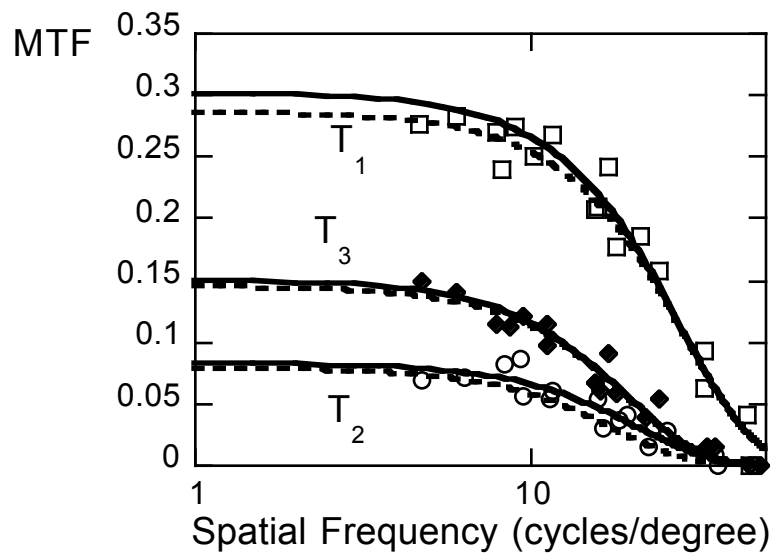
Figure 5.13: Comparison of Modulation Transfer Functions calculated by the square-wave and edge response methods, corresponding to the three frames of Fig. 5.7. Results using the square-wave response method are depicted by markers with a solid line; results using the edge response method are depicted by a dashed line.
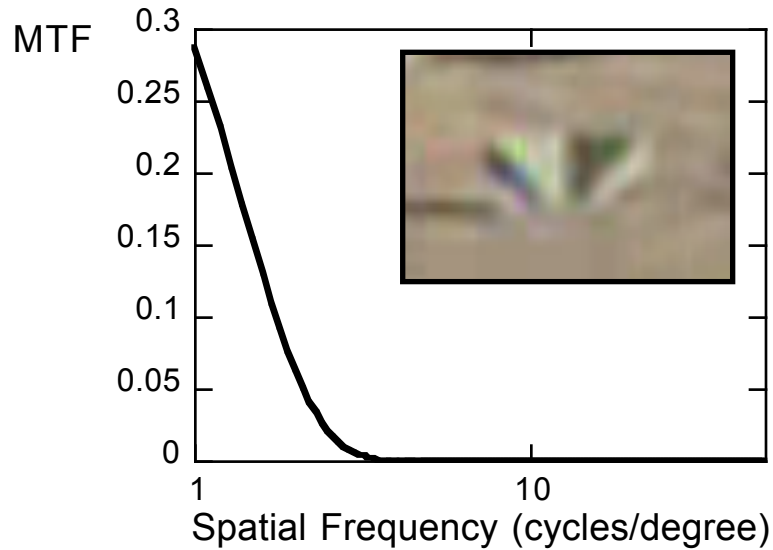
Figure 5.14: Modulation Transfer Function for a "ground target," as calculated by the edge response method.

tation of all MTF measurements, namely that they can be strongly affected by image resolution. Recalling that the best case OTF for an imaging system with pixel width a is, $\text{sinc}(2\pi\omega_x a)$, the best case OTFs for the ground and nose-mounted cameras can be plotted, as shown in Fig. 5.15.

Note that the MTF calculation techniques discussed in the foregoing yield a characterization of the degradation due to the combined effects of the entire imaging *system*, which includes not only the sediment cloud, but also the video camera, and the atmosphere between aircraft and camera with its own absorption and scattering effects. As such, the MTF results presented herein would be different for a human observer located at the same viewing location because the human eye has different characteristics and limitations than a typical video camera. Indeed, there is even a great deal of variation in the limitations of the human eye, and no two people would perceive exactly the same MTF. It should further be noted here, that although the *system* MTF is given by the cascade mul-
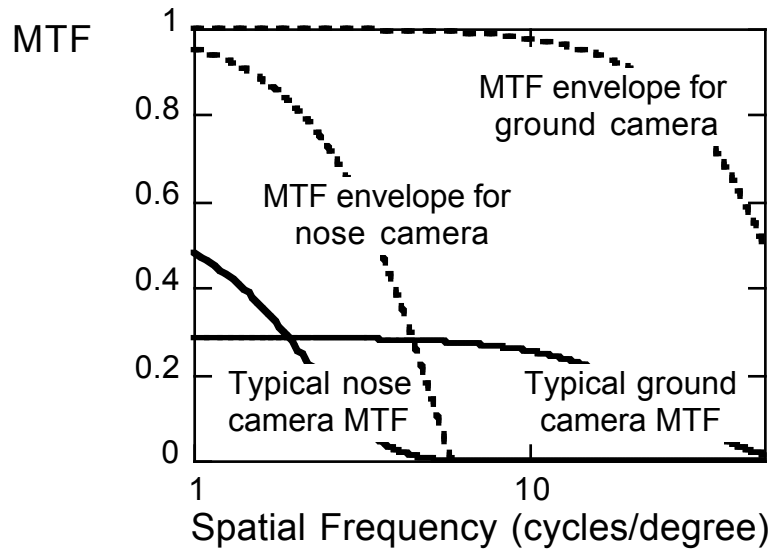
Figure 5.15: Approximate theoretical MTF limitations for the nose-mounted and ground cameras with representative MTF calculations from each camera.

tiplication of the individual component MTFs, care must be exercised in attempting to isolate the effect of just one component of the *system* (e.g., the brownout cloud) because of interdependent effects of the imaging system limitations (Ref. 84).

The MTF results help quantify rigorously two intuitive concepts. First, the results show that brownout is a time-dependent process for an approach to landing, as indicated by the fact that visibility becomes worse at time $T_2 > T_1$ but then improves at $T_3 > T_2$. Second, they illustrate the fact that the degradation is not the same at all spatial frequencies: the sediment cloud acts as a low-pass filter because contrast is lost more at high frequencies than low frequencies. Although the results do not include MTFs between the pilot's position and the ground in the immediate vicinity of the helicopter (such measurements were not possible due to safety-of-flight considerations) it can be argued that the MTF can also quantify the intuitively known fact that in brownout conditions pilots lose microtexture cues, i.e., fine-grained detail on the ground, before they lose macrotexture

267

cues, i.e., large objects. Therefore, it could help quantify Usable Cue Environment ratings (Ref. 12). The MTF could also be used as the basis for a metric for pilot-in-the-loop simulation fidelity assessment, in the sense that a simulator should be capable of matching the space and time variation of MTF observed in actual brownout conditions.

Automating the MTF Calculations

With the ability to calculate the MTF by a given edge, the potential exists to devise algorithms to automate MTF calculations by tracking a particular edge (or edges) through sequential frames. By tracking multiple edges in a video clip and by automating MTF measurements, it would be possible to quantify both the spatial and temporal variations of the brownout cloud. In turn, this approach could be useful to validate numerical simulations of the entire cloud development process.

Although any identifiable feature in the camera FOV could, in principle, be used for this purpose, the measurements were performed on the edges of the silhouette of the helicopter to evaluate the feasibility of using "feature edges" for MTF calculation. The distinction is made here between a "designed edge," e.g., the edge between dark and light regions in a test pattern, and a "feature edge," e.g., the edge between the dark helicopter silhouette and the sky or the edges of significant terrain features. While it is clear that each edge consists of a dark and light component, the effect of the cloud will potentially be quite different for each type of edge.

For example, Fig. 5.16(a) and (b) depict the edge response for a "designed edge" in a test pattern. It is expected that the effects of the brownout cloud would be relatively

268
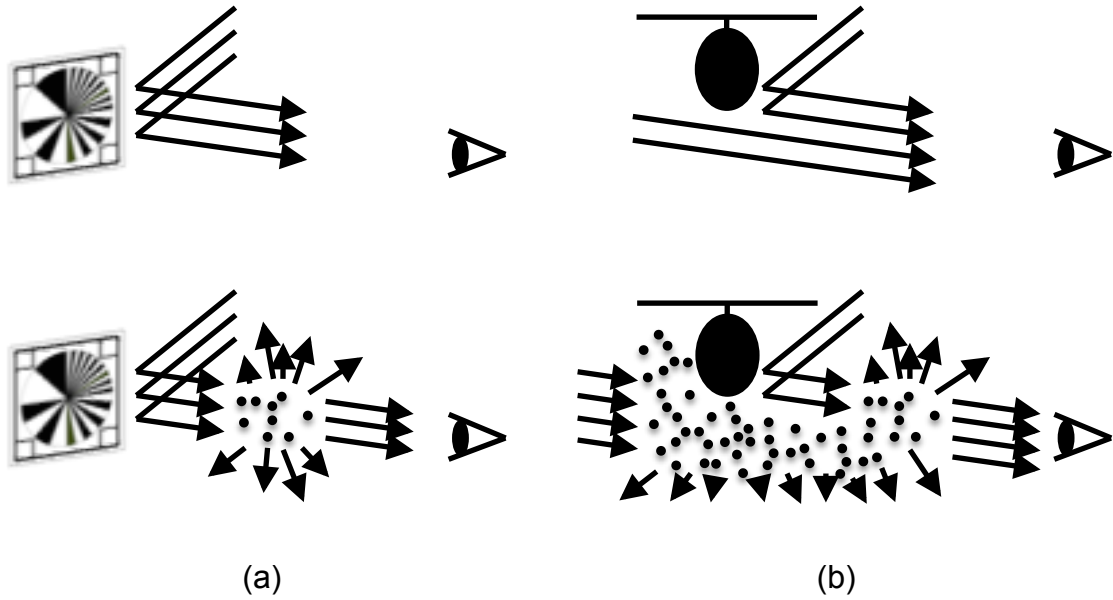
Figure 5.16: Comparison of edge response calculations for (a) a "designed edge" versus (b) a "feature edge."

constant for both the dark and light regions of the edge because both dark and light are components of the same object, i.e., the test pattern. In the case of the "feature edge" of the helicopter silhouette, depicted in Fig. 5.16(c) and (d), however, the effect of the brownout cloud could be different for the light component of the edge, i.e., the atmospheric irradiance, than for the dark component of the edge, i.e., the irradiance of the helicopter fuselage, because the atmospheric irradiance will have a significantly longer path length through the cloud than for the fuselage irradiance. Note that this will not be the case for all "feature edges," for example, a mountain silhouetted against the sky would be more akin to the test pattern than the helicopter silhouette.

The first step in automating the MTF calculations involves the creation of a correlation mask to be used in tracking the edges of interest (in this case, the silhouette of the helicopter fuselage) throughout the duration of the recording. To create this mask,

the initial frame of the sequence is binarized using Otsu's method for picture segmenta-

tion (Ref. 140), as implemented in Matlab's `graythresh` function. The binarization is

depicted in Fig. 5.17(a) and (b). This method involves the selection of a threshold in the

gray-level histogram of the image, and each pixel value in the binarized image is assigned

to be one (white) or zero (black) based on whether the corresponding pixel value in the

original image is greater or less than the threshold, respectively. In this method, the gray-

level histogram of the image is normalized and regarded as a probability distribution, i.e.,

$$\sum_{i=0}^{J} p_i = \sum_{i=0}^{J} \frac{n_i}{N} = 1 \tag{5.6}$$

where J is the maximum grayscale value (255 for 8-bit grayscale), p_i is the probability

that a pixel in the image will have a grayscale value of i, n_i is the number of pixels in the

image with a grayscale value of i, and N is the total number of pixels in the image. The

image is then segmented at a grayscale threshold, k, such that any pixel value below the

threshold will be set to 0, i.e., black, and any pixel value above the threshold will be set

to 255, i.e., white. The optimal estimate for the grayscale threshold value, k^*, is then the

value for which $\sigma_B^2(k)$ is maximized,

$$\sigma_B^2(k^*) = \max\left(\sigma_B^2(k)\right) = \max\left(\frac{[\mu_T\,\omega(k) - \mu(k)]^2}{\omega(k)\,[1 - \omega(k)]}\right) \text{ for } 0 \leq k \leq 255 \tag{5.7}$$

where μ_T is the mean level (i.e., the average pixel value) for the entire image, $\omega(k)$ is the

cumulative probability of a pixel value being between 0 and k, $\mu(k)$ is the mean level of

all the pixels in the image between 0 and k (i.e., $\mu(k) = \sum_{i=0}^{k} i\,p_i$), and $[1 - \omega(k)]$ is the

270

(a)

(b)

(c)

(d)
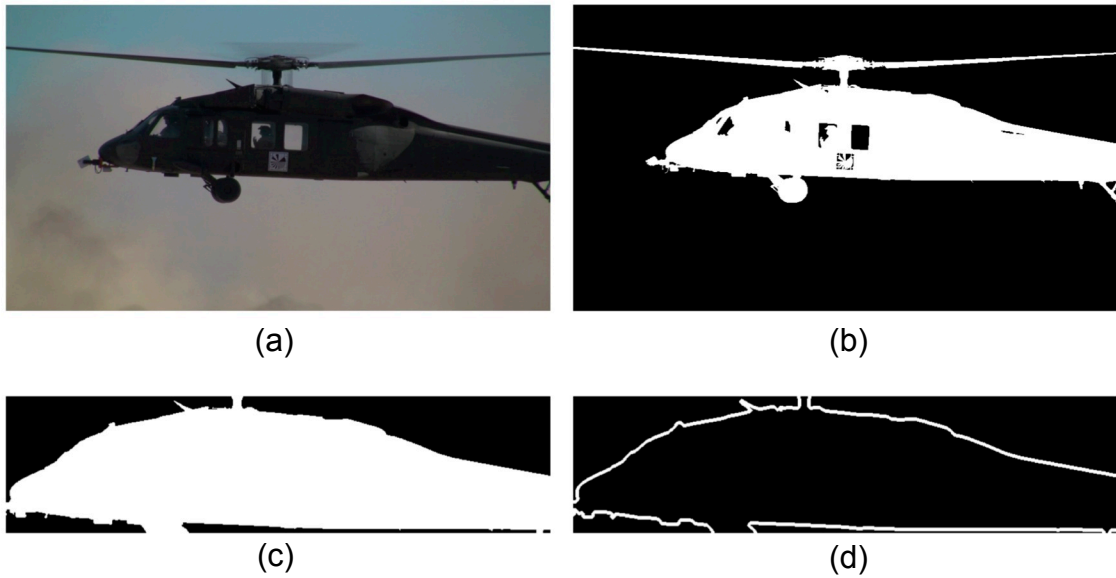
Figure 5.17: Creation of the correlation mask to be used in the tracking algorithm for MTF automation.

cumulative probability of a pixel value being between $k+1$ and 255.

The helicopter silhouette can be easily identified in the binarized image and forms the basis for the correlation mask, though it must be trimmed to exclude the portions of the helicopter that will change significantly in appearance between subsequent frames, e.g., the rotor blades, as shown in Fig. 5.17(c). Only the fuselage remains after the helicopter silhouette has been trimmed, and the correlation mask is defined to be the edges of the fuselage, as shown in Fig. 5.17(d). The edges are thickened from a single-pixel width to a five-pixel width to account for the fact that the size and shape of helicopter silhouette in the camera FOV will change during the approach sequence (albeit, the changes will be small).

Once the correlation mask has been defined, it is then used to identify the location of the helicopter within subsequent image frames. Each frame is binarized using Otsu's method, the helicopter silhouette is again isolated, and its edges are identified. The mask,

271

$M(x,y)$, is then correlated with the edges of the silhouette, $E(x,y)$, i.e.,

$$M \circ E(x,y) = \sum_{j=-N_y}^{N_y} \sum_{i=-N_x}^{N_x} M(i,j) E(x+i,y+j) \tag{5.8}$$

where $-N_x \le x \le N_x$ and $-N_y \le y \le N_y$ are the x- and y-limits of the correlation mask, referenced from its geometric centroid. Acknowledging that the helicopter may undergo minor rotations in the image FOV during the approach sequence, a series of masks corresponding to different rotation angles can be used. The position, (x^*, y^*), for which the highest value is returned corresponds to most likely location of the helicopter in that frame (Ref. 141), and the rotation, (θ^*), likewise corresponds to the likely angular orientation of the heliciopter, i.e.,

$$M(\theta^*) \circ E(x^*, y^*) = \max(M(\theta) \circ E(x,y)) \tag{5.9}$$

To reduce computational costs, and under the assumption that there is an upper limit to the distance (in pixels) that the helicopter can translate in successive frames, the range of travel for the correlation mask can be reduced. Factoring in all of these considerations, the correlation that is performed at each time, t is

$$M(\theta) \circ E(x,y) = \sum_{j=-N_y}^{N_y} \sum_{i=-N_x}^{N_x} M(i,j,\theta) E(x+i,y+j)$$

$$x^*_{t-1} - T_x \le x \le x^*_{t-1} + T_x$$

$$y^*_{t-1} - T_y \le y \le y^*_{t-1} + T_y \tag{5.10}$$

$$\theta^*_{t-1} - R_\theta \le \theta \le \theta^*_{t-1} + R_\theta$$
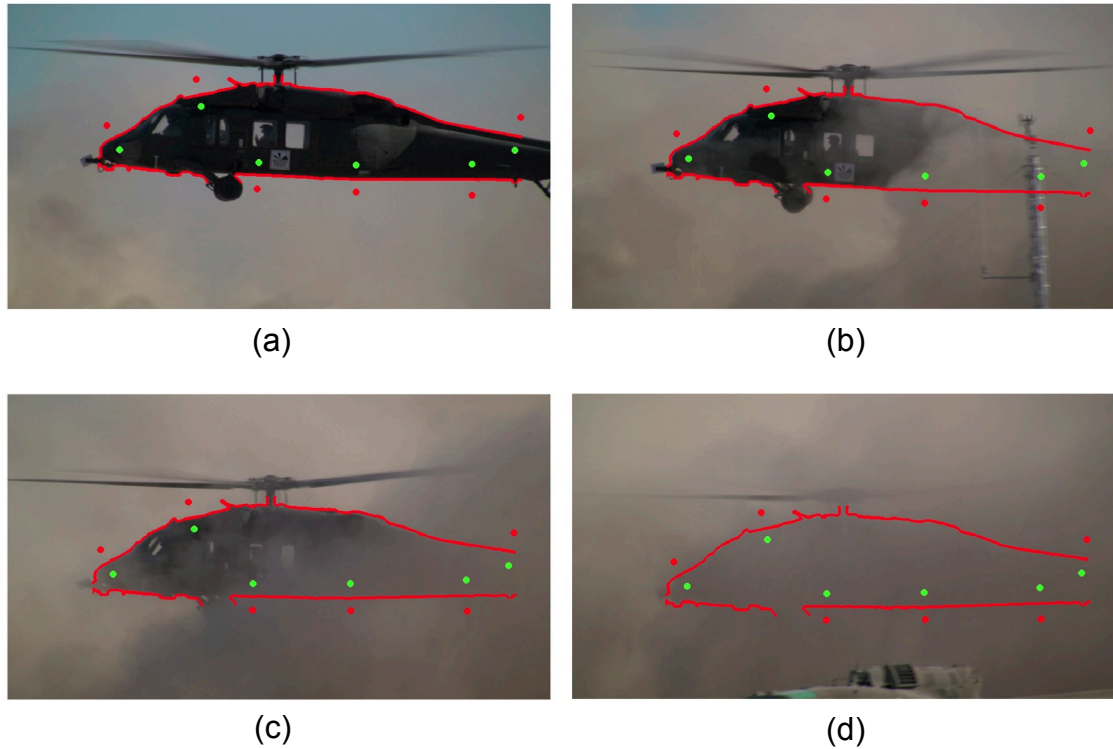
Figure 5.18: Tracking algorithm results.

under the assumption that the helicopter has limits of translation T_x and T_y and rotation R_θ from time $t-1$ to time t.

Representative results for the tracking algorithm are given in Fig. 5.18. It should be noted here that, if the mask is to be applied over a duration during which the size and shape of the helicopter silhouette varies significantly, a procedure would have to be employed to redefine the mask shape over the course of the image sequence.

As the edges of the helicopter silhouette are tracked from frame to frame, they can be used for MTF calculations. Figure 5.19 shows a three second span of an approach, and demonstrates some key capabilities of automated MTF measurements. In Fig. 5.19(a), the helicopter has not yet entered the brownout cloud, and the MTF measurements can thus be treated as baseline calculations (for characterizing other atmospheric effects, the

camera, etc.). In Fig. 5.19(b), the helicopter is beginning to enter the brownout cloud, obscuring the edges of the helicopter silhouette for locations D through F. As the helicopter continues to descend into the cloud in Fig. 5.19(c), location C also becomes obscured, and only the nose (location A) and top (location B) of the helicopter silhouette can be used for MTF measurements. Interestingly, as the helicopter becomes engulfed by the brownout cloud in Fig. 5.19(d), MTF measurements can still be extracted for locations A and B, but can also be resolved again for location D.

Care must be exercised when using a "feature edge," e.g., the helicopter silhouette, for MTF calculations. Beyond the inconsistencies in the effect of the brownout cloud on the light and dark components of the edge (the atmospheric and fuselage irradiance, respectively) because of optical path length differences, problems can potentially arise if a feature edge is used that contains some curvature. While these considerations illustrate key limitations of using "feature edges," they do not preclude the potential for effectively using such edges in the future, provided due diligence is paid to ensuring that these known complications are minimized (Ref. 142). Additionally, the automated methodology described in this section can still be used effectively by tracking a designed edge, e.g., a resolution target on the fuselage of the helicopter.

5.3 Ground-Level MTF Testing

While a general procedure for calculating the MTF of brownout clouds generated from flight test was successfully demonstrated through the proof of concept testing, those measurements were not of great potential interest for handling qualities and simulation
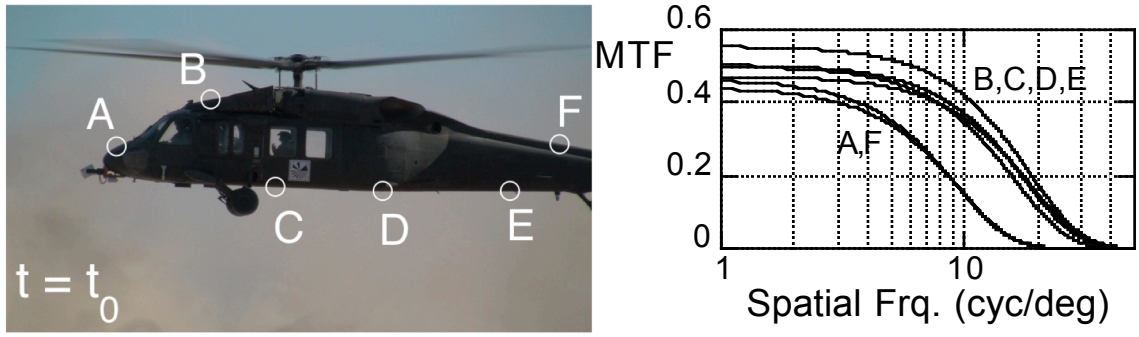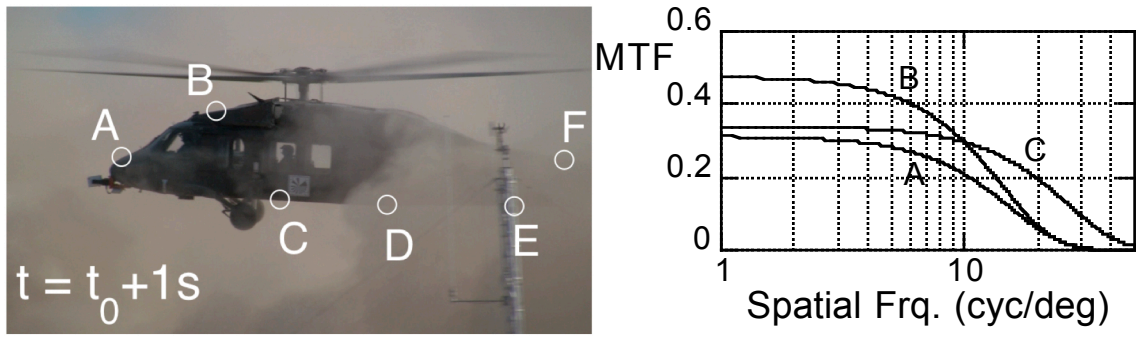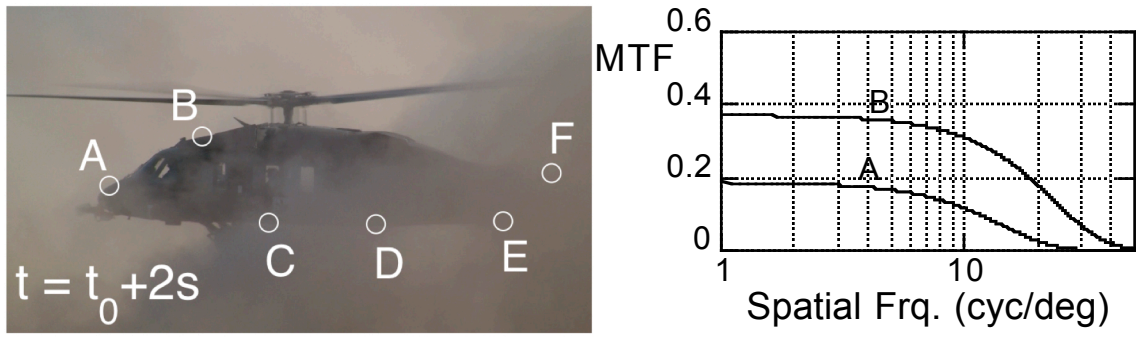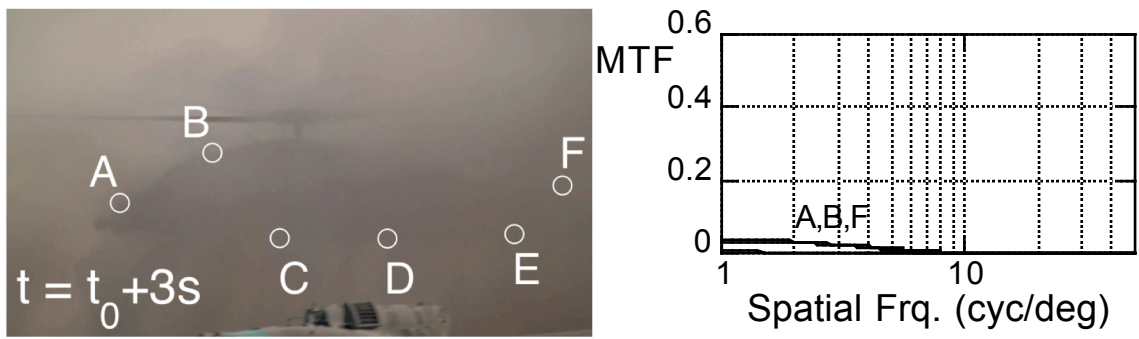
Figure 5.19: Automated MTF measurements for six locations on the helicopter silhouette over the course of three seconds.

275
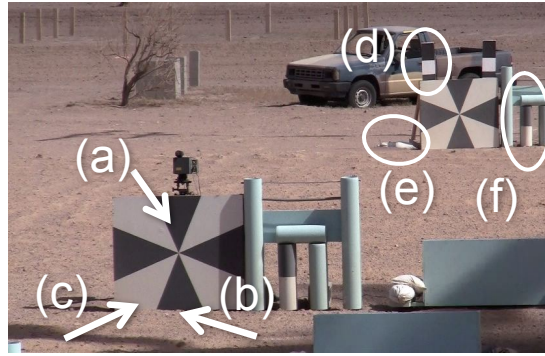
Figure 5.20: Locations utilized for MTF extraction.

applications because they were performed for external optical paths, i.e., from outside the brownout cloud, looking in. Measurements along paths from the pilot's location in the cockpit to points in the landing area are of the greatest practical importance.

5.3.1 Methodology

The importance of proper edge selection for MTF extraction was demonstrated in the proof-of-concept testing, though a systematic evaluation of potential target types was not performed. In the present brownout test campaign, several optical targets were available in the test area, and they provided various types of edges for MTF calculation. The six transition edges considered in this study are shown in Fig. 5.20. They consist of: (a) the edge between adjacent black and white segments of an optical target, (b) the edge between a black segment and the ground, (c) the edge between a white segment and the ground, (d) small "edge strips" affixed to the upper corners of the test patterns, (e) a stripe of black tape placed on a white sandbag at the ground, and (f) a cylinder fitted with black and white coverings.

Location (a) is most similar to that used for the successful MTF measurements from

prior flight testing, and it was intended to be a baseline against which the effectiveness of other edges could be assessed. The "black-to-sand" (b) and "white-to-sand" (c) edges were studied to determine if a full (i.e., white and black) test pattern was truly necessary for MTF measurement, or whether MTFs could be extracted at the interface between a generic object (e.g., a building, bush, or any other sort of obstacle) and the ground. The small "edge strips" (d) were intended to explore any issues that may arise with the use of small-scale full targets. The taped sandbag (e) was an improvised optical target; it was examined to determine if simple objects at hand could be turned into makeshift targets with a roll of black duct tape. The cylinder (f) was included in the test field for non-MTF measurements, however it was likewise examined to inspect the effect of shadows on the MTF measurements.

To assess the reliability of the MTF measurements, a statistical analysis of the repeatability of the results was performed. Two key parameters of any MTF curve are its initial magnitude, MTF_0, and spatial frequency cutoff, ω_{cutoff}, both depicted in Fig. 5.21. Greater values of MTF_0 indicate an optical target that contains greater contrast, and higher values of ω_{cutoff} indicate the presence of a sharper edge. By examining the way in which these values vary for each target over a series of frames from the video recording, an assessment of the repeatability of the MTF measurements for each target can be obtained. It is important to note that this analysis must be conducted for a series of frames prior to the development of the brownout cloud because the temporal and spatial variations of the cloud itself would dominate any assessment of the efficacy of the target.
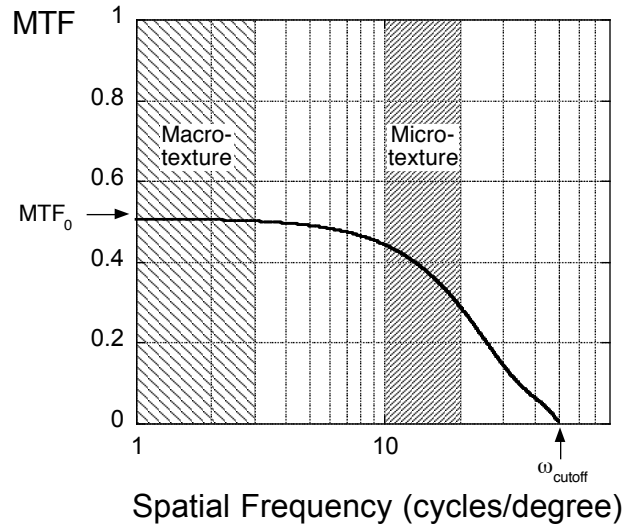
Figure 5.21: Typical MTF with MTF_0 and ω_{cutoff} labeled. Representative macro-texture and micro-texture ranges are also depicted.

5.3.2   Results

Video footage from brownout flight testing was recorded from two vantage points to facilitate the analysis. Unlike prior brownout testing, which involved the execution of an approach maneuver, the present testing involved a hover taxi maneuver by a heavy-lift helicopter. For both vantage points, the helicopter traveled from right to left across the field of view, perpendicular to the optical path of the cameras. Because the present results are not for optical paths from inside the cockpit looking out, they are of limited value for HQ and/or simulation purposes. The methods presented in obtaining these results, however, provide a proof of concept for the essential elements that will enable such tests to be performed safely and effectively in the future.

The edges labeled (a)–(f) in Fig. 5.20 were evaluated for their suitability for MTF extraction. The edge response for each transition is presented in Fig. 5.22. Again, location (a) is the edge between adjacent black and white regions within a test pattern; its
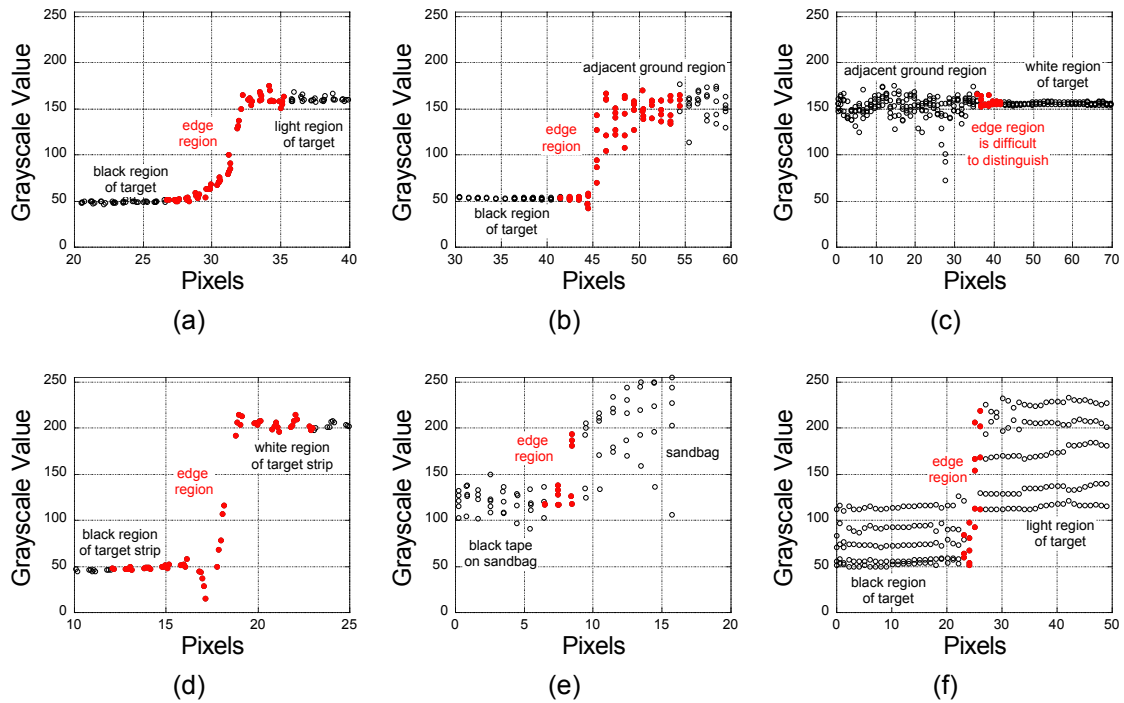
Figure 5.22: Edge response functions for locations (a)–(f) in Fig. 5.20.

usefulness for MTF extraction has been demonstrated and it is shown here as a baseline

against which other methods can be compared. In the case of location (b), the"black-to-

sand" edge, sufficient contrast exists to maintain a clearly defined edge region, though it

is clear that the grayscale response of the ground region contains considerably more noise

than that for the light region of the target in location (a). The edge region is difficult to

distinguish for location (c), the "white-to-sand" edge. Although the edge can be inferred

from the change in scatter of the grayscale response, there is not enough contrast avail-

able to clearly define a suitable edge for MTF extraction. Location (d), the small "edge

strip" provides a very sharp edge for MTF calculation. In fact, the edge strip provides a

sharper edge than the optical target at location (a). This is likely because the edge strips

were fabricated by different means than the other resolution targets (the edge strips were

high-quality poster material mounted to wooden boards while the other resolution targets were painted wood; see Fig. 5.23) and had been exposed to the elements for less time than the other resolution targets. Location (e), a sandbag with a strip of black tape, does not provide a clear edge because of the large variation in grayscale response for both the tape and sandbag. The ERF for location (f), a cylinder with black and white segments, clearly displays the effect of the curvature of the cylinder. The edge response takes on the appearance of five step functions that are displaced in the y-direction. Each of these step functions represents a sample along one of five parallel lines, which, in the case of location (f), corresponds to one of five levels of shadow. The magnitude of the contrast varies significantly for each of these five levels. The magnitude of the contrast along the least responsive sampling line is approximately 60 grayscale levels (about 25% of the maximum contrast for 8-bit grayscale), while the magnitude of contrast along the most responsive sampling line is approximately 120–30 grayscale levels (about 50% of the maximum contrast for 8-bit grayscale).

The MTFs for each of these ERFs were calculated and are shown in Fig. 5.24. The baseline MTF at location (a) is consistent with prior work in its overall magnitude and spatial frequency cutoff. Despite the fact that the ERF for location (b) exhibited noticeable scatter in the grayscale values of the adjacent ground region, the high contrast between the black portion of the target and adjacent sand allowed for successful MTF extraction of comparable quality to the baseline. Likewise, the MTF was successfully calculated for location (d). The high contrast between the black and white segments of the edge strip resulted in a MTF of greater magnitude than the baseline. Furthermore, the

Figure 5.23: Detailed view of the edge strips and optical target.
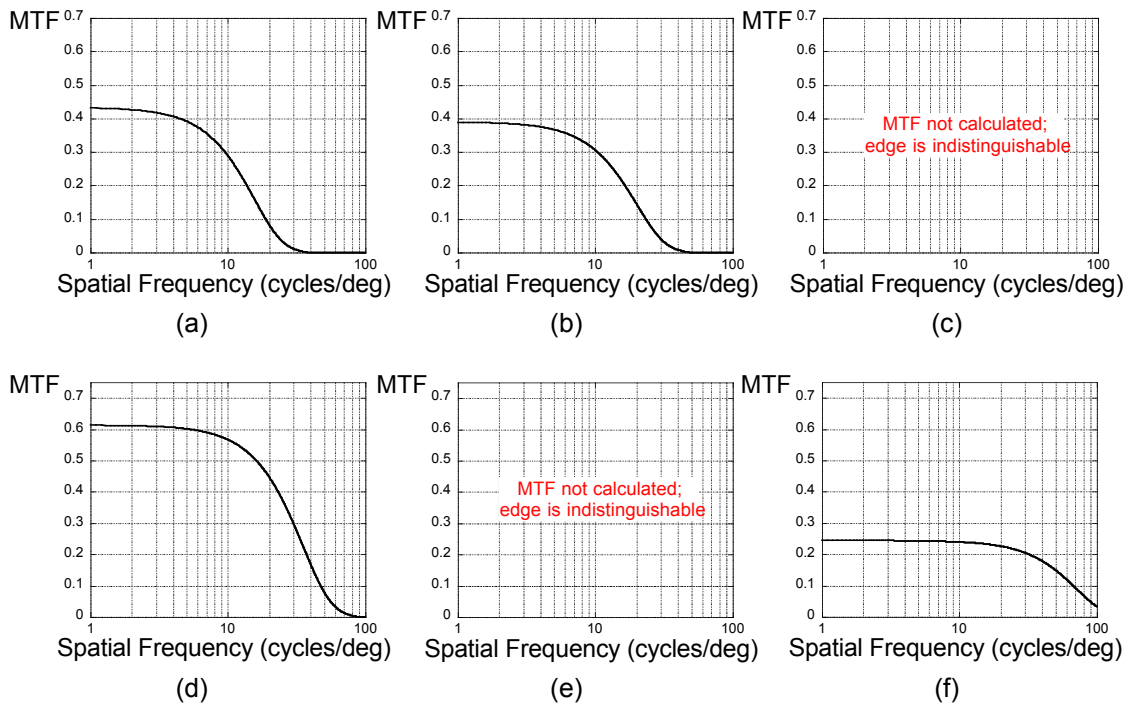
Figure 5.24: MTFs for locations (a)–(f) in Fig. 5.20.
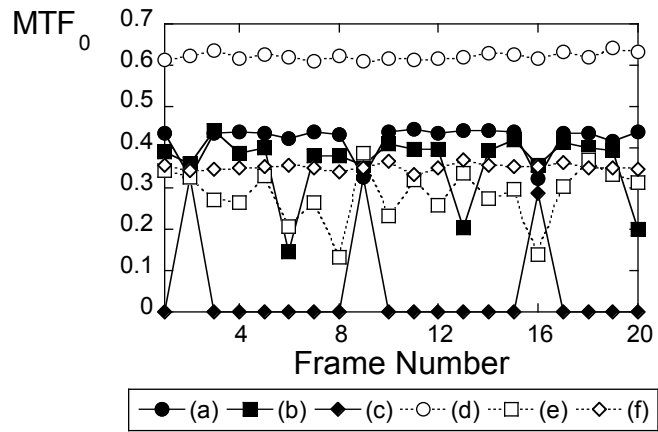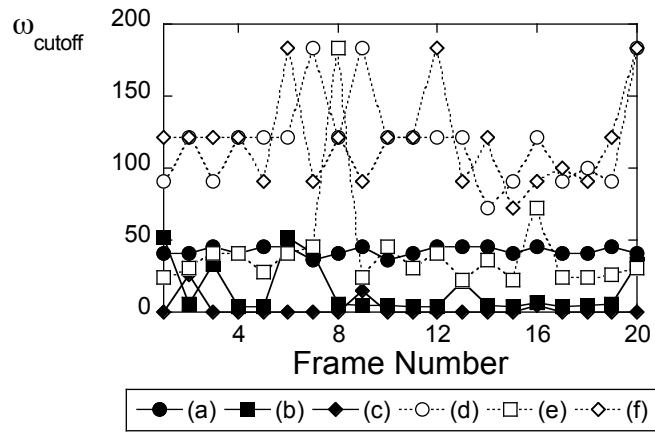
Figure 5.25: Variation in (a) MTF_0 and (b) ω_{cutoff} over 20 successive frames of the video recording.

sharpness of the black-to-white transition resulted in a wider MTF bandwidth. The MTF at location (f) exhibited a very high bandwidth because of the sharp edge region, however the overall magnitude was significantly lower than the baseline from the reduced contrast caused by the shadow. This result confirms prior findings that indicated the presence of curvature can be problematic for MTF calculation. Because the edge regions could not reliably be distinguished at locations (c) and (e), MTF calculations were not possible.

To assess the statistical significance of these results, the parameters MTF_0 and ω_{cutoff} were calculated for 20 successive frames of the video recording (spanning two-thirds of a second) for each location. The results are presented in Fig. 5.25 and provide some intuitive insights. For example, it is clear from Fig. 5.25(a) that location (d), the edge strip, provides the greatest contrast, followed by location (a), which is the baseline target. However, Fig. 5.25(b) shows that the typical ω_{cutoff} for location (d), while greater than that for location (a), experiences significant variations. In practice, it is desirable to utilize targets that will maximize MTF_0 and ω_{cutoff} while maintaining a high degree of repeatability.

Figure 5.26 shows the mean values and standard deviations for (a) MTF_0 and (b) ω_{cutoff}. Examining Fig. 5.26(a) first, it is clear that the contrast levels were highest and most consistent for locations that involved black-to-white transitions (i.e., locations (d), (a), and (f)). The black-to-sand transition, location (b), exhibited reasonably high contrast, although it was considerably less consistent. It is believed that the higher variances for (a) and (e) are because shadows were intermittently cast on those locations as the helicopter flew overhead. Shadows were not cast on locations (d) and (f).
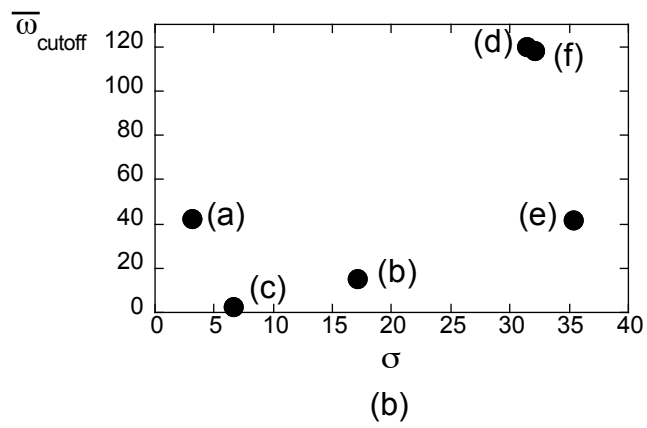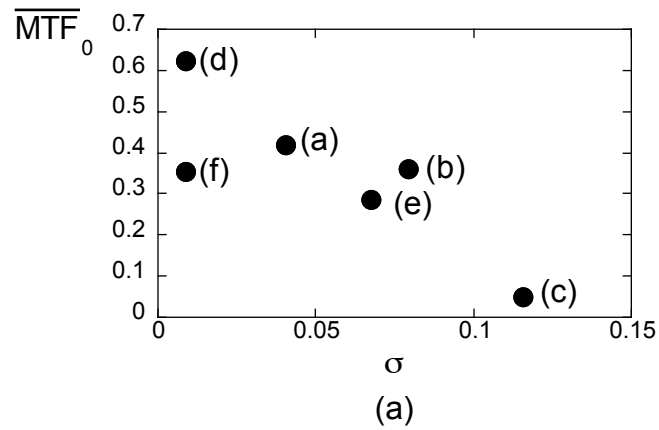
Figure 5.26: Mean values and standard deviations for (a) MTF_0 and (b) ω_{cutoff} over 20 successive frames of the video recording.

Examining Fig. 5.26(b), it is clear that locations (d) and (f) exhibit the highest mean values for ω_{cutoff} (i.e., the edges were sharpest at those locations), however it is important to note that these locations also exhibited higher variances. It is hypothesized that the high variances in ω_{cutoff} for locations (d)–(f) are because those locations were in the far-field, and that any auto-focusing by the camera would emphasize the near-field target. This is supported by the fact that ω_{cutoff} at the near-field location (a) was extremely repeatable, however the mean ω_{cutoff} value was significantly lower. It is believed that the low mean ω_{cutoff} values for location (a) and, conversely, the high mean ω_{cutoff} values for locations (d) and (f) are related to the orientation of the edges within the frame. It is hypothesized that the highest ω_{cutoff} values are achieved when the edge is oriented near-horizontally or near-vertically in the image frame because such orientations lead to sharper edges due to the pixel arrangements within the image. This result is anecdotally supported by Fig. 5.22(a), (d), and (f), which depict sharper edges for the locations with near-horizontal edges (namely locations (d) and (f)).

5.4 Interpreting MTF in Space and Time

The MTF of a brownout cloud varies significantly with space and time, leading to complicated multidimensional quantities. In light of this fact, interpreting MTF values over space and time can be particularly challenging. The present test campaign afforded opportunities to examine these considerations in detail.

5.4.1 Methodology

To interpret the evolution of the MTFs in space and time, the mean values for the MTF at representative macro- and micro-texture scales were defined to be

$$\overline{\text{MTF}}_{\text{macro}} = \frac{1}{2} \int_{1}^{3} \text{MTF}(\omega_x) \, d\omega_x \qquad (5.11)$$

and

$$\overline{\text{MTF}}_{\text{micro}} = \frac{1}{10} \int_{10}^{20} \text{MTF}(\omega_x) \, d\omega_x \qquad (5.12)$$

where macro-texture denotes low spatial frequencies in the 1–3 cycles per degree range and micro-texture denotes high spatial frequencies in the 10–20 cycles per degree range. For example, consider the generic MTF curve depicted in Fig. 5.21. For this sample case, $\overline{\text{MTF}}_{\text{macro}} = 0.5$ and $\overline{\text{MTF}}_{\text{micro}} = 0.37$. Note that the specific ranges of spatial frequencies utilized here are notional only, and are based on human perception thresholds (Ref. 84). The specific limits for each range (or, likewise, the number of ranges) could easily be adjusted in practice. The identification of specific spatial frequency ranges that have the strongest implications for HQ analyses will require further research.

By calculating $\overline{\text{MTF}}_{\text{macro}}$ and $\overline{\text{MTF}}_{\text{micro}}$ at a given instant in time for 11 regularly-spaced optical targets (see Fig. 5.27), the spatial effects of the brownout cloud on macro- and micro-texture cues can be quantified. In a similar fashion, the calculation of mean macro- and micro-texture MTF values results in a format more amenable for examining the time variation of the brownout cloud. For a single optical path, $\overline{\text{MTF}}_{\text{macro}}$ and $\overline{\text{MTF}}_{\text{micro}}$ will vary with time, thereby providing quantitative information on what scales

286

Figure 5.27: Locations utilized for MTF extraction over a broad field of view.

of visual cues are available, and at what times.

5.4.2 Results

To develop methodologies for interpreting the MTF measurements in space, the array of optical targets shown in Fig. 5.27 was utilized. In each of the optical targets, a black-to-white edge was identified and used for MTF extraction. A series of images is given in Fig. 5.28(a)–(d) that depicts four successive instants of a hover taxi maneuver. In Fig. 5.28(a), the dust cloud is still outside the target field, though it is forming to the right. In Fig. 5.28(b)–(d), the cloud is progressively dissipating.

The center column, Fig. 5.28(e)–(h), depicts contour plots of the mean macro-texture MTF values, $\overline{\text{MTF}}_{\text{macro}}$, for the time instances given by Fig. 5.28(a)–(d), as measured at each of the optical targets in the field. Values are interpolated in between the

$$\overline{\text{MTF}}_{\text{macro}} \qquad \overline{\text{MTF}}_{\text{micro}}$$

(a)   (e)   (i)

(b)   (f)   (j)

(c)   (g)   (k)

(d)   (h)   (l)

0.1

0.0
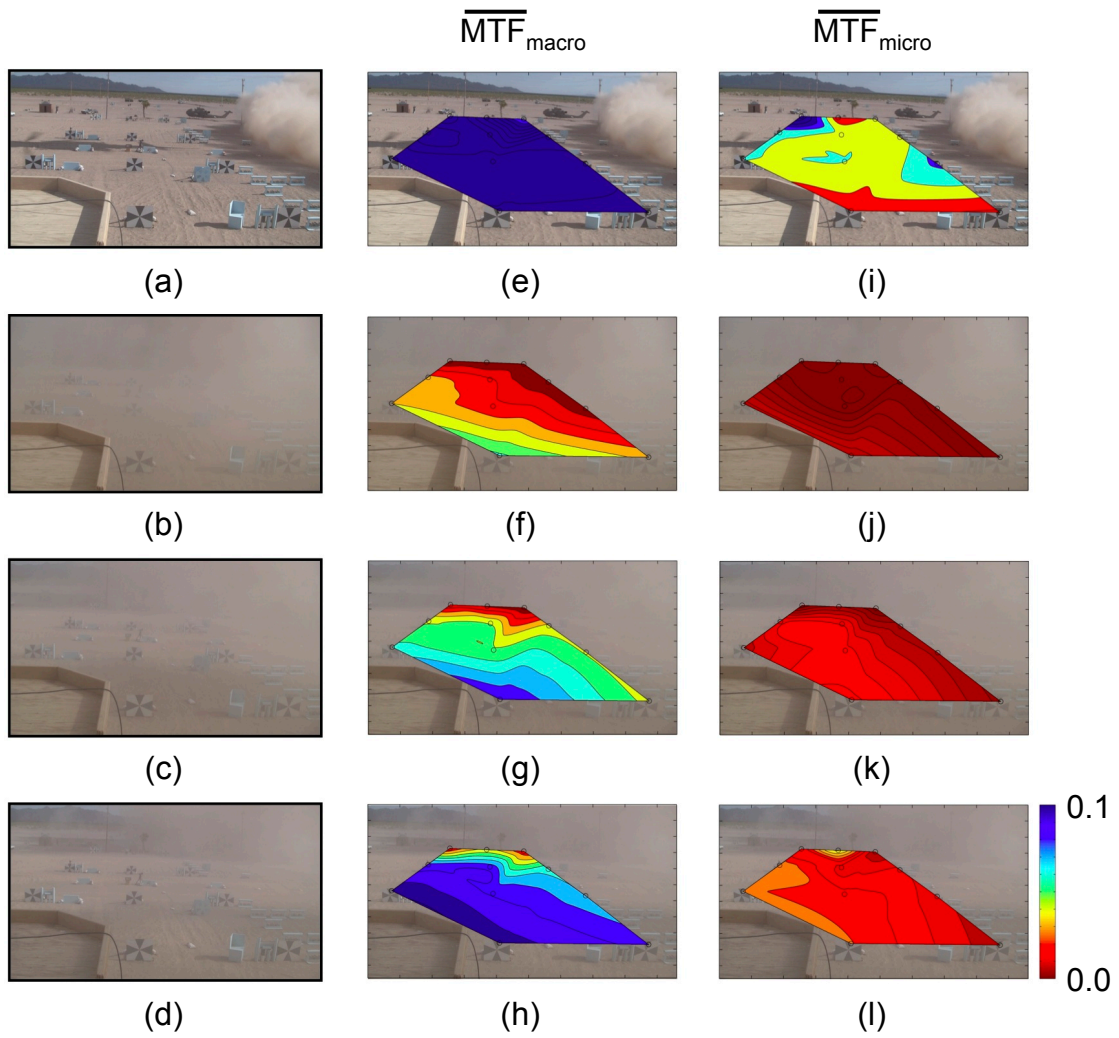
Figure 5.28: Contour plots of mean MTF over a broad FOV for low and high spatial frequencies (center and right columns, respectively).

11 exact calculations. Constant contours represent lines of equal $\overline{\text{MTF}}_{\text{macro}}$, or, equivalently, lines of equal macro-texture visual degradation. It is apparent in Fig. 5.28(e) that $\overline{\text{MTF}}_{\text{macro}} \geq 0.1$ over the visual field. Figure 5.28(f) depicts the scene as the cloud is beginning to dissipate. In the near-field, $\overline{\text{MTF}}_{\text{macro}} \approx 0.05$, and the visual degradation increases (i.e., $\overline{\text{MTF}}_{\text{macro}}$ decreases) towards the far-field. Figure 5.28(g)–(h) shows the same trend; visibility continues to increase over broader regions of the field of optical targets, with a preference for the near-field. This improvement in the near field is because the optical depth, a measure of the integrated particle density over an optical path, is lower in the near-field than for the far-field targets.

The contour plots in the right column, Fig. 5.28(i)–(l), show the same information, only for $\overline{\text{MTF}}_{\text{micro}}$. It is noteworthy in Fig. 5.28(i) that $\overline{\text{MTF}}_{\text{micro}}$ does not generally increase towards the near-field. This is likely because the MTF of the camera itself will not be simultaneously uniform over its entire field of view, and that the range of spatial frequencies utilized in $\overline{\text{MTF}}_{\text{micro}}$ are close to the cutoff frequency of the imaging system (i.e., the camera, the atmosphere, etc.). Figure 5.28(j)–(l) shows the improvement in visual cues at micro-texture scales that occurs as the cloud dissipates. It is important to note that, when considered together with the macro-texture contour plots, these contours quantify the intuitively-known fact that brownout clouds obscure small details on the ground before they obscure large objects.

A similar approach can be utilized to interpret the variation of MTF values in time. While the array of targets in Fig. 5.27 could once again have been used, only two optical paths from the vantage point in Fig. 5.20 were examined for simplicity. Figure 5.29(a)

depicts those two optical paths, which terminated at black-to-white transitions in the near- and far-field optical targets. Figure 5.29(b) and (c) provide the same FOV at instances 0.75 and 1.5 s later, respectively. Video footage was recorded at a 30 frames-per-second rate, and the MTFs along optical paths A and B were calculated for each image. From each of these MTFs, $\overline{\mathrm{MTF}}_{\mathrm{macro}}$ and $\overline{\mathrm{MTF}}_{\mathrm{micro}}$ were computed and they are plotted as functions of time in Fig. 5.30. Both Fig. 5.30(a) and (b) depict some minor variations in $\overline{\mathrm{MTF}}$ before a sudden and sharp decrease over a few tenths of a second. This drop occurs first for optical path B because the brownout cloud develops from right to left across the image.

Such a representation is unique in its ability to capture the rate of onset of the brownout cloud, although care must be exercised in drawing conclusions from the present results because they are for a vantage external to the cloud and perpendicular to the flight path (as opposed to a viewpoint from inside the cockpit). A similar temporal representation from other viewpoints could provide a concise, HQ-based assessment of the pilot's ability to close the necessary aircraft control loops.

5.4.3   Implications for Future MTF Testing

The methods that have been demonstrated can be considered as a "proof of concept" for brownout MTF calculations from the cockpit during a landing maneuver. In this case, the video camera would be mounted in the cockpit, looking outside, rather than being fixed outside the cloud, looking in. The cloud would thus develop in front of the helicopter and engulf it, rather than developing in the field of view from right to left. The measurement and processing techniques, however, would be identical to those presented
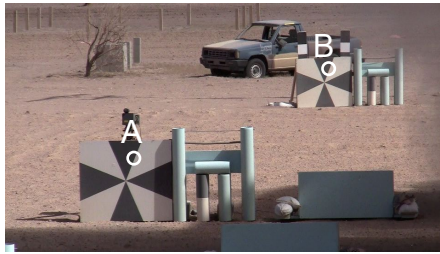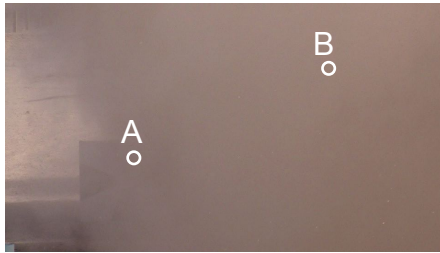
Figure 5.29: Snapshots corresponding to Fig. 5.30 at (a) 0 s, (b) 0.75 s, and (c) 1.5 s.
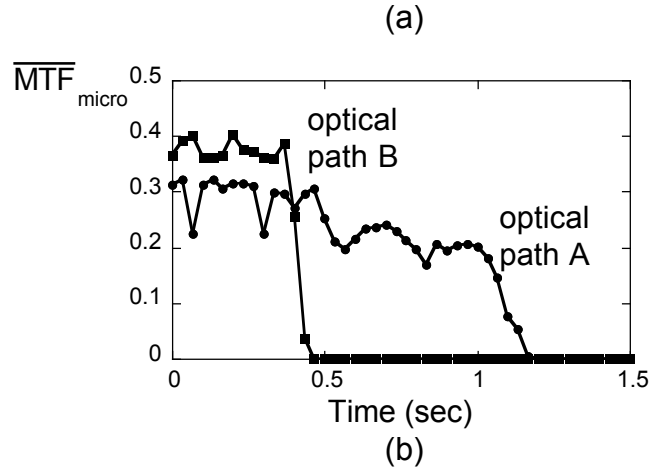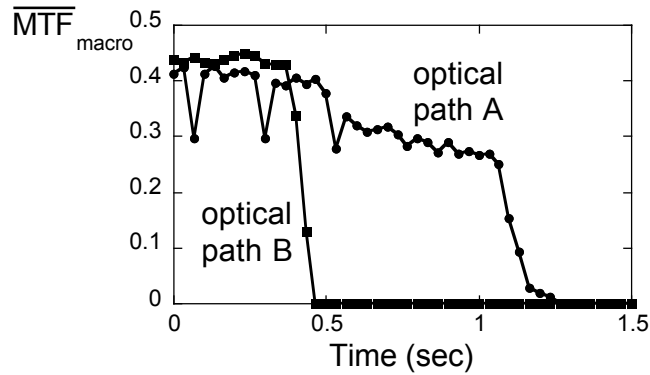
Figure 5.30: Mean MTF values, i.e., (a) $\overline{\text{MTF}}_{\text{macro}}$ and (b) $\overline{\text{MTF}}_{\text{micro}}$, versus time for a hover taxi maneuver.

here.

The present work also implies that ground level MTF measurements during landing could be performed using small targets that consist of a narrow strip with a black/white edge. Figure 5.22 indicates that the strips would only have to be large enough to accommodate a sampling region within the image frame that is 20 pixels wide on the video camera sensor and approximately 10 pixels in height. Because of their small size, it would be possible to place and safely secure these targets in the landing area.

Chapter 6

Predictions of the Visual Degradation Caused by a Brownout Cloud

The MTF measurements in Chapter 5 clearly demonstrated the ability of the MTF to characterize the spatial frequency-dependent effects of the brownout cloud: specifically, that the cloud attenuates visual cues at high spatial frequencies, i.e., micro-texture cues, more so than at low spatial frequencies, i.e., macro-texture cues. The ability to characterize the degradation of visual cues as a function of their texture scale can provide insight into the pilot's ability to perform certain control functions in those conditions. In this sense, the MTF shows great potential for use as the basis of a brownout characterization metric.

Beyond these experimental measurements, however, the MTF of a brownout cloud may also, in theory, be predicted from the fundamental physics of light scattering and absorption. While such predictions would clearly be of great practical value from the standpoint of operational mission planning (consider a scenario in which a small soil sample from a potential landing zone is used to "tune" the visual degradation of pilot-in-the-loop simulators for pre-mission rehearsals), the ability to predict the MTF of a brownout cloud would provide a number of additional benefits. For instance, the ability to predict the MTF of a simulated brownout cloud would potentially enable the formulation of simulation-based brownout mitigation studies in which optimal operational and design parameters could be determined from the predicted severity (in terms of the visual

degradation quantified by MTF) of the brownout cloud.

The goal of the present chapter is to explore the potential for predicting the MTF of a brownout cloud through simulation. The specific objectives are:

1. To present an initial methodology for the prediction of the MTF of a brownout cloud from fundamental light scattering and absorption theory.

2. To examine the sensitivity of the predictions to key physical parameters (such as the cloud density or imaging system limitations).

3. To present the results of a study in which MTF predictions are compared with MTF measurements in controlled conditions.

6.1   Dust Cloud Simulation Methodology

The prediction of the MTF of a brownout cloud is a multi-step process that begins with the simulation of the dust cloud. The methodology for the simulation of the brownout dust cloud development was described in Sections 2.1.1 and 2.1.2 as well as in Refs. 19 and 111, and only its key elements will be briefly summarized here. Notice that the methodology for predicting the MTF of a brownout cloud is completely independent of the method used to simulate the cloud. Therefore, the dust cloud simulation methodology utilized herein could be replaced by any other method for simulating the development of the dust cloud.

6.1.1 Flow Field and Dust Cloud Modeling

In the present work, the aerodynamic flow field of the rotor was modeled using a time-accurate Free-Vortex Method (FVM) configured to predict the flow for a rotorcraft under maneuvering flight conditions (Ref. 109). An image approach was utilized to model ground effect (Ref. 110), and a semi-empirical inviscid-viscous method was used to model the flow field that arises from a combination of the rotor flow (modeled as an inviscid potential flow) and the resulting (viscous) flow in the boundary layer region at the ground (Ref. 19).

For the present calculations, a semi-empirical, composite model based on the exceedance of a threshold friction velocity (Ref. 124) with corrections for unsteady pressure effects (Ref. 20) was used for the initiation of sediment motion on the ground. The dynamic motion of these particles was then modeled in synchronization with the solution for the rotor flow, as well as in the subsequent interactions of particles with the sediment bed. For example, dust particles in saltation or those that were reingested through the rotor disk could impact the sediment bed with greater momentum and subsequently eject many more particles in a process called bombardment. Both saltation bombardment and reingestion bombardment processes were modeled in the present simulations. Once the particles were entrained into the flow field near the ground, their convective motion was governed by the resulting forces acting upon the particles.

Initially, the dust particles were assumed to lie on the sediment bed in layers. Monodisperse, 20-micron diameter particles were considered for the present simulations. The sediment bed comprised 1.7×10^5 uplift-eligible particles in several layers, excluding

the many additional particles that were entrained as a consequence of bombardment. The particle simulation algorithm was implemented in double precision on graphics processing units (GPUs) for improved computational efficiency.

6.1.2   Analysis from the Pilot's Perspective

Once the dust cloud was modeled, the position of each particle of the cloud was projected in the pilot's FOV. This process involved the transformation of each particle location from the inertial Cartesian coordinate system used in the cloud model to a pilot-fixed spherical coordinate system. The necessary coordinate transformations were performed at each time step in the cloud simulation, and they were presented in Section 2.3.1. After these transformations, each particle was characterized by an eccentricity (i.e., an azimuth angle), θ_P, and an elevation angle, ϕ_P, in the pilot's FOV, as well as a radial distance, ρ, from the pilot. This procedure resulted in a distribution of particle density as seen by the pilot that was binned into discrete volume elements surrounding the pilot; see Fig 6.1. The particle count density (i.e., the number of particles per unit volume) for each bin was calculated as the number of particles in the bin divided by the overall volume of the bin.

6.2   MTF Prediction Methodology

Once the brownout cloud has been modeled, the MTF for an optical path through the cloud may be predicted from the fundamental physics of light scattering and absorption. In the present study, Kopeika's methodology (Refs. 80, 84) was utilized to compute the MTF of the simulated cloud. The methodology is derived from Radiative Transfer
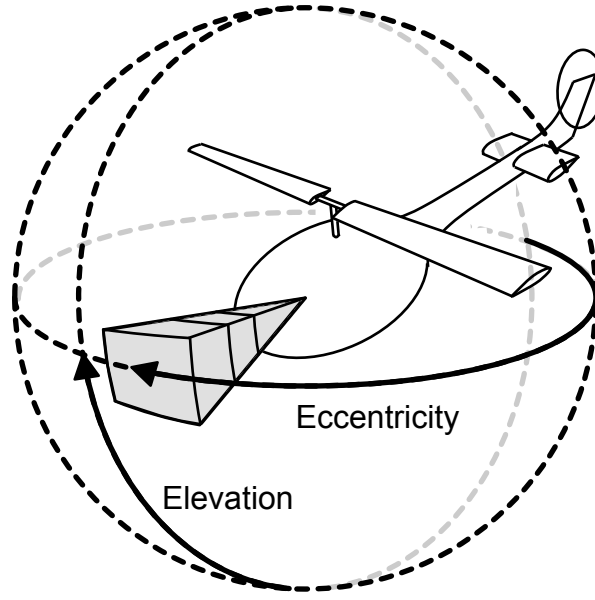
Figure 6.1: Schematic diagram of the bins for MTF calculation along a single optical path.

Theory (RTT), a heuristic approach to the problem of light scattering and absorption. For the sake of completeness, the present section will begin with a review of the general (analytical) problem of light scattering and absorption by small particles before introducing the heuristic RTT and specific MTF formulations.

6.2.1 Analytical Formulation Light Scattering/Absorption

The fundamental problem of light scattering and absorption can be stated succinctly as follows: given a particle (or a collection of particles) of specified size, shape, and optical properties that is illuminated by an arbitrarily polarized monochromatic wave, determine the electromagnetic field at all points of the medium in which the particle is embedded.

To solve this problem, the single-scattering case was considered first. This spe-

cial case involves an assumption that, "the number of particles is sufficiently small and their separation sufficiently large that, in the neighborhood of any particle, the total field scattered by all the particles is small compared with the external field" (Ref. 143). The formulations in the present section follow those presented in Chapters 2 and 3 of Ref. 143.

Maxwell's Equations

Light wave propagation is an electromagnetic phenomenon; therefore, the scattering and absorption of light are governed by Maxwell's equations (which are reviewed in detail in Appendix C), i.e.,

$$\nabla \cdot \boldsymbol{D} = \rho_F \qquad \text{(Gauss' Law)} \qquad (6.1)$$

$$\nabla \times \boldsymbol{E} + \frac{\partial \boldsymbol{B}}{\partial t} = 0 \qquad \text{(Faraday's Law)} \qquad (6.2)$$

$$\nabla \cdot \boldsymbol{B} = 0 \qquad \text{(Gauss' Law for Magnetism)} \qquad (6.3)$$

$$\nabla \times \boldsymbol{H} = \boldsymbol{J}_F + \frac{\partial \boldsymbol{D}}{\partial t} \qquad \text{(Ampere's Law)} \qquad (6.4)$$

where $\boldsymbol{E}$ is the electric field and $\boldsymbol{B}$ is the magnetic induction. The electric displacement $\boldsymbol{D}$ and the magnetic field $\boldsymbol{H}$ are defined by

$$\boldsymbol{D} = \varepsilon_0 \boldsymbol{E} + \boldsymbol{P} \qquad (6.5)$$

and

$$\boldsymbol{H} = \frac{\boldsymbol{B}}{\mu_0} - \boldsymbol{M} \qquad (6.6)$$

respectively, where P is the electric polarization (average electric dipole moment per unit volume), M is the magnetization (average magnetic dipole moment per unit volume). The permittivity and permeability of free space are given by ε_0 and μ_0, respectively. The charge and current densities are given by ρ_F and J_F, respectively.

Equations (6.1)–(6.4) must be supplemented by the constitutive relations, i.e.,

$$J_F = \sigma E \tag{6.7}$$

$$B = \mu H \tag{6.8}$$

$$P = \varepsilon_0 \chi E \tag{6.9}$$

where σ is the conductivity, μ is the permeability, and χ is the electric susceptibility. The phenomenological constants σ, μ, and χ depend on the medium under consideration, but are generally assumed for optics/imaging problems to be independent of the fields (i.e., linearity), independent of position (i.e., homogeneity), and independent of direction (i.e., isotropicity).

For the fields to be physically realizable, they must satisfy Maxwell's equations at all points where μ and ε are continuous. Beyond the assumptions of linearity, homogeneity, and isotropicity, it is further assumed that the material is charge-free, i.e., $\rho_F = 0$, and non-magnetic, i.e., $M = 0$. Additionally, the fields are assumed to be time-harmonic, i.e.,

$$E = E_0 \exp(i k \cdot x - i \omega t) \tag{6.10}$$

$$H = H_0 \exp(i k \cdot x - i \omega t) \tag{6.11}$$

where $\boldsymbol{k}$ is the wave vector for the surrounding medium, $\boldsymbol{x}$ is the position vector, and ω is the angular frequency.

Under these assumptions, Maxwell's equations can be simplified to

$$\nabla \cdot \boldsymbol{E} = 0 \tag{6.12}$$

$$\nabla \cdot \boldsymbol{H} = 0 \tag{6.13}$$

$$\nabla \times \boldsymbol{E} = i\omega\mu\boldsymbol{H} \tag{6.14}$$

$$\nabla \times \boldsymbol{H} = -i\omega\mu\boldsymbol{E} \tag{6.15}$$

where ε is the complex permittivity given by

$$\varepsilon = \varepsilon_0 (1+\chi) + i\frac{\sigma}{\omega} \tag{6.16}$$

The curls of Faraday's and Ampere's laws are

$$\nabla \times (\nabla \times \boldsymbol{E}) = i\omega\mu\,\nabla \times \boldsymbol{H} = \omega^2\varepsilon\mu\boldsymbol{E} \tag{6.17}$$

$$\nabla \times (\nabla \times \boldsymbol{H}) = -i\omega\mu\,\nabla \times \boldsymbol{E} = \omega^2\varepsilon\mu\boldsymbol{H} \tag{6.18}$$

and using the vector identity

$$\nabla \times (\nabla \times \boldsymbol{A}) = \nabla(\nabla \cdot \boldsymbol{A}) - \nabla \cdot (\nabla\boldsymbol{A}) \tag{6.19}$$

the following relations are obtained

$$\nabla^2 \boldsymbol{E} + k^2 \boldsymbol{E} = 0 \tag{6.20}$$

$$\nabla^2 \boldsymbol{H} + k^2 \boldsymbol{H} = 0 \tag{6.21}$$

where $k^2 = \omega^2 \varepsilon \mu$ and ∇^2 is the Laplacian operator, i.e., $\nabla^2 \boldsymbol{A} = \nabla \cdot (\nabla \boldsymbol{A})$. Equations (6.20) and (6.21) are the electromagnetic wave equations, and each one is an example of the vector wave equation.

Therefore, under the current assumptions, a physically realizable electric field, $\boldsymbol{E}$, must be divergence-free per Gauss' Law, Eq. (6.12), and satisfy the vector wave equation, Eq. (6.20). The associated magnetic field, $\boldsymbol{H}$, is related to the electric field through Faraday's Law, Eq. (6.14). The resulting fields would therefore, by definition, satisfy Maxwell's equations, Eqs. (6.12)–(6.15).

Electromagnetic Fields for a Scattering/Absorbing Particle

Consider the case of an arbitrary particle residing in an incident field; see Fig. 6.2. The electric and magnetic fields inside the particle are given by $(\boldsymbol{E}_1, \boldsymbol{H}_1)$, and the fields in the medium surrounding the particle, $(\boldsymbol{E}_2, \boldsymbol{H}_2)$, are the superposition of the incident fields, $(\boldsymbol{E}_i, \boldsymbol{H}_i)$, and the scattered fields, $(\boldsymbol{E}_s, \boldsymbol{H}_s)$, i.e.,

$$\boldsymbol{E}_2 = \boldsymbol{E}_i + \boldsymbol{E}_s \tag{6.22}$$

$$\boldsymbol{H}_2 = \boldsymbol{H}_i + \boldsymbol{H}_s \tag{6.23}$$
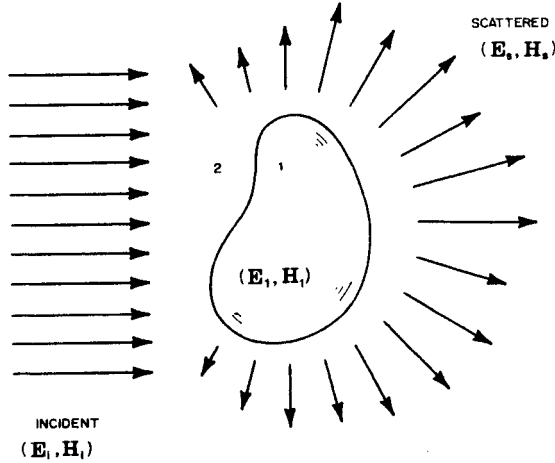
Figure 6.2: The incident fields, (E_i, H_i), give rise to the internal fields, (E_1, H_1), within the particle and the scattered fields,(E_2, H_2), in the medium outside the particle (from Ref. 143)

Although the electromagnetic fields are required to satisfy Maxwell's equations where ε and μ are continuous, the boundary between the particle and medium creates a discontinuity where there is a sudden change in these properties. Therefore, boundary conditions must be imposed at the particle surface, i.e.,

$$[E_2(x) - E_1(x)] \times \hat{n} = 0 \tag{6.24}$$

$$[H_2(x) - H_1(x)] \times \hat{n} = 0 \quad x \text{ on } S \tag{6.25}$$

where $\hat{n}$ is unit vector directed outward, normal to the surface, S, of the particle. From a physical standpoint, these boundary conditions require the tangential components of E and H to be continuous over the boundary between the particle and the medium. A physical justification for these boundary conditions is based on the principle of conservation of energy (Ref. 143).
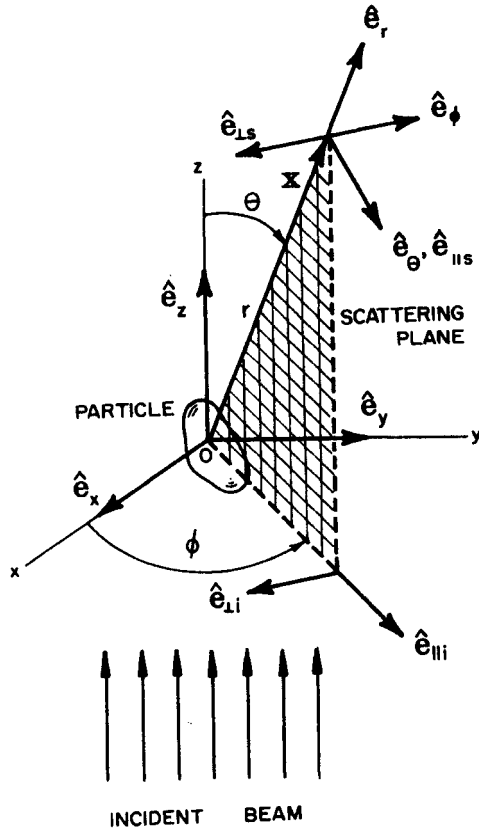
Figure 6.3: Scattering by an arbitrary particle (from Ref. 143)

Scattering Matrix

The relationship between the incident and scattered fields can be expressed rigorously, although a series of geometric transformations are required to do so. Figure 6.3 depicts the scattering of light by a particle that is illuminated by a plane harmonic wave. The z axis defines the direction of the propagation of light and is oftentimes referred to as the "forward direction." Orthonormal basis vectors are given by $\hat{e}_x$, $\hat{e}_y$, and $\hat{e}_z$, and a basis vector in the scattering direction is given by $\hat{e}_r$. The vectors $\hat{e}_r$ and $\hat{e}_z$ form the scattering plane.

While the incident field, E_i, lies in the xy plane, it can be useful to resolve it into

components that are parallel, $E_{\parallel i}$, and perpendicular, $E_{\perp i}$, to the scattering plane using the following coordinate transformations

$$\hat{e}_{\perp i} = \sin\phi \hat{e}_x - \cos\phi \hat{e}_y \tag{6.26}$$

$$\hat{e}_{\parallel i} = \cos\phi \hat{e}_x + \sin\phi \hat{e}_y \tag{6.27}$$

where ϕ is the azimuthal angle of the scattering plane. The incident field can thus be expressed

$$\boldsymbol{E}_i = \left(E_{0\parallel}\hat{e}_{\parallel i} + E_{0\perp}\hat{e}_{\perp i}\right)\exp\left(ikz - i\omega t\right) = E_{\parallel i}\hat{e}_{\parallel i} + E_{\perp i}\hat{e}_{\perp i} \tag{6.28}$$

where $k = 2\pi N_2/\lambda$ is the wave number in the medium surrounding the particle, N_2 is the refractive index of the external medium (which is ≈ 1 for atmospheric imaging), and λ is the wavelength of the incident light in vacuo. Notice that $\hat{e}_{\perp i}$ and $\hat{e}_{\parallel i}$ form a set of orthonormal basis vectors with $\hat{e}_z$, i.e., $\hat{e}_{\perp i} \times \hat{e}_{\parallel i} = \hat{e}_z$.

If the x and y components of the incident field are denoted by E_{xi} and E_{yi}, then the components that are parallel and perpendicular to the scattering plane may be expressed as

$$E_{\parallel i} = \cos\phi E_{xi} + \sin\phi E_{yi} \tag{6.29}$$

$$E_{\perp i} = \sin\phi E_{xi} - \cos\phi E_{yi} \tag{6.30}$$

An alternate set of orthonormal basis vectors may be given for the spherical coor-

dinate system by $\hat{e}_r$, $\hat{e}_\theta$, $\hat{e}_\phi$, i.e.,

$$\hat{e}_{\perp i} = -\hat{e}_\phi \tag{6.31}$$

$$\hat{e}_{\| i} = \sin\theta\hat{e}_r + \cos\theta\hat{e}_\theta \tag{6.32}$$

where θ is the scattering angle.

At large distances from the origin, i.e., in the far-field region, the scattered electric field, $\boldsymbol{E}_s$, is approximately transverse, i.e., $\hat{e}_r \cdot \boldsymbol{E}_s \approx 0$. Therefore, in the far-field region

$$\boldsymbol{E}_s = E_{\|s}\hat{e}_{\|s} + E_{\perp s}\hat{e}_{\perp s} \tag{6.33}$$

where

$$\hat{e}_{\|s} = \hat{e}_\theta \tag{6.34}$$

$$\hat{e}_{\perp s} = -\hat{e}_\phi \tag{6.35}$$

$$\hat{e}_r = \hat{e}_{\perp s} \times \hat{e}_{\|s} \tag{6.36}$$

Notice that the incident fields, Eq. (6.28), and scattered fields, Eq. (6.33), are specified relative to different sets of basis vectors. The relation between the incident and electric fields can be expressed conveniently in matrix form, i.e.,

$$\begin{pmatrix} E_{\|s} \\ E_{\perp s} \end{pmatrix} = \frac{\exp\left(ik\left(r-z\right)\right)}{-ikr} \begin{pmatrix} S_2 & S_3 \\ S_4 & S_1 \end{pmatrix} \begin{pmatrix} E_{\|i} \\ E_{\perp i} \end{pmatrix} \tag{6.37}$$

where the elements $S_j (j = 1, 2, 3, 4)$ of the amplitude scattering matrix depend, in general, on the scattering angle, θ, and the azimuthal angle, ϕ.

From the preceding, the Poynting vector can be calculated at any point. The Poynting vector, $\boldsymbol{S} = \boldsymbol{E} \times \boldsymbol{H}$, specifies the magnitude and direction of the rate of transfer of electromagnetic energy at all points in space (see further discussion in Appendix C). Typically it is the points in space that are external to the particle that are of primary importance, and the time-averaged Poynting vector at any external point can be expressed

$$\boldsymbol{S} = \frac{1}{2} \Re \left\{ \boldsymbol{E}_2 \times \boldsymbol{H}_2^* \right\} = \boldsymbol{S}_i + \boldsymbol{S}_s + \boldsymbol{S}_{\text{ext}} \tag{6.38}$$

$$\boldsymbol{S}_i = \Re \left\{ \boldsymbol{E}_i \times \boldsymbol{H}_i^* \right\} \tag{6.39}$$

$$\boldsymbol{S}_s = \Re \left\{ \boldsymbol{E}_s \times \boldsymbol{H}_s^* \right\} \tag{6.40}$$

$$\boldsymbol{S}_{\text{ext}} = \frac{1}{2} \Re \left\{ \boldsymbol{E}_i \times \boldsymbol{H}_s^* + \boldsymbol{E}_s \times \boldsymbol{H}_i^* \right\} \tag{6.41}$$

where $\boldsymbol{S}_i$ is the Poynting vector associated with the incident wave, $\boldsymbol{S}_s$ is the Poynting vector associated with the scattered wave, and $\boldsymbol{S}_{\text{ext}}$ is the term that arises from the interaction between the incident and scattered waves. Notice that the presence of an asterisk, i.e., $(\ )^*$, indicates the complex conjugate.

Scattering and Absorption

Calculating the Poynting vector from the electromagnetic fields is an essential step for computing the scattering and absorption characteristics of a particle. Figure 6.4 depicts an arbitrary particle that is illuminated by a plane harmonic wave. If the particle
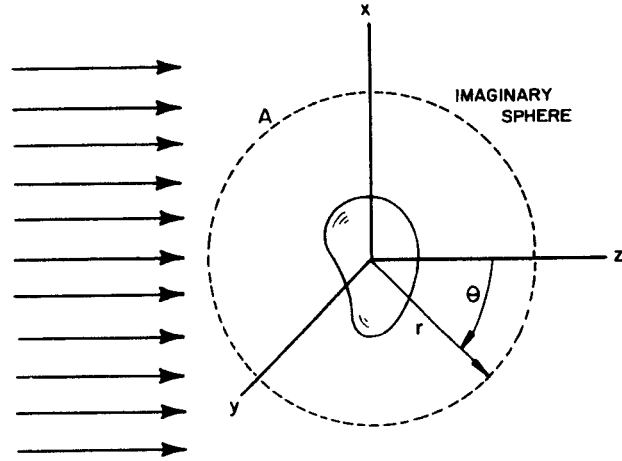
Figure 6.4: Schematic for extinction by a single particle (from Ref. 143).

were enclosed within a sphere of radius r, the net rate at which electromagnetic energy

crosses the surface, A, of that sphere is given by the integration of the radial projection of

the Poynting vector over the surface of the sphere, i.e.,

$$W_a = -\int_A \mathbf{S} \cdot \hat{e}_r \, dA \qquad (6.42)$$

where a negative W_a would indicate that energy is absorbed by the sphere. In accordance

with Eq. (6.38), W_a may be written as $W_a = W_i - W_s + W_{\text{ext}}$, where

$$W_i = -\int_A \mathbf{S}_i \cdot \hat{e}_r \, dA \qquad (6.43)$$

$$W_s = \int_A \mathbf{S}_s \cdot \hat{e}_r \, dA \qquad (6.44)$$

$$W_{\text{ext}} = -\int_A \mathbf{S}_{\text{ext}} \cdot \hat{e}_r \, dA \qquad (6.45)$$

307

Extinction and scattering cross sections can be defined as

$$C_{\text{ext}} = \frac{W_{\text{ext}}}{H_i} \tag{6.46}$$

$$C_{\text{sca}} = \frac{W_s}{H_i} \tag{6.47}$$

where H_i is the incident irradiance (irradiance is simply the magnitude of the time-averaged Poynting vector. These cross sections have units of area (i.e., W is in units of energy per unit time and H_i is in units of energy per unit area and time). Note that "extinction" includes the combination of scattering and absorption effects such that $C_{\text{ext}} = C_{\text{abs}} + C_{\text{sca}}$.

Extinction, scattering, and absorption efficiencies (or efficiency factors) may be defined as

$$Q_{\text{ext}} = \frac{C_{\text{ext}}}{G}, \quad Q_{\text{sca}} = \frac{C_{\text{sca}}}{G}, \quad Q_{\text{abs}} = \frac{C_{\text{abs}}}{G}, \tag{6.48}$$

respectively, where G is the particle cross-sectional area projected onto a plane perpendicular to the incident beam (e.g., $G = \pi a^2$ for a sphere with radius a).

Expanding to Collections of Particles

The preceding formulation has been purely analytical. It starts from the fundamental governing equations (i.e., Maxwell's equations) and maintains mathematical rigor in every step. Calculating analytcial solutions can be computationally expensive for a particle of irregular geometry, depending on the specific geometry and orientation. The presence of multiple particles can further complicate the computations, as the relative

positions and orientations of each particle will impact the result. Additionally, the single-scattering assumption will become incorrect as the number of particles per unit volume is increased. While the extension of purely analytical solutions to large collections of particles remains a topic of continued research, it is beyond the scope of this dissertation and will not be employed in the formulations herein. For more information on the application of analytical theory to problems of multiple scattering, see the textbooks from Ishimaru (Ref. 86) and Mishchenko (Refs. 144, 145).

6.2.2   Radiative Transfer Theory

At larger scales, it is impractical to maintain the mathematical rigor of finding exact analytical solutions to Maxwell's equations, and it is more typical to use the heuristic Radiative Transfer Theory (RTT). The single-scattering assumption is not present in RTT, meaning that the theory accounts for multiple scattering. The utility of RTT to a wide variety of problems has been demonstrated in prior optics research. Specifically, RTT has been employed in instances ranging from underwater visibility (Ref. 72) to the propagation of radiant energy in the atmospheres of planets, stars, and galaxies (Refs. 146, 147). There is also a growing body of medical imaging research that utilizes RTT (Refs. 148, 149). The closest existing application of RTT to the brownout problem is that of atmospheric imaging in desert environments (Refs. 79–81, 84). Indeed, much of the research on the Modulation Transfer Function (MTF) that was reviewed in the first chapter has its origins in RTT. The formulations of the present subsection follow those presented in Ref. 86.

Fundamentals of Radiative Transfer Theory

Radiative Transfer Theory (RTT) is formulated by considering the transfer of energy through a medium filled with a large number of particles while imposing the conservation of energy. In RTT, a medium filled with a large number of particles is treated as continuous and locally homogenous, and the concepts of scattering and absorption of light by individual particles are replaced by the scattering and absorption by a small volume element (Ref. 144).

The specific intensity, $I(r, \hat{e}_s)$, also called the brightness, spectral radiant emittance, or spectral radiance, is the primary radiometric quantity in calculations of RTT. It is the amount of radiant power, dP, per unit area, da, solid angle, $d\omega$, and frequency range, $d\nu$, at any location, r, and in any direction, $\hat{e}_s$, in space. Specific intensity is typically given in units of $[\text{W}][\text{m}^{-2}][\text{ster}^{-1}][\text{Hz}^{-1}]$ (where [ster] is steradian, i.e., unit solid angle).

The fundamental equation of RTT is known as the "equation of transfer." It is a differential equation that describes specific intensity (i.e., "brightness") at all locations and directions in space, $I(r, \hat{e}_s)$, caused by three distinct effects. First, there is a reduction of specific intensity due to scattering and absorption by a volume element consisting of a collection of particles, i.e.,

$$\frac{dI(r, \hat{e}_s)}{ds} = -\sigma I(r, \hat{e}_s) \tag{6.49}$$

where ds is the length of the volume element with unit cross-section and σ is the extinction coefficient of the volume element (i.e., the combination of the effects of scattering and absorption).
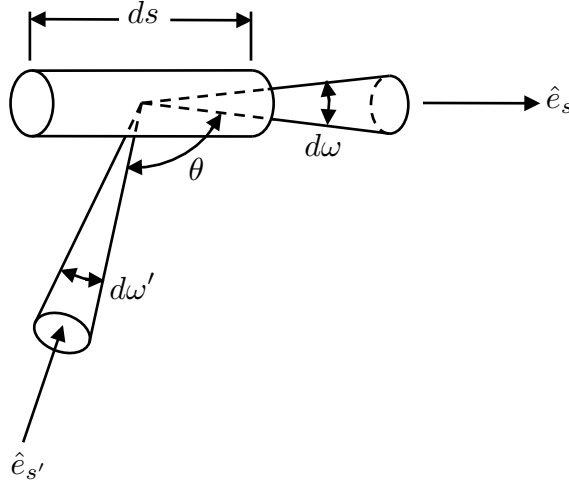
Figure 6.5: Scattering of specific intensity upon the volume ds from the direction $\hat{e}_{s'}$ into the direction $\hat{e}_s$ (adapted from Ref. 86).

Additionally, there may be an increase due to specific intensity that is incident on the same volume element, though originating from other directions, i.e.,

$$\frac{dI\left(r,\hat{e}_s\right)}{ds} = \frac{S_a}{4\pi} \int_{\Omega} P(\theta)\, I\left(r,\hat{e}_{s'}\right)\, d\omega' \tag{6.50}$$

where S_a is the scattering coefficient of the volume element, $P(\theta)$ is the normalized phase function of the medium (i.e., a function that describes the relative distribution of scattered light in all directions), and $\hat{e}_{s'}$ and $d\omega'$ are the unit normal and differential solid angle for an arbitrary direction. Notice that the expression $S_a\, P(\theta)\, I\left(r,\hat{e}_{s'}\right)$ describes the light that is scattered in the $\hat{e}_s$ direction from the specific intensity that is incident on location r in the $\hat{e}_{s'}$ direction (see Fig. 6.5). Notice also that the integral in Eq. (6.50) is an integration with respect to solid angle, ω', over all directions around the particle, and Ω denotes the entire surface of an imaginary sphere surrounding the particle. The 4π in the denominator normalizes the phase function, where, in this formulation, $\int_{\Omega} P(\theta) d\omega' = 4\pi$.

Finally, specific intensity may increase due to emission from within the volume element, i.e.,

$$\frac{dI(\boldsymbol{r}, \hat{e}_s)}{ds} = \varepsilon(\boldsymbol{r}, \hat{e}_s) \tag{6.51}$$

where $\varepsilon(\boldsymbol{r}, \hat{e}_s)$ is the emission at location $\boldsymbol{r}$ in direction $\hat{e}_s$. Emission is typically zero in atmospheric imaging applications.

The full equation of transfer can thus be expressed as the sum of the three afore-mentioned effects (Ref. 86), i.e.,

$$\frac{dI(\boldsymbol{r}, \hat{e}_s)}{ds} = \underbrace{-\sigma I(\boldsymbol{r}, \hat{e}_s)}_{\text{scattering and absorption}} + \underbrace{\frac{S_a}{4\pi} \int_{\Omega} P(\theta) I(\boldsymbol{r}, \hat{e}_{s'}) \, d\omega'}_{\text{incident SI from other directions}} + \underbrace{\varepsilon(\boldsymbol{r}, \hat{e}_s)}_{\text{emission}} \tag{6.52}$$

where the primary unknowns are the extinction and scattering coefficients of the volume element, σ and S_a, and the phase function of the volume element, $P(\theta)$. A standard assumption in RTT (Refs. 84, 144) is that the scattering and absorption characteristics of a small volume element are reasonably approximated by the sums of the respective characteristics of the constituent particles, as solved analytically from Maxwell's equations for the special case of spherical particles. This special solution to Maxwell's equations is commonly known as Mie theory.

Calculating Scattering/Absorption Characteristics for a Volume Element

The absorption and scattering of light by spherical particles of arbitrary radius and refractive index is known as Mie theory after Gustav Mie, who published the theory in 1908 (Ref. 150). While an exact theoretical solution is possible for the case of spherical

particles, the mathematics is "cumbersome" (Ref. 143); therefore, solutions were only generated for special cases in the age prior to the computer. Since the advent of the computer, however, Mie calculations have been made possible at relatively small computational cost. The formulations of the present subsection follow those presented in Ref. 143.

Mie theory is applicable to spherical particles of any size, although at smaller sizes (i.e., when the ratio of particle to wavelength is small: $2\pi a/\lambda < 1$ where a is the particle radius) the simpler Rayleigh theory is often utilized. At smaller particle sizes, Mie theory reduces to Rayleigh theory (Ref. 151). At larger particle sizes, however, Mie theory is necessary for computing the complicated phase functions. Although most natural problems do not consist of perfectly spherical particles, Mie theory has been shown to provide important insight into such cases (Ref. 143). A thorough treatment of Mie theory is found in Section 4.1 of Bohren and Huffman's textbook (Ref. 143).

Preliminaries   It was established in Section 6.2.1 that physically-realizable fields must satisfy Maxwell's equations. This condition is met for fields that: (i) satisfy the vector wave equation, Eq. (6.20), (ii) are divergence-free, Eq. (6.12), and (iii) are related by Faraday's Law, Eq. (6.2).

Within Mie theory, special formulations for the electromagnetic fields are derived from "generating functions" that take advantage of the inherent symmetry when the particle is assumed to be spherical. Suitable generating functions in a spherical coordinate
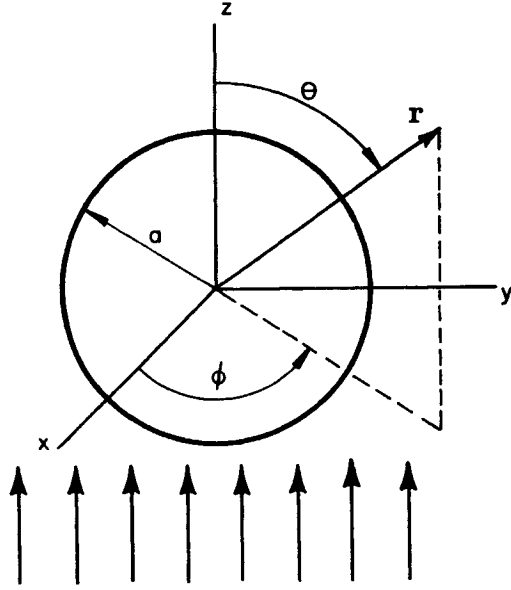
Figure 6.6: Spherical polar coordinate system centered on a spherical particle of radius a (from Ref. 143).

system (see Fig. 6.6) are shown to be

$$\psi_{emn} = \cos(m\phi) P_n^m(\cos\theta) z_n(kr) \tag{6.53}$$

$$\psi_{omn} = \sin(m\phi) P_n^m(\cos\theta) z_n(kr) \tag{6.54}$$

where: (i) the subscript o is for odd m and the subscript e is for even m, (ii) $P_n^m(\cos\theta)$ are associated Legendre functions of the first kind of degree n and order m, when $n = m, m+1, ...$, and (iii) $z_n(\rho)$ can be any one of the four spherical Bessel functions (note that $\rho = kr$ is a non-dimensionalized particle radius where k, again is the wave number in the medium surrounding the particle $k = 2\pi N_2/\lambda$). The four types of spherical Bessel functions are:

1. Bessel functions of the first kind:

$$j_n(\rho) = \sqrt{\frac{\pi}{2\rho}} J_{n+1/2}(\rho) \tag{6.55}$$

2. Bessel functions of the second kind:

$$y_n(\rho) = \sqrt{\frac{\pi}{2\rho}} Y_{n+1/2}(\rho) \tag{6.56}$$

3. Bessel functions of the third kind (also called spherical Hankel functions):

$$h_n^{(1)} = j_n(\rho) + i y_n(\rho) \tag{6.57}$$

$$h_n^{(2)} = j_n(\rho) - i y_n(\rho) \tag{6.58}$$

The spherical Bessel functions can be computed easily for the first two orders, i.e., $n = 1, 2$, and higher orders can be computed by a set of recurrence relations (Ref. 143). From a computational perspective, this is an important consideration for Mie codes in computer languages that do not include native formulations for Bessel functions.

With the definition of suitable generating functions, vector harmonics $\boldsymbol{M}$ and $\boldsymbol{N}$ can be constructed, i.e.,

$$\boldsymbol{M}_{emn} = \nabla \times (\boldsymbol{r}\psi_{emn}) \tag{6.59}$$

$$\boldsymbol{M}_{omn} = \nabla \times (\boldsymbol{r}\psi_{omn}) \tag{6.60}$$

315

$$N_{emn} = \frac{\nabla \times M_{emn}}{k} \tag{6.61}$$

$$N_{omn} = \frac{\nabla \times M_{omn}}{k} \tag{6.62}$$

Notice that these vector harmonics M and N are vector equations that satisfy the conditions for admissible electromagnetic field equations: (i) they satisfy the vector wave equation, (ii) they are divergence-free, and (iii) the curl of M is proportional to N, and the curl of N is proportional to M. Notice also that these equations are formulated in a spherical polar coordinate system.

Expressing the Fields in Vector Harmonics   Recalling that the general formulation of the light scattering problem involves the solution of the internal and external scattered fields (see Fig. 6.2), the next step is to express the incident electric field in terms of the vector harmonics, i.e.,

$$E_i = E_0 \sum_{n=1}^{\infty} i^n \frac{2n+1}{n(n+1)} \left(M_{o1n}^{(1)} - i N_{e1n}^{(1)} \right) \tag{6.63}$$

where the superscript (1) denotes that the Bessel function of the first kind, Eq. (6.55), is used in the formulation. The incident magnetic field follows from Faraday's law, i.e.,

$$H_i = \frac{-k}{\omega\mu} E_0 \sum_{n=1}^{\infty} i^n \frac{2n+1}{n(n+1)} \left(M_{e1n}^{(1)} + i N_{o1n}^{(1)} \right) \tag{6.64}$$

The boundary conditions at the surface of the particle, Eqs. (6.24) and (6.25) may

now be invoked, i.e.,

$$(\boldsymbol{E}_i + \boldsymbol{E}_s - \boldsymbol{E}_1) \times \hat{e}_r = (\boldsymbol{H}_i + \boldsymbol{H}_s - \boldsymbol{H}_1) \times \hat{e}_r = 0 \tag{6.65}$$

where the external fields, $\boldsymbol{E}_2$ and $\boldsymbol{H}_2$, result from the superposition of the incident and scattered fields.

Just as was performed for the incident field, the internal field can be expressed as

$$\boldsymbol{E}_1 = \sum_{n=1}^{\infty} \boldsymbol{E}_n \left(c_n \boldsymbol{M}_{o1n}^{(1)} - i d_n \boldsymbol{N}_{e1n}^{(1)} \right) \tag{6.66}$$

$$\boldsymbol{H}_1 = \frac{-k_1}{\omega \mu_1} \sum_{n=1}^{\infty} \boldsymbol{E}_n \left(d_n \boldsymbol{M}_{e1n}^{(1)} - i c_n \boldsymbol{N}_{o1n}^{(1)} \right) \tag{6.67}$$

where $\boldsymbol{E}_n = i^n \boldsymbol{E}_0 (2n + 1/n(n+1))$, k_1 is the wave number in the sphere, and μ_1 is the permeability of the sphere. The scattered fields may likewise be expressed in terms of the vector harmonics, i.e.,

$$\boldsymbol{E}_s = \sum_{n=1}^{\infty} \boldsymbol{E}_n \left(i a_n \boldsymbol{N}_{e1n}^{(3)} - b_n \boldsymbol{M}_{o1n}^{(3)} \right) \tag{6.68}$$

$$\boldsymbol{H}_s = \frac{k}{\omega \mu} \sum_{n=1}^{\infty} \boldsymbol{E}_n \left(i b_n \boldsymbol{N}_{o1n}^{(3)} - a_n \boldsymbol{M}_{e1n}^{(3)} \right) \tag{6.69}$$

where the superscript (3) denotes that the Hankel function of the first kind (i.e., a Bessel function of the third kind), Eq. (6.57), is used in the formulation. The variables a_n, b_n, c_n, and d_n are weighting factors.

Angle-Dependent Functions It is convenient to introduce two angle-dependent functions, π_n and τ_n. While their formal definitions include Legendre functions, they can be numerically computed by upward recurrence from the relations

$$\pi_n = \frac{2n-1}{n-1}\mu_{n-1} - \frac{n}{n-1}\pi_{n-2} \tag{6.70}$$

$$\tau_n = n\,\mu\,\pi_n - (n+1)\,\pi_{n-1} \tag{6.71}$$

where $\mu = \cos\theta$, beginning with $\pi_0 =$ and $\pi_1 = 1$. These relations can be used in simplifying the expressions for the vector harmonics, and they have an effect on the angular dependence of the fields. It is through these functions that the effects of increased forward scattering and narrowing scatter peaks for larger particle sizes are introduced. The first five angle-dependent functions are shown in Fig. 6.7.

Scattering Coefficients Equations (6.63)–(6.64) and (6.66)–(6.69) express the incident, internal, and scattered fields as infinite series of the vector harmonics, though they include four unknown coefficients, a_n, b_n, c_n, and d_n. To solve for these weighting coefficients, four more independent equations are necessary. These equations can be obtained from the boundary conditions given by Eq. (6.65), i.e.,

$$\boldsymbol{E}_{i\theta} + \boldsymbol{E}_{s\theta} = \boldsymbol{E}_{1\theta} \tag{6.72}$$

$$\boldsymbol{E}_{i\phi} + \boldsymbol{E}_{s\phi} = \boldsymbol{E}_{1\phi} \tag{6.73}$$

$$\boldsymbol{H}_{i\theta} + \boldsymbol{H}_{s\theta} = \boldsymbol{H}_{1\theta} \tag{6.74}$$

$$\boldsymbol{H}_{i\phi} + \boldsymbol{H}_{s\phi} = \boldsymbol{H}_{1\phi} \tag{6.75}$$
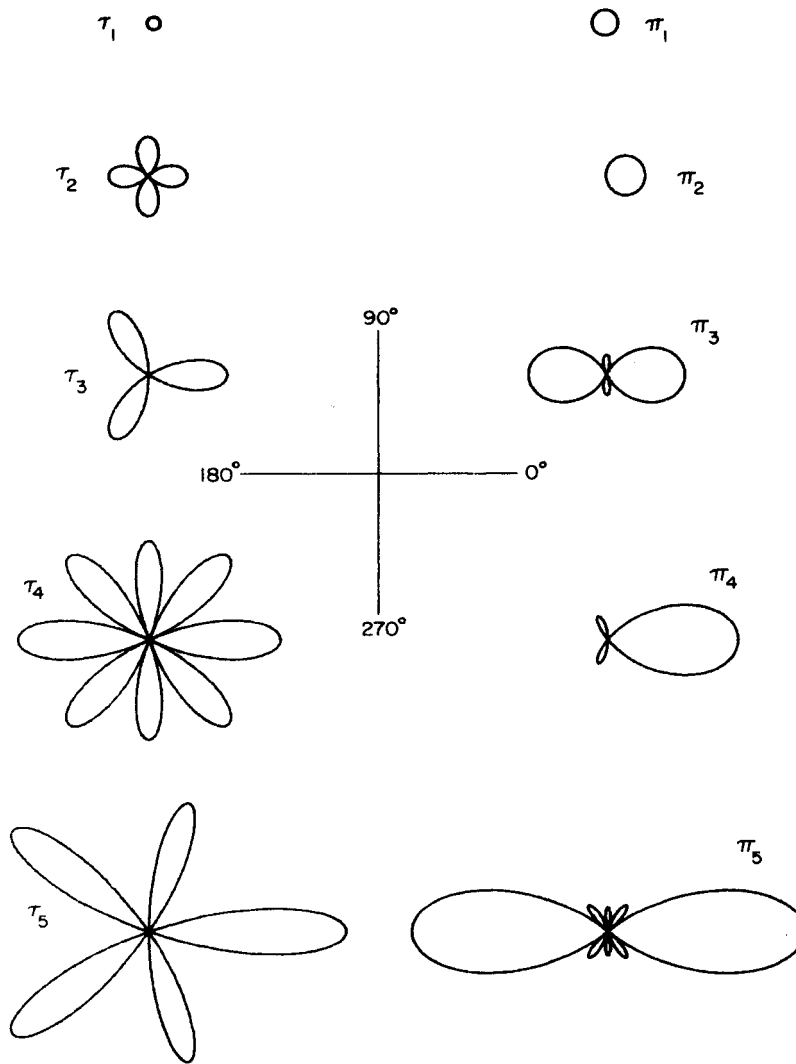
Figure 6.7: Polar plots of the first five angle-dependent functions, π_n and τ_n. Both functions are plotted to scale (from Ref. 143).

319

where $r = a$ (i.e., the boundary condition is applied at the surface of the particle).

The solutions are expressed in terms of the size parameter, x, and the relative refractive index, m, i.e.,

$$x = ka = \frac{2\pi Na}{\lambda} \tag{6.76}$$

$$m = \frac{k_1}{k} = \frac{N_1}{N} \tag{6.77}$$

where the subscript 1 still denotes the internal field. The solutions for the four unknown coefficients are

$$a_n = \frac{\mu m^2 j_n(mx) \left[x j_n(x)\right]' - \mu_1 j_n(x) \left[mx j_n(mx)\right]'}{\mu m^2 j_n(mx) \left[x h_n^{(1)}(x)\right]' - \mu_1 h_n^{(1)}(x) \left[mx j_n(mx)\right]'} \tag{6.78}$$

$$b_n = \frac{\mu_1 j_n(mx) \left[x j_n(x)\right]' - \mu j_n(x) \left[mx j_n(mx)\right]'}{\mu_1 j_n(mx) \left[x h_n^{(1)}(x)\right]' - \mu h_n^{(1)}(x) \left[mx j_n(mx)\right]'} \tag{6.79}$$

$$c_n = \frac{\mu_1 j_n(x) \left[x h_n^{(1)}(x)\right]' - \mu_1 h_n^{(1)}(x) \left[x j_n(x)\right]'}{\mu_1 j_n(mx) \left[x h_n^{(1)}(x)\right]' - \mu h_n^{(1)}(x) \left[mx j_n(mx)\right]'} \tag{6.80}$$

$$d_n = \frac{\mu_1 m j_n(x) \left[x h_n^{(1)}(x)\right]' - \mu_1 m h_n^{(1)}(x) \left[x j_n(x)\right]'}{\mu m^2 j_n(mx) \left[x h_n^{(1)}(x)\right]' - \mu_1 h_n^{(1)}(x) \left[mx j_n(mx)\right]'} \tag{6.81}$$

where a_n and b_n are called scattering coefficients and c_n and d_n are coefficients for the field inside the particle.

Expressions for the scattering coefficients can be simplified by introducing the

Riccati-Bessel functions

$$\psi_n(\rho) = \rho j_n(\rho) \tag{6.82}$$

$$\xi_n(\rho) = \rho h_n^{(1)}(\rho) \tag{6.83}$$

If the permeability of the particle and the surrounding medium are assumed to be equal, i.e.,

$$a_n = \frac{m\psi_n(mx)\psi_n'(x) - \psi_n(x)\psi_n'(mx)}{m\psi_n(mx)\xi_n'(x) - \xi_n(x)\psi_n'(mx)} \tag{6.84}$$

$$b_n = \frac{\psi_n(mx)\psi_n'(x) - m\psi_n(x)\psi_n'(mx)}{\psi_n(mx)\xi_n'(x) - m\xi_n(x)\psi_n'(mx)} \tag{6.85}$$

With these coefficients, the internal and external (i.e., incident and scattered) fields may be solved through Eqs. (6.63)–(6.64) and (6.66)–(6.69).

From a computational standpoint, Bohren and Huffman (Ref. 143) suggest the use of the logarithmic derivative

$$D_n(\rho) = \frac{d}{d\rho} \ln \psi_n(\rho) \tag{6.86}$$

in simplifying the process of obtaining a solution for the scattering coefficients in a computer code. The scattering coefficients are then expressed

$$a_n = \frac{[D_n(mx)/m + n/x]\psi_n(x) - \psi_{n-1}(x)}{[D_n(mx)/m + n/x]\xi_n(x) - \xi_{n-1}(x)} \tag{6.87}$$

$$b_n = \frac{[mD_n(mx)/m + n/x]\psi_n(x) - \psi_{n-1}(x)}{[mD_n(mx)/m + n/x]\xi_n(x) - \xi_{n-1}(x)} \tag{6.88}$$

321

where ψ_n' and ξ_n' have been eliminated by the recurrence relations

$$\psi_n'(x) = \psi_{n-1}(x) - \frac{n\,\psi_n(x)}{x} \tag{6.89}$$

$$\xi_n'(x) = \xi_{n-1}(x) - \frac{n\,\xi_n(x)}{x} \tag{6.90}$$

and the logarithmic derivative satisfies the recurrence relation

$$D_{n-1} = \frac{n}{\rho} - \frac{1}{D_n + n/\rho} \tag{6.91}$$

Efficiencies and Cross Sections   Just as for the general case of light scattering and absorption, an imaginary sphere of radius r may be constructed around the particle, and the net rate at which electromagnetic energy crosses the surface, A, of the sphere is

$$W_a = -\int_A \boldsymbol{S} \cdot \hat{\boldsymbol{e}}_r \, dA \tag{6.92}$$

For a spherical particle, the extinction and scattering cross sections (in units of area) are defined as

$$C_{\text{ext}} = \frac{W_{\text{ext}}}{H_i} = \frac{2\pi}{k^2} \sum_{n=1}^{\infty} (2n+1)\,\Re\{a_n + b_n\} \tag{6.93}$$

$$C_{\text{sca}} = \frac{W_{\text{sca}}}{H_i} = \frac{2\pi}{k^2} \sum_{n=1}^{\infty} (2n+1)\left(|a_n|^2 + |b_n|^2\right) \tag{6.94}$$

where, again, H_i is the incident irradiance, k is the wave number, and a_n and b_n are scattering coefficients. Recall that $C_{\text{ext}} = C_{\text{abs}} + C_{\text{sca}}$. From a computational standpoint,

Bohren and Huffman (Ref. 143) point out that the infinite series is suitably estimated by $n_{max} = x + 4x^{1/3} + 2$ terms (where x is the size parameter).

Furthermore, the non-dimensional extinction and scattering efficiencies can be computed

$$Q_{ext} = \frac{C_{ext}}{G} = \frac{2}{x^2} \sum_{n=1}^{\infty} (2n+1) \, \Re \{a_n + b_n\} \tag{6.95}$$

$$Q_{sca} = \frac{C_{sca}}{G} = \frac{2}{x^2} \sum_{n=1}^{\infty} (2n+1) \left(|a_n|^2 + |b_n|^2 \right) \tag{6.96}$$

Scattering Matrix   As shown for the general case, it is oftentimes convenient to resolve the incident electric field, $\boldsymbol{E}_i$, into components parallel and perpendicular to the scattering plane. For the case of a spherical particle

$$\begin{pmatrix} E_{\|s} \\ E_{\perp s} \end{pmatrix} = \frac{\exp(ik(r-z))}{-ikr} \begin{pmatrix} S_2 & 0 \\ 0 & S_1 \end{pmatrix} \begin{pmatrix} E_{\|i} \\ E_{\perp i} \end{pmatrix} \tag{6.97}$$

where

$$S_1 = \sum_n \frac{2n+1}{n(n+1)} (a_n \pi_n + b_n \tau_n) \tag{6.98}$$

$$S_2 = \sum_n \frac{2n+1}{n(n+1)} (a_n \tau_n + b_n \pi_n) \tag{6.99}$$

and the elements S_1 and S_2 depend only on the scattering angle, θ. In comparison with the formulation for the general case, i.e., Eq. (6.37), there is no longer a dependency on the azimuthal angle, ϕ, because of the symmetry of the sphere.

It is also convenient to define dimensionless intensity parameters $i_\perp$ and $i_\parallel$, i.e.,

$$i_\perp = |S_1|^2 = S_1 S_1^* \tag{6.100}$$

$$i_\parallel = |S_2|^2 = S_2 S_2^* \tag{6.101}$$

Numerical Computation of Mie Solutions   In the present work, Bohren and Huffman's numerical algorithm for Mie solutions was utilized (Ref. 143) to calculate the scattering and absorption characteristics of an individual particle embedded within a medium. The algorithm requires the prescription of the particle size parameter, $x = ka = 2\pi a/\lambda$ (where a is particle radius and λ is the imaging wavelength), and the complex refractive indices, $m = n + i\kappa$, of both the particle and the medium. The algorithm numerically solves for the electromagnetic fields both internal and external to the particle. The procedure results in the calculation of the non-dimensional extinction and scattering efficiencies (Q_{ext} and Q_{sca}, respectively, where $Q_{\text{abs}} = Q_{\text{ext}} - Q_{\text{sca}}$) as well as the complex amplitudes of the scattered electric fields, S_1 and S_2.

Extension to Collections of Particles   The formulation of Mie Theory to this point has been for a single particle; however, for the brownout case (and, in general, for problems of atmospheric scattering) the problem involves collections of particles. This is discussed in detail in Deirmendjian's book, Ref. 152. The simpler case is that of monodispersions, in which all of the particles are identical in size and optical properties. The more complicated case is that of polydispersions, in which the particle size ranges according to a defined distribution.

For a collection of monodisperse particles, the scattering coefficient for the medium can be computed

$$S_a(N, x) = N\pi a^2 Q_{\text{sca}}(x) \tag{6.102}$$

where N is the number of particles per unit volume, a is the particle radius, and x is the particle size factor. Thus, S_a is in units of scattering cross section per unit volume. Similarly, the extinction and absorption coefficients, respectively, may be computed

$$\sigma(N, x) = N\pi a^2 Q_{\text{ext}}(x) \tag{6.103}$$

$$A_a(N, x) = N\pi a^2 Q_{\text{abs}}(x) \tag{6.104}$$

where, just as $C_{\text{ext}} = C_{\text{abs}} + C_{\text{sca}}$ for an individual particle, $\sigma(N, x) = S_a(N, x) + A_a(N, x)$ for the medium consisting of a collection of particles. A normalized phase function for the medium may also be computed. From a physical standpoint, the normalized phase function provides the differential scattering cross section divided by the total scattering cross section. The differential scattering cross section is the energy scattered per unit time into a solid angle about a direction $\hat{e}_r$ that is specified by the scattering angle, θ, and the azimuth angle, ϕ (see Fig. 6.3)–for unit incident irradiance (for Mie theory this is dependent solely on the scattering angle).

Deirmendjian (Ref. 152) defines the normalized phase function of the medium, i.e.,

$$P(\theta) = \frac{1}{2}\left[P_1(\theta) + P_2(\theta)\right] \tag{6.105}$$

subject to a normalization condition, i.e.,

$$\int_{\Omega} P(\theta)\, d\omega = 4\pi \tag{6.106}$$

where $\int_{\Omega} d\omega$ is an integration with respect to solid angle ω over all directions around the point occupied by the particle. The capitol Ω denotes the entire surface of the sphere and $d\omega$ is the differential sold angle.

The terms in the normalized phase function, Eq. (6.105), are

$$P_1(\theta) = \frac{4i_{\perp}(\theta)}{x^2 Q_{sca}(x)} \tag{6.107}$$

$$P_2(\theta) = \frac{4i_{\parallel}(\theta)}{x^2 Q_{sca}(x)} \tag{6.108}$$

so that, for the case of monodisperse particles

$$P(\theta) = \frac{2}{x^2 Q_{sca}(x)} \left[i_{\perp}(\theta) + i_{\parallel}(\theta) \right] \tag{6.109}$$

Notice that the extinction and scattering coefficients for the medium, σ and S_a, and the medium's phase function, $P(\theta)$, are the scattering and absorption characteristics that are required for the equation of transfer within RTT, Eq. (6.52).

For the case when particles are not of uniform size, it is common for the size distribution of particles to be given by

$$N = \int_{r_1}^{r_2} n(r)\, dr \tag{6.110}$$

326

where N is the total number of particles per unit volume and $n(r)$ is a continuous and integrable function defined within the range, representing the partial concentration per unit volume and per unit increment of the radius r. The distribution function can be expressed in terms of the size parameter, $x = ka = 2\pi a/\lambda$, i.e.,

$$N = k^{-1} \int_0^\infty n(x)\,dx \tag{6.111}$$

and the scattering, extinction, and absorption coefficients are, therefore,

$$S_a(\lambda, x) = \pi k^{-3} \int_0^\infty x^2 n(x) Q_{\text{sca}}(x)\,dx \tag{6.112}$$

$$\sigma(\lambda, x) = \pi k^{-3} \int_0^\infty x^2 n(x) Q_{\text{ext}}(x)\,dx \tag{6.113}$$

$$A_a(\lambda, x) = \pi k^{-3} \int_0^\infty x^2 n(x) Q_{\text{abs}}(x)\,dx \tag{6.114}$$

where $n(x)$ is the particle size distribution, i.e., $N = \int_{a_1}^{a_2} n(a)\,da = k^{-1} \int_0^\infty n(x)\,dx$. The terms of the normalized phase function, Eq. (6.105), for the case of polydispersions are

$$P_1(\theta) = \frac{4\pi}{k^3 S_a} \int_0^\infty n(x) i_\perp(\theta) \tag{6.115}$$

$$P_2(\theta) = \frac{4\pi}{k^3 S_a} \int_0^\infty n(x) i_\parallel(\theta) \tag{6.116}$$

such that:

$$P(\theta) = \frac{2\pi}{k^3 S_a} \int_0^\infty n(x) \left[i_\perp(\theta) + i_\parallel(\theta) \right] dx \tag{6.117}$$

Notice that the limits of integration in Eqs. (6.112)–(6.114) and (6.117) include a range of

particle sizes, and recall that the scattering and absorption characteristics are a function of particle size. In practice, these integrals are solved numerically, and each discrete particle size in the numerical integration, therefore, requires its own computation of the pertinent parameters (i.e., $Q_{\text{ext}}(x)$, $Q_{\text{sca}}(x)$, $S_1(x, \theta)$ and $S_2(x, \theta)$) from Mie theory.

Key Assumptions in RTT

A number of assumptions have been identified in the preceding description of the heuristic RTT. A consolidated review of the primary assumptions includes:

1. The medium filled with a large number of particles may be treated as continuous and locally homogenous, and the concepts of scattering and absorption of light by individual particles may be replaced by the scattering and absorption by a small volume element.

2. The scattering and absorption characteristics of a volume element may be reasonably approximated by the sums of the respective characteristics of the constituent particles, as solved analytically by Mie theory (which assumes spherical particles).

3. The analytical solutions from Mie theory assume that the phenomenological constants are independent of the fields (i.e., linearity), independent of position (i.e., homogeneity), and independent of direction (i.e., isotropicity).

4. The effects of emission are negligible in the present work.

6.2.3 Calculating the MTF

Once the scattering and absorption characteristics of a volume element have been computed, the MTF along an optical path through that volume element can be calculated. This procedure requires the calculation of the aerosol MTF (i.e., the MTF of the particles in the brownout cloud) as well as the consideration of the limitations of imaging system.

Formulations of the Aerosol MTF

The aerosol MTF characterizes the contrast reduction and image blur that occurs because of the scattering and absorption of light passing through the sediment cloud. A variety of formulations for the aerosol MTF exist in the literature, and the present dissertation will primarily utilize two of these formulations that have been derived from RTT, namely an asymptotic form and a continuous form.

Asymptotic Form of the MTF   The first formulation is known as the asymptotic form of the "classical" aerosol MTF, and it was originally derived by Lutomirski (Ref. 85). Kopeika (Ref. 84) provides the final expression for the MTF in asymptotic form as

$$
\text{MTF}(\omega) =
\begin{cases}
\exp\left[-A_a z - S_a z \left(\frac{\omega}{\omega_c}\right)^2\right] & \omega \le \omega_c \\[2ex]
\exp\left[-\left(A_a + S_a\right) z\right] & \omega > \omega_c
\end{cases}
\tag{6.118}
$$

where z is the path length, A_a is the absorption coefficient, S_a is the scattering coefficient, ω is the spatial frequency, and ω_c is the "cutoff" spatial frequency (i.e., the spatial frequency above which the MTF equals the atmospheric transmission). In practice, the cutoff
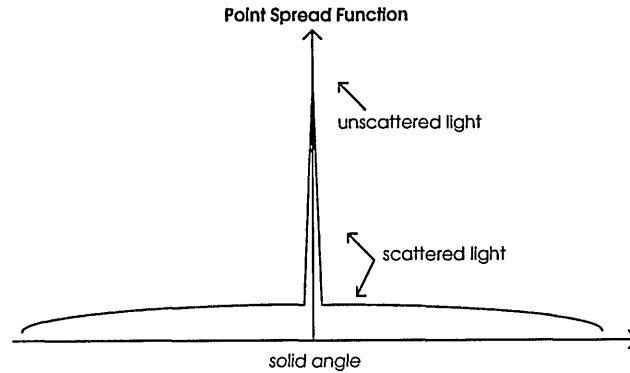
Figure 6.8: Typical pattern of light scattering by particulates (from Ref. 81).

frequency is given by $\omega_c = a/\lambda$ where a is the particle radius and λ is the wavelength of light.

Sadot and Kopeika (Ref. 81) suggested a correction to this MTF formulation to properly account for the effects of absorption. Similar to the illustrative example of the PSF shown in Fig. 5.2, Fig. 6.8 shows a typical pattern of light scattering by particles. The light that passes through the medium has two parts: scattered and unscattered. The unscattered light is a delta function because the unscattered light has no angular spread (i.e., it is not blurred by the medium). The scattered light, however, has a wide angular spread (i.e., it is blurred by the medium). A typical MTF curve is shown in Fig. 6.9, and it differentiates between the contributions of the scattered and unscattered components.

Notice that the "classical" aerosol MTF of Eq. (6.118) treats absorption as a constant effect at all spatial frequencies, even though the absorption effect should be applied to only the relative part of the unscattered light and not to the total radiation, which also includes scattered light. To account for this, Sadot and Kopeika (Ref. 81) formulated a

330
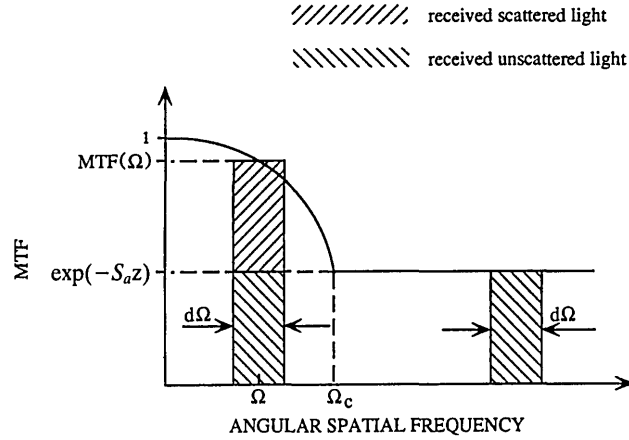
Figure 6.9: Typical aerosol MTF indicating the received unscattered light component and the received scattered light component (from Ref. 81).

corrected form of the aerosol MTF, i.e.,

$$
\text{MTF}(\omega) = \begin{cases} \exp\left\{-S_a z \left(\frac{\omega}{\omega_c}\right)^2\right\} \cdots \\ \quad \times \exp\left\{\left[\exp\left\{-S_a z \left(1-\left(\frac{\omega}{\omega_c}\right)^2\right)\right\} - \exp\left\{-S_a z\right\}\right](-A_a z)\right\}, \quad \omega < \omega_c \\ \exp\left\{-S_a z\right\} \cdot \exp\left\{[1-\exp\left\{-S_a z\right\}](-A_a z)\right\}, \quad \omega > \omega_c \end{cases}
$$

$$(6.119)$$

where Eq. (6.119) reduces to Eq. (6.118) when there is no absorption. A comparison of

MTF results using the "classical" and corrected formulations is shown in Fig. 6.10.

Continuous Form of the MTF   Ishimaru (Ref. 86) provided a continuous expression

for the MTF, i.e.,

$$
\text{MTF}(\omega) = \exp\left\{-\int_0^z (S_a + A_a)\left[1 - W_0 \exp\left(\frac{-\omega^2}{\alpha_p}\right)\right] dz'\right\}
$$

$$(6.120)$$

331
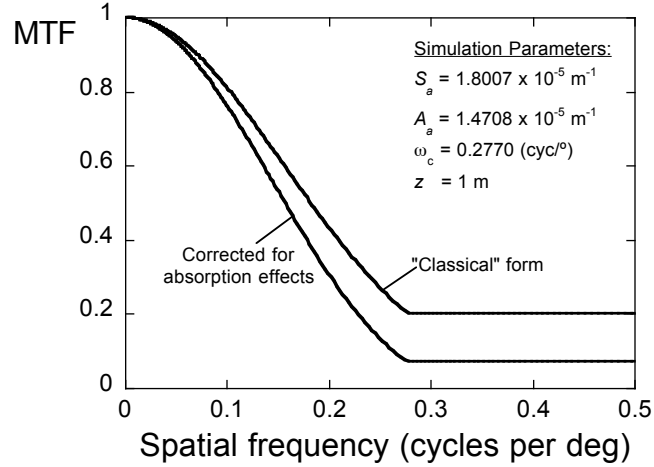
Figure 6.10: The "classical" aerosol MTF versus the corrected form given by Eq. (6.119).

where $W_0 = S_a / (S_a + A_a)$ and α_p is a constant that is solved for by assuming a Gaussian

fit to the phase function, $P(\theta)$, i.e.,

$$P_{\text{app}}(\theta) = 4\alpha_p W_0 \, \exp\left(-\alpha_p \theta^2\right) \tag{6.121}$$

Kopeika (Ref. 80) provided alternative formulations of these expressions as:

$$\text{MTF}(\omega) = \exp\left\{-\int_0^z (T_{\text{eff}}/z)\left[1 - \exp\left(\frac{-\pi^2 \omega^2}{\alpha_p}\right)\right] dz'\right\} \tag{6.122}$$

$$P_{\text{app}}(\theta) = 4\sqrt{\pi\alpha_p} \, \exp\left(-\alpha_p \theta^2\right) \tag{6.123}$$

where, in this formulation, $P_{\text{app}}(\theta)$ is subject to the normalization condition $\int_\Omega P(\theta)d\omega = 4\pi$

and the effective optical depth, T_{eff}, is calculated from Eq. (6.119), i.e., $T_{\text{eff}} = -\ln\left(\text{MTF}(\infty)\right)$.

Kopeika stated that the estimation of α_p by Eq. (6.123) is "not necessary" although no

alternative method for its estimation was explicitly presented.
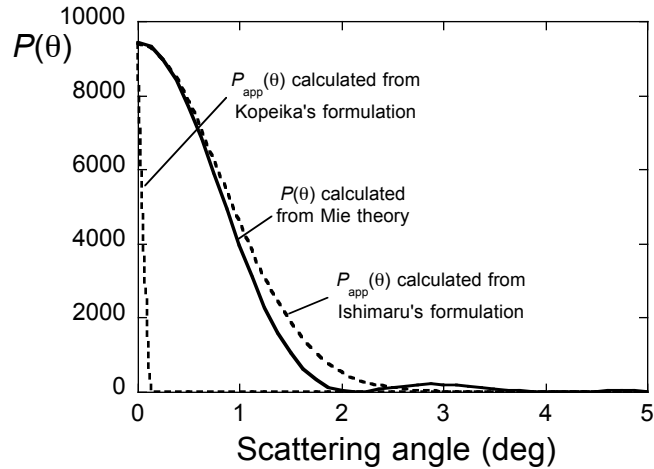
Figure 6.11: Comparison of approximate phase function formulations, $P_{app}(\theta)$, from Ishimaru, Eq. (6.121), and Kopeika, Eq. (6.123) with a phase function calculated from Mie theory, Eq. (6.109).

Comparisons of these formulations are shown in Figs. 6.11 and 6.12. Figure 6.11 shows a comparison of the approximations to a representative phase function, $P(\theta)$, that may be obtained by Eqs. (6.121) and (6.123). Equation (6.121) clearly results in a better fit for this example. Once these fits to the phase function have been calculated, the associated values for α_p are utilized by Eq. (6.120) or (6.122) to approximate the MTF.

Figure 6.12 shows a comparison of the MTF curves that are obtained by each of these methods as well as the MTF that is obtained by the asymptotic formulation, i.e., Eq. (6.119). Notice that the MTF formulation provided by Eq. (6.120) does not result in an MTF that is normalized to unity. This effect is caused by the W_0 term. Additionally, a curve is shown in Fig. 6.12 that shows the MTF that results from Eq. (6.122) where α_p is calculated from Eq. (6.121). This MTF is in closest agreement with the one that is calculated by the asymptotic formulation.

333
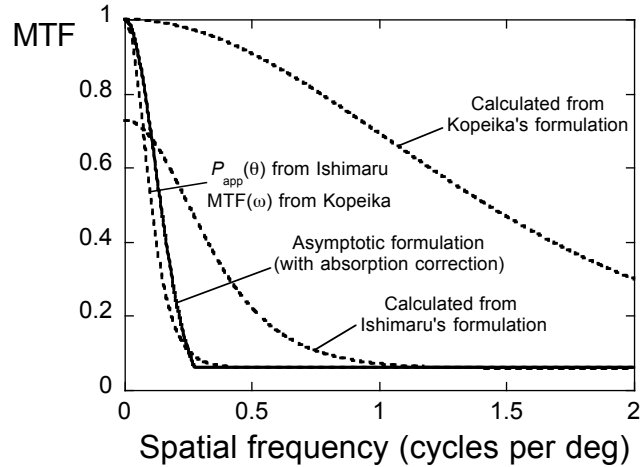
Figure 6.12: Comparison of various MTF formulations: (i) the asymptotic formulation, Eq. (6.119), (ii) Ishimaru's formulation using Eqs. (6.121) and (6.120), (iii) Kopeika's formulation using Eqs. (6.123) and (6.122), and (iv) $P(\theta)$ from Ishimaru, Eq. (6.121), with MTF(ω) from Kopeika, Eq. (6.122).

"Practical, Instrumentation-Based" MTF

Kopeika and Sadot (Refs. 80, 84) proposed additional steps to solve for, what they called, a "practical, instrumentation-based" MTF. The procedure takes advantage of the fact that the PSF and MTF are related by a Fourier transform, i.e., Eq. (5.2). In the first instance, the theoretical MTF for the medium is calculated using one of the methods described previously, i.e., by Eq. (6.119), (6.120) or (6.122). A representative MTF is shown in Fig. 6.13(a). The next step is to calculate the specific intensity function by performing an inverse Fourier transform of the MTF, i.e.,

$$I(\theta) = \frac{1}{(2\pi)^2} \int_{-\infty}^{\infty} \text{MTF}(\omega) \text{MTF}_0(\omega) \exp\left(-j\theta\omega\right) d\omega \qquad (6.124)$$

334

where $\mathrm{MTF}_0(\omega)$ is the MTF of the imaging equipment. If $\mathrm{MTF}_0(\omega)$ is not known precisely, the specific intensity function can alternatively be obtained by

$$I(\theta) = \frac{1}{(2\pi)^2} \int_{-\omega_{\mathrm{max}}}^{\omega_{\mathrm{max}}} \mathrm{MTF}(\omega) \exp\left(-j\theta\omega\right) d\omega \qquad (6.125)$$

where ω_{max} is the estimated spatial frequency bandwidth limitation of the imaging equipment.

A notional specific intensity function is shown in Fig. 6.13(b), and it is analogous to the PSF of Eq. (5.2). Notice that the instrumentation limits will impact the angular extent to which light is actually received by the imaging equipment. The "practical, instrumentation-based" MTF can then be calculated by performing a Fourier transform of the specific intensity function, where the limits of integration, $\pm\theta_{\mathrm{max}}$, are derived from the instrumentation limitations, i.e.,

$$\mathrm{MTF}_{\mathrm{prac}}(\omega) = \int_{-\theta_{\mathrm{max}}}^{\theta_{\mathrm{max}}} I(\theta) \exp\left(j\theta\omega\right) d\theta \qquad (6.126)$$

A representative "practical, instrumentation-based" MTF is compared with the MTF of the particulate medium in Fig. 6.13(c).

Specific Formulations Used in the Present Work

In the present analysis, the "practical, instrumentation-based" MTF (Refs. 79, 80, 84) was computed along an optical path through a computer-simulated brownout cloud. In the first instance, Sadot and Kopeika's corrected form of the asymptotic MTF equation,
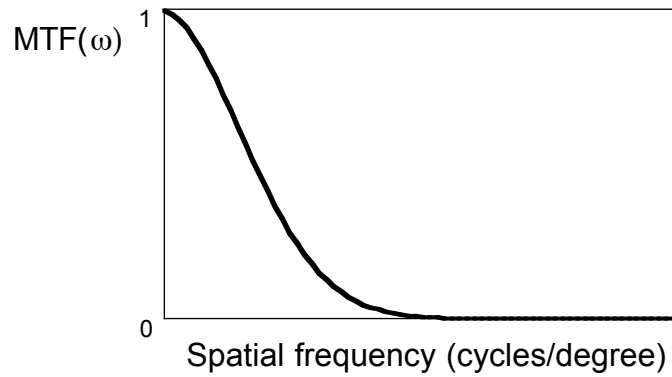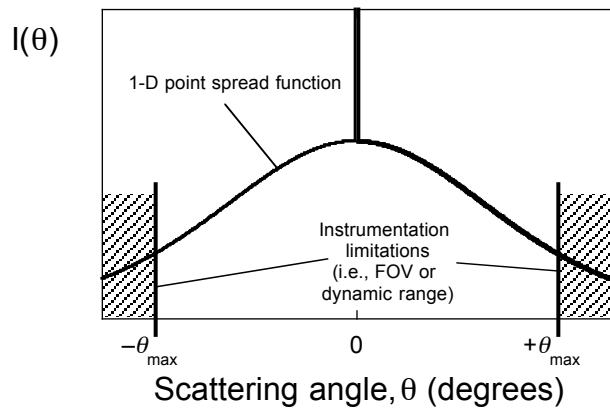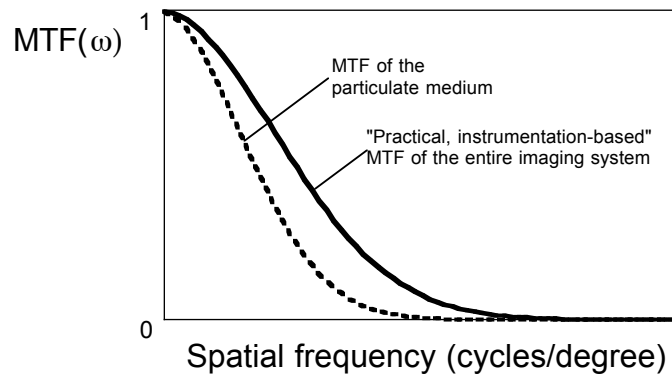
Figure 6.13: Basic procedure of the "practical, instrumentation-based" MTF proposed by Kopeika and Sadot (adapted from Refs. 80, 84).

Eq. (6.119) was utilized. The phase function, $P(\theta)$, was approximated by a Gaussian fit, Eq. (6.121). Notice that this formulation of the approximate phase function was chosen over that provided in Eq. (6.123) because it provided a better fit to the phase function that was calculated from Mie theory for the present case. The MTF was next expressed as a continuous function using Eq. (6.122) and the specific intensity function was obtained by performing an inverse Fourier transform of the MTF, i.e.,

$$I(\theta) = \frac{1}{(2\pi)^2} \int_{-\omega_{max}}^{\omega_{max}} \mathrm{MTF}(\omega) \exp\left(-j\theta\omega\right) d\omega \qquad (6.125)$$

where ω_{max} is the estimated bandwidth limitation of the imaging equipment (the present study assumed $\omega_{max} = 75$ cycles per degree).

Figure 6.14 shows a schematic representation of the imaging limitations for two representative specific intensity functions, $I(\theta)$. Notice that the convention is to show $I(\theta)$ for positive angles only, even though $I(\theta)$ will also be defined for negative angles. Each $I(\theta)$ curve consists of both unscattered light and scattered light. The angular extent to which the scattered light is received by the imager, however, is limited by the instrumentation limits. For the dynamic range-limited specific intensity curve, scattered light is received over the range of angles $-\theta_{max}^{D.R.} \leq \theta \leq \theta_{max}^{D.R.}$ Likewise, scattered light is received over the range of angles $-\theta_{max}^{FOV} \leq \theta \leq \theta_{max}^{FOV}$ for the FOV-limited specific intensity curve.

The "practical, instrumentation-based" MTF (Refs. 79, 80, 84) was then calculated for the individual volume element by performing a Fourier transform of the specific intensity function, where the limits of integration were derived from the instrumentation field
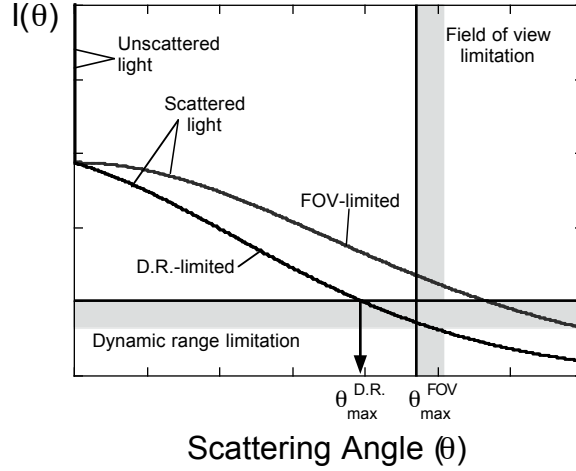
Figure 6.14: Schematic representation of the imaging limitations for two representative specific intensity functions.

of view or dynamic range limitations, i.e.,

$$\text{MTF}_{\text{prac}}(\omega) = \int_{-\theta_{\text{max}}}^{\theta_{\text{max}}} I(\theta) \exp(j\theta\omega) \, d\theta \qquad (6.126)$$

where θ_{max} is the more restrictive of the field of view and dynamic range limitations of the equipment, i.e., $\theta_{\text{max}} = \min\left(\theta_{\text{max}}^{\text{FOV}}, \theta_{\text{max}}^{\text{D.R.}}\right)$.

Once the "practical, instrumentation-based" MTF was calculated for each volume element along a given optical path, the total MTF along that optical path was calculated as the series multiplication of all of the MTFs for the volume elements, i.e.,

$$\text{MTF}_{\text{prac}}(\omega) = \prod_{i=1}^{n} \text{MTF}_{\text{prac}}^{i}(\omega) \qquad (6.127)$$

where $\text{MTF}_{\text{prac}}^{i}(\omega)$ denotes the MTF of the i-th volume element in the optical path and there are a total of n volume elements in the optical path. This portion of the proce-

dure may be intuitively explained by the convolution theorem, which states that convolution in the spatial domain is equivalent to multiplication in the frequency domain. Because the MTF and specific intensity function are related by a Fourier transform, i.e., $\text{MTF}(\omega) = \mathcal{F}[I(\theta)]$, the series multiplication of the MTF for each of the volume elements is equivalent to performing a series of convolutions of the specific intensity function for each of the volume elements, i.e.,

$$\text{MTF}_{\text{prac}}(\omega) = \prod_{i=1}^{n} \text{MTF}_{\text{prac}}^{i}(\omega) = \mathcal{F}[I^1(\theta) \circ I^2(\theta) \circ \ldots \circ I^n(\theta)] \qquad (6.128)$$

where $I^i(\theta)$ is the specific intensity function associated with the i-th volume element in the optical path.

6.3   Results

Initial MTF predictions were performed for a simulated brownout cloud generated by a four-bladed, medium-lift, single main rotor helicopter executing an approach-to-landing maneuver. Note that only the main rotor was modeled (i.e., the simulation included neither a fuselage nor a tail rotor). A uniform sediment bed consisting of spherical, monodisperse particles of 20 μm diameter was modeled, and the space surrounding the pilot was divided into 360 bins in eccentricity by 180 bins in elevation by 20 bins in distance from the pilot.

Figure 6.15 shows the MTFs for a series of bins along a single optical path through the cloud at a single instant in time. Because the number of particles in the simulation is
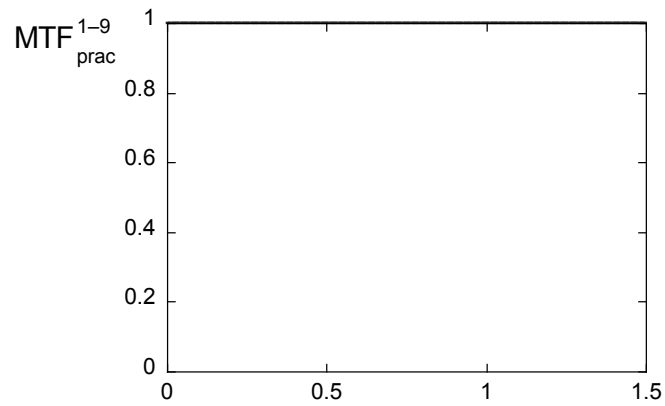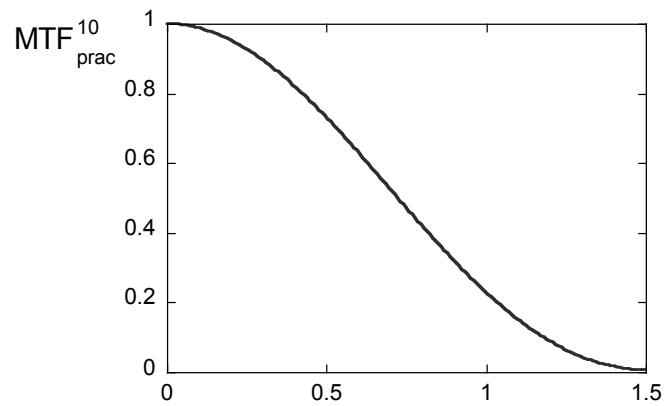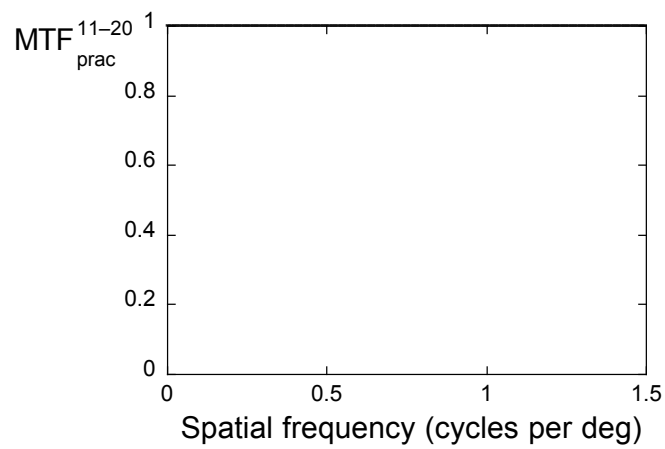
Figure 6.15: Predictions for the practical, instrumentation-based MTF of a brownout cloud for (a) layers 1–9, (b) layer 10, and (c) layers 11–20 along an optical path.
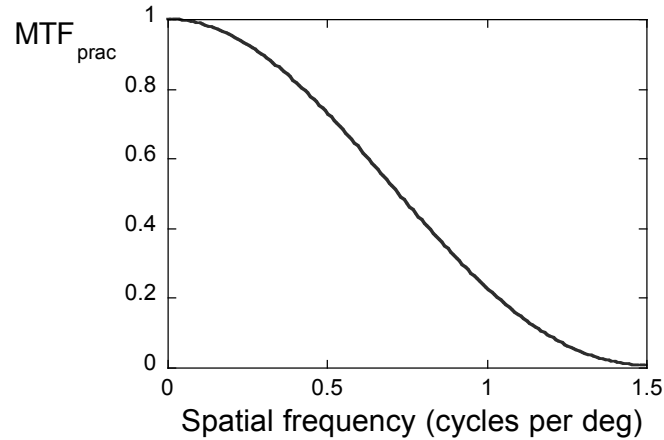
Figure 6.16: Prediction of the practical, instrumentation-based MTF of a brownout cloud for the full optical path.

orders of magnitude smaller than the total number of particles in a true brownout cloud, the simulated cloud must be scaled. Although clustering methods exist that allow for significantly increased particle counts versus standard brownout cloud simulations at reasonable computational cost (Ref. 22), the file storage cost is still prohibitive for extending these methods to particle counts that are commensurate with actual brownout conditions. As such, the particle densities of the simulated brownout cloud were multiplied by a scaling factor to yield cloud densities similar to those reported in the literature (on the order of 10^9 particles per cubic meter, Ref. 15).

Notice that the MTF is equal to unity at all spatial frequencies for most of the radial layers in this example, Fig. 6.15(a) and (c), indicating no appreciable obscuration through these layers. For one layer, however, there is significant visual degradation; see Fig. 6.15(b). The total MTF along this optical path is the series multiplication of the MTF for each layer; see Fig. 6.16. Notice that the calculations shown in Figs. 6.15 and 6.16 are valid for an equipment FOV of $200°$ (meant to represent a pilot's binocular FOV),
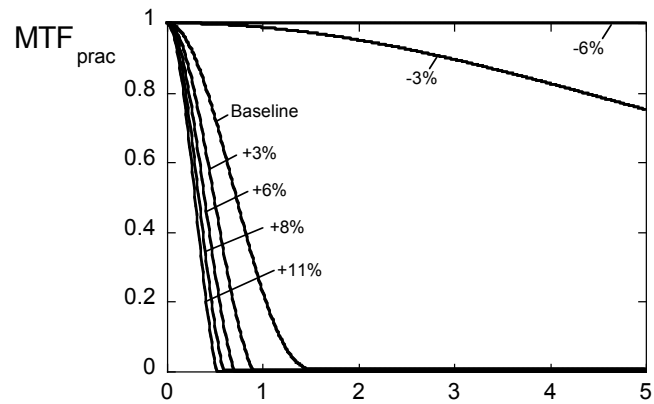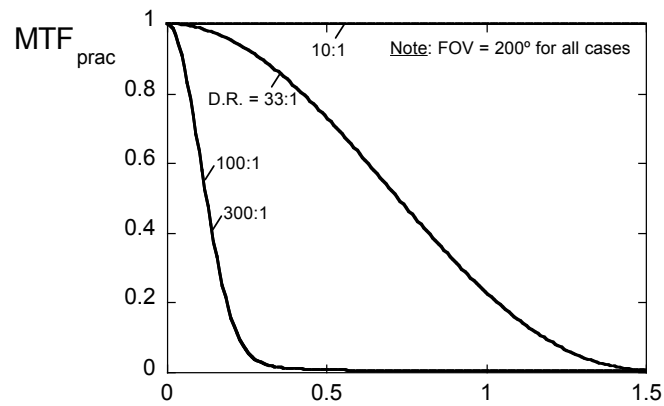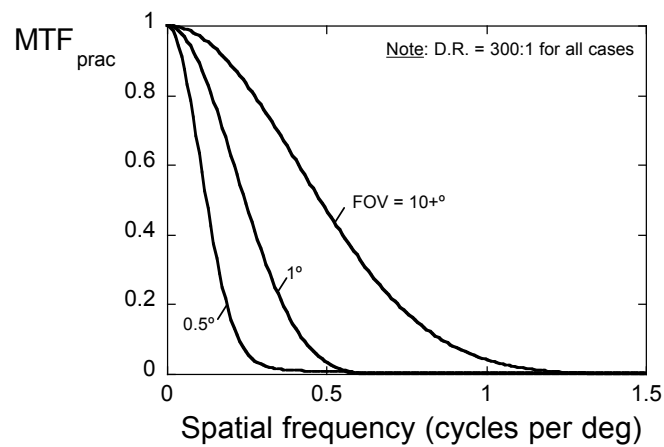
Figure 6.17: MTF curves illustrating the sensitivity of MTF predictions to (a) cloud density, (b) dynamic range limitations, and (c) FOV limitations.

a dynamic range of 33 : 1, an imaging wavelength of 0.63 μm, and a relative refractive index of $1.55 + 0.008i$ for the sediment particles.

The sensitivity of the MTF predictions to a variety of factors is shown in Fig. 6.17. In the first instance, the sensitivity to cloud density was examined. To explore this relationship, the total number of particles in the simulation was perturbed by values ranging from -6% to $+11\%$ and the resulting MTFs were computed; see Fig. 6.17(a). Notice the nonlinear relationship between the cloud density and the MTF predictions. For a cloud with just 6% fewer particles than the baseline, the MTF equals unity at all spatial frequencies (indicating no obscuration). The visual degradation increases significantly (i.e., the MTF decreases) as the particle counts are increased from the -3% perturbation to the $+6\%$ perturbation, although the visual degradation increases less significantly as the perturbations are increased to $+8\%$ and $+11\%$. This nonlinear relationship between cloud density and visual degradation indicates that visibility will abruptly decrease when the cloud (or some region within the cloud) reaches a critical density. This phenomenon is potentially a contributing factor to the rapidity of the brownout problem that has been anecdotally reported. These results indicate that MTF predictions are very sensitive to minor variations in the cloud density, and, from a practical standpoint, this outcome means that the brownout cloud simulations need to be extremely accurate in predicting the brownout cloud densities if the MTF is to be predicted accurately.

Next, the sensitivity of the predictions to the instrumentation limits was inspected. The two primary instrumentation limits are the dynamic range and FOV as shown previously in Fig. 6.14. Examining the effects of these limitations on MTF predictions can be

343

difficult, however, because of their interdependencies. While an imaging system with a large FOV is likely to be limited by dynamic range and a system with a large dynamic range is likely to be limited by FOV, the active limitation is typically dictated by the specifics of the dust cloud. Figure 6.17(b)–(c) shows the effect of varied dynamic range and FOV limitations on the resulting MTF predictions. For the investigation into dynamic range, a wide FOV, $200°$, was selected to ensure that the dynamic range limitations would be dominant. Conversely, a large dynamic range, $300:1$, was selected for the investigation into FOV to ensure that the FOV limitations would be active. In each case, the instrumentation limits were shown to have a significant impact on the resulting MTF predictions. These results indicate that detailed knowledge of the imaging system limitations is essential for generating accurate MTF predictions.

6.4 Comparison of MTF Prediction Methodology with Controlled Experiments

To examine the efficacy of the MTF prediction methodology, a series of simple experiments were performed and compared with predictions. The purpose of these experiments was to perform comparative tests that would be representative of the optical degradation experienced in brownout, though under controlled conditions. More specifically, the goal of the experiments was to perform comparison tests for a range of particle count densities using naturally-occurring (and well-characterized) sediment samples in a manner that is simple, cost-effective, and repeatable. It should be noted that Kopeika's prediction methodology has also been extensively verified with experimental measurements

344

of the MTF for imaging applications through naturally-occurring atmospheric aerosols in Refs. 82, 83.

6.4.1   Experimental Methodology

The edge response method for MTF calculation was used in the present study, as detailed in Section 5.2.1. A mathematical "Edge Response Function" (ERF) is defined as the grayscale level variation (or "response") along a line normal to the edge of interest. The derivative of the edge response function gives the edge spread function, i.e.,

$$\frac{d}{dx}\text{ERF}(x) = \text{ESF}(x) \tag{5.3}$$

where the ESF is the one-dimensional analogue to the two-dimensional PSF. The MTF is, therefore, calculated as the Fourier transform of the ESF, i.e.,

$$\mathcal{F}\left[\text{ESF}(x)\right] = \text{MTF}(\omega_x) \tag{5.4}$$

There are a number of key considerations in employing the edge response method. First, the resolution of the camera plays a critical role in that it provides a practical limitation to the MTF measurements. Another important consideration is the quality of the edge. For example, using the edge of an object that has some curvature or texture can cause the effect of lighting location and intensity to strongly impact the MTF measurements. A final consideration is the importance of sampling normal to the edge. If the edge response is taken at an angle that is not perpendicular to the edge, the ERF will be artifi-

345
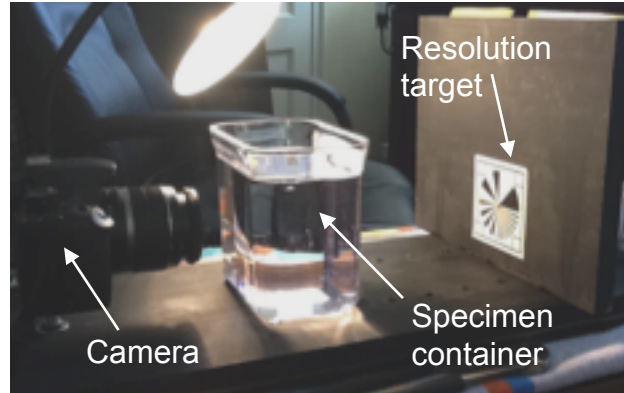
Figure 6.18: Experimental setup for the MTF comparison tests.

cially spread out over a larger number of pixels, leading to erroneous MTF calculations.

6.4.2 Experimental Setup

An experimental test rig was developed for the comparison tests; see Fig. 6.18. The setup included a Canon EOS Rebel XS DSLR camera, capable of recording 10MP images. The camera was mounted to the test rig and oriented to image through a specimen container that was utilized to suspend the sediment sample in water. Suspending the sediment sample in water served two purposes: (i) to keep the dust particles suspended for longer durations than they would in air and (ii) to uniformly distribute the dust particles within the volume. A modified Siemens star test pattern was mounted on the other side of the specimen container, and the MTF measurements were extracted from the black/white edge between the two largest wedges of the test pattern.

A sample of kaolinite (also known as China clay, mass density $\rho_s = 2160 \text{ kg m}^{-3}$) was used in the comparison tests. The sample was characterized by an outside lab, and the size distribution is shown in Fig. 6.19. An enlarged image of the dust particles is shown
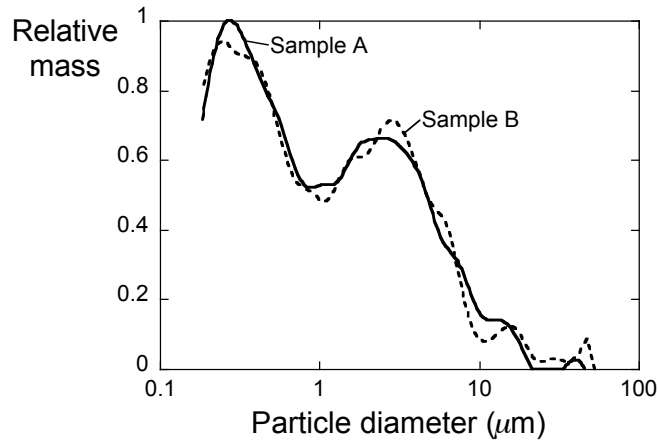
Figure 6.19: Particle size distributions for two samples from the kaolinite utilized in the comparison tests (from Ref. 153).

in Fig. 6.20. Plots of the complex refractive index as a function of wavelength are shown

in Fig. 6.21.

6.4.3   Results from Comparison Testing

Four images of the modified Siemens star test pattern, as imaged through varying amounts of sediment, are shown in Fig. 6.22. Figure 6.23 shows MTFs that have been extracted from the images in Fig. 6.22. Notice that the MTF was calculated at two locations along the black/white edge between the largest wedges of the test pattern, and therefore two MTF curves are presented for each image. Notice also that the MTF for the unobscured image may be taken to be the baseline for the imaging system, i.e., $MTF_0(\omega)$.

The MTF measurements shown in Fig. 6.23 exhibit similar nonlinear effects to those observed in Fig. 6.17(a). Increasing the cloud density from the baseline to the 0.1 gram and 0.2 gram samples results in drastic reduction of the MTF over a range of spatial frequencies. Increasing the cloud density from the 0.2 gram to the 0.3 gram samples,

347
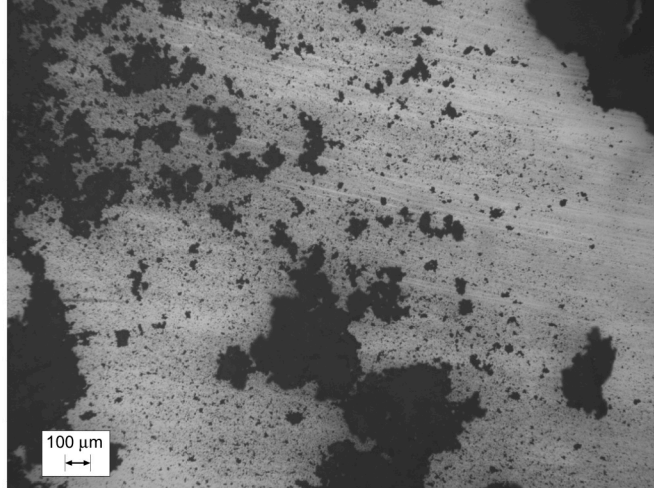
Figure 6.20: Image of kaolinite particles under a microscope (from Ref. 153).

however, does not result in as drastic a difference. This result further supports the notion that the visibility in a brownout cloud will abruptly decrease when the cloud (or some region within the cloud) reaches a critical density.

Predictions of the MTF were also computed for each of the test cases. In the first instance, the composition of each sample was estimated from the known particle size distribution and sample weight. In estimating the composition of each sample, a discrete number of particle sizes must be assumed. Notice that the number of discrete particle sizes will affect the numerical integrations in Eqs. (6.112)–(6.114) and (6.117). For example, if two discrete particle sizes were utilized to estimate the composition of a 0.3 gram sample, the estimated sample would consist of 7.93×10^{10} particles of 6.65 μm radius and 5.66×10^3 particles of 19.85 μm radius. If three discrete particle sizes were assumed, however, the estimated sample would consist of 2.64×10^{11} particles of 4.46 μm radius, 4.17×10^4 particles of 13.25 μm radius, and 1.46×10^3 particles of 22.05 μm radius. The estimated sample with three discrete sizes consists of more than three times the total

348
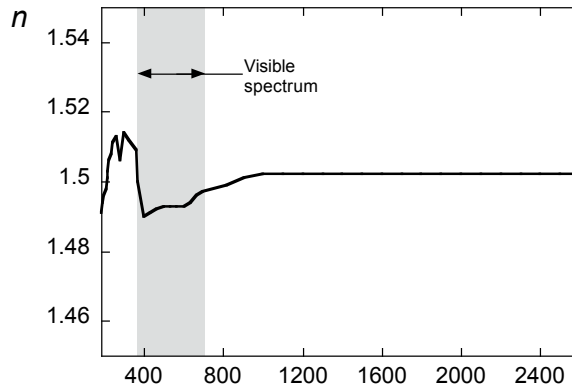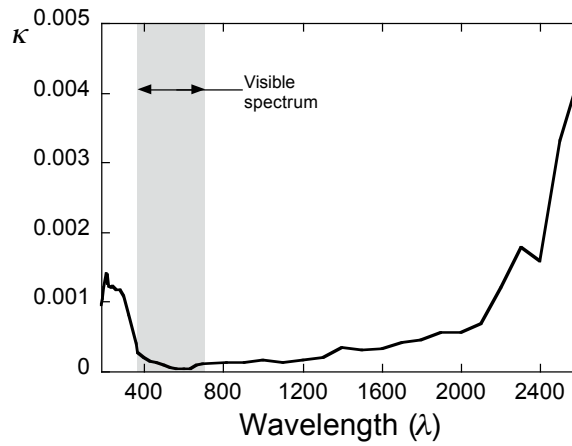
Figure 6.21: Complex refractive index of kaolinite: (a) real and (b) imaginary parts as a function of wavelength.
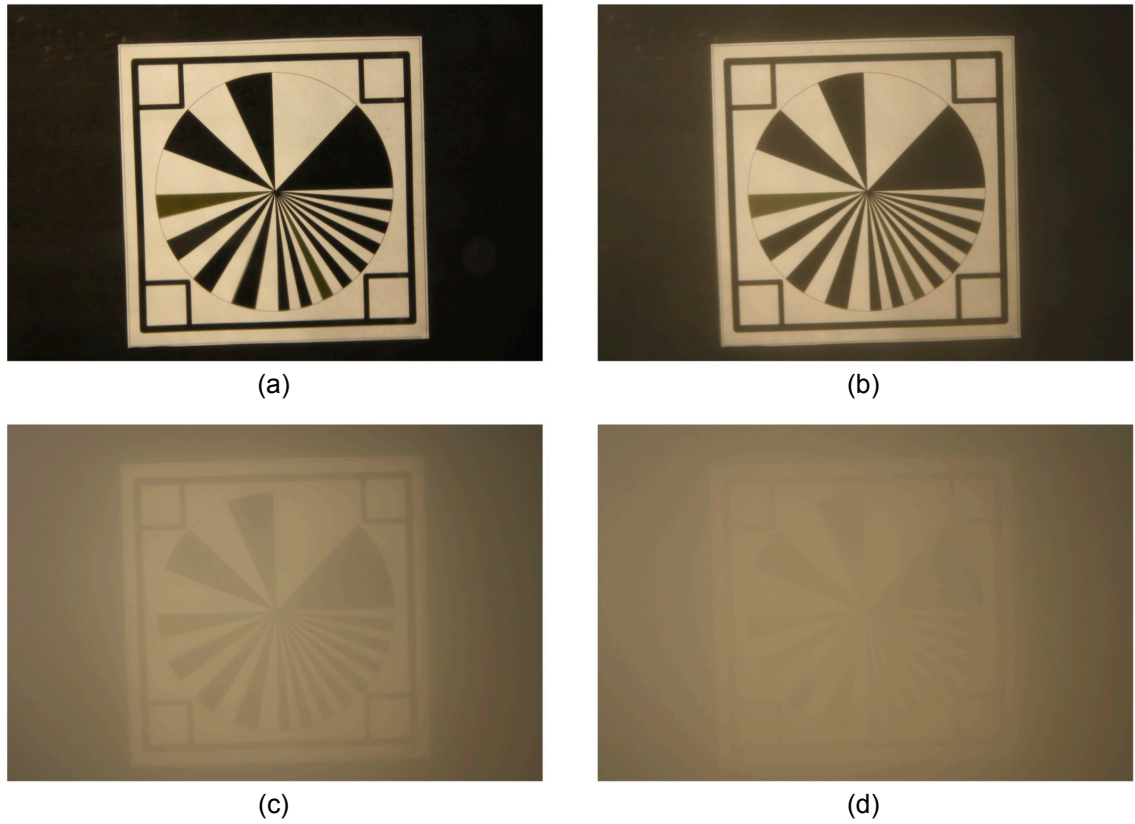
Figure 6.22: Images of the modified Siemens star test pattern, imaged through (a) no sediment, (b) 0.1 grams of sediment, (c) 0.2 grams of sediment, and (d) 0.3 grams of sediment.
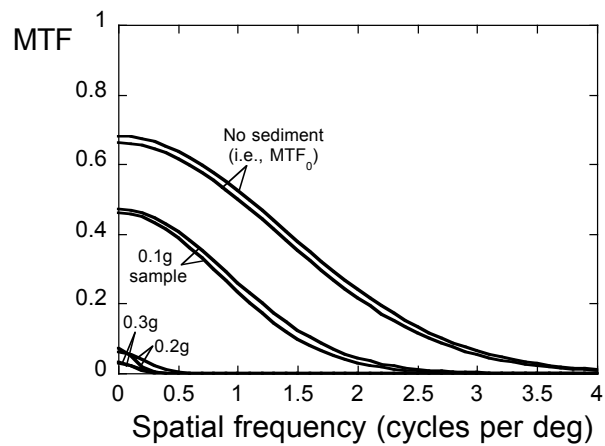
Figure 6.23: Experimental measurements of the MTF from the images shown in Fig. 6.22 Two MTF measurements were obtained from each image.
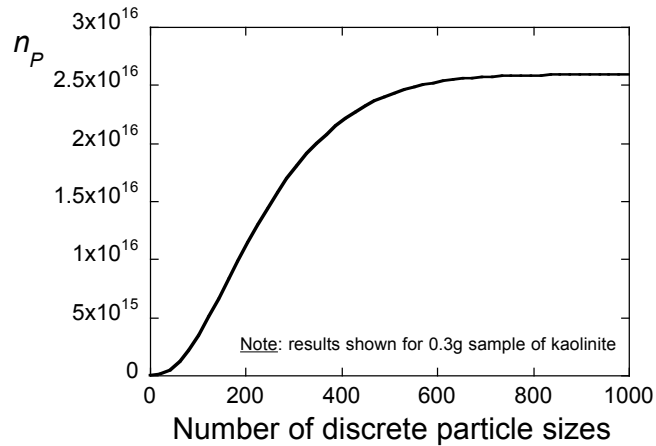
Figure 6.24: The total number of particles in an estimated sample of kaolinite weighing 0.3 grams, as a function of the number of discrete particle sizes utilized in the estimated sample.

number of particles than the estimated sample with two discrete sizes.

Clearly two or three discrete sizes are insufficient; however, this simple example emphasizes the point that care must be exercised in determining the proper number of discrete particle sizes to be used in the estimated sample. Figure 6.24 shows the total number of particles, n_P, in an estimated sample of kaolinite weighing 0.3 grams, as a function of the number of discrete particle sizes utilized in the estimated sample. This figure indicates that more than 500–600 discrete particle sizes are needed to obtain consistent total particle counts. The estimated samples for the present simulations utilized 800 discrete particle sizes.

Figure 6.25 shows a comparison of the experimental results with predictions of the MTF for the experimental setup. Notice that the MTF curves for the predictions have been normalized to the maximum value of MTF_0. Notice also that the predictions exhibit a sharp drop in MTF at very low spatial frequencies (about 0.1–0.2 cycles per degree),
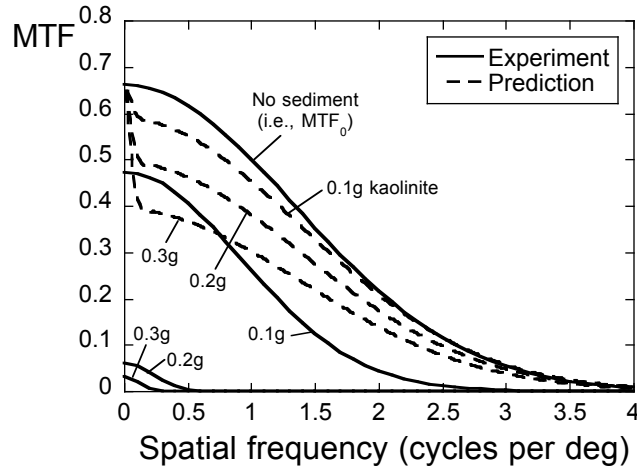
Figure 6.25: Comparison of measured and predicted MTFs for the images shown in Fig. 6.22.

beyond which point they follow similar trends to MTF_0. In essence, the predicted MTFs indicate that the effect of the sediment is to: (i) drastically reduce MTF at very low spatial frequencies (i.e., < 0.1–0.2 cycles per degree) and (ii) act as a relatively uniform degradation of MTF (when compared with the baseline, MTF_0) at higher spatial frequencies (i.e., > 0.1–0.2 cycles per degree). Notice that the cutoff frequency (approximately 0.1–0.2 cycles per degree, in this case) has been shown in prior optics research (Ref. 78) to be strongly affected by the instrument limitations (i.e., the limitations that impact the limits of integration in Eq. (6.126)). It is therefore hypothesized that the specimen container had some effect on the imaging limitations of the overall test setup that was not properly reflected in the prediction methodology (the imaging limitations utilized for the predictions were the limitations of the camera only), and that this may be a likely cause of the apparent discrepancies between the predictions and experimental results.

Recall from Section 5.1 that multiple formulations of the MTF are possible. In the
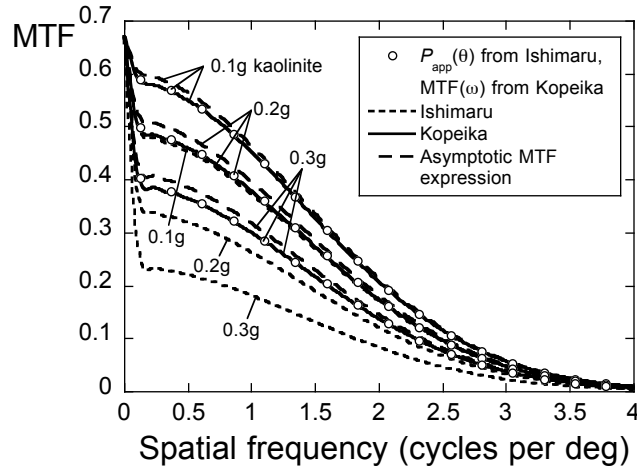
Figure 6.26: Comparison of predicted MTFs by multiple methods for the concentrations represented by the images shown in Fig. 6.22.

present comparative study, the MTF prediction methodology that was detailed in Section 6.2 was used to calculate the predicted MTFs. This methodology involved the use of a continuous expression for the MTF, Eq. (6.122), that was determined, in part, by a Gaussian fit to the phase function, Eq. (6.121). The effects of the instrument limitations were then accounted for in subsequent steps, i.e., Eqs. (6.124) and (6.126).

Notice, however, that alternate expressions existed for both the MTF and the fit to the phase function. Predictions based upon these alternative expressions were also computed and are shown in Fig. 6.26. The results obtained using the methodology given in Section 6.2 are given by markers. Results obtained from Kopeika's expressions for the MTF and fit to the phase function (Eqs. (6.122) and (6.123), respectively) are shown by a solid line, and they are in close agreement with the previous results. Results obtained from the asymptotic expression for the MTF, Eq. (6.119), are shown by a dashed line, and they are likewise in relatively close agreement with the previous results. The results that may be obtained from Ishimaru's expressions for the MTF and fit to the phase function
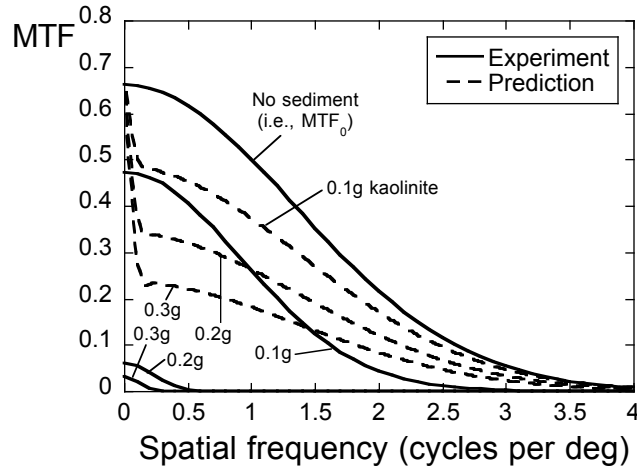
Figure 6.27: Comparison of measured and predicted MTFs for the images shown in Fig. 6.22. The predictions are based on Eqs. (6.120) and (6.121) for the MTF and fit to the phase function, respectively.

(Eqs. (6.120) and (6.121), respectively) are given by a dotted line, and they are noticeably different from the results of the other three methods, specifically with respect to the MTF magnitude. These results are compared with the experimental measurements in Fig. 6.27. Notice that the predictions once again exhibit a sharp drop in MTF at very low spatial frequencies (about 0.1–0.2 cycles per degree), beyond which point they follow similar trends to MTF_0. Again, this is hypothesized to be caused by instrumentation effects that were not properly reflected in the prediction methodology.

6.5 A Possible MTF-based Objective Function for Brownout Mitigation

The ability to predict the MTF of a brownout cloud may be extended to enable the prediction of the anticipated effects on HQ that a pilot would experience. As such, the MTF may be an appropriate basis for defining an improved objective function to be used in brownout mitigation analysis, e.g. $B_{MTF}(\mathbf{X})$. This objective function would be
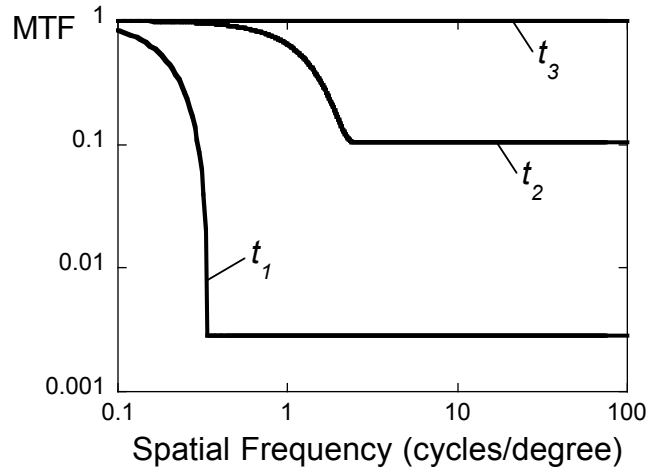
Figure 6.28: Plot of representative MTF predictions at three time steps ($t_1 \approx 42.5$ sec, $t_2 \approx 43$ sec, $t_3 \approx 49$ sec).

computed using the following steps:

1. **Compute the MTF:** For each time step over the course of a landing maneuver, the MTF must be calculated. For the present example, it was calculated for a single optical path oriented directly forward and down from the helicopter (a region the pilot would be likely to scan during the approach and landing). The methodology and key parameters of the analyses were identical to those presented in Section 6.2.3, i.e., utilizing: (i) the corrected form of the asymptotic MTF equation, Eq. (6.119), (ii) a Gaussian fit to the phase function, Eq. (6.121), and (iii) the "practical, instrumentation-based MTF" procedure, Eqs. (6.122), (6.125), and (6.126). Representative MTFs for three time steps are shown in Fig. 6.28.

2. **Assess whether the MTF is adequate for piloting purposes:** The second step in the process is to determine whether the MTF at each time step affords sufficient visibility for the pilot to maintain aircraft control. Recall from Section 1.2.2 that the

355

MTF was originally proposed by Hoh (Ref. 12) as a potential metric for assessing visual cue degradation because of its ability to "define the level of texture or detail visible to the pilot as a useable cue in terms of the spatial frequency and the modulation of the image." Indeed, he identified a notional region on the MTF axes that characterized the critical visual cues for pilot control; see Fig. 6.29(a). Although this region was well-defined in terms of spatial frequency (i.e., approximately 1–10 cycles per degree), the corresponding limits along the y-axis (i.e., the "modulation", "MTF", or "contrast" axis) were not clearly defined. For the sake of this analysis, the notional region presented in Fig. 6.29(a) has been assigned more clearly-defined boundaries in Fig. 6.29(b). These boundaries were selected for consistency with a typical contrast sensitivity threshold curve for a human eye from Ref. 84.

The visibility thresholds from Fig. 6.29(b) are shown in comparison to the representative MTF curves in Fig. 6.30. Notice that the MTF of the brownout cloud is below the shaded thresholds at all spatial frequencies for time t_1. This result indicates that the cloud will degrade any available visual cues to such an extent that the pilot will be unable to use them to control the aircraft. At time t_2, the MTF of the brownout cloud passes through the region in which visual cues are needed. This result indicates that, although the brownout cloud will degrade available visual cues to some degree, the pilot will still be able to perceive some cues in the ranges needed to control the aircraft. Finally, the MTF is unity for all spatial frequencies at time t_3, indicating that there would be no visual degradation along that optical path.
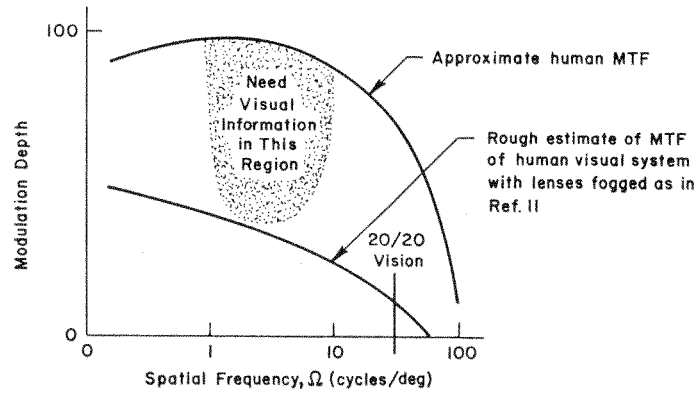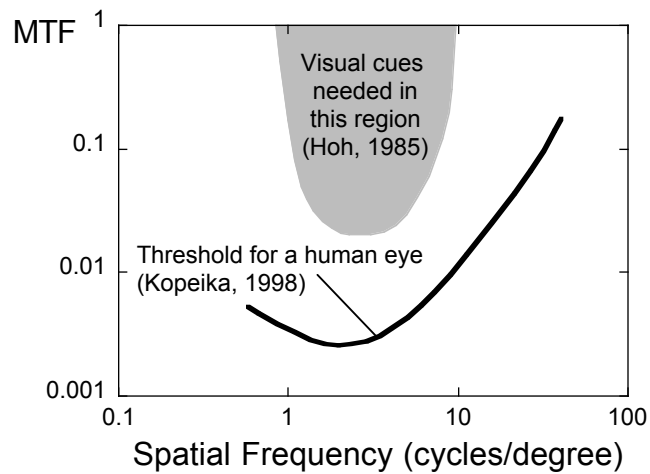
Figure 6.29: Defining visibility limits in terms of the MTF: (a) a plot of representative MTFs and a notional region for critical visual cues (Ref. 12) and (b) a physiological contrast threshold curve for a human eye (Ref. 84).

357
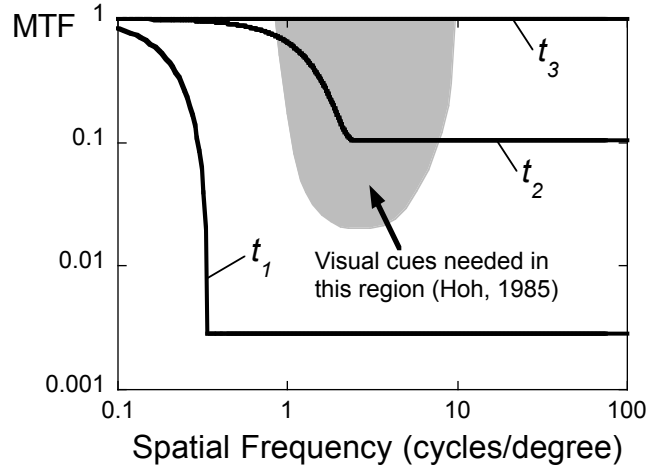
Figure 6.30: Plot of representative MTF predictions at three time steps ($t_1 \approx 42.5$ sec, $t_2 \approx 43$ sec, $t_3 \approx 49$ sec) compared to the region for critical visual cues.

3. **Compute the control dwell fraction:** The presence of sufficient or insufficient cueing, as determined by the predicted MTF, is shown as a function of time in Fig. 6.31. The times corresponding to t_1, t_2, and t_3 in Fig. 6.30 are identified. Sufficient visibility is afforded by the cloud continuously until about 42.5 seconds into the approach, at which time the brownout cloud intermittently causes the MTF to go below the defined visibility thresholds. This intermittent visual degradation may be considered to be a form of divided attention operations for the pilot (Ref. 68). Divided attention operations will be in effect for the final 12.5 seconds of the approach, and this duration is referred to as the sampling time, T_s. During this period, the times for which the pilot has sufficient visual cues to control the aircraft contribute to the "control dwell time," T_d. A "control dwell fraction," η, is defined as the ratio of the control dwell time to the sample time. For the present analysis,

$$\eta = \frac{T_d}{T_s} = \frac{7.47 \text{ sec}}{12.5 \text{ sec}} = 0.6 \qquad (6.129)$$

358
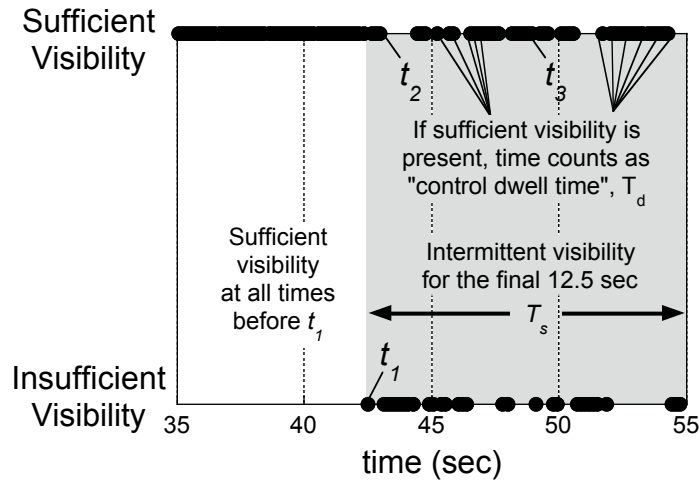
Figure 6.31: The presence of sufficient or insufficient cueing, as determined by the predicted MTF, over the course of a maneuver.

4. **Compute the phase margin loss as the objective function to be minimized:**

Once the control dwell fraction has been calculated, the phase margin of the pilot-vehicle system lost due to brownout, ϕ_M, may be estimated (Ref. 68); see Fig. 6.32. For the present case, $\phi_M \approx 36°$. The phase margin will provide an indication of the brownout cloud's effects on the pilot, and it may be used in HQ analyses that model the total pilot-vehicle system.

There are a number of assumptions in the present analysis that must be considered:

1. For step 1 (predicting the MTF), the present methodology may be considered to be extremely tentative. Although the methodology presented herein may reflect the actual physics, it has been shown to be extremely sensitive to the scaling of the simulated cloud and the specifics of the imaging limitations (Section 6.3). For these reasons, this portion of the methodology requires further validation prior to further use.

359
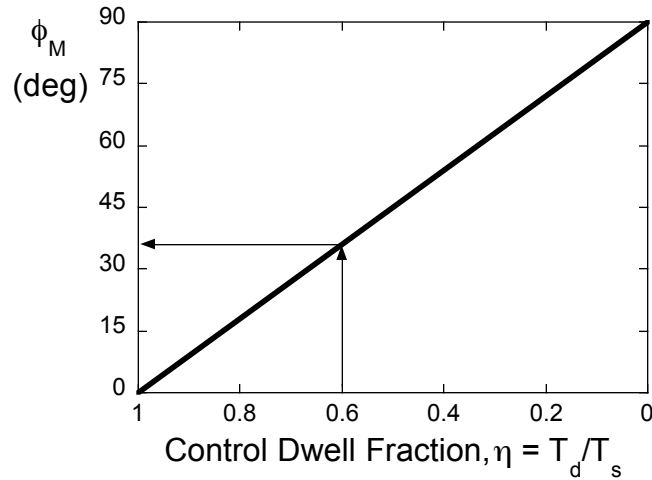
Figure 6.32: Effect of divided attention on phase margins for minimum mean-squared error (adapted from Ref. 68).

2. For step 2 (assessing whether the MTF is adequate for pilot control), it is important to notice that the proposed visibility limits, although plausible, will also require further validation. Although the visibility thresholds are based on physiological limitations, the actual limitations of a human pilot will include his or her cognitive ability to perceive, understand, and react to the visual degradation caused by brownout.

3. For step 3 (computing the control dwell fraction), the specific definitions of the sampling times and control dwell times must be examined in greater detail. For example, in the present analysis the sampling time was defined to begin when the brownout cloud first reduced the MTF below the visibility limits. There may, however, be human factors-based arguments for considering other methods for defining T_s (e.g., dividing the maneuver into multiple sampling times of a set duration, each of which would have its own control dwell fraction).

4. In a general sense, it is also important to notice that the MTF calculations in the present analysis are performed for a single optical path at each time step. A method for considering multiple MTFs over the pilot's FOV may provide a more appropriate basis for performing HQ-based mitigation analyses.

Although these assumptions are not insignificant (and the results must be interpreted in this context), it is important to notice that the present methodology is firmly rooted in the fundamental physics of the problem. Furthermore, the methodology provides a tractable path from the simulation of a brownout cloud to the assessment of the HQ effects that could potentially be encountered. In this sense, the present methodology represents a first step towards the definition of a MTF-based objective function for brownout mitigation.

Part III

Conclusions and Future Work

Chapter 7

Summary and Conclusions

Rotorcraft brownout is a complex operational problem that has contributed to numerous mishaps and has resulted in the loss of many lives and much property. A variety of methods have been pursued to mitigate the effects of brownout, including: (i) the use of advanced avionics equipment and rotorcraft stability augmentation, (ii) the adoption of specialized piloting techniques to minimize the effects of the brownout cloud, and (iii) the development of rotorcraft design strategies or modifications that may result in a more benign brownout signature. An important consideration in any brownout research is the definition of a metric for characterizing brownout severity. The complexity of the brownout phenomenon makes the dust clouds difficult to characterize through quantitative metrics, though a few researchers have proposed measurement and characterization methods to differentiate a "bad" brownout cloud from a "good" one.

This dissertation has presented contributions to the mitigation and characterization of rotorcraft brownout. Part I of the dissertation examined new methods for operational and aerodynamic brownout mitigation. Part II of the dissertation presented a new method for characterizing the severity of a brownout cloud in terms of its optical properties. The present chapter will summarize the work performed in each component of the research, and it will highlight the key conclusions.

7.1 Brownout Mitigation

In this dissertation, new methods for achieving brownout mitigation through flight path and rotor design optimization were presented. In both instances, the optimization was formulated as an approximate problem in which an objective function, which was created to be a surrogate for the visual degradation caused by the dust cloud, was minimized. The analyses were simulation-based, utilizing a free-vortex wake model and simulating the dynamics of the dust particles immersed in the rotor downwash.

7.1.1 Brownout Mitigation Through Flight Path Management

For the flight path optimization, a mathematical model of a visual approach-to-landing was parameterized and constrained to avoid maneuvers that would be conducive to the onset of vortex ring state or would result in flight within the "avoid" regions of a typical helicopter height-velocity diagram. The specific goals of the flight path optimization were:

1. To present a systematic brownout mitigation procedure based on flight path optimization that incorporates operational constraints to ensure the safety of flight over the duration of the maneuver.

2. To present the results of a brownout mitigation study that highlight the key physical mechanisms involved in the mitigation process.

3. To compare the results with prior experimental results and examine potential operational interpretations of the outcomes.

On the basis of the results of the approach-to-landing trajectory optimization, it can be concluded that:

1. The approach profile design space is nonconvex and contains multiple optima, including both shallow and steep approach angles. These results are consistent with operational mitigation strategies that have been formed over time by pilots operating in desert environments. The optimization methodology presented in this work is capable of identifying both classes of optima.

2. It appears likely that adjusting the approach profile can be an effective means towards brownout mitigation. "Preferred" approach profiles for brownout mitigation are more aggressive than typical approach profiles, and they tend to minimize the amount of time that the aircraft spends in brownout conditions.

3. The primary mechanism for mitigation is through the effect that the approach profile has on the flow field, particularly on the way in which the vortex wake interacts with the ground. The formation of a ground vortex as the wake impinges on the ground appears to be responsible for the initial uplift of dust particles, and the onset of brownout conditions appears to occur nearly simultaneously with the development of the ground vortex.

4. Steady-state flight profiles that have been previously identified for ground vortex and recirculation flow regimes appear to be invalid for maneuvering flight in ground-effect. However, it may still be possible to identify consistent features in the flow developments for drastically different maneuvers.

5. From the approaches that were evaluated in the course of the optimization procedure, boundaries may be defined that identify the flight conditions for which the formation of a ground vortex is imminent. Because the ground vortex is responsible for significant amounts of sediment uplift, such boundaries may provide insight into the formation of a brownout cloud during an approach-to-landing maneuver. Further investigation is required before any such results can be generalized; however, the ability to reduce such information to simplified representations (e.g., a height-velocity diagram) could potentially provide valuable information to the operational community.

7.1.2 Brownout Mitigation Through Main Rotor Design

For the rotor design optimization, key rotor parameters were examined (i.e., rotor radius, blade chord, blade twist rate, and number of blades), and rotor designs were constrained to preserve the propulsive and maneuver margins of the baseline design. The specific goals of the rotor design optimization were:

1. To present a systematic brownout mitigation procedure based on rotor design optimization that incorporates mixed continuous (i.e., blade chord, rotor radius, blade twist rate) and integer (i.e., number of blades) design variables.

2. To present the results of a brownout mitigation study that highlight the mathematical properties of the proposed optimization procedure and the key physical mechanisms involved in the mitigation process.

3. To demonstrate methods for extracting system-level preliminary design guidelines

366

from the optimization data.

On the basis of the results of the rotor design optimization, it can be concluded that:

1. The optimization problem leading to brownout mitigation is nonconvex over large portions of the design space. While this property does not prevent the optimization methodology from achieving significant reduction in the objective function, it suggests that some algorithms, e.g., Branch-and-Bound, would be ill-suited for this problem.

2. The proposed GA-based methodology is suitable for formulating design optimization problems with mixed integer and continuous design variables. When utilized in a rotor design optimization for brownout mitigation, the methodology results in significant improvements in relatively few optimization steps.

3. For the single main rotor configuration studied in the present work, brownout mitigation was apparently effected through the impact that the rotor design had on the development and evolution of the ground vortex. Generally speaking, reduced N_b led to reduced brownout severity. The results further indicated that relatively small changes in certain key rotor parameters can potentially have profound effects on the size and intensity of a dust cloud surrounding the rotor.

4. The results of the optimization procedures were shown to be useful in deriving preliminary design guidelines in terms of common system-level design parameters (i.e., disk loading, wake-reduced frequency, tip vortex strength). Such guidelines provide a methodology for developing an improved understanding of important sen-

sitivities early in the design process.

7.2 Brownout Characterization

In this dissertation, a new method for characterizing brownout severity was presented. This characterization method involves the assessment of the visual obscuration caused by the brownout cloud, as quantified by the Modulation Transfer Function (MTF). The research presented herein was comprised of experimental and analytical studies.

7.2.1 Experimental Measurements of the Visual Degradation Caused by a Brownout Cloud Generated in Flight Test

The experimental studies included both proof-of-concept testing, in which methods for extracting the MTF from flight test were initially examined, as well as advanced testing, in which MTF measurements close to the ground were performed and new methods for interpreting the spatial and temporal variations of the MTF were developed. Multiple methods for extracting the MTF were demonstrated, and practical recommendations for future MTF testing were identified. The specific goals of the experimental studies were:

1. To adapt existing optics test techniques for the purposes of extracting MTF measurements from flight testing.

2. To present MTF measurements obtained from brownout flight testing.

3. To explore new methods for interpreting the temporal and spatial variations of the brownout cloud in order to provide insight into the cloud's development.

4. To determine practical guidelines for future MTF testing (e.g., camera selection, optical target design, etc.).

On the basis of the experimental results presented in this dissertation, it can be concluded that:

1. MTFs of brownout clouds can be extracted easily and inexpensively from flight tests, wherever appropriate optical targets can be filmed. The square-wave response method is intuitive and simple, although specific test patterns are necessary which may have spatial frequency limitations. The edge response method, on the other hand, requires only an edge with suitable contrast and can yield MTF measurements for all spatial frequencies (within the limitations of the imaging system).

2. Brownout visibility degradation is dependent on spatial frequency: high frequency features, i.e., fine-grained details, are lost before low frequency features, i.e., large objects. This frequency-dependent degradation can be captured quantitatively by the MTF.

3. Because of its ability to quantify the loss of visual detail at various spatial frequencies, the MTF is a viable building block for a metric to characterize a brownout cloud from the point of view of the visual cues available to a pilot, and could help provide important information for HQ analyses and pilot-in-the-loop simulation fidelity assessment.

4. It is possible to measure the Modulation Transfer Function of a brownout cloud at or near ground level by analyzing the black/white transitions of an edge on an

optical target. Because the physical size of the optical targets needed for MTF calculations is very small, it is possible that multiple targets could be safely placed in the immediate vicinity of the landing area.

5. It is possible to interpret a large number of MTF calculations over a range of space and time in ways that succinctly quantify the effects of the brownout cloud. At a given instant in time it is possible to compose contour plots that describe the loss of visibility over wide regions (e.g., an entire landing area). Similarly, the temporal variation in visibility degradation due to the brownout cloud can be plotted to gain a more complete understanding of the brownout problem. The intuitively known fact that small details and ground texture are obscured before larger objects, i.e., that the sediment cloud acts as an optical low-pass filter, is correctly captured quantitatively.

7.2.2 Theoretical Predictions of the Visual Degradation Caused by a Simulated Brownout Cloud

Analytical studies explored the potential for predicting the MTF of a brownout cloud through simulation. The prediction method was based on Radiative Transfer Theory (RTT), a heuristic method for computing the effects of scattering and absorption by a volume in which many sediment particles reside. Sensitivities to the cloud density and the imaging system limitations were examined, and comparison tests were conducted in which MTF predictions were compared with the results of controlled experiments. The specific goals of the analytical studies were:

1. To present an initial methodology for the prediction of the MTF of a brownout

cloud from fundamental light scattering and absorption theory.

2. To examine the sensitivity of the predictions to key physical parameters (such as the cloud density or imaging system limitations).

3. To present the results of a study in which MTF predictions are compared with MTF measurements in controlled conditions.

On the basis of the analytical results presented in this dissertation, it can be concluded that:

1. It is possible, in principle, to predict the Modulation Transfer Function of a brownout cloud using models that are firmly rooted in the fundamental physics of light scattering and absorption. The accuracy of these predictions is drastically impacted by the accuracy of the dust cloud simulation and the accuracy of the imaging system limitations.

2. The relationship between cloud density and visual degradation appears to be nonlinear, indicating that visibility will abruptly decrease when the cloud (or some region within the cloud) reaches a critical density. This characteristic could be a contributing factor to the rapidity of the brownout problem that has been anecdotally reported.

3. It is possible to construct simple, controlled experiments to verify computational methods for MTF prediction; however, care must be exercised in characterizing the dust cloud composition (i.e., the relative count densities as a function of particle size) and imaging system limitations for such comparison studies to be effective.

371

Chapter 8

Future Work

The research presented in this dissertation has demonstrated that (a) numerical optimization provides an appropriate framework within which brownout mitigation strategies may be formulated and (b) the MTF is uniquely capable characterizing the visual degradation caused by a brownout cloud. The present chapter will suggest potential ways in which these research findings may be leveraged in future work.

8.1 Brownout Mitigation and Characterization

The state of the art of brownout mitigation and characterization may be further advanced by the following:

1. **Improved measurements of the MTF in flight testing:** While the results presented in Chapter 5 demonstrated the ability of the MTF to characterize the visual degradation caused by a brownout cloud in flight test, those results were obtained for viewpoints external to the cloud. The viewpoints of the greatest practical significance, however, are those from inside the helicopter (i.e., the pilot's perspective), and MTF measurements from these viewpoints should be performed. Such measurements would require a video camera to be mounted in the cockpit and an array of small "edge strips" (similar to those demonstrated in Chapter 5) to be placed in the vicinity of landing zone. The measurement and processing techniques, however,

would be identical to those presented in this dissertation.

2. **Improving the fidelity of the flight dynamics simulation:** The flight dynamics simulation used for the mitigation studies in Chapters 3 and 4 included many simplifying assumptions (see Section 3.1.8), and the overall fidelity of the simulation may be improved in a variety of ways. In the first instance, more advanced simulations may be performed by coupling the FVM to a flight dynamic simulation (Ref. 154). Under this approach, a time-history of flight control inputs that results in the desired approach profile may be determined by inverse simulation, and the motion and accelerations of the aircraft would therefore be more realistic than those obtained in this dissertation. A subsequent improvement to the simulation may be achieved by incorporating a mathematical model for the human pilot. The pilot model would provide control inputs at each time step as a function of the difference between the perceived states of the aircraft and the desired states of the aircraft at that instant.

3. **Validating the results of the mitigation studies through experimentation and flight test:** The optimization studies presented in Chapters 3 and 4 yielded optimal approach trajectories and rotor designs, respectively, for brownout mitigation. These results may be validated in laboratory conditions, and would require two-phase measurements of a rotor flow and developing brownout cloud for a rotor that traverses the ground in accordance with a prescribed motion. Additionally, the boundaries of the notional H-V diagram for brownout approaches presented in Fig. 3.30 should be evaluated through flight testing in brownout conditions. Such

flight tests would require the execution of a range of approaches for varying approach angles and degrees of maneuver aggression. Each approach profile could be plotted on the axes of Fig. 3.30, and the onset of brownout verified against the notional boundaries identified from simulation. Such tests would provide an invaluable source of data to the research community, and they may be seen as an essential step towards the formal development of operational criteria for brownout mitigation.

4. **Extension of the trajectory optimization procedure to include multiship operations:** Multiship operations are commonly a contributing factor to brownout mishaps, and they should be examined in greater detail. The optimization methodology presented in Chapter 3 may be readily adapted to accommodate a trajectory optimization study including multiple aircraft. Recall that the approach profile design vector presented in Chapter 3 was defined as

$$\mathbf{X} = \begin{bmatrix} \alpha_{\mathrm{app}} & v_0 & r_{\mathrm{pd}} \end{bmatrix}^T \tag{8.1}$$

where α_{app} was the approach angle, v_0 the initial velocity, and r_{pd} the range at which peak deceleration occurred. A potential design vector for the multiship case is

$$\mathbf{X} = \begin{bmatrix} \alpha_{\mathrm{app}}^1 & v_0^1 & r_{\mathrm{pd}}^1 & \alpha_{\mathrm{app}}^2 & v_0^2 & r_{\mathrm{pd}}^2 & \Delta d_{\mathrm{lat}} & \Delta d_{\mathrm{lon}} & \Delta t \end{bmatrix}^T \tag{8.2}$$

where $\begin{bmatrix} \alpha_{\mathrm{app}}^1 & v_0^1 & r_{\mathrm{pd}}^1 \end{bmatrix}^T$ is the approach profile for the first aircraft, $\begin{bmatrix} \alpha_{\mathrm{app}}^2 & v_0^2 & r_{\mathrm{pd}}^2 \end{bmatrix}^T$ describes the approach profile for the second aircraft, Δd_{lat} and Δd_{lon} provide the

lateral and longitudinal offsets between the landing points of the two aircraft, and Δt is the difference between the landing times of the two aircraft. The optimization may be performed as discussed in Chapter 3, although the objective function would need be adjusted to include the visual degradation experienced by the pilots of both aircraft. The additional variables in the design vector would likely require that more function evaluations be performed for this optimization than for the single-ship optimization presented in this dissertation.

5. **Extension of the rotor design optimization to include multiple configurations:** A variety of rotorcraft configurations exist in the present inventory, and the future of rotorcraft will likely involve the examination of many more advanced concepts. The methodology presented in Chapter 4 may be adapted to accommodate virtually any configuration (e.g., tandem rotor helicopters, tilt-rotor aircraft, coaxial helicopters, etc.). Notice that some configurations may require the inclusion of additional design variables (e.g., longitudinal/lateral spacing between rotors for tandems and tilt-rotors, rotor spacing for coaxials, etc.), which would likely necessitate extra function evaluations in comparison with the design optimization study presented in this dissertation.

8.2   Related Fields of Study

The work presented in this dissertation may also be extended into related fields of study by the following:

1. **Examining the efficacy of using the MTF for characterizations of other forms of DVE:** The efficacy of the MTF in characterizing other forms of DVE (e.g., fog, smoke, rain, snow, battlefield contaminants, etc.) should be examined. In the first instance, the MTF prediction methodology presented in Chapter 6 may be readily extended to other forms of DVE by replacing the size and absorption/scattering properties of sand with those of the other particles. Subsequently, visual scenes with MTFs corresponding to each type of DVE could be developed for display on pilot-in-the-loop simulators in order to examine the relationship between reduced MTFs and degraded HQ. If the MTF proves to be suitable as a general characterization metric for any type of DVE, it would potentially provide a basis for more quantitative assessments of Visual Cue Ratings (VCR) and Usable Cue Environment (UCE) in ADS-33.

2. **Applying trajectory optimization techniques to other complicated rotorcraft problems:** The trajectory optimization procedure provided in Chapter 3 may potentially be used for solving other complicated rotorcraft problems. The key elements of the technique are: (i) a parameterization of the maneuver to be optimized and (ii) an objective that may be computed. For example, optimal procedures for minimal fuel burn by a hypothetical rotorcraft (e.g., a large civil tiltrotor) at take-off may be determined by adopting a methodology similar to the one presented for brownout mitigation in this dissertation.

Appendices

Appendix A

Planning Considerations for MTF Testing

A variety of factors must be considered in designing a test pattern for MTF testing:

1. The intended MTF calculation method(s) must be identified. While square wave response is intuitive and easy to calculate, there are a variety of limitations (as discussed in the paper). Conversely, the edge response method is highly versatile but requires a greater investment in post-processing capabilities. Designing a test pattern that can be used for both square-wave and edge response calculations is thus preferred in that it provides the ability to calculate the MTF by either method (or both).

2. If the test pattern is to be used for square-wave response calculations, it should contain a suitable range of spatial frequencies. Radial patterns, in particular, provide a wide range of spatial frequencies. The spatial frequencies in a test pattern can be obtained as follows. First, it is helpful to define two coordinate systems, that of the observer, $\left[\hat{i}_o \ \hat{j}_o \ \hat{k}_o\right]^T$, and that of the aircraft, $\left[\hat{i}_{a/c} \ \hat{j}_{a/c} \ \hat{k}_{a/c}\right]^T$. These coordinate systems can be related through the following transformation:

$$
\begin{Bmatrix} \hat{i}_o \\ \hat{j}_o \\ \hat{k}_o \end{Bmatrix} = [T] \begin{Bmatrix} \hat{i}_{a/c} \\ \hat{j}_{a/c} \\ \hat{k}_{a/c} \end{Bmatrix} + \begin{Bmatrix} x_o \\ y_o \\ z_o \end{Bmatrix} \tag{A.1}
$$

378

where

$$T_{11} = \cos\theta\cos\psi \tag{A.2}$$

$$T_{12} = \cos\theta\sin\psi \tag{A.3}$$

$$T_{13} = -\sin\theta \tag{A.4}$$

$$T_{21} = \sin\phi\sin\theta\cos\psi - \cos\phi\sin\psi \tag{A.5}$$

$$T_{22} = \sin\phi\sin\theta\sin\psi + \cos\phi\cos\psi \tag{A.6}$$

$$T_{23} = \sin\phi\cos\theta \tag{A.7}$$

$$T_{31} = \cos\phi\sin\theta\cos\psi + \sin\phi\sin\psi \tag{A.8}$$

$$T_{32} = \cos\phi\sin\theta\sin\psi - \sin\phi\cos\psi \tag{A.9}$$

$$T_{33} = \cos\phi\cos\theta \tag{A.10}$$

$[x_o \; y_o \; z_o]^T$ is the location of the reference point on the aircraft with respect to the observer, and $[\phi\,\theta\,\psi]$ is the angular orientation of the aircraft with respect to the observer. If the location of two endpoints of a black/white line pair of width w can be expressed in the aircraft coordinate system, they can likewise be expressed as vectors in the observer coordinate system, $\vec{v}_1$ and $\vec{v}_2$. Using the law of cosines, the angle subtended in the observer's FOV (see Fig. A.1) can be approximated:

$$\alpha = \cos^{-1}\left[\frac{w^2 - |\vec{v}_1|^2 - |\vec{v}_2|^2}{-2|\vec{v}_1||\vec{v}_2|}\right], \tag{A.11}$$
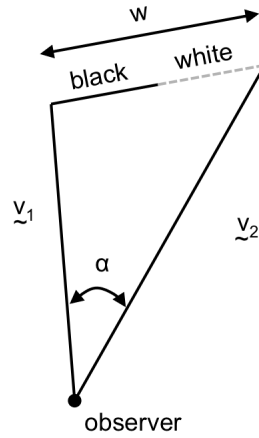
Figure A.1: Schematic diagram for calculating spatial frequency.

and the spatial frequency is

$$\omega = \frac{n_{\text{cyc}}}{\alpha} = \frac{1}{\alpha} \qquad (A.12)$$

where n_{cyc} is the number of black/white cycles subtended in α. Note that Hoh [12] suggested that the range of spatial frequencies that a pilot uses in controlling the aircraft are in the range of $1-10$ cycles per degree.

3. For test patterns that will be placed in the vicinity of the landing area, the proximity to the landing zone and anchoring methods must be considered so as not to compromise the safety of flight. For test patterns that are mounted on the rotorcraft, a primary concern is the method of attachment.

A suitable camera must also be selected:

1. Ensuring that the camera has sufficient resolution can be done as follows. Recalling that the "cutoff frequency" for a camera with pixel width a is $\omega = (2a)^{-1}$, a camera with a FOV of x by y degrees and a resolution of i by j pixels will have a pixel width of approximately $a \approx x/i \approx y/j$. The cutoff frequency of the camera is then

380

$\omega \approx \left(\dfrac{2x}{i}\right)^{-1} \approx \left(\dfrac{2y}{j}\right)^{-1}$. For example, if a camera has a FOV of 30° laterally, and each frame contains 1920 pixels laterally,

$$\omega \approx \left(\frac{2 \times 30°}{1920 \text{ p}}\right)^{-1} \approx 32 \text{ cycles per degree.} \tag{A.13}$$

Note that an *optical* zoom effectively decreases the FOV while maintaining the same number of pixels (leading to finer resolution), whereas a *digital* zoom, decreases the number of pixels, i.e., it simply crops the actual image, so it results in no improvements in resolution.

2. The auto-focus feature could be a potential issue, depending on the time of day and proximity of the camera to the cloud, if the focus adjusting mechanism is based on maximizing image contrast. In the present study, changes in contrast caused by autofocus were not taken into account, but it is believed that they were negligible.

Appendix B

MTF Extraction Using the Square-Wave and Edge Response Methods

MTF Extraction Using the Square-Wave Response Method:

1. Extract a single frame from the video footage and convert that image into grayscale. The image can now be represented by a single matrix, in which each pixel of the image is assigned a numerical grayscale value.

2. Determine the specific sampling locations within the test pattern to be utilized. Each sampling location can be any line segment that perpendicularly crosses some number of black/white transitions in the test pattern. For example, 12 separate sampling locations for a billboard resolution target are identified in Fig. 5.5 and 17 sampling locations for the Siemens star resolution target are depicted in Fig. 5.8(a). From a practical standpoint, this step amounts to the selection of the endpoints of each "sampling segment" within the digital image, as depicted by small circles in Fig. 5.8(a). The coordinates of each endpoint correspond to specific pixel locations within the digital image.

3. The angle subtended by each sampling segment in the FOV of the camera can be calculated using Eqs. A.1–A.11 and the corresponding spatial frequency can be calculated using Eq. A.12.

4. The available contrast at each sampling location can be calculated by plotting the

grayscale value for each pixel encountered along the sampling segment, as shown in Fig. 5.8(b). It is conventional to normalize this value by either the maximum grayscale value ("255" for 8-bit grayscale) or by the maximum grayscale value of the data points (essentially normalizing the maximum MTF value to unity).

5. The available contrast for each sampling location, calculated in step 4, can be plotted vs. its spatial frequency, calculated in step 3. A best fit to these data using the classical aerosol MTF equation (Eq. 5.5) can be used to better visualize the results.

MTF Extraction Using the Edge Response Method:

1. Extract a single frame from the video footage and convert that image into grayscale. The image can now be represented by a single matrix, in which each pixel of the image is assigned a numerical grayscale value.

2. Determine a single sampling location within the test pattern to be utilized. This sampling location can be any line segment that perpendicularly crosses a black/white edge. From a practical standpoint, this step amounts to the selection of the endpoints of a "sampling segment" within the digital image; the coordinates of each endpoint correspond to specific pixel locations.

3. Calculate the Edge Response Function (ERF) at that sampling location by (a) calculating the available contrast using step 4 from Appendix B and (b) fitting a suitably-scaled Gaussian CDF to the data.

4. Calculate the Edge Spread Function (ESF), Eq. 5.3, noting that the calculation of the ERF as a Gaussian CDF means that the corresponding ESF is given by the

Gaussian Probability Density Function (PDF).

5. Calculate the MTF by Fourier transforming the ESF (using a Fast Fourier Transform, FFT, algorithm). Note that the ESF is given as a function of distance along the sampling segment in the digital image, measured in pixels. This must be converted to angular units using Eqs. A.1–A.11 prior to the Fourier transform to yield a MTF that is given as a function of spatial frequency in units of cycles per degree or cycles per radian.

6. Normalize the MTF such that MTF(0) equals either (a) the "percent contrast" of the ERF, which is found by dividing the magnitude of the contrast in the ERF by the maximum grayscale value ("255" for 8-bit grayscale), or (b) unity.

Appendix C

Review of Maxwell's Equations and the Poynting Vector

Because electromagnetic theory is not necessarily the most familiar to a typical aerospace engineer, a review of the physical meanings of Maxwell's equations and the Poynting vector is included in this appendix. The discussion of Maxwell's equations is adapted from Ref. 155 and the discussion of the Poynting vector is adapted from Ref. 143.

Gauss' Law

To begin, consider Coulomb's Law, which states that the force on a point charge, q, located at $\vec{r}$ exerted by another point charge, q', located at $\vec{r}'$ is:

$$\vec{F} = q\boldsymbol{E}\left(\vec{r}\right) \tag{C.1}$$

where

$$\boldsymbol{E}(\vec{r}) = \frac{q'}{4\pi\varepsilon_0} \frac{(\vec{r} - \vec{r}')}{|\vec{r} - \vec{r}'|^3} \tag{C.2}$$

where ε_0, the permittivity, is simply a proportionality constant.

Notice that, because $(\vec{r} - \vec{r}') / |\vec{r} - \vec{r}'|$ is the unit vector between q' and q, the strength

of the field is proportional to the inverse of the squared distance from the charge, i.e.,

$$\boldsymbol{E}(\vec{r}) = \underbrace{\frac{q'}{\varepsilon_0}}_{\text{charge divided by a const.}} \underbrace{\frac{1}{4\pi|\vec{r}-\vec{r}'|^2}}_{\text{1/the surface area of a sphere}} \underbrace{\frac{(\vec{r}-\vec{r}')}{|\vec{r}-\vec{r}'|}}_{\text{unit vector along }|\vec{r}-\vec{r}'|} \tag{C.3}$$
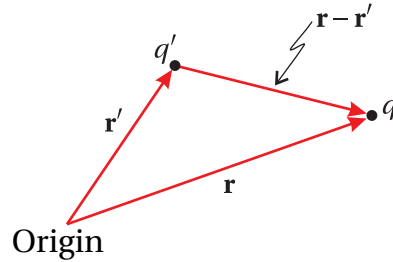
Figure C.1: The geometry of Coulomb's law for a point charge (from Ref. 155).

For a collection of charges, the force on a point charge q located at $\vec{r}$

$$\vec{F} = \sum_{n=1}^{N} q\boldsymbol{E}_n(\vec{r}) \tag{C.4}$$

If charges are distributed continuously through space with a charge density $\rho(\vec{r}')$ (in units of charge per volume):

$$\boldsymbol{E}(\vec{r}) = \frac{1}{4\pi\varepsilon_0} \int_V \rho(\vec{r}') \frac{(\vec{r}-\vec{r}')}{|\vec{r}-\vec{r}'|^3} dv' \tag{C.5}$$

Gauss' Law is, in differential form:

$$\nabla \cdot \boldsymbol{E}(\vec{r}) = \frac{\rho(\vec{r})}{\varepsilon_0} \tag{C.6}$$

we can obtain the integral form of Gauss' Law:

$$\underbrace{\int_V \nabla \cdot \boldsymbol{E}(\vec{r})\, dv}_{\text{use divergence thm.}} = \int_V \frac{\rho(\vec{r})}{\varepsilon_0}\, dv \tag{C.7}$$

$$\oint_S \boldsymbol{E}(\vec{r}) \cdot \hat{n}\, da = \frac{1}{\varepsilon_0} \int_V \rho(\vec{r})\, dv \tag{C.8}$$

Gauss' Law for Magnetism

Consider a magnetic field to arise from a distribution of moving charges described by a current density $\boldsymbol{J}(\vec{r}')$ throughout space. Note that current density has units of charge times velocity per volume or current per cross-sectional area. The magnetic force law analogue to Coulomb's Law is:

$$\vec{F} = q\vec{v} \times \boldsymbol{B} \tag{C.9}$$

where $\vec{v}$ is the velocity of the charge q and where

$$\boldsymbol{B}(\vec{r}) = \frac{\mu_0}{4\pi} \int_V \boldsymbol{J}(\vec{r}') \times \frac{(\vec{r} - \vec{r}')}{|\vec{r} - \vec{r}'|^3}\, dv' \tag{C.10}$$

where μ_0 is the permeability and dictates the strength of the magnetic field given the current distribution. This is the Biot-Savart Law.

Because

$$\nabla_{\vec{r}} \frac{1}{|\vec{r} - \vec{r}'|^3} = -\frac{(\vec{r} - \vec{r}')}{|\vec{r} - \vec{r}'|^3} \tag{C.11}$$

where the subscript in $\nabla_{\vec{r}}$ indicates that the divergence operates on $\vec{r}$, not $\vec{r}'$, the Biot-

387

Savart Law may be expressed as:

$$\boldsymbol{B}(\vec{r}) = -\frac{\mu_0}{4\pi} \int_V \boldsymbol{J}(\vec{r}') \times \nabla_{\vec{r}} \frac{1}{|\vec{r} - \vec{r}'|} \, dv' \tag{C.12}$$

$$= \frac{\mu_0}{4\pi} \nabla \times \int_V \frac{\boldsymbol{J}(\vec{r}')}{|\vec{r} - \vec{r}'|} \, dv' \tag{C.13}$$

The divergence of the curl is always zero, so

$$\nabla \cdot \boldsymbol{B} = 0 \tag{C.14}$$

which is Gauss' Law for magnetic fields (in differential form). Gauss' Law for magnetic fields can also be expressed in integral form:

$$\oint_S \boldsymbol{B}(\vec{r}) \cdot \hat{n} \, da = 0 \tag{C.15}$$

Simply put, this gauss' law for magnetic fields states that the net magnetic flux out of any closed surface is zero.

Faraday's Law [of Induction]

Faraday discovered that changing magnetic fields induces electric fields—this is called induction. He showed that a change in magnetic flux through a circuit loop induces an electromotive force around the loop.
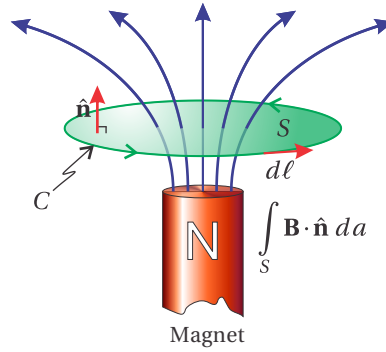
Figure C.2: Schematic of Faraday's Law (from Ref. 155).

The integral form of Faraday's Law is:

$$\underbrace{\oint_C \boldsymbol{E} \cdot dl}_{\text{voltage}} = \underbrace{-\frac{\partial}{\partial t} \int_S \boldsymbol{B} \cdot \hat{n}\, da}_{\text{change in magnetic flux through a surface}} \tag{C.16}$$

By applying Stokes' Theorem to the left-hand side, Faraday's Law may be expressed as:

$$\oint_C \boldsymbol{E} \cdot dl = \int_S \nabla \times \boldsymbol{E} \cdot \hat{n}\, da = -\frac{\partial}{\partial t} \int_S \boldsymbol{B} \cdot \hat{n}\, da \tag{C.17}$$

and Faraday's Law can be written in differential form:

$$\nabla \times \boldsymbol{E} = -\frac{\partial \boldsymbol{B}}{\partial t} \tag{C.18}$$

Ampere's Law

Ampere's Law, as originally formulated is (in differential form):

$$\nabla \times \boldsymbol{B} = \mu_0 \boldsymbol{J} \tag{C.19}$$

Implicit in this formulation is that the charge distribution ρ does not vary much with time. This is not a valid assumption for optical phenomena (Ref. 155).
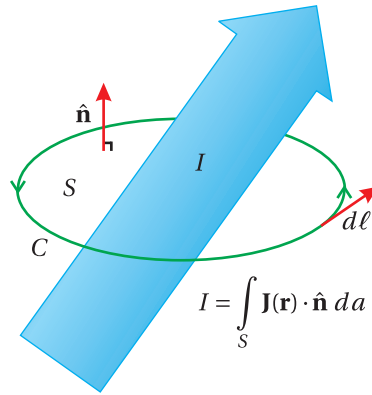
Figure C.3: Schematic of Ampere's Law (from Ref. 155).

A better physical interpretation of Ampere's Law comes from its integral form, which is obtained by integrating both sides of the differential form over an open surface S, bounded by contour C.

$$\underbrace{\int_S \nabla \times \boldsymbol{B} \cdot \hat{n}\, da = \oint_C \boldsymbol{B} \cdot dl}_{\text{Stokes' Theorem}} = \mu_0 \int_S \boldsymbol{J} \cdot \hat{n}\, da \equiv \mu_0 I \qquad (\text{C.20})$$

A physical interpretation of this expression is that the line integral of $\boldsymbol{B}$ around a closed loop C is proportional to the total current flowing through the loop.

Maxwell's adjustment to Ampere's Law stems from a realization that situations exist where the charge distribution is not time-invariant, i.e., $\nabla \cdot \boldsymbol{J} = -\partial \rho / \partial t$.

Maxwell's adjustment to Ampere's Law stems from a realization that situations exist where the charge distribution is not time-invariant, i.e., $\nabla \cdot \boldsymbol{J} = -\partial \rho / \partial t$. This yields

(in integral form):

$$\nabla \times \boldsymbol{B} = \mu_0 \boldsymbol{J} + \frac{\mu_0}{4\pi} \frac{\partial}{\partial t} \int_V \rho\left(\vec{r}'\right) \frac{(\vec{r} - \vec{r}')}{|\vec{r} - \vec{r}'|^3} \, dv' \tag{C.21}$$

or in differential form:

$$\nabla \times \frac{\boldsymbol{B}}{\mu_0} = \boldsymbol{J} + \varepsilon_0 \frac{\partial \boldsymbol{E}}{\partial t} \tag{C.22}$$

where the last term is known as the displacement current (density).

Poynting Vector

The Poynting vector, $\boldsymbol{S} = \boldsymbol{E} \times \boldsymbol{H}$, specifies the magnitude and direction of the rate of transfer of electromagnetic energy at all points in space, and it is of primary importance in problems of propagation, absorption, and scattering of electromagnetic waves. For a planar surface, A, with unit normal vector, $\hat{\boldsymbol{n}}$, electromagnetic energy is transferred across the surface at a rate $\boldsymbol{S} \cdot \hat{\boldsymbol{n}} A$ (for a constant $\boldsymbol{S}$ over the surface). This can be generalized to:

$$\int \boldsymbol{S} \cdot \hat{\boldsymbol{n}} \, dA \tag{C.23}$$

The net rate W at which electromagnetic energy crosses the boundary of a closed surface, A, which encloses a volume, V, is:

$$W = -\int_A \boldsymbol{S} \cdot \hat{\boldsymbol{n}} \, dA \tag{C.24}$$

where the minus sign makes W positive for a net transfer of electromagnetic energy into the volume. V (i.e., energy is absorbed in V). Likewise, W is negative for a net transfer of electromagnetic energy out of the volume.

Bohren and Huffman (Ref. 143) point out that "Most instruments are not capable of following the rapid oscillations of the instantaneous Poynting vector, but respond to some time average $\langle S \rangle$." An expression for the time-averaged Poynting vector for time-harmonic fields is:

$$\langle S \rangle = \frac{1}{2} \Re \{ E_c \times H_c^* \} \tag{C.25}$$

although the brackets are often omitted when it is obvious (i.e., obvious to a physicist) that the time-averaged Poynting vector is being used. The asterisk in H_c^* denotes the complex conjugate of H_c. The magnitude of the time-averaged Poynting vector is called the irradiance, H, and its dimensions are energy per unit area and time.

Bibliography

[1] Mapes, P., Kent, R., and Wood, R., "DOD Helicopter Mishaps FY85–05: Findings and Recommendations," Presentation, US Air Force, 2008.

[2] Rosenker, M. V., Conners, E. E., Hersman, D. A. P., and Higgins, K. O., "Special Investigation Report on Emergency Medical Services Operations," Aviation Special Investigation Report NTSB/SIR-06/01, National Transportation Safety Board, Washington, DC, 2006.

[3] Key, D. L., "Analysis of Army Helicopter Pilot Error Mishap Data and the Implications for Handling Qualities," 25th European Rotorcraft Forum Proceedings, Rome, Italy, September 14–16, 1999.

[4] Key, D. L., Blanken, C. L., and Hoh, R. H., "Some Lessons Learned in Three Years with ADS-33C," *Piloting Vertical Flight Aircraft: A Conference on Flying Qualities and Human Factors*, San Francisco, CA, January 20–22, 1993.

[5] Padfield, G. D., *Helicopter Flight Dynamics*, Blackwell Publishing, Oxford, UK, 2nd ed., 2007.

[6] Johnson, B., Leishman, J. G., and Sydney, A., "Investigation of Sediment Entrainment Using Dual-Phase, High-Speed Particle Image Velocimetry," *Journal of the American Helicopter Society*, Vol. 55, (4), October, 2010, pp. 042003–1–16.

[7] Sydney, A., Baharani, A., and Leishman, J. G., "Understanding Brownout using Near-Wall Dual-Phase Flow Measurements," American Helicopter Society International 67th Annual Forum Proceedings, Virginia Beach, VA, May 3–5, 2011.

[8] Milluzzo, J., Sydney, A., Rauleder, J., and Leishman, J. G., "In-Ground-Effect Aerodynamics of Rotors with Different Blade Tips," American Helicopter Society International 66th Annual Forum Proceedings, Phoenix, AZ, May 11–13, 2010.

[9] Milluzzo, J., and Leishman, J. G., "Assessment of Rotorcraft Brownout Severity in Terms of Rotor Design Parameters," *Journal of the American Helicopter Society*, Vol. 55, (3), July, 2010, pp. 032009–1–9.

[10] Anonymous, *TC 3-04.93: Aeromedical Training for Flight Personnel*, Headquarters, Department of the Army, Washington, DC, 2009.

[11] Wolfe, J. M., Kluender, K. R., Levi, D. M., Bartoshuk, L. M., Herz, R. S., Klatzky, R. L., Lederman, S. J., and Merfeld, D. M., *Sensation & Perception*, Sinauer Associates, Inc., 2008.

[12] Hoh, R. H., "Investigation of Outside Visual Cues Required for Low Speed and Hover," 12th AIAA Atmospheric Flight Mechanics Conference Proceedings, Snowmass, CO, August 19–21, 1985, pp. 337–349.

[13] Rodgers, S. J., "Evaluation of the Dust Cloud Generated by Helicopter Rotor Downwash," Final Report 67-81, US Army Aviation Materiel Laboratories, Fort Eustis, VA, March, 1968.

[14] Muleski, G. E., "Sandblaster 2 Support of See-Through Technologies for Particulate Brownout: Task 1 Technical Report," MRI Project No. 110565, Defense Advanced Research Projects Agency (DOD) Strategic Technology Office, 2007.

[15] Cowherd, C., "Sandblaster 2 Support of See-Through Technologies for Particulate Brownout: Task 5 Technical Report," MRI Project No. 110565, Defense Advanced Research Projects Agency (DOD) Strategic Technology Office, 2007.

[16] Gillies, J. A., Etyemezian, V., Kuhns, H., McAlpine, J. D., King, J., Uppapalli, S., Nikolich, G., and J., E., "Dust Emissions Created by Low-Level Rotary-Winged Aircraft Flight Over Desert Surfaces," *Atmospheric Environment*, Vol. 44, 2010, pp. 1043–1053.

[17] Wong, O., and Tanner, P., "Photogrammetric Measurements of an EH-60L Brownout Cloud," American Helicopter Society International 66th Annual Forum Proceedings, Phoenix, AZ, May 11–13, 2010.

[18] Tanner, P., "Photogrammetric Characterization of a Brownout Cloud," American Helicopter Society International 67th Annual Forum Proceedings, Virginia Beach, VA, May 3–5, 2011.

[19] Syal, M., Govindarajan, B., and Leishman, J. G., "Mesoscale Sediment Tracking Methodology to Analyze Brownout Cloud Developments," American Helicopter Society International 66th Annual Forum Proceedings, Phoenix, AZ, May 11–13, 2010.

[20] Syal, M., and Leishman, J. G., "Comparisons of Predicted Brownout Dust Clouds with Photogrammetry Measurements," American Helicopter Society International 67th Annual Forum Proceedings, Virginia Beach, VA, May 3–5, 2011.

[21] Syal, M., Rauleder, J., Tritschler, J. K., and Leishman, J. G., "On the Possibilities of Brownout Mitigation Using a Slotted-Tip Rotor Blade," 29th AIAA Applied Aerodynamics Conference Proceedings, Honolulu, HI, June 27–30, 2011.

[22] Govindarajan, B., and Leishman, J. G., "Evaluation of Particle Clustering Algorithms in the Prediction of Brownout Dust Clouds," American Helicopter Society International 67th Annual Forum Proceedings, Virginia Beach, VA, May 3–5, 2011.

[23] Hu, Q., Gumerov, N., Duraiswami, R., Syal, M., and Leishman, J. G., "Toward Improved Aeromechanics Simulations Using Recent Advancements in Scientific Computing," American Helicopter Society International 67th Annual Forum Proceedings, Virginia Beach, VA, May 3–5, 2011.

[24] Kalra, T. S., Lakshminarayan, V. K., and Baeder, J. D., "CFD Validation Of Micro Hovering Rotor In Ground Effect," American Helicopter Society International 66th Annual Forum Proceedings, Phoenix, AZ, May 11–13, 2010.

[25] Thomas, S., Lakshminarayan, V. K., Kalra, T. S., and Baeder, J. D., "Eulerian-Lagrangian Analysis of Cloud Evolution using CFD Coupled with a Sediment Tracking Algorithm," American Helicopter Society International 67th Annual Forum Proceedings, Virginia Beach, VA, May 3–5, 2011.

[26] D'Andrea, A., "Numerical Analysis of Unsteady Vortical Flows Generated by a Rotorcraft Operating on Ground: a First Assessment of Helicopter Brownout," American Helicopter Society International 65th Annual Forum Proceedings, Grapevine, TX, May 27–29, 2009.

[27] D'Andrea, A., "Unsteady Numerical Simulations of Helicopters and Tiltrotors Operating in Sandy-Desert Environments," AHS International Specialists Conference on Aeromechanics Proceedings, San Francisco, CA, January 20–22, 2010.

[28] D'Andrea, A., and Scorcelletti, F., "Enhanced Numerical Simulations of Helicopter Landing Maneuvers in Brownout Conditions," American Helicopter Society International 66th Annual Forum Proceedings, Phoenix, AZ, May 11–13, 2010.

[29] D'Andrea, A., "Development and Application of a Physics-Based Computational Tool to Simulate Helicopter Brownout," 37th European Rotorcraft Forum Proceedings, Gallarate (VA), Italy, September 13–15, 2011.

[30] Keller, J. D., Whitehouse, G. R., Wachspress, D. A., Teske, M. E., and Quackenbush, T. R., "A Physics-Based Model of Rotorcraft Brownout for Flight Simulation Applications," American Helicopter Society International 62nd Annual Forum Proceedings, Phoenix, AZ, May 9–11, 2006.

[31] Wachspress, D. A., Keller, J. D., Quackenbush, T. R., Whitehouse, G. R., and Yu, K., "High Fidelity Rotor Aerodynamic Module for Real-Time Rotorcraft Flight Simulation," American Helicopter Society International 64th Annual Forum Proceedings, Montréal, Canada, April 29–May 1, 2008.

[32] Wachspress, D. A., Whitehouse, G. R., Keller, J. D., Yu, K., Gilmore, P., Dorsett, M., and McClure, K., "A High Fidelity Rotor Brownout Model for Real-Time Flight Simulations and Trainers," American Helicopter Society International 65th Annual Forum Proceedings, Grapevine, TX, May 27–29, 2009.

[33] Whitehouse, G. R., Wachspress, D. A., Quackenbush, T., and Keller, J. D., "Exploring Aerodynamic Methods for Mitigating Brownout," American Helicopter Society International 65th Annual Forum Proceedings, Grapevine, TX, May 27–29, 2009.

[34] Whitehouse, G. R., Wachspress, D. A., and Quackenbush, T., "Aerodynamic Design of Helicopter Rotors for Reduced Brownout," International Powered Lift Conference Proceedings, Philadelphia, PA, October 5–7, 2010.

[35] Phillips, C., and Brown, R. E., "The Effect of Helicopter Configuration on the Fluid Dynamics of Brownout," 34th European Rotorcraft Forum Proceedings, Liverpool, England, September 16–19, 2008.

[36] Phillips, C., and Brown, R. E., "Eulerian Simulation of the Fluid Dynamics of Helicopter Brownout," *Journal of Aircraft*, Vol. 46, (4), July–August, 2009, pp. 1416–1429.

[37] Phillips, C., Kim, H. W., and Brown, R. E., "The Flow Physics of Helicopter Brownout," American Helicopter Society International 66th Annual Forum Proceedings, Phoenix, AZ, May 11–13, 2010.

[38] Phillips, C., Kim, H., and Brown, R. E., "Helicopter brownout—Can it be modelled?" *The Aeronautical Journal*, Vol. 115, (1164), February, 2011, pp. 123–133.

[39] Ryerson, C. C., Haehnel, R. B., Koenig, G. G., and Moulton, M. A., "Visibility Enhancement in Rotorwash Clouds," 43rd AIAA Aerospace Sciences Meeting and Exhibit Proceedings, Reno, NV, January 10–13, 2005.

[40] Haehnel, R. B., Moulton, M. A., Wenren, Y., and Steinhoff, J., "A Model to Simulate Rotorcraft-Induced Brownout," American Helicopter Society International 64th Annual Forum Proceedings, Montréal, Canada, April 29–May 1, 2008.

[41] Lee, T. E., Leishman, J. G., and Ramasamy, M., "Fluid Dynamics of Interacting Blade Tip Vortices with a Ground Plane," *Journal of the American Helicopter Society*, Vol. 55, (2), April, 2010, pp. 022005–1–16.

[42] Curtiss, H., Sun, M., Putnam, W., and Hanker, E., "Rotor Aerodynamics in Ground Effect At Low Advance Ratios," *Journal of the American Helicopter Society*, Vol. 29, (1), January, 1984, pp. 48–55.

[43] Rauleder, J., and Leishman, J. G., "Measurements of the Turbulent Flow Environment on the Ground Below a Hovering Rotor," RTO HFM Symposium on Current Aeromedical Issues in Rotary Wing Operations, San Diego, CA, October 19–21, 1998.

[44] Nathan, N. D., and Green, R. B., "Measurements of a rotor flow in ground effect and visualisation of the brown-out phenomenon," American Helicopter Society International 64th Annual Forum Proceedings, Montréal, Canada, April 29–May 1, 2008.

[45] Haehnel, R. B., and Dade, W. B., "Physics Of Particle Entrainment Under The Influence Of An Impinging Jet," 26th Army Science Conference Proceedings, Orlando, FL, December 1–4, 2008.

[46] Wadcock, A. J., Ewing, L. A., Solis, E., Potsdam, M., and Rajagopalan, R. G., "Rotorcraft Downwash Flow Field Study to Understand the Aerodynamics of Helicopter Brownout," American Helicopter Society Southwest Region Technical Specialists Meeting: Technologies for the Next Generation of Vertical Lift Aircraft, Dallas-Fort Worth, TX, October 15–17, 2008.

[47] Szoboszlay, Z. P., Albery, W. B., Turpin, T. S., and Neiswander, G. M., "Brown-Out Symbology Simulation (BOSS) on the NASA Ames Vertical Motion Simulator," American Helicopter Society International 64th Annual Forum Proceedings, Montréal, Canada, April 29–May 1, 2008.

[48] Szoboszlay, Z. P., and Neiswander, G. M., "A Comparison of Linear and Logarithmic Scale Display Designs for Rotorcraft Landing in Brownout," 37th European Rotorcraft Forum Proceedings, Gallarate (VA), Italy, September 13–15, 2011.

[49] Neiswander, G. M., "Improving Deceleration Guidance for Rotorcraft Brownout Landing," American Helicopter Society International 67th Annual Forum Proceedings, Virginia Beach, VA, May 3–5, 2011.

[50] Turpin, T. S., Sykora, B., Neiswander, G. M., and Szoboszlay, Z. P., "Brownout Landing Aid System Technology (BLAST)," American Helicopter Society International 66th Annual Forum Proceedings, Phoenix, AZ, May 11–13, 2010.

[51] Sykora, B., "Rotorcraft Visual Situational Awareness Solving the Pilotage Problem for Landing in Degraded Visual Environments," American Helicopter Society International 65th Annual Forum Proceedings, Grapevine, TX, May 27–29, 2009.

[52] Harrington, W. W., Braddom, S. R., Savage, J. C., Szoboszlay, Z. P., McKinley, R. A., and Burns, H. N., "3D-LZ Brownout Landing Solution," American Helicopter Society International 66th Annual Forum Proceedings, Phoenix, AZ, May 11–13, 2010.

[53] Szoboszlay, Z. P., McKinley, R. A., Braddom, S. R., Harrington, W. W., Burns, H. N., and Savage, J. C., "Landing an H-60 Helicopter in Brownout Conditions Using 3D-LZ Displays," American Helicopter Society International 66th Annual Forum Proceedings, Phoenix, AZ, May 11–13, 2010.

[54] Lueken, T., and Doehler, H., "ALLFlight - A Synthetic Vision Sensor Suite with See-Through Capability for Helicopter Applications," American Helicopter Society International 66th Annual Forum Proceedings, Phoenix, AZ, May 11–13, 2010.

[55] Doehler, H. U., and Peinecke, N., "Image-Based Drift and Height Estimation for Helicopter Landings in Brownout," Image Analysis and Recognition, International Conference ICIAR 2010, Springer Lecture Notes in Computer Science, 2010.

[56] Link, N., Brown, D., Trickey, E., and Jennings, S., "Development of an Augmented Visionics System to Aid Flight Operations in Degraded Visual Environments," American Helicopter Society International 66th Annual Forum Proceedings, Phoenix, AZ, May 11–13, 2010.

[57] Jansen, C., Wennemers, A., Vos, W., and Groen, E., "FlyTact: A Tactile Display Improves a Helicopter Pilots Landing Performance in Degraded Visual Environments," HAPTICS: PERCEPTION, DEVICES AND SCENARIOS Lecture Notes in Computer Science, 2008.

[58] Cummings, M. L., and Smith, C. A., "Improving Precision Vertical Flight Operations Through a Direct-PerceptionAction Display," *Journal of Aircraft*, Vol. 46, (4), July–August, 2009, pp. 1270–1279.

[59] Pfledderer, L., and Pepi, M., "Sand Erosion Test Method for DOD Unique Environments," Proceedings of the 2007 Tri-Service Corrosion Conference, paper 1783, Denver, CO, December 3–6, 2007.

[60] Thomas, W., Hong, S., Yu, C., and Rosezweig, E. L., "Enhanced Erosion Protection for Rotor Blades," American Helicopter Society International 65th Annual Forum Proceedings, Grapevine, TX, May 27–29, 2009.

[61] Cooper, G. E., and Harper, R. P., "The Use of Pilot Ratings in the Evaluation of Aircraft Handling Qualities," Technical Memorandum TM D-5133, NASA, 1969.

[62] Vincenti, W. G., *What Engineers Know and How They Know It: Analytical Studies from Aeronautical History*, Johns Hopkins University Press, Baltimore, MD, 1990.

[63] Anonymous, "Performance Specification: Handling Qualities Requirements for Military Rotorcraft," Aeronautical Design Standard ADS 33-E-PRF, US Army, Redstone Arsenal, AL, 2000.

[64] Padfield, G. D., Lee, D. N., and Bradley, R., "How Do Helicopter Pilots Know When to Stop, Turn or Pull Up?" American Helicopter Society International 57th Annual Forum Proceedings, Washington, DC, May 9–11, 2001.

[65] Padfield, G. D., Clark, G., and Taghizad, A., "How Long Do Pilots Look Forward? Prospective Visual Guidance in Terrain-Hugging Flight," 31st European Rotorcraft Forum Proceedings, Florence, Italy, September, 2005.

[66] Hoh, R. H., "The Effects of Degraded Visual Cueing and Divided Attention on Obstacle Avoidance in Rotorcraft," Final Report DOT/FAA/RD-90/40, FAA, Washington, DC, 1990.

[67] Hoh, R. H., and Mitchell, D. G., "Handling Qualities Specification—A Functional Requirement for the Flight Control System," *Advances in Aircraft Flight Control*, edited by M. B. Tischler, chap. 1, Taylor & Francis, Philadelphia, PA, 1996, pp. 18–20.

[68] McRuer, D. T., Clement, W. F., Thompson, P. M., and Magdaleno, R. E., "Minimum Flying Qualities Volume II: Pilot Modeling for Flying Qualities Applications," Final Report STI-TR-1235-1-II, U.S. Air Force Wright Research & Development Center, Wright-Patterson AFB, 1989.

[69] Campbell, F. W., and Robson, J. G., "Application of Fourier analysis to the visibility of gratings," *Journal of Physiology*, Vol. 197, 1968, pp. 551–566.

[70] Yura, H. T., "Small-Angle Scattering of Light by Ocean Water," *Applied Optics*, Vol. 10, (1), January, 1971, pp. 114–118.

[71] Fante, R. L., "Mutual Coherence Function and Frequency Spectrum of a Laser Beam Propagating Through Atmospheric Turbulence," *Journal of the Optical Society of America*, Vol. 64, (5), May, 1974, pp. 592–598.

[72] Kuga, Y., and Ishimaru, A., "Modulation Transfer Function and Image Transmission Through Randomly Distributed Particles," *Journal of the Optical Society of America A*, Vol. 2, (12), 1985, pp. 2330–2336.

[73] Rovamo, J., Kukkonen, H., and Mustonen, J., "Foveal Optical Modulation Transfer Function of the Human Eye at Various Pupil Sizes," *Journal of the Optical Society of America A*, Vol. 15, (9), September, 1998, pp. 2504–2513.

[74] Kohm, K., "Modulation Transfer Function Measurement Method and Results for the Orbview-3 High Resolution Imaging Satellite," *International Archives of the Photogrammetry, Remote Sensing, and Spatial Information Sciences*, Vol. 35, 2004, pp. 7–12.

[75] Bravo-Zanoguera, M. E., Rivera-Castillo, J., Vera-Pérez, M., and Reyna-Carranza, M. A., "Use of the Modulation Transfer Function to Measure Quality of Digital Cameras," Proceedings of the 16th IEEE International Conference on Electronics, Communications and Computers (CONIELECOMP 2006), Cholula, Puebla, Mexico, February 27–March 1, 2006.

[76] Kopeika, N., Solomon, S., and Gencay, Y., "Wavelength variation of visible and near-infrared resolution through the atmosphere: dependence on aerosol and meteorological conditions," *Journal of the Optical Society of America A*, Vol. 71, (7), 1981, pp. 892–901.

[77] Dror, I., and Kopeika, N., "Aerosol and Turbulence Modulation Transfer Functions: Comparison Measurements in the Open Atmosphere," *Optics Letters*, Vol. 17, (21), 1994, pp. 1532–1534.

[78] Dror, I., and Kopeika, N., "Experimental comparison of turbulence modulation transfer function and aerosol modulation transfer function through the open atmosphere," *Journal of the Optical Society of America A*, Vol. 12, (5), 1995, pp. 970–980.

[79] Sadot, D., and Kopeika, N., "Imaging through the atmosphere: practical instrumentation-based theory and verification of aerosol modulation transfer function," *Journal of the Optical Society of America A*, Vol. 10, (1), January, 1993, pp. 172–179.

[80] Kopeika, N., and Sadot, D., "Imaging through the atmosphere: practical instrumentation-based theory and verification of aerosol modulation transfer function: reply to comment," *Journal of the Optical Society of America A*, Vol. 12, (5), May, 1995, pp. 1017–1023.

[81] Sadot, D., and Kopeika, N., "Effects of absorption on image quality through a particulate medium," *Applied Optics*, Vol. 33, (30), October, 1994, pp. 7107–7111.

[82] Sadot, D., Kitron, G., Kitron, N., and Kopeika, N., "Thermal Imaging Through the Atmosphere: Atmospheric Modulation Transfer Function Theory and Verification," *Optical Engineering*, Vol. 33, (3), March, 1994, pp. 881–888.

[83] Sadot, D., Shamriz, S., Sasson, I., Dror, I., and Kopeika, N., "Prediction of Overall Atmospheric Modulation Transfer Function with Standard Weather Parameters: Comparison with Measurements with Two Imaging Systems," *Optical Engineering*, Vol. 34, (11), November, 1995, pp. 3239–3248.

[84] Kopeika, N. S., *A System Engineering Approach to Imaging*, SPIE Optical Engineering Press, Bellingham, WA, 1998.

[85] Lutomirski, R. F., "Atmospheric degradation of electrooptical system performance," *Applied Optics*, Vol. 17, (24), July–August, 1978, pp. 3915–3921.

[86] Ishimaru, A., *Wave Propagation and Scattering in Random Media*, IEEE Press, New York, NY, 1997 (Re-issue of two-volume set from Academic Press, 1978).

[87] Jones, D. R., "A Taxonomy of Global Optimization Methods Based on Response Surfaces," *Journal of Global Optimization*, Vol. 21, 2001, pp. 345–383.

[88] Vanderplaats, G. N., "Approximation Concepts for Numerical Airfoil Optimization," Technical Paper 1370, NASA, 1979.

[89] Vanderplaats, G. N., *Numerical Optimization Techniques for Engineering Design: With Applications*, McGraw-Hill, New York, NY, 1984.

[90] Ganguli, R., "Optimum Design of a Helicopter Rotor for Low Vibration Using Aeroelastic Analysis and Response Surface Methods," *Journal of Sound andVibration*, Vol. 258, (2), 2002, pp. 327–344.

[91] Hosder, S., Watson, L. T., Grossman, B., Mason, W. H., Kim, H., Haftka, R. T., and Cox, S. E., "Polynomial Response Surface Approximations for the Multidisciplinary Design Optimization of a High Speed Civil Transport," *Optimization and Engineering*, Vol. 2, 2001, pp. 431–452.

[92] Venter, G., Haftka, R. T., and Starnes, J. H., "Construction of Response Surface Approximations for Design Optimization," *AIAA Journal*, Vol. 36, (12), December, 1998, pp. 2242–2249.

[93] Gutman, H. M., "A Radial Basis Function Method for Global Optimization," *Journal of Global Optimization*, Vol. 19, 2001, pp. 201–227.

[94] Simpson, T. W., Mauery, T. M., Korte, J. J., and Mistree, F., "Kriging Models for Global Approximation in Simulation-Based Multidisciplinary Design Optimization," *AIAA Journal*, Vol. 39, (12), December, 2001, pp. 2233–2241.

[95] Batill, S. M., Stelmack, M. A., and Sellar, R. S., "Framework for Multidisciplinary Design Based on Response-Surface Approximations," *Journal of Aircraft*, Vol. 36, (1), January–February, 1999, pp. 287–297.

[96] Haftka, R., and Gurdal, Z., *Elements of Structural Optimization*, Kluwer Academic Publishers, Norwell, MA, 3rd ed., 1992.

[97] Grossman, I. E., "Review of Nonlinear Mixed-Integer and Disjunctive Programming Techniques," *Optimization and Engineering*, Vol. 3, 2002, pp. 227–252.

[98] Thanedar, P. B., and Vanderplaats, G. N., "Survey of Discrete Variable Optimization for Structural Design," *Journal of Structural Engineering*, Vol. 121, (2), February, 1995, pp. 301–306.

[99] Buonanno, M. A., and Mavris, D. N., "Aerospace Vehicle Concept Selection Using Parallel, Variable Fidelity Genetic Algorithms," 10th AIAA/ISSMO Multidisciplinary Analysis and Optimization Conference, Albany, NY, August 30–September 1, 2004.

[100] Buonanno, M. A., and Mavris, D. N., "Small Supersonic Transport Concept Evaluation Using Interactive Evolutionary Algorithms," AIAA 4th Aviation Technology, Integration and Operations (ATIO) Forum, Chicago, IL, September 20–22, 2004.

[101] Buonanno, M. A., and Mavris, D. N., "A New Method for Aircraft Concept Selection Using Multicriteria Interactive Genetic Algorithms," 43rd AIAA Aerospace Sciences Meeting and Exhibit, Reno, NV, January 10–13, 2005.

[102] Eele, A., and Richards, A., "Path-Planning with Avoidance Using Nonlinear Branch-and-Bound Optimization," *Journal of Guidance, Control, and Dynamics*, Vol. 32, (2), March–April, 2009, pp. 384–394.

[103] Gantovnik, V. B., Anderson-Cook, C. M., Gurdal, Z., and Watson, L. T., "A genetic algorithm with memory for mixed discrete-continuous design optimization," *Computers and Structures*, Vol. 81, (20), August, 2003, pp. 2003–2009.

[104] Gantovnik, V. B., Gurdal, Z., Watson, L. T., and Anderson-Cook, C. M., "Genetic Algorithm for Mixed Integer Nonlinear Programming Problems Using Separate Constraint Approximations," *AIAA Journal*, Vol. 43, (8), August, 2005, pp. 1844–1849.

[105] Gant, R., "Owning the Aviation Edge: NVGPID—A Simple Device to Train Crucial Skills," *Army Aviation*, April/May, 2007, pp. 22–24.

[106] Pickford, M., "Operating Helicopters Safely in a Degraded Visual Environment in Support of Military Operations," Royal Aeronautical Society Rotorcraft Group Conference, Operating Helicopters Safely in a Degraded Visual Environment, London, UK, June 16–17, 2010.

[107] Leishman, J. G., Bhagwat, M. J., and Ananthan, S., "The Vortex Ring State as a Spatially and Temporally Developing Wake Instability," *Journal of the American Helicopter Society*, Vol. 49, (2), April, 2004, pp. 160–175.

[108] Phillips, C., Kim, H. W., and Brown, R. E., "The Effect of Rotor Design on the Fluid Dynamics of Brownout," 35th European Rotorcraft Forum Proceedings, Hamburg, Germany, September 22–25, 2009.

[109] Leishman, J. G., Bhagwat, M. J., and Bagai, A., "Free-Vortex Filament Methods for the Analysis of Helicopter Rotor Wakes," *Journal of Aircraft*, Vol. 39, (5), September–October, 2002, pp. 759–775.

[110] Griffiths, D. A., Ananthan, S., and Leishman, J. G., "Predictions of Rotor Performance in Ground Effect Using a Free-Vortex Wake Model," *Journal of the American Helicopter Society*, Vol. 50, (4), 2005, pp. 302–314.

[111] Syal, M., *Development of a Mesoscale Sediment Tracking methodology for Brownout Applications*, Ph.D. thesis, University of Maryland, 2012.

[112] Bhagwat, M. J., and Leishman, J. G., "Accuracy of Straight-Line Segmentation Applied to Curvilinear Vortex Filaments," *Journal of the American Helicopter Society*, Vol. 46, (2), April, 2001, pp. 166–169.

[113] Weissinger, J., "The Lift Distribution of Swept-Back Wings," NACA TM 1120, 1947.

[114] Ananthan, S., *Analysis of Rotor Wake Aerodynamics During Maneuvering Flight Using a Free-Vortex Wake Methodology*, Ph.D. thesis, University of Maryland, 2006.

[115] Bhagwat, M. J., *Mathematical modeling of the Transient Dynamics of Helicopter Rotor wakes Using a Time-Accurate Free-Vortex Method*, Ph.D. thesis, University of Maryland, 2001.

[116] Bhagwat, M. J., and Leishman, J. G., "Time-Accurate Modeling of Rotor Wakes Using A Free-Vortex Wake Method," 18th AIAA Applied Aerodynamics Conference Proceedings, Denver, CO, August, 2000.

[117] Vatistas, G. H., Kozel, V., and Mih, W. C., "A Simpler Model for Concentrated Vortices," *Experiments in Fluids*, Vol. 31, 1991, pp. 73–76.

[118] Bhagwat, M. J., and Leishman, J. G., "Generalized Viscous Vortex Core Models for Application to Free-Vortex Wake and Aeroacoustic Calculations," American Helicopter Society International 58th Annual Forum Proceedings, Montréal, Canada, June 11–13, 2002.

[119] Ramasamy, M., and Leishman, J. G., "A Generalized Model for Transitional Blade Tip Vortices," American Helicopter Society International 60th Annual Forum Proceedings, Baltimore, MD, June 7–11, 2004.

[120] Ananthan, S., and Leishman, J. G., "Role of Filament Strain in the Free-Vortex Modeling of Rotor Wakes," *Journal of the American Helicopter Society*, Vol. 49, (2), April, 2004, pp. 176–191.

[121] Bagnold, R. A., *The Physics of Blown Sand and Desert Dunes*, Dover Publications, Mineola, NY, 1941.

[122] Greeley, R., and Iversen, J. D., *Wind as a Geological Process on Earth, Mars, Venus, and Titan*, Cambridge University Press, New York, NY, 1985.

[123] Shao, Y., *Physics and Modeling of Wind Erosion*, Springer Science + Business Media, 2nd ed., 2008.

[124] Shao, Y., and Lu, H., "A Simple Expression for Wind Erosion Threshold Friction Velocity," *Journal of Geophysical Research*, Vol. 105, (D17), 2000, pp. 437–443.

[125] Shao, Y., Raupach, M. R., and Findlater, P. A., "Effect of Saltation Bombardment on the Entrainment of Dust by the Wind," *Journal of Geophysical Research*, Vol. 98, (D7), 1993, pp. 12719–12726.

[126] Lu, H., and Shao, Y., "A New Model for Dust Emission by Saltation Bombardment," *Journal of Geophysical Research*, Vol. 104, (D14), 1999, pp. 16827–16842.

[127] Aoyama, Y., and Nakano, J., *RS/6000 SP: Practical MPI Programming*, IBM Redbooks, 1999.

[128] Anonymous, "NVIDIA CUDA C Programming Guide," Version 4.1, NVIDIA, 2011.

[129] Griva, I., Nash, S. G., and Sofer, A., *Linear and Nonlinear Optimization*, Society for Industrial and Applied Mathematics, Philadelphia, PA, 2nd ed., 2009.

[130] Nocedal, J., and Wright, S. J., *Numerical Optimization*, Springer, New York, NY, 2nd ed., 2006.

[131] Regis, R. G., and Shoemaker, C. A., "Improved strategies for radial basis function methods for global optimization," *Journal of Global Optimization*, Vol. 37, 2007, pp. 131–135.

[132] Reeves, C. R., and Rowe, J. E., *Genetic Algorithms: Principles and Perspectives*, Kluwer Academic Publishers, New York, NY, 2002.

[133] Rash, C. E., McLean, W. E., Mozo, B. T., Licina, J. R., and McEntire, B. J., "Human Factors and Performance Concerns for the Design of Helmet-Mounted Displays," 37th European Rotorcraft Forum Proceedings, Gallarate (VA), Italy, September 13–15, 2011.

[134] Ivey, R. H., Rash, C. E., Levine, R. R., Wentworth, S. L., and McGowin, E., "Utilization of Visual Ports in U.S. Army Rotary-wing Aircraft," USAARL Report No. 95-34, U.S. Army Aeromedical Research Laboratory, Fort Rucker, AL, August 1995.

[135] Heffley, R. K., "A Model for Manual Decelerating Approaches to Hover," 15th Annual Conference on Manual Control Proceedings, November, 1979, pp. 545–554.

[136] Moen, G. C., DiCarlo, D. J., and Yenni, K. R., "A Parametric Analysis of Visual Approaches for Helicopters," Technical Note D-8275, NASA, 1976.

[137] Drees, J. M., and Hendal, W. P., "Airflow Patterns in the Neighborhood of Helicopter Rotors," *Aircraft Engineering*, Vol. 23, (266), 1951, pp. 107–11.

[138] Leishman, J. G., *Principles of Helicopter Aerodynamics*, Cambridge University Press, New York, NY, 2nd ed., 2006.

[139] Johnson, W., *Helicopter Theory*, Princeton University Press, Princeton, NJ, 1980.

[140] Otsu, N., "A Threshold Selection Method from Gray-Level Histograms," *IEEE Transactions on Systems, Man, and Cybernetics*, Vol. 9, (1), 1971, pp. 62–66.

[141] Sonka, M., Hlavac, V., and Boyle, R., *Image Processing, Analysis, and Machine Vision*, Thomson Learning, Toronto, ON, 2008.

[142] Jepson, A., and Richards, W., "What makes a good feature?" *Spatial Vision in Humans and Robotsl*, edited by Harris and Jenkin, chap. 6, Cambridge University Press, New York, NY, 1993.

[143] Bohren, C. F., and Huffman, D. R., *Absorption and Scattering of Light by Small Particles*, John Wiley & Sons, New York, 1983.

[144] Mishchenko, M. I., Travis, L. D., and Lacis, A. A., *Scattering, Absorption, and Emission of Light by Small Particles*, Cambridge University Press, New York, NY, 2002.

[145] Mishchenko, M. I., Travis, L. D., and Lacis, A. A., *Multiple Scattering of Light by Particles: Radiative Transfer and Coherent Backscattering*, Cambridge University Press, New York, NY, 2006.

[146] Madau, P., "Radiative Transfer in a Clumpy Universe: The Colors of High-Redshift Galaxies," *The Astrophysical Journal*, Vol. 441, (1), 1995, pp. 18–27.

[147] Razoumov, A., Norman, M., Abel, T., and Scott, D., "Cosmological Hydrogen Reionization with Three-Dimensional Radiative Transfer," *The Astrophysical Journal*, Vol. 572, (2), June 2002, pp. 695–704.

[148] Arridge, S. R., and Hebden, J. C., "Optical Imaging in Medicine: II. Modeling and Reconstruction," *Phys. Med. Biol.*, Vol. 42, 1997, pp. 841–853.

[149] Patterson, M. S., Wilson, B. C., and Wyman, D. R., "The Propagation of Optical Radiation in Tissue: I. Models of Radiation Transport and their Application," *Lasers in Medical Science*, Vol. 6, (2), 1991, pp. 155–168.

[150] Mie, G., "Beiträge zur Optik trüber Medien speziell kolloidaler Metallösungen," *Ann Phys.*, Vol. 25, 1908, pp. 377–445.

[151] Driggers, R. G., editor, *Encyclopedia of Optical Engineering, Volume 2*, Marcel Dekker, New York, 2003.

[152] Deirmendjian, D., *Electromagnetic Scattering on Spherical Polydispersions*, Elsevier, New York, 1969.

[153] Baharani, A., *Effects of Aeolian Scaling Parameters on Sediment Mobilization Below a Hovering Rotor*, Master's thesis, University of Maryland, 2011.

[154] Ribera, M., *Helicopter Flight Dynamics Simulation with a Time-Accurate Free-Vortex Wake Model*, Ph.D. thesis, University of Maryland, 2007.

[155] Peatross, J., and Ware, M., *Physics of Light and Optics*, available at optics.byu.edu, 2011c ed., 2011.